

SCALES AND STRUCTURES OF BAROCLINIC WAVES  
AND THEIR INFLUENCE ON CLIMATIC STATES

by

LEE EDWARD BRANSCOME

B.S., Florida State University, 1975

SUBMITTED IN PARTIAL FULFILLMENT  
OF THE REQUIREMENTS FOR THE  
DEGREE OF

DOCTOR OF PHILOSOPHY

at the

MASSACHUSETTS INSTITUTE OF TECHNOLOGY

November 1980

Signature of Author .....  
Department of Meteorology & Physical Oceanography  
November 1980

Certified by .....  
Thesis Supervisor

Accepted by .....  
Chairman, Departmental Committee on Graduate Students

LIBRARY  
MASSACHUSETTS INSTITUTE OF TECHNOLOGY  
WITHDRAWN  
FROM  
MIT LIBRARIES

SCALES AND STRUCTURES OF BAROCLINIC WAVES  
AND THEIR INFLUENCE ON CLIMATIC STATES

by

LEE EDWARD BRANSCOME

Submitted to the Department of Meteorology and Physical Oceanography on November 6, 1980 in partial fulfillment of the requirements for the degree of Doctor of Philosophy.

ABSTRACT

The classic Charney problem of baroclinic instability in a quasi-Boussinesq fluid on a  $\beta$ -plane is examined through perturbation techniques in the short-wave limit and near the neutral curve separating Green and Charney modes. This analysis allows relatively simple representation of the unstable Charney and Green modes. The rapidly growing Charney modes have a vertical scale of  $H/(1+\gamma)$  and a horizontal scale of  $\frac{NH}{f(1+\gamma)}$  where  $H$  = density scale height,  $\gamma = \frac{\beta N^2 H}{f^2 \frac{\partial \bar{u}}{\partial z}}$ , and  $\bar{u}$  = mean zonal flow. For  $\gamma \gg 1$  the waves are short and shallow. For weak  $\beta$ -effect ( $\gamma \ll 1$ ) the waves approach an Eady limit and have the traditional horizontal scale of baroclinic instability,  $NH/f$ .

The results of the perturbation analysis are used to suggest heat flux parameterizations for the Charney modes. The wave amplitude is assumed to be proportional to the zonal available potential energy across the perturbation meridional scale. The wave's vertical and horizontal scales as related to the mean flow parameters determine the strength of the flux. For large  $\gamma$  the vertically averaged flux is weak since the waves are short and shallow. This is analogous to the two-level model which is stable (i.e. no baroclinic fluxes) for  $\gamma > 1$ .

The parameterization scheme is tested in a symmetric general circulation model and reproduces several features of the extra-tropical eddy heat transports. Feedbacks involving the vertical flux as it is forced by the meri-

dional temperature gradient dominate the selection of the wave scales and the efficiency of the baroclinic transports.

Similar concepts of eddy mixing are used with potential vorticity and entropy conservation to develop a momentum flux parameterization. Applications are made in an analytical momentum balance model which includes eddy transport and surface stress. The barotropic mean zonal flow found in the model roughly agrees with the observed distribution and strength of the surface zonal wind. This model is also combined with the energy balance model to predict the strength of both baroclinic and barotropic mean flow.

Asymmetric motions are evidently important in maintaining the zonal circulation of Jupiter's atmosphere. An estimate of the strength of the mean meridional circulation is made on the basis of observed eddy momentum transports. The estimated meridional flow of a few  $\text{cm sec}^{-1}$  is unlikely to be observable and it is suggested that asymmetric motions are at least as important in cloud formation. The weak horizontal gradients in infrared emissions from Jupiter do not eliminate the possibility of baroclinic instability. The zonal wind-profile suggests the planetary-scale meridional temperature gradient may be significant below the cloud tops.

With consideration given to the complex Jovian cloud structure, an Eady model with vertically varying shear and static stability is examined in the long-wave limit. The most unstable wavelength is a vertically averaged radius of deformation that is weighted to levels of strong shear. The results of the long-wave analysis are applied to a simple model of the Jovian cloud system to estimate an instability scale of 8000 Km and are also used in a Jovian energy balance model.

Thesis supervisor: Peter H. Stone  
Title: Professor of Meteorology

## DEDICATION

To my parents.

## ACKNOWLEDGEMENTS

My advisor, Professor Peter H. Stone, provided many of the questions and insights that motivated this thesis. His guidance and encouragement is greatly appreciated and I consider myself fortunate to have been one of his students.

I am also very appreciative of Professor Jule G. Charney's support and encouragement during my stay at M.I.T. His deep understanding of the atmosphere is inspirational and enlightening. I enjoyed several entertaining and informative discussions with Professor Charney and Professor Ronald Prinn and thank them for serving on my thesis committee.

Wit and wisdom from my fellow students was greatly enjoyed throughout my time at M.I.T. I am especially grateful to Jon Pollack and John and Susanne Carlson for providing friendly places to stay during the final thesis preparation. John Carlson's comments are responsible for more than one good year. I also thank Carlos Nobre, Randy and Ellen Dole, Bill Gutowski, Brad Colman, Steve Ghan, Inez Fung, Charles Lin, Glenn Ray, Dushan Bukvic, Till Stoeckenius, Dave Heinold, John Sheldon, and Dan Golan for making these times more bearable.

During the first two years of my graduate study I was supported by a UCAR Fellowship and found this experience invaluable. My thesis work was supported through National Science Foundation grant ATM 76-20070.

I am indebted to Patricia Farrell for her excellent typing and Isabelle Kole for her fine drafting. Their work was indispensable.

I also thank Dr. M.-S. Yao of GISS for providing the results of his symmetric climate model in which some of my ideas on eddy fluxes are applied. It was gratifying to see these concepts at work.

## TABLE OF CONTENTS

	Page
Abstract . . . . .	2
Dedication . . . . .	4
Acknowledgements . . . . .	5
Table of Contents . . . . .	6
List of Figures . . . . .	8
List of Tables . . . . .	11
I. Introduction . . . . .	12
II. Approximate Solutions of the Charney Problem . . . . .	20
1. Scaling Analysis . . . . .	20
2. Review of Solutions . . . . .	25
3. Short-Wave Approximation . . . . .	31
4. Expansion Near First Neutral Curve . . . . .	45
5. Summary . . . . .	65
III. Parameterization of Heat Fluxes . . . . .	67
1. Development of Parameterization . . . . .	67
2. Applications to Observations and Symmetric Model . . . . .	86
3. Energy Balance Model . . . . .	104
4. Summary . . . . .	124
IV. Momentum Balance Model . . . . .	126
1. Modeling Eddy Momentum Flux . . . . .	126
2. Momentum Balance Model . . . . .	130
V. Jovian Dynamics . . . . .	144
1. Observations and Theories . . . . .	144
2. Eady Model With Vertically Varying Shear and Static Stability . . . . .	161
VI. Conclusions and Future Work . . . . .	177

	Page
Appendix A1 - Higher Orders of the Short-Wave Approximation . . . .	183
Appendix A2 - Uniform Approximation for Short-Wave Expansion . . .	185
Appendix B1 - Matching $\text{Ln} \delta $ Terms in the Near-Neutral Curve Expansion . . . . .	189
Appendix B2 - Higher Orders of the Near-Neutral Curve Expansion . .	190
References . . . . .	193
Biographical Note . . . . .	201

## LIST OF FIGURES

Figure		Page
1.1	Spectra of eddy kinetic energy and conversion of zonal available potential energy to eddy available potential energy. (from Tenenbaum, 1976).....	15
2.1a	Vertical structure of amplitude and phase of typical short Charney mode. (from Geisler and Garcia, 1977).....	27
2.1b	Same as 2.1a but for long Green mode.....	27
2.2	Stability regions of Charney model of baroclinic instability in $\gamma^{-1}$ vs. wavelength plane.....	29
2.3a	Phase speed ( $\hat{c}_r$ ) for Charney modes from short-wave approximation vs. wavenumber ( $K$ ), compared with numerical solutions of Lindzen et al (1980) and Charney (1973). $\gamma = 1$ .....	38
2.3b	Same as 2.3a but for growth rate ( $K\hat{c}_i$ ). $\gamma = 1$ .....	38
2.4a	Same as 2.3a but for $\gamma \gg 1$ . Phase speed is scaled by $\gamma$ .....	39
2.4b	Same as 2.3b but for $\gamma \gg 1$ .....	39
2.5	Amplitude and phase of rapidly growing Charney mode from short-wave approximation for $\gamma \gg 1$ . Compared with exact solution of Kuo (1973).....	41
2.6	Heat and potential vorticity fluxes from short-wave expansion as function of $z$ .....	44
2.7a	Phase speed ( $\hat{c}_r$ ) for Green and Charney modes as found to $O( \delta ^{3/2})$ from near neutral curve expansion. Compared with numerical solutions of Lindzen et al (1980) and Charney (1973). $\gamma = 1$ .....	55
2.7b	Same as 2.7a but for growth rate. $\gamma = 1$ .....	55
2.8a	Same as 2.7a but for $\gamma \gg 1$ . Phase speed scaled by $\gamma$ .....	56
2.8b	Same as 2.7b but for $\gamma \gg 1$ .....	56
2.9a	Phase and amplitude calculated to $O( \delta ^{1/2})$ from near-neutral curve expansion for typical, weakly unstable Charney mode ( $K = .98$ ). $\gamma = 1$ .....	57
2.9b	Same as 2.9a but for $K \gg 1$ , i.e. a very short Charney mode.....	57
2.10	Same as 2.9a except for $K = 1.6$ or a rapidly growing Charney mode.....	59
2.11	Same as 2.9a except for weakly unstable Green mode ( $K = .775$ ). Terms to $O( \delta ^{3/2})$ included.....	61
2.12	Potential vorticity and heat fluxes for Charney modes as functions of $z$ .....	64

Figure	Page
3.1	Ratio of vertical and horizontal heat fluxes for Charney modes as function of $z$ ..... 70
3.2	Dimensionless vertical average of parameterized horizontal heat flux vs. vertical shear. Shear is scaled by its value at $\gamma = 1$ ..... 79
3.3	Same as 3.2 but for horizontal flux vs. static stability scaled by its value at $\gamma = 1$ ..... 80
3.4.	Same as 3.2 but for vertical average of vertical heat flux vs. shear..... 82
3.5	Same as 3.3 but for vertical heat flux vs. static stability.. 83
3.6	Transient, horizontal eddy heat flux vs. height for 30°, 50°, 70° N during summer and winter. (from Oort and Rasmusson, 1971)..... 87
3.7a	Parameterized horizontal heat flux and observed total flux from Newell et al (1972) as functions of height. For same latitudes and seasons as 3.6..... 93
3.7b	Same as 3.7a except observations are transient flux from Oort and Rasmusson, 1971..... 94
3.8	Zonal wind as function of height and latitude from symmetric model and observations (Newell et al (1972))..... 96
3.9	Vertically integrated sensible heat transport in symmetric model and observed January transient and total transports (Oort and Rasmusson, 1971). Shown as functions of latitude..... 97
3.10	Northward sensible heat flux in symmetric model and observations of January transient and total eddy flux (Oort and Rasmusson). Shown as functions of height and latitude..... 99
3.11	Vertical eddy heat flux, $-\rho g \overline{w'\theta'}$ , for symmetric and three-dimensional GISS models as function of height and latitude..... 100
3.12a	Values of $\gamma$ from symmetric and three-dimensional models and observations..... 102
3.12b	Static stability in 500-1000 mb layer for symmetric and three-dimensional models and observations..... 102
3.13	Terrestrial radiative dynamical model with variable radiative equilibrium shear, $\partial \bar{u} / \partial z$ , and statically neutral radiative lapse rate, $N_r^2 = 0$ ..... 113

Figure	Page
3.14	Same as 3.13 but with fixed $\partial\bar{u}_r/\partial z$ and variable radiative time scale, $\tau_r$ .....115
3.15	Same as 3.13 but with specified static stability.....117
3.16	Same as 3.13 but with fixed $\partial\bar{u}_r/\partial z$ and variable radiative static stability, $N_r^2$ .....120
4.1	Surface zonal wind from momentum balance model and observed 1000 mb zonally averaged zonal wind for annual mean (Oort and Rasmusson, 1971).....139
5.1	Longitudinal-time mean zonal velocity observed by Voyager I on Jupiter (from Beebe et al, 1980). Planetary and zonal flow vorticity gradients are also shown.....145
5.2	Traditional view of Jovian zone-belt cloud structure and circulation.....147
5.3	Zonal velocities developed by meridional displacement of momentum-conserving parcels. Compared with observed zonal flow of Jupiter.....149
5.4	Indirect circulation pattern as alternative explanation of zone-belt structure.....154
5.5	Temperature differences between equator and other latitudes as found from thermal wind, infrared observations, and radiative equilibrium.....157
5.6	Basic state zonal flows and weighting functions, $F$ , as functions of height for Eady-type model.....167
5.7	Amplitude of lowest order vertical velocity and vertical heat flux for perturbations on zonal flows shown in 5.6.....169

## LIST OF TABLES

	Page
Table 1. Comparison of parameterized horizontal heat flux using observed mean flow parameters with observed heat flux.....	89
Table 2. Radiative-dynamical model applied to atmospheres of Mars and Jupiter for a range of external and internal parameters..	122

## CHAPTER I

## INTRODUCTION

The development of baroclinic stability theory has greatly added to our understanding of the dynamics of a variety of rotating fluid systems. The early studies of Charney (1947), Eady (1949), and Green (1960) examined the linear stability of simple atmospheric states and recognized the importance of baroclinically unstable waves in determining the structure and time scales of the observed large-scale fluctuations. The stability of more complicated atmospheric profiles has been examined, primarily by numerical methods similar to Green's analysis, but the basic results are unchanged from the original studies.

The transport properties of baroclinic waves have considerable influence in determining the mean structure of the atmospheric circulation and thermal fields in extratropical latitudes. Once the perturbations reach significant amplitudes, the conversion of mean flow available potential energy to eddy kinetic energy, Reynolds stresses, and the forcing of mean meridional circulations will all modify the original state. The atmosphere is never completely free of these modifying processes nor are these transports steady-state. Only by statistical techniques is it possible to assess the average role of the baroclinic eddies in maintaining the general circulation as described by Lorenz (1967) and many studies by Starr.

The behavior of baroclinic waves and their transport mechanisms has considerable importance in the modeling of terrestrial climatic states. To understand response of the total atmospheric-oceanic system to changes in the external forcing we must first understand how each important dynamical process responds. Certainly, the feedbacks associated with

baroclinic instability are vital in explaining the mean atmospheric structure and its response to forcing changes.

As noted by Stone (1972), baroclinic transports will be important in determining not only the horizontal temperature structure but also the vertical structure. It is rather inconsistent to model the effects of the horizontal heat flux without also including vertical stabilization caused by vertical fluxes. Ignoring the effect of vertical heat transports of baroclinic waves is an assumption that is often made in one-layer climate models and two-layer baroclinic models with fixed static stability.

The primary objective of this thesis is to study the scales and structures of baroclinically unstable waves as they relate to their heat and momentum transporting properties. The emphasis will be on finding a method of parameterizing these transports. These representations of the time-zonal mean baroclinic fluxes can then be used in analytical and numerical climate models.

The effect of a variable Coriolis parameter (the  $\beta$ -effect) has been recognized elsewhere (Charney, 1947; Green, 1960; Held, 1978) to be a crucial factor in determining the scales and structures of baroclinic waves. Convenient expressions for the linear wave structure on a  $\beta$ -plane will be found by perturbation techniques and then used in the development of flux parameterizations. In the past the complexity of exact solutions of the linear stability problem has prevented practical application to parameterization problems. The perturbation methods presented here provide comparatively simple means of representing the vertical structure of the waves and determining the most rapidly growing wavelength.

The stability analysis and parameterization methods will be limited

to the behavior of baroclinic instability of a zonally averaged circulation. Since the average state of the atmosphere is partly determined by the eddy redistribution of heat and momentum, the mean flow representation in stability analyses is somewhat arbitrary. Traditionally, the analysis uses a basic state profile of the observed zonal average of zonal wind and stratification (e.g. Gall, 1976), often neglecting latitudinal variations (Geisler and Garcia, 1977). This mean flow implicitly includes the effects of finite amplitude eddies.

An alternative is to study the stability of the thermal wind field of radiative-moist convective equilibrium or of an axisymmetric circulation driven by thermal forcing (i.e., a Hadley cell). Therefore, the mean flow is found without eddy influences. Of course, the atmospheric circulation is never in a purely axisymmetric state and temperature gradients of the magnitude found in these basic states are never allowed to develop on planetary scales.

To account for asymmetries of the surface, the stability of steady forced waves in a zonal flow should be considered. This allows eddies to draw from both standing eddy and zonal available potential energy. The instantaneous zonal flow is far from being zonally uniform. Free baroclinic waves themselves may be subject to secondary instabilities (e.g. Lin, 1979). These longitudinal nonuniformities will lead to a broad spectrum of scales in energy conversion processes as evidenced by observations (see Fig. 1.1). Substantial energy conversion occurs not only at "baroclinic" scales (wavenumber 6) but also at planetary scales (wavenumber  $\leq 3$ ).

By the subjective nature of the mean flow choice alone, it is clear that the stability analysis can give only approximate representations to

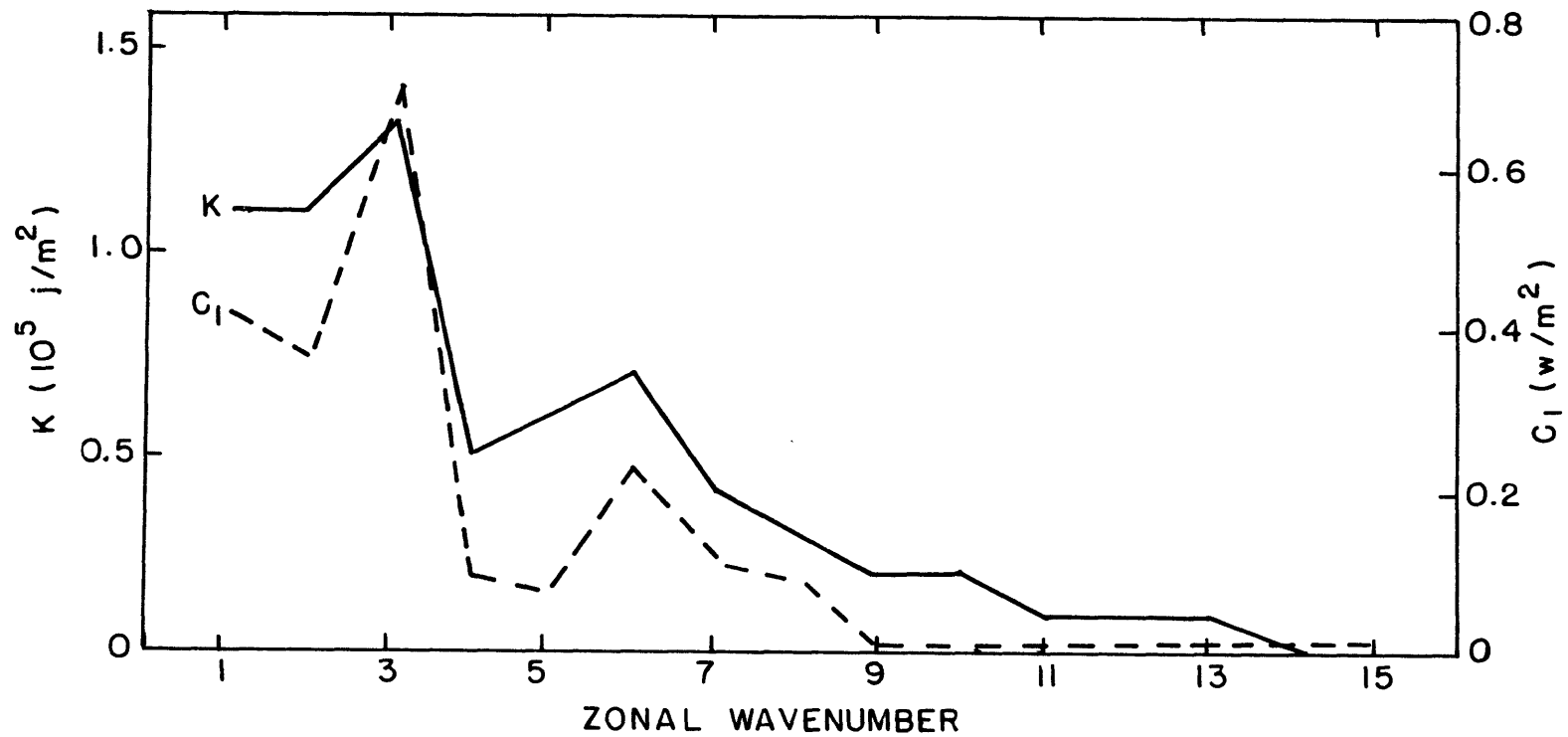


Fig. 1.1 Spectra of eddy kinetic energy ( K ) and conversion of zonal available potential energy to eddy available potential energy ( C<sub>1</sub> ). (from Tenenbaum, 1976)

the scales and structures of observed baroclinic waves. It would be a poorly defined problem to look for the exact scale and structure of baroclinic instability as it appears in the atmosphere. The important consideration must be to study the general properties of baroclinic waves and how they influence the mean flow that they appear in.

The stability analysis of zonal mean structures considers the properties of transient eddies only. From observational studies the transient eddies transfer much more heat and momentum than stationary eddies in summer and as much in winter. It is not clear what portion of the transient fluxes is caused by instability of the zonal mean flow or asymmetries in that flow. A significant part (30%) of the transient fluxes occurs at planetary scales and may be caused by instability of the mean flow, planetary-scale free baroclinic waves, or forced standing waves. Nor is it completely evident from the observations how the mean flow affects the stationary transports. However, it is clear that the primary energy source must be the differential solar heating and whether the eddy kinetic energy is realized by transient or standing eddy conversions may not be crucial in determining the zonal mean structure.

In general circulation models removal of stationary forcing increases transports by transient eddies, compensating almost fully for the loss of stationary fluxes (e.g., removal of topography, Manabe and Terpstra, 1974). Furthermore, observational studies (Holopainen, 1970; Oort and Peixoto, 1974) and models of topographically forced waves (Yao, 1980) show that the stationary eddies feed on the zonal available potential energy. Stone and Miller (1980) have shown that the total (transient plus standing) eddy heat flux has a higher correlation with the meridional temperature gradient than either of the individual components. Removal

of topography by Manabe and Terpstra(1974) from the GFDL GCM substantially reduced contributions to potential energy conversion at planetary scales, leaving a prominent spectral peak at baroclinic scales. The zonally averaged state and total energy conversion was relatively unchanged from the realistic topography simulation. The two

types of heat fluxes appear to jointly respond to changes in the external forcing.

This thesis will confine its attention to the nature of transient baroclinic waves developing on a mean zonal flow. Secondary instabilities and those caused by asymmetric forcing will not be considered, although it should be noted some of the qualitative behavior of the initial instability will also apply to waves growing in zonally non-uniform flow. Because of the negative feedbacks between stationary and transient eddies, modeling the zonal mean atmospheric structure is likely to be satisfactory when including only transient eddies as is found in general circulation models with zonally uniform surfaces. Comparisons of parameterizations developed in this thesis will be made with both observed transient and total heat fluxes.

Though the vertical structure and horizontal scale of the unstable wave can be computed by numerical methods, it is often more instructive to simplify the basic state and employ analytical techniques. By examining the classic Charney problem of baroclinic instability through perturbation analysis, approximate representations of the vertical structure of the wave streamfunction can be obtained. The stability of the mean flow with respect to the disturbance can also be ascertained.

This perturbation analysis of the simplified zonal flow profile of the Charney model is contained in Chapter II. Previous investigators have concentrated on demonstrating the instability of the flow. The analysis of Chapter II will examine the structure and horizontal and vertical scales of the linear waves in detail. The vertical structure will be described by functions that are much simpler than the exact solutions, clarifying the behavior of the linear waves and allowing

relatively convenient application to parameterizations.

The emphasis will be on the  $\beta$ -effect and will amplify the scaling analysis of Held (1978), who suggested the horizontal and vertical scales depend on the dimensionless parameter

$$\gamma = \frac{\beta N^2 H}{f^2 \frac{\partial \bar{u}}{\partial z}}$$

a dimensionless measure of the  $\beta$ -effect in baroclinic fluid with  $H =$  density scale height and  $\bar{u} =$  mean flow. The importance of this parameter to baroclinic waves is also noted by Green (1960, 1970) who recognizes  $\gamma$  as the ratio of vorticity changes from meridional advection to changes from vertical stretching. The perturbation expansion developed in Chapter II will clarify the influence of this parameter on the linear waves.

A heat flux parameterization based on these results is developed in Chapter III. As the linear stability analysis does not yield wave amplitudes, a closure assumption is required. An amplitude dependent on the mean flow parameters is chosen and is analogous to Stone's (1972) assumption of equi-partitioning of energy. Evidence from finite-amplitude theory and experimental and numerical results is reviewed in support of this hypothesis.

The parameterization scheme is tested by using observed data of the zonal mean state and comparing the predicted flux with observations of related quantities. Further testing and application is made in an axisymmetric climate model developed by Yao and Stone. This flux representation is also used in an analytic model of the planetary scale heat balance using physical parameters appropriate to earth, Mars, and Jupiter.

In the fourth chapter further use is made of these concepts to model

transient eddy momentum fluxes. Applications are made in an analytical model of the terrestrial momentum balance with emphasis on the effect of eddy scales on surface winds or barotropic zonal flow distribution.

The nature of Jovian dynamics is examined in the fifth chapter with a review of observations and theory and the suggestion for the existence of baroclinic waves. The Jovian atmosphere is expected to have considerable vertical structure from the condensation of various constituents and the deposition of solar radiation. These remarks motivate a discussion of baroclinic instability in a fluid of vertically varying shear and static stability through use of an  $f$ -plane model. A few calculations are made for an idealized representation of the Jovian cloud structure. Comments concerning the modeling of the Jovian circulation and heat balance are also offered.

In the final chapter a review of the major results is given and some conclusions are drawn concerning the influence of baroclinic waves on climatic states and general circulations of planetary atmospheres. Future work is suggested for a better understanding of baroclinic instability in more complicated fluid systems. The further development of eddy flux parameterizations for use in climate modeling and studies of the Jovian circulation may be assisted by a few speculative thoughts offered in the final section.

## CHAPTER II

## APPROXIMATE SOLUTIONS OF THE CHARNEY PROBLEM

## 1. Scaling Analysis

By performing a scaling analysis of Charney's (1947) classic model of baroclinic instability, Held (1978) noted that the horizontal wavelength of the fastest growing mode is dependent on the dimensionless parameter

$$\gamma = \frac{\beta N^2 H}{f^2 \frac{\partial \bar{u}}{\partial z}} = H/h$$

where  $H$  = density scale height,  $h = \frac{\partial \bar{u}}{\partial z} f^2 / \beta N^2$ , and  $\frac{\partial \bar{u}}{\partial z}$  = mean zonal flow vertical shear.

If  $\gamma \gg 1$  the appropriate vertical scale of the wave is  $h$  and the wavelength is on the order of  $Nh/f$ . Conversely, if  $\gamma \ll 1$  the appropriate wave depth is  $H$  and horizontal scale  $NH/f$ , the radius of deformation as it is traditionally defined. This result was also mentioned by Green (1960) in his numerical study of baroclinic instability. The scaling analysis is reviewed here.

We will examine adiabatic, inviscid, quasi-geostrophic motion on a mid-latitude  $\beta$ -plane, following the development of Charney (1973, Ch. 7). The first order equations in the Rossby number expansion can be reduced to a single equation expressing the conservation of quasi-geostrophic, pseudo-potential vorticity,  $q$  :

$$\left( \frac{\partial}{\partial t} + \vec{v} \cdot \nabla \right) q = 0 \quad (2.1.1)$$

$$\left. \begin{aligned} \text{with } q &= \nabla^2 \psi + \frac{f_0^2}{\rho_s} \frac{\partial}{\partial z} \left( \frac{\rho_s}{N_s^2} \frac{\partial \psi}{\partial z} \right) + \beta_0 \gamma \\ \psi &= \frac{p - p_s}{f_0} \quad \vec{V} = \hat{k} \times \nabla \psi \quad \frac{\partial \psi}{\partial z} = \frac{g}{f_0} (\ln \theta - \ln \theta_s) \\ N_s^2 &= \frac{\partial \ln \theta_s}{\partial z} \quad f_0 = 2\Omega \sin \phi_0 \quad \beta_0 = \frac{2\Omega}{a} \cos \phi_0 \\ \nabla &= \hat{i} \frac{\partial}{\partial x} + \hat{j} \frac{\partial}{\partial y} \end{aligned} \right\} \quad (2.1.2)$$

where  $a$  = planetary radius and other symbols have their usual meaning.

The subscript  $s$  refers to a motionless basic state that is a horizontal and time mean of the thermodynamic variables,  $\rho$ ,  $p$ , and  $\theta$ . The  $\beta$ -plane is centered on latitude  $\phi = \phi_0$  with  $y = 0$  at  $\phi_0$ .

At the lower boundary we assume a rigid, uniform surface so that the vertical velocity vanishes at  $z = 0$ . From the thermodynamic equation (cf. Charney (1973), eq. 7.38), the stream function will obey:

$$\left(\frac{\partial}{\partial t} + \vec{v} \cdot \nabla\right) \frac{\partial \psi}{\partial z} = 0 \quad \text{at } z = 0. \quad (2.1.3)$$

For the upper boundary we assume some boundness condition on  $\psi$  as  $z \rightarrow \infty$ . For our purposes, it is sufficient to use:

$$\psi \rightarrow 0 \quad \text{as } z \rightarrow \infty. \quad (2.1.4)$$

Horizontal boundary conditions are discussed below.

Next consider a linear perturbation on a zonal flow of  $\bar{u} = \bar{u}(y, z)$ . Linearizing eq. (2.1.1) we obtain an equation for the perturbation stream function:

$$\left(\frac{\partial}{\partial t} + \bar{u} \frac{\partial}{\partial x}\right) \varrho' + \frac{\partial \psi'}{\partial x} \frac{\partial \bar{u}}{\partial y} = 0. \quad (2.1.5)$$

The boundary conditions (2.1.3) and (2.1.4) become:

$$\left.\begin{aligned} \left(\frac{\partial}{\partial t} + \bar{u} \frac{\partial}{\partial x}\right) \frac{\partial \psi'}{\partial z} - \frac{\partial \psi'}{\partial x} \frac{\partial \bar{u}}{\partial z} &= 0 & \text{at } z = 0 \\ \psi' &\rightarrow 0 & \text{as } z \rightarrow \infty. \end{aligned}\right\} \quad (2.1.6)$$

The primed quantities refer to the perturbation and overbar to the mean flow. From eqs. (2.1.2), we find:

$$\varrho' = \nabla^2 \psi' + \frac{f_0^2}{\rho_s} \frac{\partial}{\partial z} \left( \frac{\rho_s}{N_s^2} \frac{\partial \psi'}{\partial z} \right) \quad (2.1.7)$$

and

$$\frac{\partial \bar{q}}{\partial y} = \beta_0 - \frac{f_0^2}{\rho_s} \frac{\partial}{\partial z} \left( \frac{\rho_s}{N_s^2} \frac{\partial \bar{u}}{\partial z} \right) - \frac{\partial^2 \bar{u}}{\partial y^2}. \quad (2.1.8)$$

Eq. (2.1.5) has been extensively studied in the examination of baroclinic and barotropic stability. Here we will consider a simple basic state which constitutes the Charney problem.

Assume that  $\frac{\partial \bar{u}}{\partial y} = 0$ ,  $\frac{\partial \bar{u}}{\partial z} = \text{constant} > 0$ ,  $\bar{u}(z=0) = 0$ ,  $N_s^2 = \text{constant}$ , and  $\rho_s(z) = \rho_s(0) e^{-z/H}$  with  $H$  also constant. Using a normal mode analysis, we let the perturbation take the form:

$$\psi' = A \Psi(z) \exp[i(kx + ly - kct)]$$

where  $\Psi(z)$  is the dimensionless vertical structure and  $A$ , an arbitrary amplitude. The motion is taken as periodic in  $x$  and  $y$  with zonal and meridional wavelengths,  $L_x = 2\pi/k$  and  $L_y = 2\pi/l$ . Rigid channel boundaries could be assumed at some  $y_{\pm}$  sufficiently distant from the center of the  $\beta$ -plane (on the order of the planetary radius) without altering the basic arguments. We will primarily be concerned with the zonal wavelength and could also assume  $l = 0$  or no meridional structure.

Eq. (2.1.5) becomes, after substituting for  $\psi'$ ,  $\bar{u}$ ,  $q'$ , and  $\frac{\partial \bar{q}}{\partial y}$ ,

$$\begin{aligned} \left( \frac{d\bar{u}}{dz} z - c \right) \left( -(k^2 + l^2) + \frac{f_0^2}{N_s^2} \frac{d^2}{dz^2} - \frac{f_0^2}{N_s^2 H} \frac{d}{dz} \right) \Psi(z) \\ + \Psi(z) \left( \beta_0 + \frac{f_0^2}{N_s^2 H} \frac{d\bar{u}}{dz} \right) = 0. \end{aligned} \quad (2.1.9)$$

The lower boundary condition (2.1.6) is:

$$c \frac{d\Psi}{dz}(0) + \frac{d\bar{u}}{dz} \Psi(0) = 0. \quad (2.1.10)$$

Now use the following scales to obtain a dimensionless form, (2.1.11), of eq. (2.1.9):  $z = H z'$ ;  $c = \frac{d\bar{u}}{dz} H c'$ ;  $(k, l) = \left(\frac{N_s H}{f_0}\right)^{-1} (k', l')$

$$\frac{d^2}{dz'^2} \Psi - \frac{d}{dz'} \Psi - \left( k'^2 - \frac{1+\gamma}{z'-c'} \right) \Psi = 0 \quad (2.1.11)$$

with  $\gamma = \frac{\beta_0 N_s^2 H}{f_0^2 \frac{d\bar{u}}{dz}} = H/h$  and  $k'^2 = k'^2 + l'^2$ .

The boundary conditions are

$$c' \frac{d\Psi}{dz'}(0) + \Psi(0) = 0 \quad \Psi(\infty) \rightarrow 0. \quad (2.1.12)$$

If  $\gamma \gg 1$  (strong static stability, large  $\beta_0$ , or weak shear), then the  $\beta_0$  term of  $\frac{\partial \bar{z}}{\partial y}$  dominates and eq. (2.1.11) is approximately:

$$\frac{d^2}{dz'^2} \Psi - \frac{d}{dz'} \Psi - \left( k'^2 - \frac{\gamma}{z'-c'} \right) \Psi = 0. \quad (2.1.13)$$

To obtain balance between the last term in eq. (2.1.13) and at least one of the first two terms, we must rescale  $z'$ ,  $c'$ ,  $k'$ , by

$$(z', c') = \gamma^{-1} (z'', c'') \quad k' = \gamma k''$$

to obtain

$$\frac{d^2}{dz''^2} \Psi - \frac{d}{dz''} \Psi - \left( k''^2 - \frac{1}{z''-c''} \right) \Psi = 0. \quad (2.1.14)$$

Similarly, eq. (2.1.12) is rescaled to:

$$c'' \frac{d\Psi}{dz''}(0) + \Psi(0) = 0.$$

Upon neglecting the second term in (2.1.14), we see that the mean flow parameters can be eliminated from the eigenvalue problem for  $c''$  in the limit  $\gamma \gg 1$ . Therefore, the appropriate scaling in

this problem is:

$$z = h z'' ; \quad c = \frac{d\bar{u}}{dz} h c'' ; \quad (k, l) = \left( \frac{N_s h}{f_0} \right)^{-1} (k'', l'')$$

where  $h = \frac{d\bar{u}}{dz} f_0^2 / \beta_0 N_s^2$  and the wavelength of maximum growth rate must be  $O\left(\frac{N_s h}{f_0}\right)$  with a growth rate of  $O(kc) = O\left(\frac{f_0}{N_s} \frac{d\bar{u}}{dz}\right)$ . This limit was noted by Green (1960) and clarified by Held (1978). Since  $\gamma$  is large for large  $H$ , this may be considered a Boussinesq or deep fluid limit. The vertical scale,  $h$ , is given by dynamical parameters and is independent of  $H$ . The stability of the zonal flow in this limit was numerically determined by Kuo (1973).

In the limit  $\gamma \ll 1$ , the term  $-\frac{f_0^2}{\rho_s} \frac{\partial}{\partial z} \left( \frac{\rho_s}{N_s^2} \frac{\partial \bar{u}}{\partial z} \right)$  dominates in  $\frac{\partial \bar{q}}{\partial y}$  and eq. (2.1.11) is approximately:

$$\frac{d^2}{dz'^2} \bar{\Psi} - \frac{d}{dz'} \bar{\Psi} - \left( k'^2 - \frac{1}{z' - c'} \right) \bar{\Psi} = 0.$$

As in the opposite limit, reference to the mean flow is removed and the original scaling is adequate with a horizontal scale of  $\frac{NH}{f_0}$  and growth rate again of  $O\left(\frac{f_0}{N_s} \frac{d\bar{u}}{dz}\right)$ .

Therefore, for strong shear or weak stratification ( $H \ll h, \gamma \ll 1$ ) measured against  $\beta_0$  in  $\gamma$ , the waves will have a vertical scale on the order of the density scale height,  $H$ , and a horizontal scale of the radius of deformation,  $\frac{N_s H}{f_0}$ . This limit will be called the Eady limit because the waves correspond to Eady's (1949)  $f$ -plane model of baroclinic instability. The vertical scale here is  $H$ , the density scale height, rather than the depth of the bounded fluid that Eady examined.

For weak shear or strong stratification ( $H \gg h$ ) the baroclinic waves are comparatively shallow with a vertical scale of  $h$ . The horizontal scale is  $\frac{N_s h}{f_0} = f_0 \frac{d\bar{u}}{dz} / \beta_0 N_s$  so that increasing the

the static stability will shorten the horizontal scale unlike the traditional radius of deformation,  $\frac{N_s H}{f_0}$ .

The dimensionless parameter,  $\gamma$ , has an interesting correspondence to the stability criterion of the Phillips two-level model as elucidated by Held (1978). The vertical shear required in a two-level model for baroclinic instability is  $\Delta u > \frac{\beta_0 \Delta \theta \Delta \Phi}{\theta_2 f_0^2}$  where  $\Delta$  represents the difference between the upper and lower levels,  $\Phi$  is the geopotential, and  $\theta_2$  is the mid-level potential temperature. Rearrangement of the inequality yields a 2-level approximation of  $\gamma < 1$ . Thus, if the unstable waves are relatively shallow ( $\gamma \gg 1$ ), they cannot be represented by a two-layer model with a depth of the density scale height and will not appear as instabilities.

On the basis of this scaling analysis, we cannot find the form of the vertical structure,  $\Psi(z)$ . However, in later discussion, some perturbation techniques will be used to obtain approximate solutions to the eigenvalue problem given by eqs. (2.1.11,12).

## 2. Review of Solutions

The Charney model and similar problems have been studied extensively since Charney's original analysis. This section will review the solutions of previous investigators and the implications for atmospheric motions.

A dimensionless measure of wavelength important in describing the stability of the mean flow is

$$r = \frac{1 + \gamma}{2(\kappa'^2 + \gamma/4)^{1/2}}$$

with  $\gamma$ ,  $\kappa'$  defined in Section II-1. Charney (1947) demonstrated graphically that for  $0 < r < 1$ , the flow is unstable, i.e.  $C$ , the phase speed, is complex. Neutral modes exist for  $r=n$  ( $n = 1, 2, 3, \dots$ ). The exact solutions of eq. (2.1.11) can be found for any  $r$  in the form

of confluent hypergeometric functions. These functions can be expressed as infinite series which terminate for  $r=n$ . For further details, the reader is referred to Charney (1973, Ch.9) or Pedlosky (1979<sub>a</sub>, Ch.7).

While application of the upper boundary condition is straightforward, applying the lower boundary condition to find the eigenvalue,  $C$ , is not trivial. By trial and error Kuo (1952) found the complex eigenvalues for  $r < 1$ . As shown by Charney (1947) the imaginary part of  $C$  is  $O((1-r)^{\frac{1}{2}})$  for  $r < 1$ . The unstable modes for  $r < 1$  are usually called "Charney modes (or waves)" and their largest streamfunction amplitudes are near the surface, esp. for short wavelengths. (See Fig. 2.1a).

In the numerical study of Green (1960) who examined a similar problem in baroclinic instability, more unstable waves were found for wavelengths greater than the Charney modes. These waves, usually termed "Green modes", have more vertical structure attaining maximum amplitudes well above the lower boundary (see Fig. 2.1b). By studying the behavior of the hypergeometric functions near the lower boundary, instability near  $r=n$  was found analytically by Burger (1962) and clarified by Miles (1964a). Near the neutral curves of  $r=n$ , growth rates are  $O((n-r)^{\frac{1}{2}})$  for  $r < n$  and  $O((r-n)^{\frac{3}{2}})$  for  $r > n$ . Neutral curves of  $r=n$  have  $n$  real values of the phase speed or eigenvalue,  $C$ , with one value of zero while the rest are negative, i.e. westward propagating waves. For  $n < r < n + 1$ ,  $n$  real eigenvalues exist and are negative (Burger, 1962; Charney, 1973).

Previous analytical studies of the Charney problem have concentrated on demonstrating the instability of the profile. They did not obtain the simple relations for vertical structure and scales of the most rapidly growing waves required to model eddy transports. In the following sections

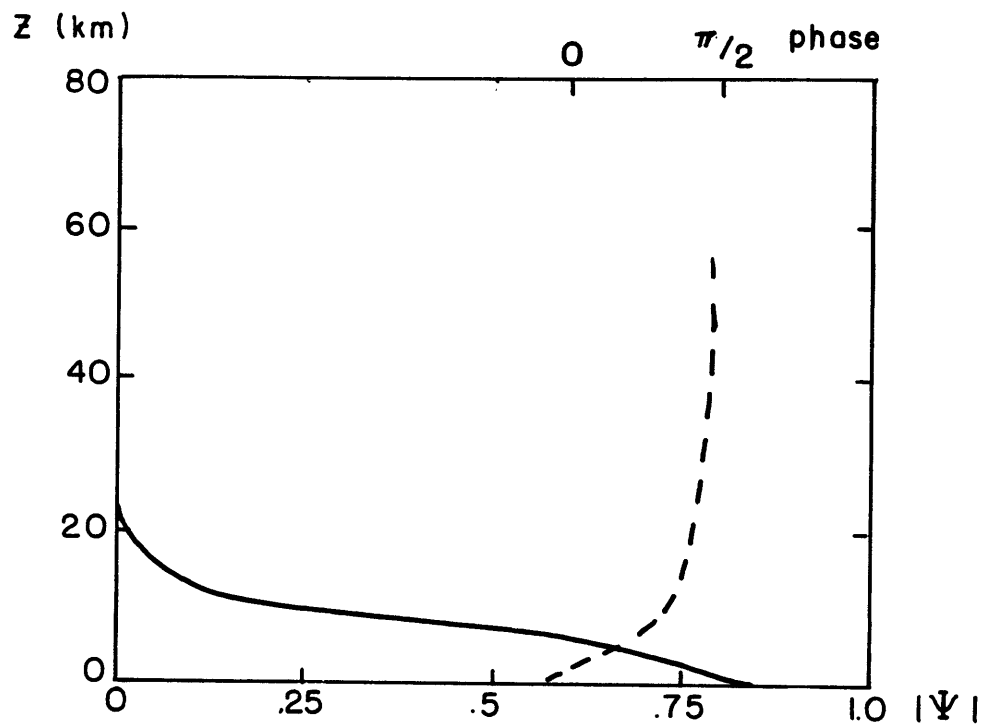


Fig. 2.1a. Typical short Charney mode (zonal wavenumber 9) from Geisler and Garcia (1977). Amplitude-solid, phase-dashed.

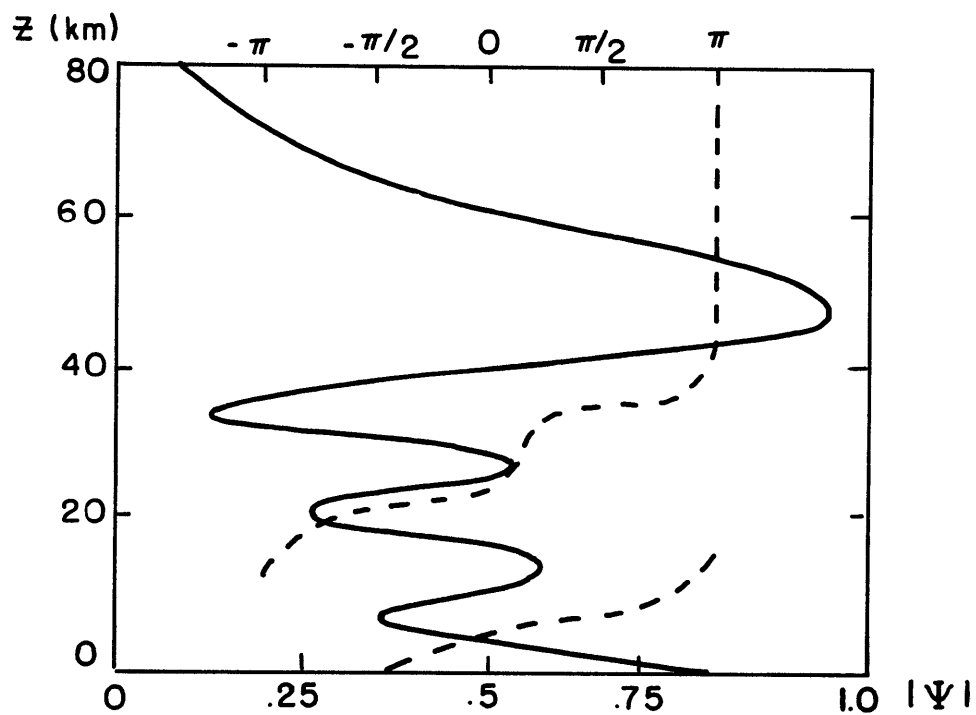


Fig. 2.1b. Same as Fig. 2.1a except for long Green mode (wavenumber 2).

expansions for the short Charney waves and near the neutral curve separating Charney and Green modes allow us to find such relations. The results clarify the dependence of the scales and the vertical structure on the mean flow parameters and differences between Charney and Green mode structures near the neutral curve.

The neutral curves and regions of instability are shown schematically in Fig. 2.2 for the  $\gamma^{-1} - k'^{-1}$  plane. The fundamental or first neutral curve ( $r = 1$ ) separates the Charney and Green modes. Near and below each neutral curve, the growth rate is  $O((r-n)^{3/2})$  and above it,  $O((n-r)^{1/2})$ . The dashed curve indicates the wavelength of maximum linear growth which occurs in the Charney mode region. This curve asymptotes to an  $O(1)$  factor of  $2\pi/k'$  for  $\gamma \ll 1$ . More detailed diagrams of the stability properties will be shown later.

The unstable waves have the characteristic baroclinic conversion process found in the simpler Eady (1949) model. Sensible heat is transported down the meridional temperature gradient, converting zonal available potential energy (A.P.E.) into eddy A.P.E. Entropy is also transported vertically converting eddy A.P.E. into eddy kinetic energy. Using observed mid-latitude parameters the wavelength of the fastest growing mode is about 4000-5000 km with a doubling time of about two days.

The remainder of this chapter will focus on the properties of the Charney modes which are the fastest growing perturbations in this model. Whether the fastest growing modes of linear analysis are the waves that accomplish most of the atmospheric energy conversion by transient waves is an open, and, perhaps, unanswerable question. Linear theory does predict the correct length and time scales and sign of energy transports and peaks in energy conversions do occur at these scales.

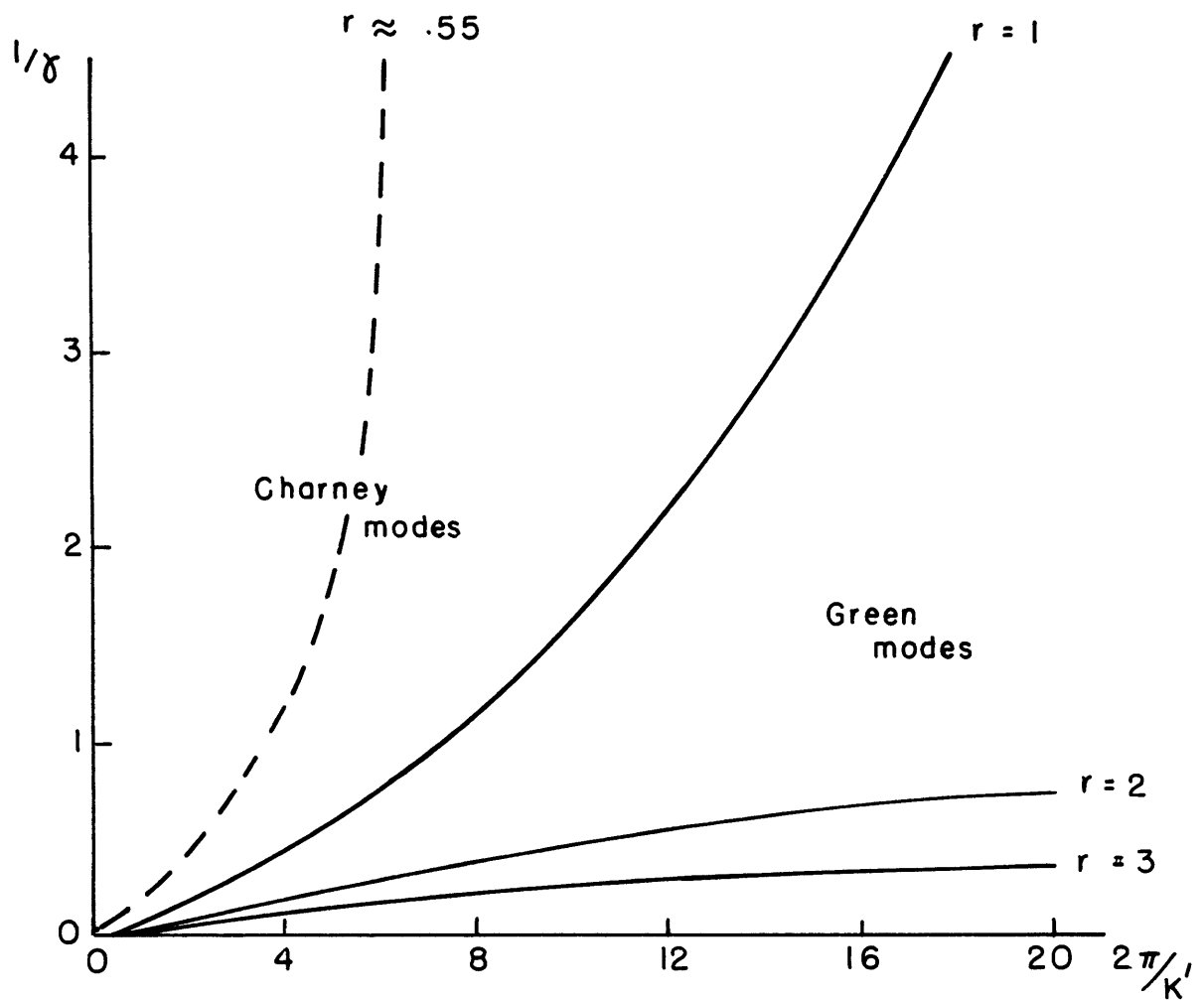


Fig. 2.2. Stability regions of Charney model. Curves of  $r=n$  ( $n=1,2,3,\dots$ ) have  $n$  neutral modes. Exponentially growing modes occur elsewhere with the most unstable waves along the dashed line in the Charney mode region ( $r < 1$ ). Along with unstable Green modes ( $r > 1$ ),  $n$  neutral modes exist for  $n < r < n+1$ . (from Charney, 1973)

Besides the considerations of zonal asymmetries discussed in Chapter I, nonlinear and dissipative effects will influence scale selection and have been compared with linear theory in the numerical investigations of Gall et al (1979) and Simmons and Hoskins (1978). The conclusions of these studies are similar. Linear analysis of observed vertically and latitudinally varying profiles found the most rapid growth at large wavenumbers (in Gall's example, zonal wavenumber 14; Simmons and Hoskins, 8-11) in apparent disagreement with observed motions and analyses using simpler profiles.

In Gall's (1976) linear analysis, the mean flow has a lower tropospheric region at 40°N with Richardson numbers of about 10, indicating the mean location of the polar front. Not surprisingly, short, shallow waves with maximum amplitudes in this region were found to have the largest growth rates in the spectrum. As suggested by Charney (personal communication), it is likely this mean polar front was formed by the action of longer waves. The basic state had already been adjusted by baroclinic waves and the choice of the mean flow proved to be crucial.

Time integrations of growing waves which allowed for interaction with the mean flow and frictional dissipation indicated the longer wavelengths (zonal wavenumber of 6-7) were likely to reach the largest amplitudes. Short waves, through having slightly larger growth rates, were damped more effectively by friction and by their stabilization of the mean flow. By the end of the time integration of Gall's study in which all waves were allowed to grow simultaneously, the linear growth rate spectrum had been shifted to lower wavenumbers through modification of the mean flow. Interestingly, once the waves reached large amplitudes, the linear stability analysis of the zonal mean flow would have predicted

the wavenumber of greatest kinetic energy.

While it is unable to determine the amplitude of waves, linear analysis will describe the general behavior of the scales and structures of the growing modes. In Chapter III, an energy balance model is developed which simultaneously solves for the characteristics of the linearly most unstable mode and the mean atmospheric state as it is adjusted by that mode. Though details of nonlinear interaction and dissipation are not included, it provides a method of studying baroclinic transports that determine the mean state.

### 3. Short-Wave Approximation

In this section we will use a perturbation expansion from the short-wave end of the spectrum to study the properties of the Charney modes. Miles (1964b) has also examined the short-wave limit and demonstrated the instability of these modes. In this section we expand this analysis to higher order to find the most unstable wave and to study vertical structure and transports. The mathematical method to be used here was first developed by McIntyre (1970) and successfully applied to other stability analyses (McIntyre, 1974; Grotjahn, 1980).

The dimensionless eigenvalue problem as given in eqs. (2.1.11,12) is repeated here, dropping primes.

$$\left. \begin{aligned} \left( \frac{d^2}{dz^2} - \frac{d}{dz} - \kappa^2 + \frac{1+\gamma}{z-c} \right) \Psi(z) &= 0 & (0 \leq z < \infty) \\ c \frac{d\Psi}{dz}(0) + \Psi(0) &= 0 & \Psi(\infty) \rightarrow 0 \end{aligned} \right\} \quad (2.3.1)$$

For mathematical purposes, we rescale the vertical co-ordinate,  $z$ , and eigenvalue,  $c$ , by

$$(\bar{z}, \bar{c}) = \kappa^{-1} (z', c')$$

and define  $B = 1 + \gamma$  and  $\epsilon = B/\kappa$ . In the new variables,

eqs. (2.3.1) become:

$$\left. \begin{aligned} \left( \frac{d'}{dz'^2} - \frac{\epsilon}{B} \frac{d}{dz'} - 1 + \frac{\epsilon}{z'-c'} \right) \Psi &= 0 \quad (0 \leq z' < \infty) \\ c' \frac{d\Psi}{dz'}(0) + \Psi(0) &= 0 \quad \Psi(\infty) \rightarrow 0 \end{aligned} \right\} (2.3.2)$$

The eigenvalue problem is considerably complicated by the basic state of  $\frac{\partial \bar{q}}{\partial y} \neq 0$  ( $\epsilon \neq 0$ ) as opposed to the much simpler Eady problem where  $\beta_0 = 0$ ,  $\rho_s = \text{constant}$ , and therefore,  $\frac{\partial \bar{q}}{\partial y} = 0$ .

We use a short-wave expansion assuming  $\epsilon \ll 1$ . This implies that  $K \gg B \geq 1$  or, in dimensional terms,

$$(k^2 + l^2)^{-1/2} \ll \frac{N_s H}{f_0 (1 + \gamma)}$$

where  $(k^2 + l^2)^{-1/2} = \frac{L_x}{2\pi (1 + (L_x/L_y)^2)^{1/2}}$  and  $L_x, L_y$

are the zonal and meridional wavelengths. We take  $L_y \geq L_x$  as no finite meridional scale is selected in this problem. With  $h = H/\gamma$  we see that if  $\gamma \gg 1$  ( $H \gg h$ ),  $L_x \ll \frac{N_s h}{f_0}$  and conversely,  $\gamma \ll 1$  implies the expansion is for  $L_x \ll \frac{N_s H}{f_0}$ . Therefore, the waves are short compared to the correct horizontal scale which is  $\frac{N_s H}{f_0 (1 + \gamma)}$  and the expansion is valid for any value of  $\gamma$ .

The imaginary part of  $c'$  is a dimensionless measure of the growth rate. The dimensioned growth rate is:

$$\sigma_i^* = \frac{k}{(k^2 + l^2)^{1/2}} \frac{d\bar{u}}{dz} \frac{f_0}{N_s} c_i'$$

where subscripts  $i, r$  will represent imaginary and real parts.

For  $l = 0$   $c_i'$  is exactly the growth rate scaled by  $\frac{d\bar{u}}{dz} \frac{f_0}{N_s}$ .

The real part of the phase speed in dimensional form is:

$$c_r^* = \frac{d\bar{u}}{dz} \frac{f_0}{N_s} \frac{1}{(k^2 + l^2)^{1/2}} c_r'$$

Expanding in powers of  $\epsilon$ :

$$\Psi(z) = \Psi_0(z) + \epsilon \Psi_1(z) + \epsilon^2 \Psi_2(z) + \dots$$

$$C' = C_0' + \epsilon C_1' + \epsilon^2 C_2' + \dots$$

the lowest order problem, dropping primes, is:

$$\left. \begin{aligned} \frac{d^2}{dz^2} \bar{\Psi}_0 - \bar{\Psi}_0 &= 0 & (0 \leq z < \infty) \\ C_0 \frac{d\bar{\Psi}_0(0)}{dz} + \bar{\Psi}_0(0) &= 0 & \bar{\Psi}_0(\infty) \rightarrow 0. \end{aligned} \right\} \quad (2.3.3)$$

The solutions for  $\bar{\Psi}_0$  and  $C_0$  are:

$$\bar{\Psi}_0 = e^{-z} \quad (2.3.4)$$

$$C_0 = 1 \quad (2.3.5)$$

where the arbitrary amplitude is chosen so that  $\bar{\Psi}_0(0) = 1$ . In dimensional form these become:

$$\begin{aligned} \bar{\Psi}_0 &= \exp \left[ - (k^2 + l^2)^{1/2} \frac{N_s}{f_0} z \right] \\ C_0^* &= \frac{d\bar{u}}{dz} \frac{f_0}{N_s} (k^2 + l^2)^{-1/2}. \end{aligned}$$

The waves have the typical exponential decay with height of Charney modes with shorter waves being shallower. The eigenvalue at this order is real and shows the shorter waves have lower steering levels.

We can write the general  $n$ th order forms of (2.3.2) as:

$$\frac{d^2}{dz^2} \bar{\Psi}_n - \bar{\Psi}_n = F_n(z) \quad (2.3.6a)$$

$$C_0 \frac{d\bar{\Psi}_n(0)}{dz} + \bar{\Psi}_n(0) = \gamma_n, \quad \bar{\Psi}_n(\infty) \rightarrow 0. \quad (2.3.6b)$$

The inhomogeneous terms are

$$F_n(z) = -\mathcal{L}_1 \Psi_{n-1} - \mathcal{L}_2 \Psi_{n-2} - \dots - \mathcal{L}_n \Psi_0$$

where  $\mathcal{L}_i$  is the  $i$ th order operator and

$$\gamma_n = -c_n \frac{d\Psi_0}{dz}(0) - c_{n-1} \frac{d\Psi_1}{dz}(0) - \dots - c_1 \frac{d\Psi_{n-1}}{dz}(0) .$$

To find  $C_n$  we find an orthogonality relation from (2.3.6a) by multiplying by  $\Psi_0$  and integrating over all  $z$ . This relation is

$$-\frac{d\Psi_n}{dz}(0) - \Psi_n(0) = \int_0^\infty \Psi_0(z) F_n(z) dz \equiv \tau_n . \quad (2.3.7)$$

Using (2.3.6b), eq. (2.3.7) can be written as

$$-\gamma_n = \tau_n \quad \text{or solving for } C_n ,$$

$$C_n (n > 1) = C_{n-1} \frac{d\Psi_1}{dz}(0) + \dots + c_1 \frac{d\Psi_{n-1}}{dz}(0) - \tau_n \quad (2.3.8)$$

$$\text{with } C_1 = -\tau_1 .$$

A Green's function method is used to find  $\Psi_n(z)$ . The equation for the generalized Green's function  $G(z;s)$  is

$$\frac{\partial^2 G}{\partial z^2} - G = A \Psi_0(z) \Psi_0(s) + \delta(z-s)$$

where  $\delta(z-s)$  is a delta function. The inhomogeneous term,  $A \Psi_0(z) \Psi_0(s)$ , must be included to allow consistency between the boundary conditions

and the equation for  $G$ . The boundary conditions are  $\frac{\partial G}{\partial z} + G = 0$

at  $z = 0$  and  $G \rightarrow 0$  as  $z \rightarrow \infty$ . The constant  $A$  is found through orthogonality of the Green's function equation with  $\Psi_0$ , namely  $A = - \left[ \int_0^\infty \Psi_0^2(z) dz \right]^{-1}$ .

The function,  $G(z;s)$ , can then be found:

$$G(z;s) = \begin{cases} -\frac{e^{s-z}}{2} + (z+s)e^{-s-z} & (\infty > z \geq s) \\ -\frac{e^{z-s}}{2} + (z+s)e^{-s-z} & (s > z \geq 0) . \end{cases}$$

To eliminate arbitrariness of adding a constant multiple of  $\Psi_0$  to  $G$ , we have taken:

$$\int_0^\infty G(z; s) \Psi_0(z) dz = 0.$$

Requiring  $\int_0^\infty \Psi_n(z) \Psi_0(z) dz = 0$ , the  $n^{\text{th}}$  order solution is:

$$\Psi_n(z) = -G(0; z) \tau_n + \int_0^\infty G(s; z) F_n(s) ds. \quad (2.3.9)$$

The order  $\epsilon$  contribution to the eigenvalue is found as follows:

$$F_1 = -\mathcal{L}_1 \Psi_0 = \left( \frac{1}{B} \frac{d}{dz} - \frac{1}{z - c_0} \right) \Psi_0$$

and from (2.3.8)

$$C_1 = -\tau_1 = - \int_0^\infty \Psi_0 \left( \frac{1}{B} \frac{d}{dz} - \frac{1}{z - c_0} \right) \Psi_0 dz.$$

Substituting from (2.3.4,5),

$$C_1 = \int_0^\infty \frac{e^{-2z}}{z - c_0} dz + \int_0^\infty \frac{e^{-2z}}{B} dz \quad (2.3.10)$$

and we find the first integral in (2.3.10) has a simple pole at  $z = c_0$ .

Following a procedure outlined by McIntyre (1970), we indent the

contour of integration into the complex  $z$  plane to avoid the pole.

Indenting into the negative imaginary half plane will yield a positive

imaginary contribution to  $C_1$ , a growing solution. This procedure is

equivalent to assuming  $c_0$  has a small, positive imaginary part, thereby

allowing integration along the real axis. We find:

$$C_1 = \frac{1}{2B} - e^{-2} \text{Ei}(2) + i\pi e^{-2} \quad (2.3.10a)$$

where  $-\text{Ei}(2) = \text{principal value of } \int_0^\infty \frac{e^{-2z}}{z-1} dz = -4.954$ .

Miles (1964b) obtained the same result for the imaginary part of  $C_1$ .

However, we must continue the analysis to obtain an estimate of the

fastest growing wavelength.

The dimensional form,  $C^*$ , to  $O(\epsilon)$  is:

$$C_r^* = \frac{d\bar{u}}{dz} \frac{f_0}{N_s} (k^2 + l^2)^{-1/2} \left[ 1 - \frac{(1+\gamma)f_0}{2N_s H} (k^2 + l^2)^{-1/2} \left( 1.34 - \frac{1}{1+\gamma} \right) \right]$$

$$C_i^* = \pi e^{-2} \frac{f_0^2}{N_s^2 H} \frac{d\bar{u}}{dz} (k^2 + l^2)^{-1} (1+\gamma).$$

The  $O(\epsilon)$  correction to  $C_r^*$  is negative for all  $\gamma$  and larger for longer waves or larger  $\beta_0$ , i.e. larger  $\epsilon$ . The growth rate,  $k C_i^*$ , approaches zero for the shortest waves ( $\epsilon \rightarrow 0$ ).

Details of calculating  $\Psi_1$  and  $C_2$  are not of interest to this discussion and are found in Appendix A1. We are primarily interested in finding the next contribution to  $C_i$  to obtain the fastest growing wavelength and the vertical structure of the phase to find heat fluxes. To  $O(\epsilon^2)$ ,

$$C_i = \epsilon \pi e^{-2} (1 - .26\epsilon) \quad (2.3.11)$$

or, in dimensional terms, the growth rate is:

$$\sigma_i^* = \frac{\pi e^{-2} \frac{d\bar{u}}{dz} f_0^2 k (1+\gamma)}{(k^2 + l^2) N_s^2 H} \left[ 1 - \frac{.26(1+\gamma)f_0}{(k^2 + l^2)^{1/2} N_s H} \right]. \quad (2.3.12)$$

For  $l = 0$  maximum growth occurs at

$$k_m = .52 (1+\gamma) \frac{f_0}{N_s H} \quad \text{or} \quad L_x = \frac{12 N_s H}{f_0 (1+\gamma)}$$

with a growth rate of  $\sigma_i^* = .41 \frac{d\bar{u}}{dz} \frac{f_0}{N_s}$ .

For  $l = k$  it occurs at

$$k_m = \frac{.52 (1+\gamma) f_0}{\sqrt{2} N_s H} \quad \text{or} \quad L_x = \frac{8.5 N_s H}{f_0 (1+\gamma)}$$

with a growth rate of  $\sigma_i^* = .29 \frac{d\bar{u}}{dz} \frac{f_0}{N_s}$ .

Using values typical of the lower winter troposphere at  $45^\circ\text{N}$  ( $\gamma = 1$ ,

$\frac{\partial \bar{u}}{\partial z} = 2 \text{ m sec}^{-1} \text{ km}^{-1}$ ,  $N_s = 1.3 \times 10^{-2} \text{ sec}^{-1}$ ,  $H = 7.6 \text{ km}$ ), we find the

most unstable wavelength with  $\ell = k$  is  $L_x = 4100$  km (zonal wavenumber 7) with an e-folding growth in 2.6 days.

The accuracy of the expansion is most easily tested by comparing the solution to numerical results. The convergence of the series is expected to be slow near  $k = k_m$  for which the second term in the series for  $C_i$  in (2.3.11) is  $-\frac{1}{2}$ . Figures 2.3a,b and 2.4a,b compare growth rates and phase speeds estimated from the expansion with numerical results for  $\gamma = 1$  and  $\gamma \gg 1$ . In these figures, phase speed is scaled by  $\frac{d\bar{u}}{dz} H$  so that dimensionless value  $\hat{c} = c/k$  is plotted. Note that growth rates and wavelength of most rapid growth are overestimated though the accuracy improves for short waves as expected in this expansion. A long-wave cutoff is predicted in accordance with the neutral curve separating rapidly growing Charney modes and slowly growing Green modes.

The nature of the solution does not change dramatically if  $\gamma = 0$  ( $B=1$ ) rather than  $\gamma = 1$  ( $B=2$ ). A non-zero basic state potential vorticity gradient is maintained by the vertical gradient of density. The short waves remain unstable and have a vertical scale of  $H$ . Furthermore, the growth rate of the most unstable wave is independent of  $\gamma$ .

The important aspect of this expansion is the short-wave behavior as it depends on mean flow parameters. We now have expressions that approximate this response for all  $\delta = H/h$ . The correct horizontal scale for the Charney modes is  $\frac{N_s H}{f_0 (1 + H/h)}$ . To first order the geopotential amplitude of the fastest growing wave has a vertical structure of

$$\Psi_0 = \exp \left[ - .52 (1 + H/h) z/H \right].$$

In agreement with scaling analysis, when  $\gamma \gg 1$ , the vertical scale

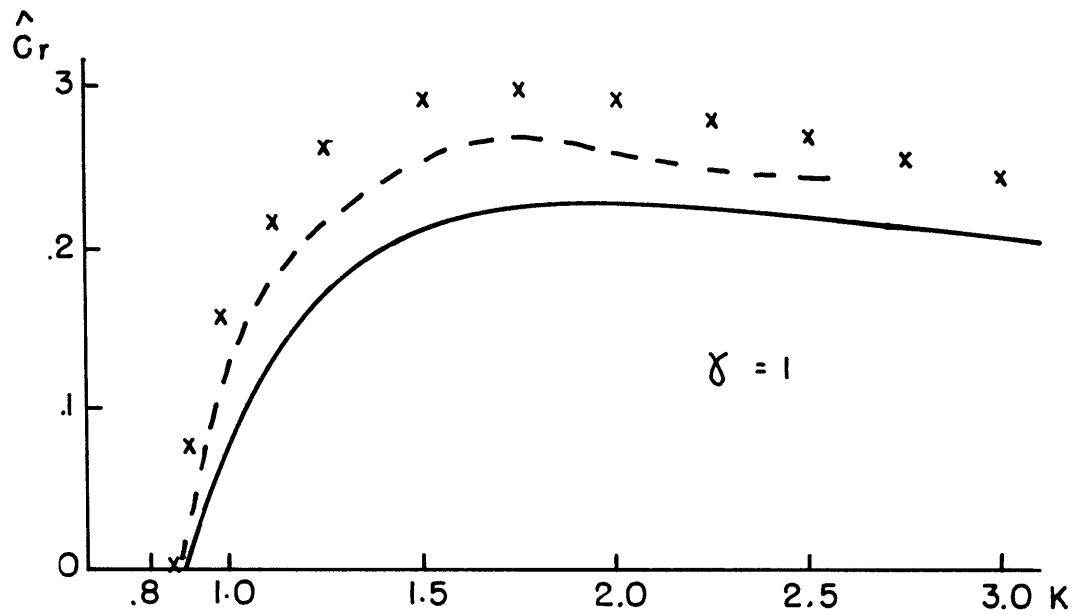


Fig. 2.3a. Wave phase speed ( $\hat{C}_r$ ) vs. wavenumber ( $K$ ) for Charney modes ( $K > .87$ ). Short-wave approximation (x) to  $O(\epsilon)$  is compared to numerical results from Lindzen et al (1980) (solid) and Charney (1973) (dashed). Phase speed scaled by  $\frac{d\bar{u}}{dz} H$ ; wavenumber by  $(\frac{N_S H}{f_0})^{-1}$ .

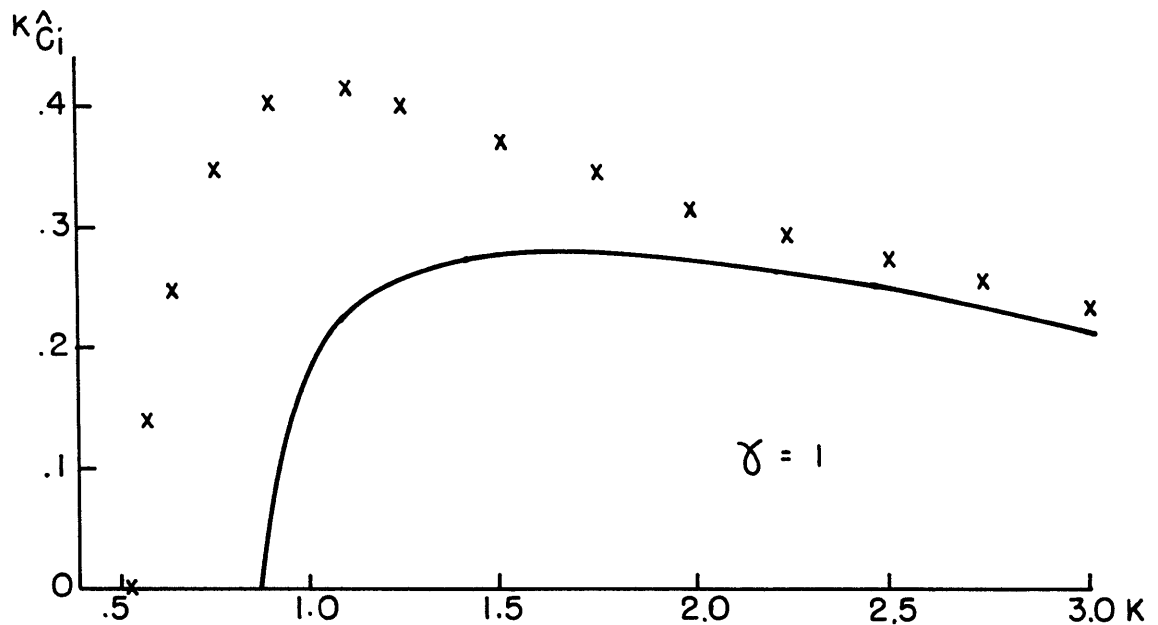


Fig. 2.3b. Growth rate measured by  $K \hat{C}_i$  for Charney modes. Short-wave approximation (x) to  $O(\epsilon^2)$  in  $\hat{C}$  is compared with results of Lindzen et al (1980). Growth rates from Charney (1973) identical to Lindzen et al. To find the actual growth rate multiply by  $[k/(k^2 + \ell^2)]^{\frac{1}{2}} \frac{d\bar{u}}{dz} \frac{f_0}{N_S}$ .

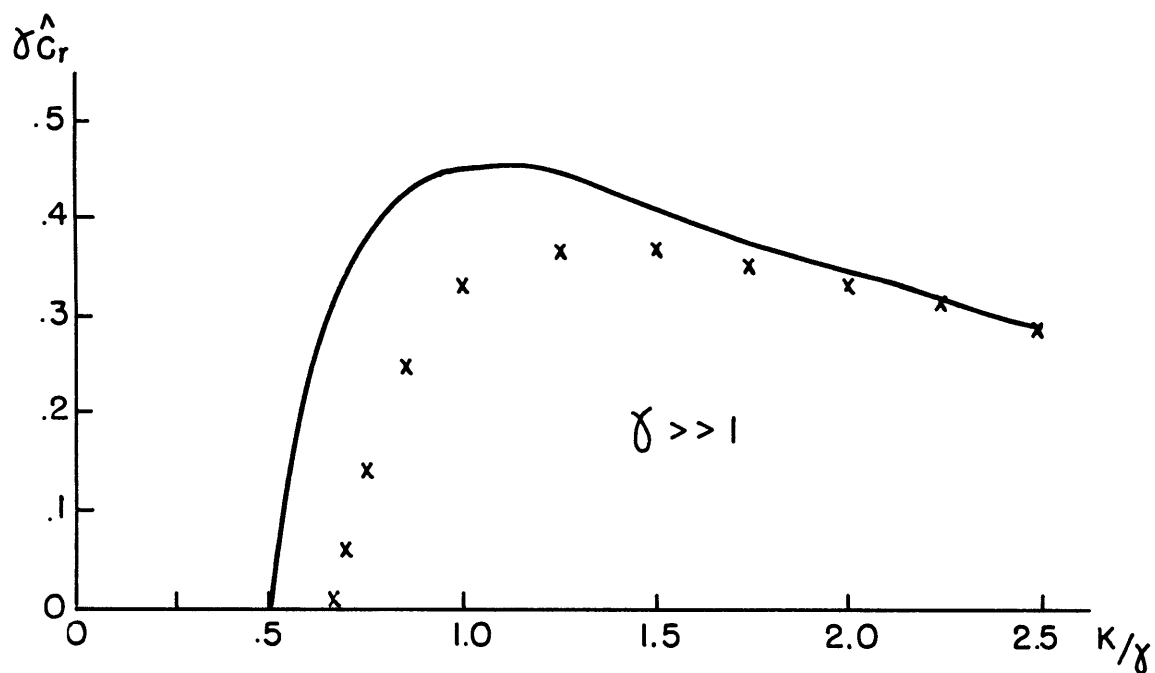


Fig. 2.4a.  $\gamma \gg 1$ : Wave phase speed ( $\gamma \hat{C}_r$ ) vs. wavenumber ( $K/\gamma$ ) for Charney modes. Short-wave approximation (x) to  $O(\epsilon)$  compared with numerical results of Kuo (1973). Dimensional phase speed  $\hat{C}_r \frac{d\bar{u}}{dz} H$ , wavenumber  $K$  ( $\frac{N_S H}{f_0}$ ).

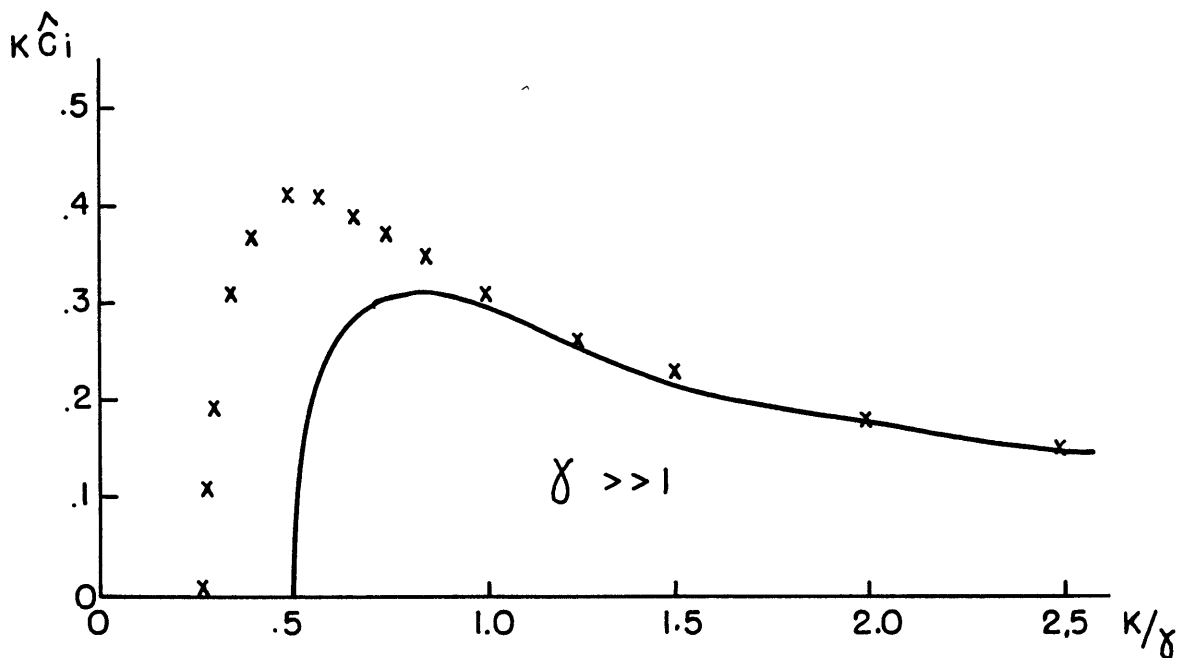


Fig. 2.4b.  $\gamma \gg 1$ : Same as Fig. 2.4a except for growth rate ( $K \hat{C}_i$ ).

is  $h = \frac{d\bar{u}}{dz} f_0^2 / N_s^2 \beta_0$  and horizontal scale  $N_s h / f_0$ .

Conversely, if  $\gamma \lesssim 1$ , the wave decays exponentially with a scale of the order of  $H$  and has a horizontal scale of  $\frac{N_s H}{f_0}$ . The growth rate remains  $O\left(\frac{d\bar{u}}{dz} f_0 / N_s\right)$  for all  $\gamma$ , while the phase speed is  $O\left(\frac{d\bar{u}}{dz} \frac{H}{1+H/h}\right)$  or the zonal flow speed at the scale height of the wave amplitude.

These scales can also be important in oceanic stability analyses as found by Gill et al (1974). The fastest growing waves were very shallow, short, near-surface modes since  $\gamma \sim 60$  in the uppermost layers of their basic state profiles. Much deeper, longer, more slowly growing waves were also found much like atmospheric Green modes. Gill et al also pointed out that the shallow waves were not represented in a two-level model corresponding to the previous discussion of resolving shallow waves in Phillips' model. Therefore, the vertical resolution of numerical studies of baroclinic waves must be at least  $O(H/(1+\gamma))$ . Since  $\gamma \sim 1$  for many atmospheric and oceanic profiles, the two-level model has been fairly successful.

The vertical structure of amplitude and phase is compared with exact solutions in Fig. 2.5 near the wavelength of maximum growth for  $\gamma \gg 1$ . The lowest order solution gives a good representation of the amplitude's nearly exponential decay with height. This structure is also seen in the short waves of the numerical calculations of Geisler and Garcia (1977) as seen in Fig. 2.1.a and Lindzen et al (1980) in which  $\gamma \sim 1$ . The phase approximation has a discontinuity in derivative at  $z = c_0$  but simulates the vertical variation fairly well. This discontinuity in phase leads to discontinuities in the wave fluxes and will be discussed in more detail below.

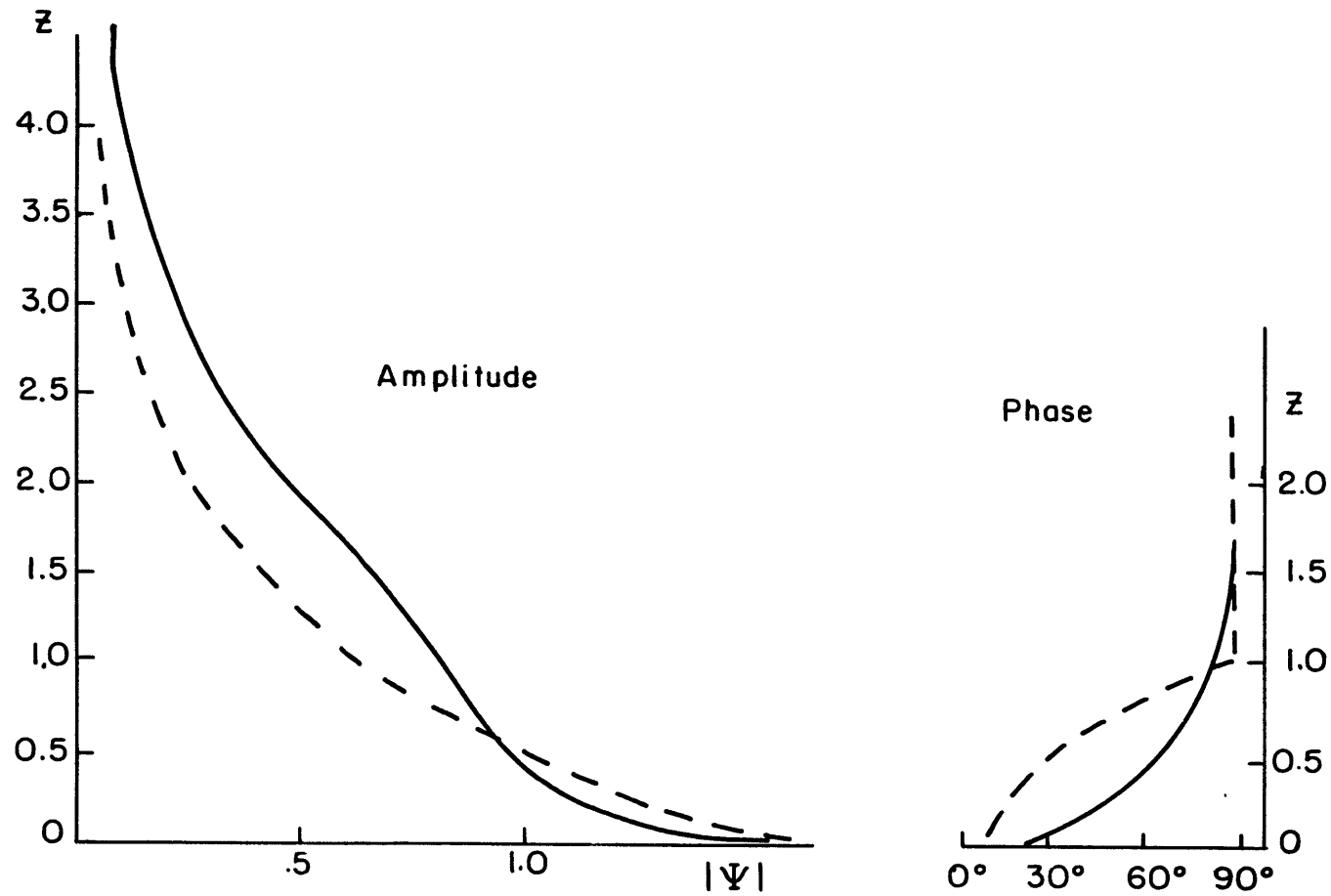


Fig. 2.5. Amplitude and phase of short-wave expansion (dashed) vs. exact solution (solid) from Kuo (1973) for  $\gamma \gg 1$  and  $K = \gamma$  ( $r = 0.5$ ). This wavelength is close to most rapidly growing mode ( $r = 0.55$ ). The vertical co-ordinate is scaled by  $H/K$ .

With the following scaling (the original scaling of eg. 2.1.11),

$$(x^*, y^*) = \frac{N_s H}{f_0} (x, y) ; \quad z^* = H z ; \quad t^* = \frac{d\bar{u}}{dz} \frac{f_0}{N_s} t$$

dimensionless vertical structures of heat and potential vorticity

fluxes are calculated as follows:

$$\overline{v'\theta'} \propto \overline{\frac{\partial \psi'}{\partial x} \frac{\partial \psi'}{\partial z}} \quad \overline{w'\theta'} \propto \overline{\left(-\frac{\partial}{\partial t} + \bar{u} \frac{\partial}{\partial x}\right) \frac{\partial \psi'}{\partial z} + \frac{d\bar{u}}{dz} \frac{\partial \psi'}{\partial x}} \frac{\partial \psi'}{\partial z}$$

$$\overline{v'q'} \propto \overline{\frac{\partial \psi'}{\partial z} \left(\nabla^2 \psi' + \left(\frac{\partial^2}{\partial z^2} - \frac{\partial}{\partial z}\right) \psi'\right)}$$

where all variables are real and the overbar is a zonal average.

For  $(A, B) = (a(z), b(z)) e^{i(k'x + l'y - k'c't)}$

$$\overline{A_r B_r} = \frac{1}{2} (ab^*)_r e^{2k'c't}$$

where the asterick signifies complex conjugate and  $k', l'$ , and  $c'$  are dimensionless wavelengths and complex phase speed. Using the complex

form of the perturbation streamfunction  $\psi' = \Psi(z) e^{i(k'x + l'y - k'c't)}$ ,

the fluxes are,

$$\begin{aligned} \overline{v'\theta'} &\propto \frac{1}{2} \left[ ik' \Psi \frac{d\Psi^*}{dz} \right]_r \\ \overline{w'\theta'} &\propto \frac{1}{2} \left[ -ik' \left( (z - c') \frac{d\Psi}{dz} - \Psi \right) \frac{d\Psi^*}{dz} \right]_r \\ \overline{v'q'} &\propto \frac{1}{2} \left[ ik' \left( -(k'^2 + l'^2) \Psi + \left( \frac{d^2}{dz^2} - \frac{d}{dz} \right) \Psi \right) \Psi^* \right]_r \end{aligned}$$

with the secular term,  $e^{2k'c't}$ , absorbed into an arbitrary constant.

Concentrating on the vertical structure, the remaining constant,

$k/2$ , appearing the expressions above is dropped and the fluxes become:

$$\overline{v'\theta'} \propto - \left( \Psi \frac{d\Psi^*}{dz} \right)_i \quad (2.3.13a)$$

$$\overline{w'\theta'} \propto - \left| \frac{d\Psi}{dz} \right|^2 c'_i - \left( \Psi \frac{d\Psi^*}{dz} \right)_i \quad (2.3.13b)$$

$$\overline{v'\theta'} \propto - [\Psi^* (\frac{d^2}{dz^2} - \frac{d}{dz}) \Psi]_i . \quad (2.3.13c)$$

Substituting from the perturbation expansion in this section and Appendix A1, we retain  $O(\epsilon)$  terms in (2.3.13a-c) to obtain:

$$\overline{v'\theta'} \propto - \Psi_{1i} \frac{d\Psi_0}{dz} + \Psi_0 \frac{d\Psi_{1i}}{dz} = H(z) \quad (2.3.14a)$$

$$\begin{aligned} \overline{w'\theta'} &\propto - \left| \frac{d\Psi_0}{dz} \right|^2 c'_{ii} - \Psi_{1i} \frac{d\Psi_0}{dz} + \Psi_0 \frac{d\Psi_{1i}}{dz} \\ &= H(z) - e^{-z(k'^2 + l'^2)^{1/2} z} \end{aligned} \quad (2.3.14b)$$

$$\begin{aligned} \overline{v'q'} &\propto \Psi_{1i} (\frac{d^2}{dz^2} - \frac{d}{dz}) \Psi_0 - \Psi_0 (\frac{d^2}{dz^2} - \frac{d}{dz}) \Psi_{1i} \\ &= H(z) \end{aligned} \quad (2.3.14c)$$

$$\text{where } H(z) = \begin{cases} 1 & 0 \leq z \leq (k'^2 + l'^2)^{-1/2} \\ 0 & (k'^2 + l'^2)^{-1/2} < z < \infty \end{cases} .$$

A constant factor of  $(k'^2 + l'^2)^{1/2} \pi e^{-2}$  has been dropped from the R.H.S. of eqs. (2.3.14a-c) so that  $\overline{v'\theta'}$  is normalized to unity at  $z = 0$ .

The vertical structures are displayed in Fig. 2.6. The horizontal heat and potential vorticity fluxes are represented by a step function with a vertical depth of  $(k'^2 + l'^2)^{-1/2} f_0/N_s$  in dimensional terms. The depth of the fluxes will decrease with wavelength. For the fastest growing waves these flux depths are proportional to  $H/(1+\gamma)$  as suggested by Held's scaling analysis. The vertical heat flux has a zero-order discontinuity at  $z = (k'^2 + l'^2)^{-1/2} f_0/N_s$ . However, its structure suggests the waves will stabilize the lower part of the atmosphere as expected and again, the depth of transport is  $O(H/(1+\gamma))$ .

The approximate solution found in this section is not uniformly

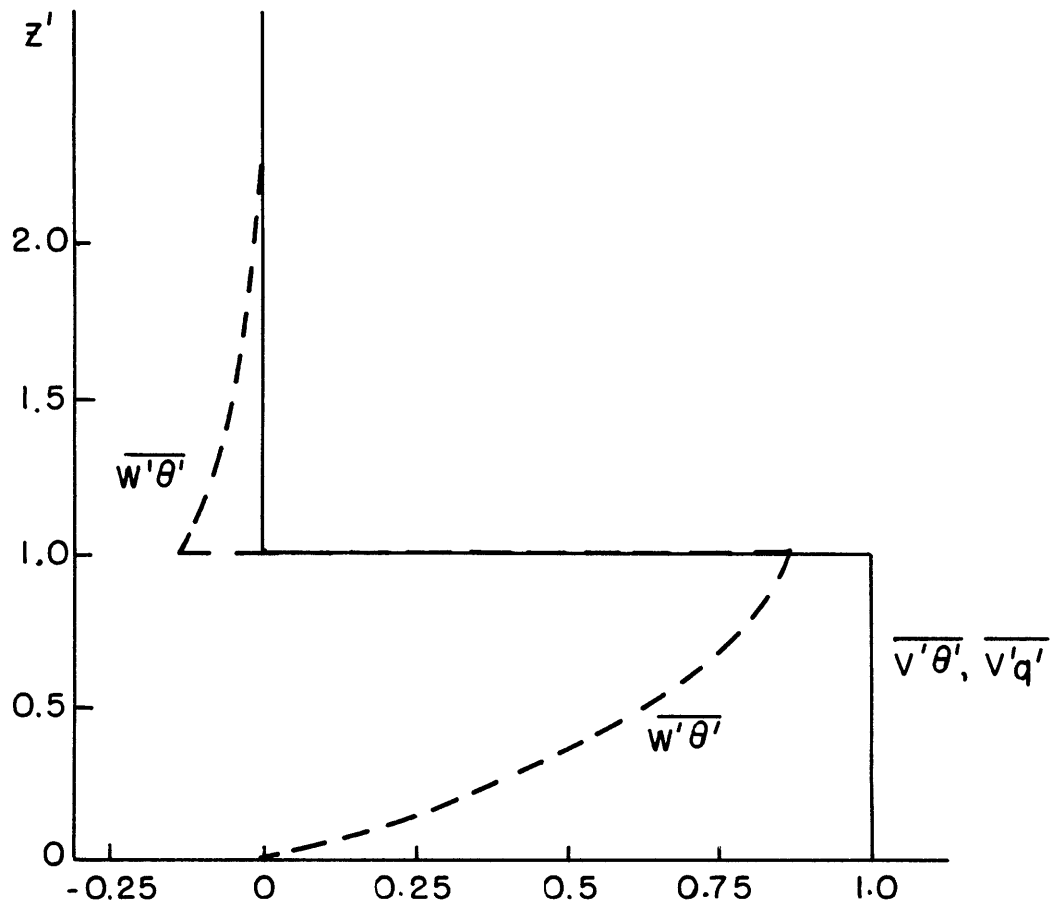


Fig. 2.6. Heat and potential vorticity fluxes from short-wave expansion. Vertical co-ordinate scaled by  $H/K$ .

valid throughout  $0 \leq z < \infty$  and this non-uniformity causes the discontinuities seen in Figs. 2.5 and 2.6. We have essentially neglected a region of  $O(\epsilon)$  thickness near  $z = c_0$  in which the expansion is not strictly valid. A uniform approximation, as found to  $O(\epsilon)$  in the eigenvalue in Appendix A2, will smooth out these discontinuities. The qualitative behavior of the instability is unchanged and outside the critical layer near  $z = c_0$ , the expressions for the eigenfunction,  $\Psi(z)$ , are the same. To at least  $O(\epsilon)$ , the value of  $c$  is also identical in either expansion method. The advantage of the technique employed in this section is its less difficult calculation of the eigenvalue to  $O(\epsilon^2)$  to obtain the fastest growing mode.

In summary the perturbation method of this section has confirmed Held's scaling arguments and described the properties of the short-wave Charney modes through simple dependences on mean flow parameters. The structure of unstable modes near the first neutral curve is examined in the next section. From the results of this and the following section, we will formulate a heat flux parameterization in Chapter III which includes the effect of a non-zero  $\beta$  parameter approximating the dynamical effect of a spherical planet.

#### 4. Expansion Near First Neutral Curve

In this section we will examine in detail unstable modes near the neutral ( $r=1$ ) separating the Charney & Green modes (refer to Fig. 2.2). Though concentrating on the long wave side of the Charney mode spectrum, the analysis will be carried out to sufficiently high order to demonstrate the instability of the slower growing Green modes at their shortest wavelengths.

Depending on the value of  $\gamma$ , further neutral curves ( $r=n$ ), along which  $c$  has only real values, may exist, separating Green modes (both unstable and neutral) at longer wavelengths, i.e.  $r > 1$ . For any positive  $\gamma$ , at least one neutral curve exists where  $r = \frac{1+\gamma}{\sqrt{4k'^2+1}} = 1$  with  $\gamma$ ,  $k'$  defined in Section II-1. For  $0 < \gamma \leq 2$ , only this neutral curve exists separating Charney and Green modes. As  $\gamma$  increases and exceeds an integer greater than 2, another neutral curve is added, separating Green modes. The analysis presented in this section can be repeated near other neutral curves of  $r = n > 1$  to study instability of longer Green modes.

The eigenvalue problem is repeated below using the formulation of eqs. (2.3.2):

$$\left[ \frac{d^2}{dz^2} - \frac{1}{k} \frac{d}{dz} - 1 + \frac{B}{k(z-c)} \right] \Psi(z) = 0 \quad (2.4.1a)$$

$$c \frac{d\Psi}{dz}(0) + \Psi(0) = 0 \quad \Psi(\infty) \rightarrow 0 \quad (2.4.1b)$$

To expand about the neutral curves, let  $B = B_n(k) + \delta'$  where  $B_n(k)$  is the value of  $B = 1 + \gamma$  for which the wavenumber,  $k$ , becomes a neutral mode along the  $r=n$  neutral curve. That is, the function  $B_n(k)$  defines the  $n^{\text{th}}$  neutral curve in  $\gamma - k$  space and  $\delta'$  is the deviation in  $\gamma$  from this curve. Then Eq. (2.4.1a) can be rewritten as

$$\left[ \frac{d^2}{dz^2} - \frac{1}{k} \frac{d}{dz} - 1 + \frac{B_n + \delta}{k(z-c)} \right] \Psi = 0 \quad (2.4.2)$$

with  $\delta \equiv \delta'/k$ .

Knowing that  $r=n$  ( $n=1,2,3,\dots$ ) along the neutral curves, the

function  $B_n(k)$  must be:  $B_n(k) = n\sqrt{4k^2+1}$  and thus,

$$\delta = (r-n) \frac{\sqrt{4k^2+1}}{k} .$$

Based on the analysis of Miles (1964a), the expansion parameter will be  $|\delta|^{1/2}$ . For  $\delta = 0$ , the solutions are the neutral curves and take the form

$$\Psi = (z-c) e^{-\alpha z} P_{n-1}(z)$$

where  $P_{n-1}(z)$  is a polynomial of order  $n-1$  and  $\alpha = -\frac{1}{2k} + \sqrt{\frac{1}{4k^2} + 1}$ .

Substitution into the lower boundary condition gives an  $n^{\text{th}}$  order polynomial equation in  $c$  with one root being zero and the rest negative.

As  $n$  increases, these neutral modes develop more complicated vertical structure.

In this section we will examine instability near  $r=1$ . The following perturbation analysis is similar to Pedlosky's (1979b) nonlinear study of Charney modes near the  $r=1$  curve. The treatment here goes to higher orders to examine the growth rates, phase speeds, structures, and transport properties of the linear waves.

The expansions for  $\Psi$  and  $c$  are:

$$\Psi(z) = \Psi_0(z) + |\delta|^{1/2} \Psi_1(z) + |\delta| \Psi_2 + \dots$$

$$c = c_0 + |\delta|^{1/2} c_1 + |\delta| c_2 + |\delta|^{3/2} c_3 + \dots$$

The lowest order equations of (2.4.2) and (2.4.1b) form the neutral mode problem:

$$\left. \begin{aligned} \mathcal{L}_0 \bar{\Psi}_0 &= \left[ \frac{d^2}{dz^2} - \frac{1}{k} \frac{d}{dz} - 1 + \frac{B_1}{k(z-c_0)} \right] \bar{\Psi}_0 = 0 \\ c_0 \frac{d\bar{\Psi}_0(0)}{dz} + \bar{\Psi}_0(0) &= 0 \quad \bar{\Psi}_0(\infty) \rightarrow 0 \end{aligned} \right\} \quad (2.4.3)$$

with  $B_1 = \sqrt{4k^2+1}$  and  $\alpha = \frac{B_1-1}{2k}$ .

Retaining the solution that decays as  $z \rightarrow \infty$  and taking an arbitrary amplitude of unity, the  $O(1)$  eigenfunction is

$$\Psi_0 = (z - c_0) e^{-\alpha z} = (z - c_0) \exp\left[-\frac{(z - c_0)}{2K} (\sqrt{1 + 4K^2} - 1)\right] \quad (2.4.4)$$

and the phase speed vanishes at this order, i.e.  $c_0 = 0$ . In dimensional form,

$$\bar{\Psi}_0 = \frac{z}{H} \exp\left[\frac{-z}{2H} \left(\sqrt{1 + \left(\frac{2N_s H}{f_0}\right)^2 (k^2 + l^2)} - 1\right)\right]$$

and again, note the shorter waves will also be shallower. The amplitude of  $\bar{\Psi}_0$  reaches a maximum at

$$z = 2H \left[ \sqrt{1 + \left(\frac{2N_s H}{f_0}\right)^2 (k^2 + l^2)} - 1 \right]^{-1}.$$

Examining higher orders in  $|\delta|^{\frac{1}{2}}$ , instability can be demonstrated for the Charney ( $\delta < 0, r < 1$ ) and Green ( $\delta > 0, r > 1$ ) mode sides of the neutral curve. At  $O(|\delta|^{\frac{1}{2}})$  eq. (2.4.2) is

$$\mathcal{L}_0 \bar{\Psi}_1 = -\mathcal{L}_1 \bar{\Psi}_0 = \frac{B_1 c_1}{K z^2} \bar{\Psi}_0 \quad (2.4.5)$$

and using the upper boundary condition,

$$\bar{\Psi}_1 = -c_1 e^{-\alpha z}. \quad (2.4.6)$$

For  $z \sim |\delta|^{\frac{1}{2}}$  eq. (2.4.2) takes on the characteristics of a boundary layer problem. That is, the vertical co-ordinate must be rescaled by

$$z = |\delta|^{\frac{1}{2}} \mathcal{S}$$

and solutions in the inner layer must be matched through a transition region to the outer solution as given in (2.4.6). In terms of the inner variable,  $\mathcal{S}$ , eq. (2.4.2) becomes:

$$\left[ \frac{d^2}{d\mathcal{S}^2} - \frac{|\delta|^{\frac{1}{2}}}{K} \frac{d}{d\mathcal{S}} - |\delta| + \left(\frac{B_1}{K} + \delta\right) \frac{|\delta|^{\frac{1}{2}}}{\mathcal{S} - c_1 - |\delta|^{\frac{1}{2}} c_2 - \dots} \right] \tilde{\Psi} = 0 \quad (2.4.7)$$

where  $\tilde{\Psi}$  is the inner solution. The boundary condition at  $z=0$  is also

rescaled from (2.4.1b) to:

$$(c_1 + |\delta|^\kappa c_2 + \dots) \frac{d}{d\mathcal{S}} \tilde{\Psi}(0) + \tilde{\Psi}(0) = 0. \quad (2.4.8)$$

The first contribution from  $\tilde{\Psi}$  comes at  $0 (|\delta|^{\frac{1}{2}})$  to match the outer solution which is  $0 (|\delta|^{\frac{1}{2}})$  for small  $z$ . The inner solution must be expanded not only in powers of  $|\delta|^{\frac{1}{2}}$ , but also  $|\delta|^{\frac{3}{2}} \ln |\delta|$ ,  $|\delta|^2 \ln |\delta|$ , etc. in order to match the exterior solution at higher orders.

At  $0 (|\delta|^{\frac{1}{2}})$  the inner solution obeys:

$$\frac{d^2}{d\mathcal{S}^2} \tilde{\Psi}_1 = 0$$

so that  $\tilde{\Psi}_1 = a_1 \mathcal{S} + b_1$ .

This must be matched to the exterior solutions of (2.4.4) and 2.4.6) at  $0 (|\delta|^{\frac{1}{2}})$  through a transition region of  $z \rightarrow 0^+$ ,  $\mathcal{S} \rightarrow \infty$ ,  $|\delta| \rightarrow 0$ .

Using  $z = |\delta|^{\frac{1}{2}} \mathcal{S}$  the outer solution is, in this region,

$$\Psi \sim |\delta|^{\frac{1}{2}} (\mathcal{S} - c_1)$$

and the matching condition requires

$$a_1 = 1 \quad \text{and} \quad b_1 = -c_1.$$

Applying the lower boundary condition at  $0 (|\delta|^{\frac{1}{2}})$  from (2.4.8),

$$c_1 \frac{d\tilde{\Psi}_1}{d\mathcal{S}}(0) + \tilde{\Psi}_1(0) = 0 \quad \text{or} \quad a_1 c_1 + b_1 = 0 \quad \text{and}$$

we see that  $c_1$  is not determined at this order.

At  $0 (|\delta|)$  the outer approximation of (2.4.2) is:

$$\mathcal{L}_0 \tilde{\Psi}_2 = -\mathcal{L}_1 \tilde{\Psi}_1 - \mathcal{L}_2 \tilde{\Psi}_0 \quad (2.4.9)$$

where  $\mathcal{L}_2 = \frac{\delta}{|\delta| z} + \frac{B_1}{\kappa z^2} (c_2 + \frac{c_1^2}{z})$ .

The inner equation is

$$\frac{d^2}{d\mathcal{S}^2} \tilde{\Psi}_2 = \frac{1}{\kappa} \left( \frac{d}{d\mathcal{S}} - \frac{B_1}{\mathcal{S} - c_1} \right) \tilde{\Psi}_1 = -\tilde{\mathcal{L}}_1 \tilde{\Psi}_1 = -2\alpha \quad (2.4.10)$$

after substituting for  $\tilde{\Psi}_1$ . The exterior and interior solutions of (2.4.9,10) are :

$$\tilde{\Psi}_2 = e^{-\alpha z} \left[ \frac{\delta}{|\delta|} \left( \frac{K}{B_1} z \ln z - \left( \frac{K}{B_1} \right)^2 \right) - c_2 \right] \quad (2.4.11)$$

$$\tilde{\Psi}_2 = -\alpha \zeta^2 + a_2 \zeta + b_2. \quad (2.4.12)$$

Including contributions from (2.4.4), (2.4.6), and (2.4.11), the asymptotic behavior of the exterior solution in the transition region is at 0 ( $|\delta|$ ):

$$\tilde{\Psi} \sim -\alpha \zeta^2 + \alpha c_1 \zeta - \frac{\delta}{|\delta|} \left( \frac{K}{B_1} \right)^2 - c_2.$$

Matching to (2.4.12) requires

$$a_2 = \alpha c_1 \quad \text{and} \quad b_2 = -\frac{\delta}{|\delta|} \left( \frac{K}{B_1} \right)^2 - c_2.$$

The lower boundary condition at 0 ( $|\delta|$ ) is

$$c_1 \frac{d}{d\zeta} \tilde{\Psi}_2(0) + \tilde{\Psi}_2(0) = -c_2 \frac{d}{d\zeta} \tilde{\Psi}_1(0) = -c_2$$

which becomes, using (2.4.12),  $c_1 a_2 + b_2 = -c_2$ . Thus, we find

$$c_1^2 = \frac{\delta}{|\delta| \alpha} \left( \frac{K}{B_1} \right)^2 \quad (2.4.13)$$

and see that  $c_1$  is imaginary for  $\delta < 0$  representing growing and decaying Charney waves and real for  $\delta > 0$ , westward and eastward propagating Green waves. Note that the eastward travelling Green wave has a critical layer ( $\bar{u} = c$ ) at this order and at higher orders, this will cause this mode to be unstable.

In terms of  $B$  and  $r = B/\sqrt{4k^2+1}$ , we see that

$$c \approx |\delta|^{1/2} c_1 = \sqrt{\frac{r-1}{2}} \sqrt{\frac{(B/r)^2 - 1}{(B/r)^2 - B/r}}. \quad (2.4.14)$$

For  $r \approx 1$ , the eigenvalue is approximately

$$c \approx \sqrt{\frac{r-1}{2}} \sqrt{\frac{B^2-1}{B^2-B}}$$

and we note the growth rate of the Charney modes is  $O(|\delta|^{\frac{1}{2}})$  or  $O(|r-1|^{\frac{1}{2}})$ , while the real phase speed of the Green modes is of the same order. In the limit  $B \rightarrow 1$  ( $\gamma \ll 1$ ) and  $r \rightarrow 1^-$ ,  $K$  must also be small with  $2K^2 > \gamma$  and  $r \approx 1 + \gamma - 2K^2 < 1$ . This implies  $c \approx i(2K^2 - \gamma)^{\frac{1}{2}}$  in agreement with Miles (1964c) who examined the instability of the mean flow in this limit. As  $\gamma$  becomes small, the unstable modes near the neutral curve attain long wavelengths compared to  $N_S/f_0$  and the growth rates are  $O(K)$  for  $\gamma \ll K^2 \ll 1$ . For  $\gamma \gg 1$  and  $r \rightarrow 1^-$ ,  $r \approx \frac{\gamma+1}{2K}$  implies  $K \approx \frac{\gamma}{2} \gg 1$  and  $c \approx (\frac{\gamma+1}{4K} - \frac{1}{2})^{\frac{1}{2}}$ . The unstable waves have horizontal scales of  $O(\frac{N_S h}{f_0})$  and growth rates of  $O((1 - \frac{\gamma+1}{2K})^{\frac{1}{2}})$ .

The  $|\delta|^{\frac{3}{2}} \Psi_2$  solution in eq. (2.4.11) will have terms of  $O(|\delta|^{\frac{3}{2}} \ln |\delta|)$  in the matching region. Therefore, as stated above, the inner expansion must include a term of this order. Since the contribution from this term is small and affects only the inner solution structure, the matching at this order is left to Appendix B1.

The general  $O(|\delta|^{\frac{n}{2}})$  equation for the exterior streamfunction is:

$$\mathcal{L}_0 \Psi_n = H_n(z) e^{-\alpha z} \quad (2.4.15)$$

$$H_n(z) \equiv -[\mathcal{L}_n \Psi_0 + \mathcal{L}_{n-1} \Psi_1 + \dots + \mathcal{L}_1 \Psi_{n-1}] e^{\alpha z}$$

and  $\mathcal{L}_i$  is the  $i^{\text{th}}$  order operator from eq. (2.4.2). Thus, the general  $n^{\text{th}}$  order contribution to  $\Psi$  is

$$\Psi_n(z) = \Psi_0(z) \left[ \int_z^\infty \frac{e^{B_1 s/k}}{s^2} \left( \int_s^\infty H_n(\eta) \eta e^{-\frac{B_1}{k} \eta} d\eta \right) ds \right] \quad (2.4.16)$$

For the inner solution, the general equation at  $O(|\delta|^{n/2})$  is

$$\frac{d^2 \tilde{\Psi}_n}{ds^2} = G_n(s) \quad (2.4.17)$$

where  $G_n(\xi) \equiv -\tilde{\mathcal{L}}_{n-1} \tilde{\Psi}_1 - \tilde{\mathcal{L}}_{n-2} \tilde{\Psi}_2 - \dots - \tilde{\mathcal{L}}_1 \tilde{\Psi}_{n-1}$

and  $\tilde{\mathcal{L}}_i$  is the  $i^{\text{th}}$  order operator from eq. (2.4.7). The lower boundary condition (2.4.8) at this order is:

$$c_1 \frac{d\tilde{\Psi}_n(0)}{d\xi} + \tilde{\Psi}_n(0) = -c_n \frac{d\tilde{\Psi}_1(0)}{d\xi} - \dots - c_2 \frac{d\tilde{\Psi}_{n-1}(0)}{d\xi}. \quad (2.4.18)$$

From eq. (2.4.17), the  $O(|\delta|^{\frac{n}{2}})$  interior solution before applying matching or boundary conditions, is:

$$\tilde{\Psi}_n(\xi) = \int_0^\xi \int_0^\xi G_n(\eta) d\eta ds + a_n \xi + b_n. \quad (2.4.19)$$

From eqs. (2.4.18) and 2.4.19), we find:

$$c_1 a_n + b_n = -c_n a_1 - \dots - c_2 a_{n-1} \quad (2.4.20)$$

and this relation, along with a matching condition between (2.4.16) and (2.4.19), will determine  $c_{n-1}$ . Through the matching requirement,  $b_n$  in (2.4.20) will include a term of  $-c_n a_1$  which cancels  $-c_n a_1$  on the R.H.S. of (2.4.20) and  $c_n$  is not determined at this order.

To demonstrate the Green mode instability which occurs at  $O(|\delta|^{\frac{3}{2}})$  (see discussion in Section II-2), we must proceed to  $n=4$  ( $O(|\delta|^2)$ ) in the eigenfunction solutions of eqs. (2.4.16) and (2.4.19). The details of calculating the higher orders are given in Appendix B2. We repeat there the values of  $c_2$  and  $c_3$  for purposes of discussion of growth rates and phase speeds.

$$c_2 = -\frac{\delta}{|\delta|} \frac{k}{2B_1} \left[ \frac{k}{B_1} + \frac{1}{\alpha} \right] \quad (2.4.21)$$

$$c_3 = \frac{\delta c_1}{|\delta| 2} \left[ -\frac{\kappa}{B_1} (\ln(-c_1) + E_0 + \ln B_1/\kappa) + \frac{1}{4\alpha} \left( \frac{\alpha\kappa}{B_1} + 1 \right)^2 \right], \quad E_0 = .577\dots \quad (2.5.22)$$

From (2.4.21) we see the  $O(|\delta|)$  contribution,  $c_2$ , to the phase speed is real for any  $\delta$ , specifically, positive for Charney modes and negative for Green modes. The phase speed of the Charney modes is therefore  $O(|\delta|)$  and Green modes are stable to this order.

In eq. (2.4.22) the evaluation of the  $\ln(-c_1)$  term requires a choice of the branch cut for the logarithmic function. If the principal value is chosen (cut along the negative  $z$  axis), assume  $c_1$  has a vanishingly small imaginary part for  $\delta > 0$  and  $c_{1r} > 0$  (eastward propagating Green wave). As  $c_{1i} \rightarrow 0^\pm$ , then  $c_{3i} \rightarrow \pm \frac{\pi\kappa}{2B_1} c_{1r}$  indicating growing and decaying modes. This corresponds to the  $O((r-1)^{\frac{3}{2}})$  growth rates found by Miles (1964a). For the limit of  $2\kappa^2 < \gamma \ll 1$  and  $r \rightarrow 1^+$ ,  $c_i \approx |\delta|^{3/2} c_{3i} \approx \frac{\pi}{2} (\gamma - 2\kappa^2)^{3/2}$

in agreement with Miles' (1964c) analysis of this limit. For small  $\gamma$  the long, unstable modes on either side of the neutral curve are slowly growing as the neutral mode moves to smaller  $\kappa$ , eventually vanishing for  $\gamma = 0$  when all modes are unstable. For  $\gamma \sim 2\kappa \gg 1$  and  $r \rightarrow 1^+$ ,

$$c_i \approx |\delta|^{3/2} c_{3i} \approx \frac{\pi}{\sqrt{2}} \left( \frac{\gamma+1}{2\kappa} - 1 \right)^{3/2}.$$

For  $\delta > 0$  and  $c_{1r} < 0$  (westward propagating Green mode),  $c_3$  is real, corresponding to the single neutral mode for  $1 < r < 2$ , as no critical level ( $\bar{u} = c_1$ ) exists along the positive real  $z$ -axis. For  $\delta < 0$  (Charney modes)  $c_3$  is a complex conjugate pair as

$$[\ln(-c_1)]_i = \pm \frac{i\pi}{2} \quad \text{for} \quad C_{1i} = \mp \frac{\kappa}{\sqrt{\alpha} B_1}$$

so the next contribution to the growth rate is negative for growing modes.

In Figures 2.7a,b and 2.8a,b the phase speeds and growth rates to 0 ( $|\delta| \frac{3}{2}$ ) are compared with numerical results for  $\gamma = 1$  and  $\gamma \gg 1$ . The accuracy is greatest near the neutral mode as expected. For Green modes the approximation for the phase speed is more accurate than for growth rate because of additional higher order contributions. Growth rates for the most unstable Charney mode are estimated to within 25-50% error. Unlike the short-wave approximation estimating the most unstable wavelength would be in considerable error as no well-defined peak in growth rate occurs. In fact, the dimensionless growth rate,  $c_i$ , asymptotes to .51 for  $K \gg 1$ .

The vertical structure of the wave amplitude and phase is depicted in Fig. 2.9a for a typical Charney mode ( $\delta = -.2$ ,  $K = .98$  or  $\gamma = 1$ ,  $r = .91$ ). The phase varies most dramatically in the lowest layer of depth 0 ( $H/K$ ) and the amplitude has a peak occurring at a similar depth. From Fig. 2.7a the wave phase speed is about  $0.1 \frac{d\bar{u}}{dz} H$  corresponding to a steering level of  $H/10 \sim .8$  km. The total phase shift is about  $90^\circ$  in rough agreement with other results for Charney modes (Geisler and Garcia, 1977; Kuo, 1973). The structure in Fig. 2.9a is computed to 0 ( $|\delta| \frac{1}{2}$ ) and in this example, corrections from 0 ( $|\delta|$ ) terms are about 10%. The structure in this figure is typical of Charney modes near the neutral curve.

As the wavelength decreases for fixed  $\gamma$ , the amplitude maximum approaches the surface and the wave appears more like the exponential decaying short waves of Section II-3. Fig. 2.9b shows the structure of the mode in this long Charney wave expansion for the limit  $K \ll 1$  and fixed  $\gamma$ . It is quite similar to the modes at the short-wave end of the spectrum. Similar structural behavior as a function of wavenumber is seen in the numerical studies of Geisler and Dickinson (1975) and Geisler

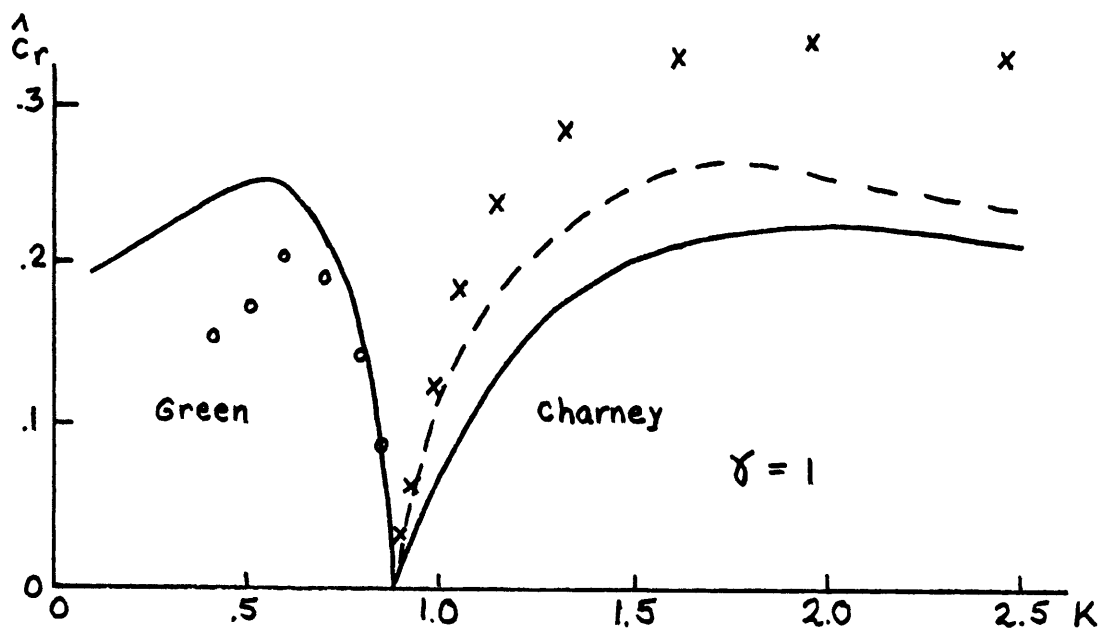


Fig. 2.7a.  $\gamma = 1$ : Phase speed ( $\hat{c}_r$ ) vs. wavenumber ( $K$ ) near  $r = 1$  ( $K = .87$ ) for Green (o) ( $K < .87$ ) and Charney modes (x) ( $K > .87$ ). Computed to  $O(|\delta|^{3/2})$ , compared with  $\hat{c}_r$  of Lindzen et al (1980) (solid) and Charney (1973) (dashed). Scaling of  $\hat{c}$  and  $K$  same as Fig 2.3a.

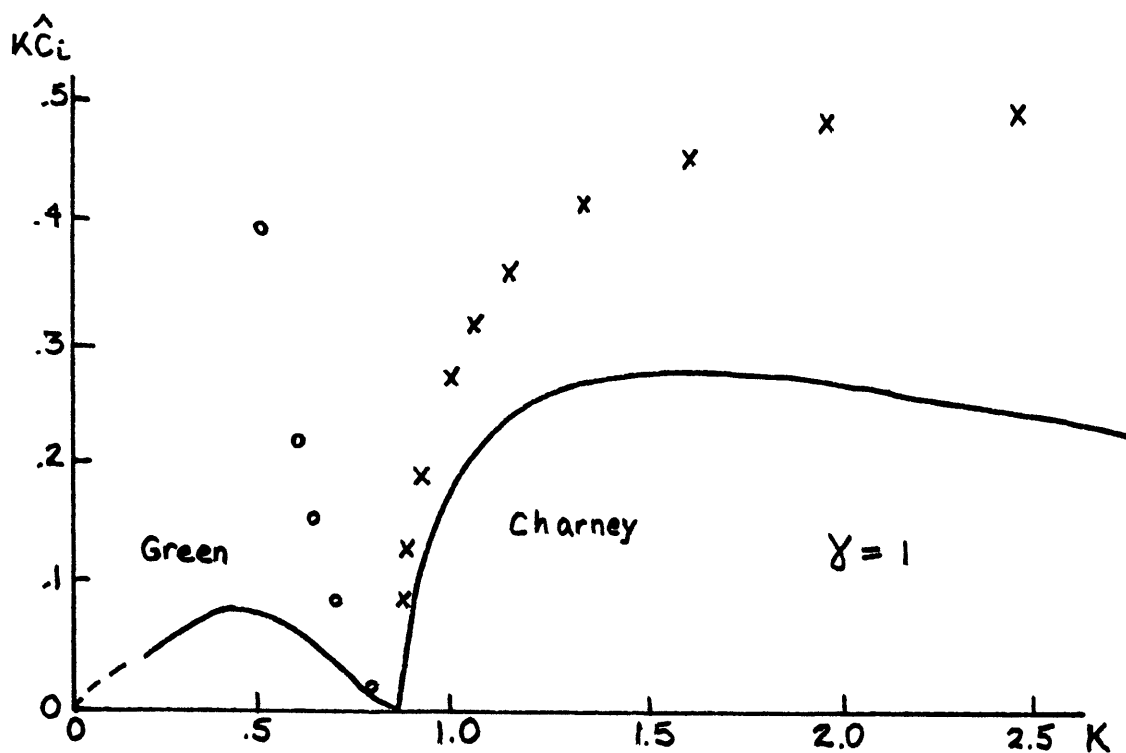


Fig. 2.7b.  $\gamma = 1$ : Same as Fig. 2.7a except for growth rate ( $K\hat{c}_i$ ). Scaling same as Fig. 2.3b.

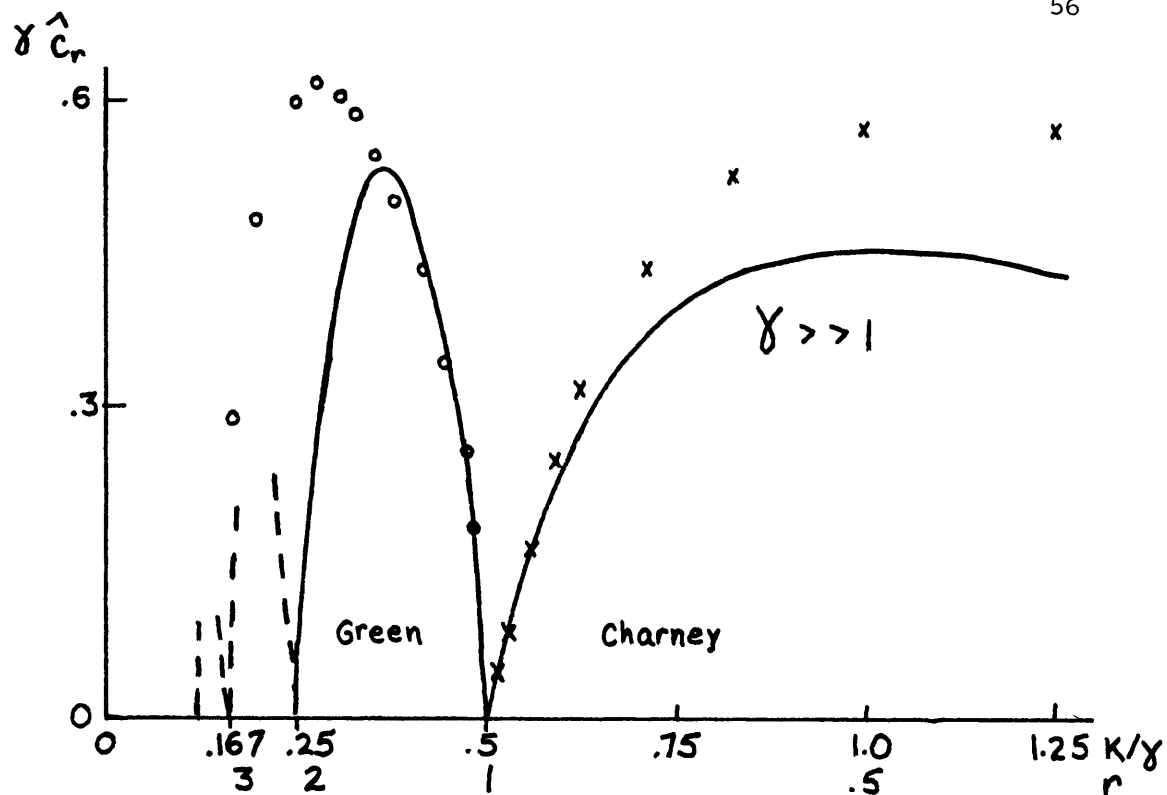


Fig. 2.8a.  $\gamma \gg 1$ : Phase speed ( $\gamma \hat{c}_r$ ) vs. wavenumber ( $K/\gamma$ ) and  $r \approx \frac{\gamma}{2K}$  near  $r = 1$  for Green (o) ( $r > 1$ ) and Charney modes (x) ( $r < 1$ ). Computed to  $O(|\delta|^{3/2})$ , compared with calculation of Kuo (1973) (solid). Dashed lines are longer Green modes. Scaling same as Fig. 2.4a.

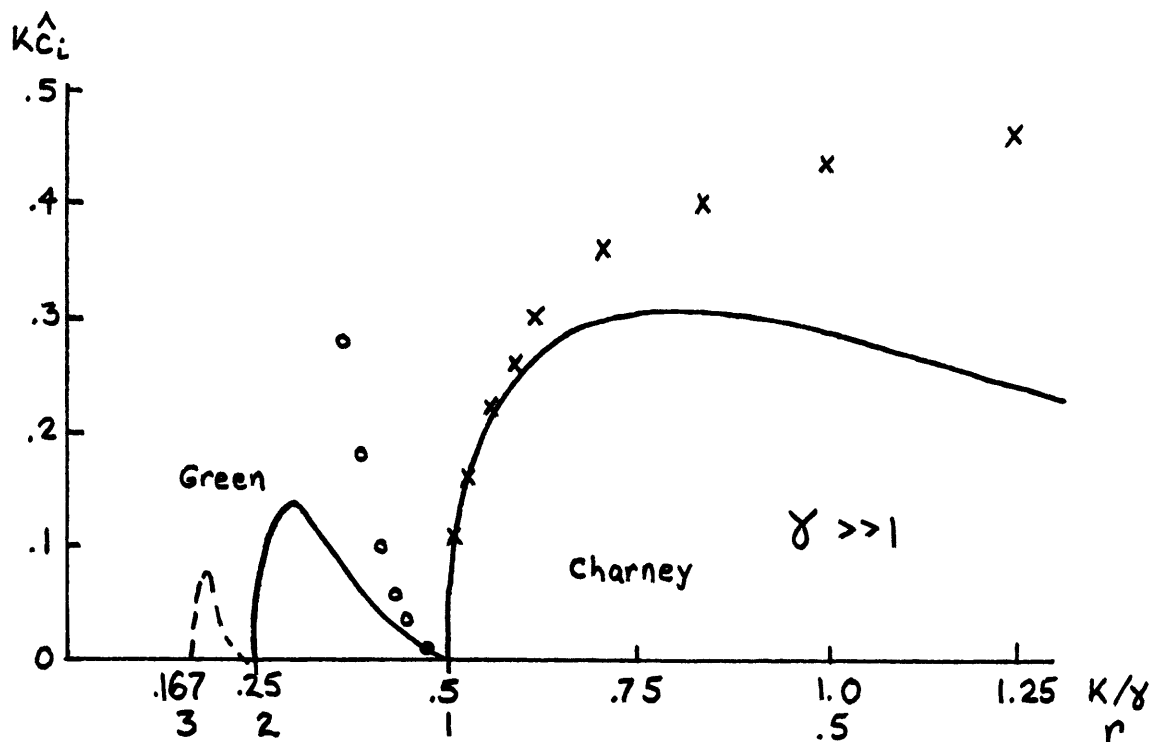


Fig. 2.8b.  $\gamma \gg 1$ : Same as Fig. 2.8a except for dimensionless growth rates ( $K \hat{c}_i$ ).

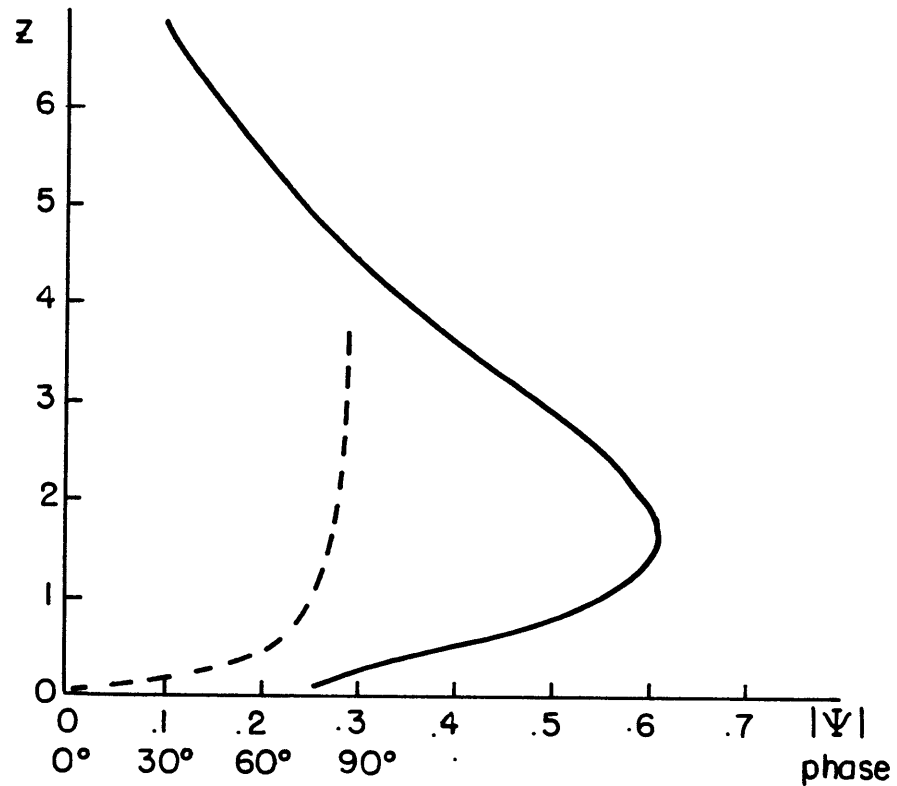


Fig. 2.9a. Phase (dashed) and amplitude (solid) to  $O(|\delta|^{1/2})$  of a typical Charney mode near  $r=1$  ( $r=.91, \gamma=1$ ) vs. height. The vertical co-ordinate is scaled by  $H/K$  (here,  $K=.98$ ).

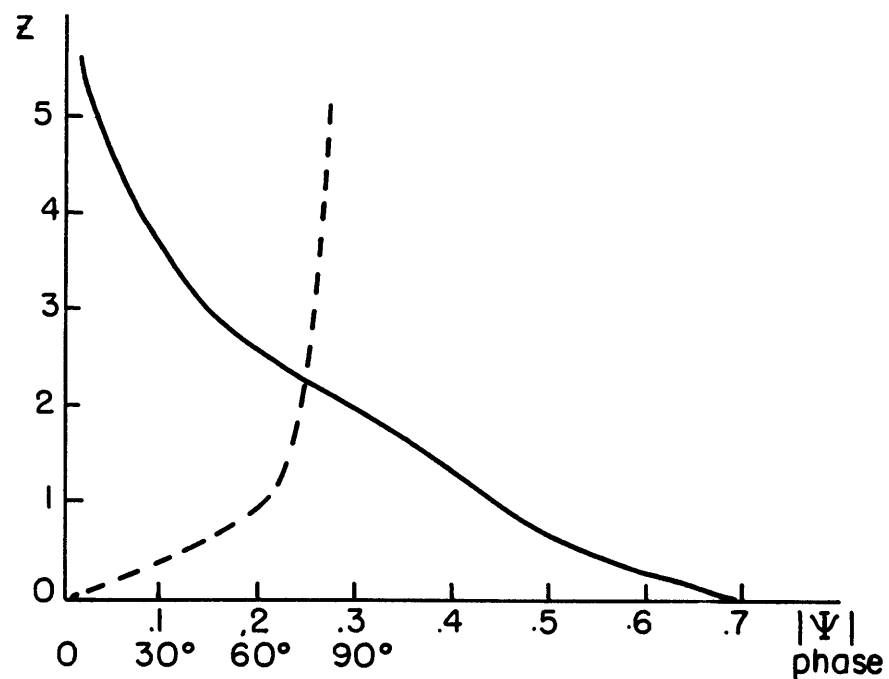


Fig. 2.9b. Same as Fig. 2.9a except for  $K \gg 1$  ( $r \ll 1$ ).

and Garcia (1977).

The amplitude and phase of a wave near the peak growth rate for  $\gamma = 1$  is shown in Fig. 2.10. It represents a transition between Figures 2.9a and 2.9b and has maxima at the surface and  $.8H$  and a steering level at  $H/3$ . Using tropospheric winter data at  $45^\circ N$  the wavelength would be 5300 km (zonal wavenumber 5) with  $l = k$ .

The amplitude and phase of these long Charney waves can be derived from the approximate expressions for  $\bar{\Psi}(z)$ , specifically:

$$\begin{aligned}\bar{\Psi}_r &\approx z e^{-\alpha z} \\ \bar{\Psi}_i &\approx -|\delta|^{1/2} c_{1i} e^{-\alpha z}\end{aligned}$$

For  $|\delta|^{1/2} c_{1i} \ll 1$  the amplitude reaches a maximum near the same level as the neutral mode, i.e. at  $z = 1/\alpha$  or, in dimensional terms,

$$z^* = \frac{2H}{\sqrt{4k^2 + 1} - 1} \quad \text{with} \quad k = (k^2 + l^2)^{1/2} \left( \frac{N_s H}{f_0} \right)^{-1}.$$

As mentioned, the shorter waves are also shallower. The phase is given by

$$\text{ph} \approx \arctan \left( \frac{-|\delta|^{1/2} c_{1i}}{z} \right)$$

which varies from  $\text{ph} = -90^\circ$  at  $z = 0$  to  $\text{ph} \rightarrow 0$  as  $z \rightarrow \infty$  with a  $45^\circ$  shift in the layer below  $z = |\delta|^{1/2} c_{1i}$ . Thus, the shift is confined to lower levels for slower growing waves. The steering or critical level is 0 ( $|\delta|$ ) and, to this order, is not crucial in obtaining instability as in the Green mode. The critical level, in essence, occurs at the surface and phase shift is limited to  $\pi/2$ . In later discussion we will see the Green mode undergoes a shift of  $\pi + 0$  ( $|\delta|$ ) since the critical level occurs above the surface.

It is interesting to note that Charney waves near  $r = 1$  can have substantial amplitudes in the middle and upper troposphere. With  $H = 8$  km

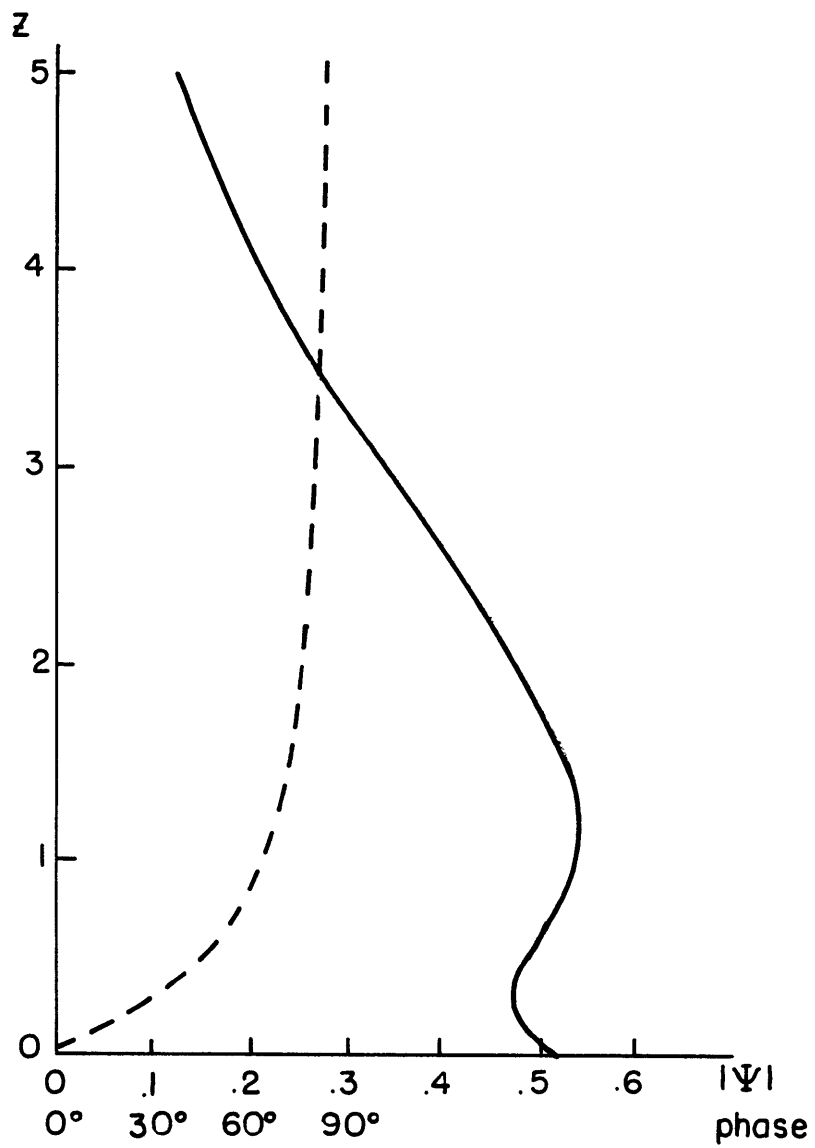


Fig. 2.10. Same as Fig. 2.9a except for  $\gamma = 1$ ,  $K = 1.6$  ( $r = .6$ ).

the wave in Fig. 2.9a reaches a maximum amplitude at  $z = 12$  km and has wavelength with  $\lambda = k$  of 8500 km or a zonal wavenumber of 3 at  $45^\circ\text{N}$ . The more rapidly growing wave of Fig. 2.10 has a maximum amplitude at 6 km. Referring to Fig. 2.7b we see the abrupt increase in growth rates for  $K > .87$  suggests these deep Charney modes can be rapidly growing waves.

The rapid, near-surface phase variation of these waves suggests the horizontal heat flux is confined to a layer shallower than the wave amplitude. Above this layer the wave is more barotropic, i.e. little phase change with height. Waves of these scales and structures figure prominently in observed atmospheric motions as noted in Charney's original study of baroclinic waves.

The vertical structure of a typical, nearly neutral Green mode ( $\delta = .2$ ,  $K = .775$  or  $\gamma = 1$ ,  $r = 1.08$ ) is depicted in Fig. 2.11. The phase shifts by slightly more than  $180^\circ$  through the fluid and varies most rapidly in a thin layer (thickness of  $O(|\delta|^{3/2})$ ) just below the approximate critical level of  $z = |\delta|^{1/2} c_1$  (in this example,  $|\delta|^{1/2} c_1 = .26$ ). This shift occurs in a region where the amplitude is a minimum, a feature typical of Green modes (see Fig. 13 of Geisler and Dickinson, 1975, or Fig. 2.1b of this thesis). The wave in Fig. 2.10 reaches a maximum amplitude well above this level and, for mid-latitudes, in the lower stratosphere ( $z \approx 20$  km.).

Of course, the model has no representation of the stratosphere. However, it demonstrates that a stratosphere is not necessary to allow these deep waves, only a non-zero  $\beta$ -parameter. Other investigators (Simmons and Hoskins, 1977; Fullmer, 1979) who examined the effect of including a stratosphere found an enhancement of streamfunction amplitude at the tropopause. Thus the detailed nature of the longer, deeper waves

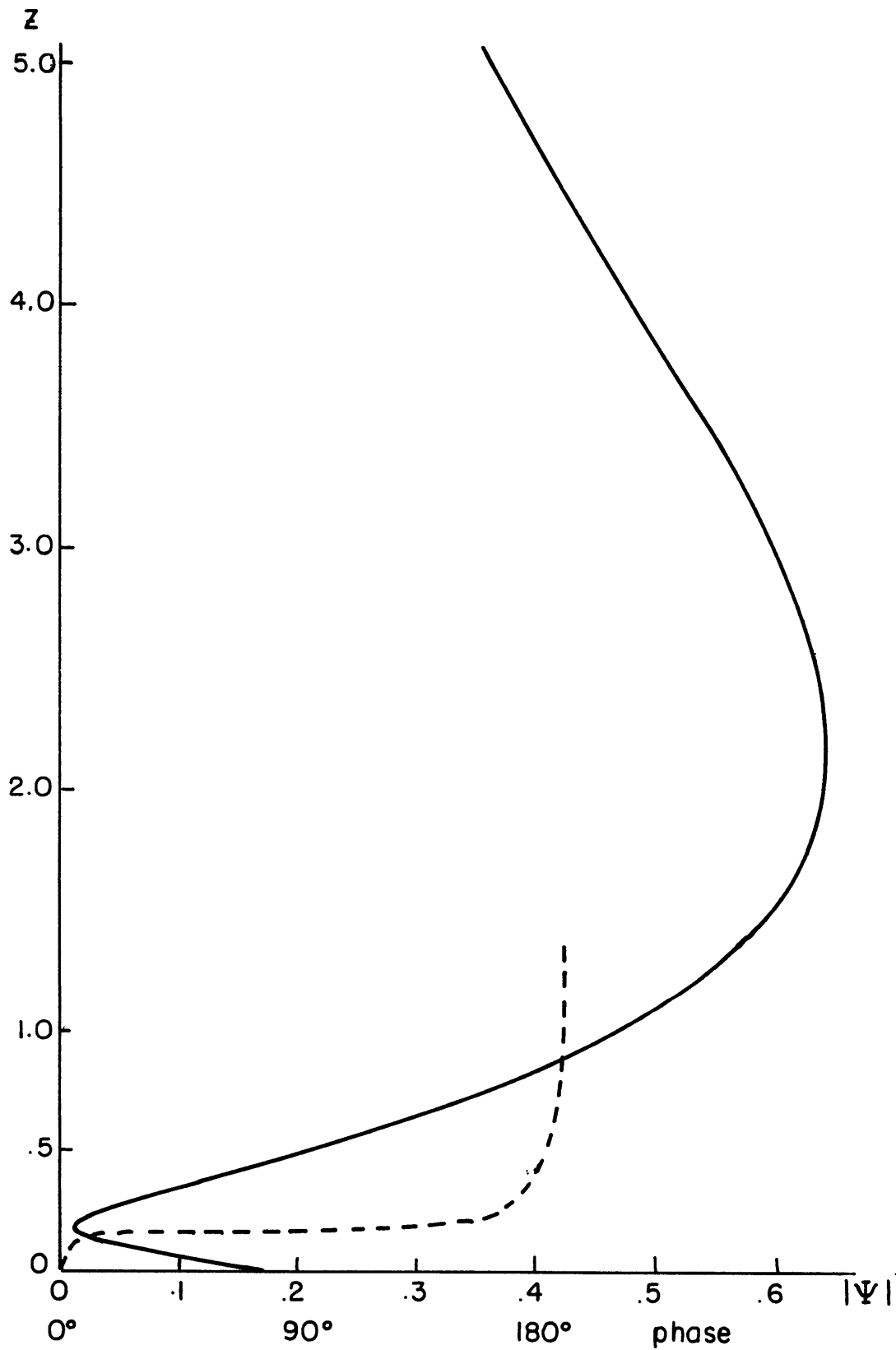


Fig. 2.11. Same as Fig. 2.9a except for Green mode near  $r = 1 \frac{3}{4}$  ( $r = 1.08$ ,  $\gamma = 1$ ,  $\delta = .2$ ,  $K = .775$ ). Terms to  $O(|\delta|^{3/2})$  are included.

is unlikely to be determined by either tropospheric or stratospheric conditions alone.

The principal features of the Green modes are found in the following expressions for  $\bar{\Psi}(z)$  from this section and Appendix B2:

$$\begin{aligned}\bar{\Psi}_r &\approx (z - |\delta|^{1/2} c_1) e^{-\alpha z} \\ \bar{\Psi}_i &\approx -|\delta|^{3/2} \left[ c_{3i} e^{-\alpha z} + \frac{\pi K}{B_1} \left( \frac{z}{|\delta|^{1/2}} - c_1 \right) H(z - |\delta|^{1/2} c_1) \right]\end{aligned}$$

where 
$$H(x) = \begin{cases} 0 & x > 0 \\ 1 & x < 0 \end{cases} \quad \text{and} \quad c_{3i} = \frac{c_1 K}{2 B_1} \pi .$$

Again the maximum amplitude occurs near  $z = 1/\alpha$  as in the neutral mode and since  $K$  is smaller for Green modes than Charney modes, the peak occurs at higher levels.

The phase is given by:  $ph \approx \arctan (\bar{\Psi}_i / \bar{\Psi}_r)$ .

For  $z = 0$  
$$\bar{\Psi}_i = |\delta|^{3/2} \frac{c_1 \pi K}{2 B_1} \quad \text{and} \quad \bar{\Psi}_r = -|\delta|^{1/2} c_1$$
 so that  $ph \approx -\pi \left( 1 - \frac{|\delta| K \pi}{2 B_1} \right)$ . As  $z$  approaches the critical level of  $|\delta|^{1/2} c_1$ , 
$$\bar{\Psi}_r \approx 0 \quad \text{and} \quad \bar{\Psi}_i \approx -|\delta|^{3/2} \frac{c_1 \pi K}{2 B_1} e^{-\alpha |\delta|^{1/2} c_1}$$
 and the phase has shifted to  $-\pi/2$ . Finally, for  $z \gg |\delta|^{1/2} c_1$ ,

$$\bar{\Psi}_r \approx z e^{-\alpha z} \quad \bar{\Psi}_i \approx -|\delta|^{3/2} \frac{c_1 \pi K}{2 B_1} e^{-\alpha z} \ll \bar{\Psi}_r$$

so that  $ph \approx \frac{-|\delta|^{3/2} c_1 \pi K}{2 B_1 z}$ , vanishing as  $z \rightarrow \infty$ .

Thus the phase varies by  $\pi + \frac{|\delta| \pi K}{2 B_1}$  with a shift of about  $\pi/2$  occurring below the critical level,  $z = |\delta|^{1/2} c_1$ . The phase varies most rapidly when 
$$\bar{\Psi}_r \sim \bar{\Psi}_i \sim |\delta|^{3/2} \quad \text{or} \quad z - |\delta|^{1/2} c_1 \sim |\delta|^{3/2}$$

which is the thin layer of rapid phase shift described above. In Fig. 2.11 most of the shift occurs slightly below  $z = |\delta|^{1/2} c_1$  because of higher order corrections to  $\bar{\Psi}_r$ , i.e.  $\bar{\Psi}_r$  vanishes at a level of  $|\delta|^{1/2} c_1 + 0(|\delta|)$ .

In more complicated profiles of  $\frac{d\bar{u}}{dz}$  and  $N_s^2$  (Geisler and Garcia,

1977; Fullmer, 1979) the neutral curve separating Green and Charney modes can vanish for  $\gamma > 0$ , often leaving a dip in the growth rate of some moderate wavenumber. The behavior of the modes on either side are quite similar to the simple profile considered here. The waves to the long wave side have more vertical structure and are usually more slowly growing than the shorter waves. Relationships between phase and amplitude are similar to that described here.

Wave fluxes are calculated to lowest order in the same manner as in Section II-3 (eqs. 2.3.13a-c). For the Charney modes, we find

$$\overline{v'z'}, \overline{v'\theta'} \propto e^{-2\alpha z} + o(|\delta|) \quad (2.4.23a)$$

$$\overline{w'\theta'} \propto (2\alpha z - \alpha^2 z^2) e^{-2\alpha z} + o(|\delta|) \quad (2.4.23b)$$

Because the  $O(|\delta|)$  contribution to  $\overline{\Psi}$  is real, the representations of the flux structures are correct to  $O(|\delta|)$  rather than simply  $|\delta|^{\frac{1}{2}}$ . These fluxes are plotted in Fig. 2.12 and it is evident that the vertical flux will stabilize the lowest layers. The fluxes of the short-wave expansion of Fig. 2.6 are crudely similar to these fluxes. The vertical scale here is  $O(\alpha^{-1})$  or dimensionally,  $O\left(\frac{H}{\sqrt{4k^2+1}-1}\right)$ .

The structures are dependent on  $K$  only. For the wavenumber of maximum growth,  $K \approx \frac{1+\gamma}{2}$  from the short-wave approximation, the vertical scale is  $O\left(\frac{H}{\sqrt{(1+\gamma)^2+1}-1}\right)$  or  $O(H)$  for  $\gamma \ll 1$  and  $O(H/\gamma)$  for  $\gamma \gg 1$ .

For the Green modes the flux forms in eqs. (2.4.23a,b) are accurate to  $O(|\delta|^{\frac{1}{2}})$ . The fluxes for either type of mode are shallower than the wave amplitude as they have an  $e$ -folding scale of  $(2\alpha)^{-1}$  instead

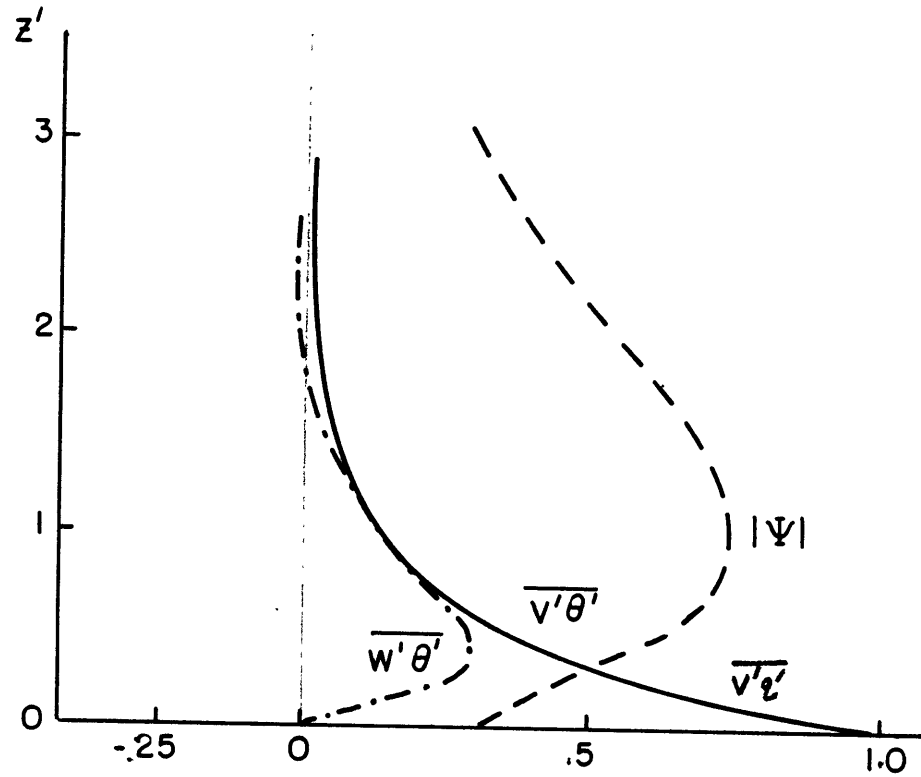


Fig. 2.12. Potential vorticity and horizontal heat flux (solid) and vertical heat flux (dash-dot) to  $O(|\delta|)$  for Charney modes vs.  $z' = \alpha z$ . Also plotted is amplitude structure (dashed) from Fig. 2.9a. in this vertical co-ordinate. Dimensional vertical co-ordinate is  $\frac{H}{K\alpha} z'$ .

of  $\alpha^{-1}$  as for wave amplitude. The relationship was also seen in the over-reflection calculations of  $\overline{v'q'}$  by Lindzen et al (1980).

## 5. Summary

Through perturbation expansions from the short wave limit and near the first neutral curve, we obtained approximate expressions for the structures and eigenvalues of the Charney modes and the shortest Green modes. It was demonstrated that the appropriate wavelength for the most unstable Charney modes is  $O\left(\frac{NH}{f(1+\gamma)}\right)$  and estimates were made from the short wave expansion for exact values of this wavelength. In the limit of  $\gamma \ll 1$  the waves are like Eady waves and have deep vertical scales of the density scale height,  $H$ . These may be long or short waves depending on the scale  $NH/f$ . For  $\gamma \gg 1$  the waves have a vertical scale of  $h \ll H$  where  $h = \frac{\partial \bar{u}}{\partial z} f^2 / \beta N^2$  and have a horizontal scale of  $Nh/f$  or much shorter than the Eady waves.

The expansion from the neutral curve on the Charney mode side does not give a most unstable wavelength. The growth rate asymptotically approaches a constant for short waves to the order found in the expansion. However, it does give a better representation of the wave structure, esp. the eddy fluxes of heat and potential vorticity, than the short wave expansion. The short-wave expansion of Section II-3 gives discontinuities in the phase and fluxes not seen in numerical calculations or observations. As mentioned, these discontinuities are caused by the mathematical treatment. Based on the short wave results for the most unstable wavelength and long Charney wave results for the flux structures, heat and momentum flux parameterizations are suggested in following chapters.

Baroclinic conversions occur on a variety of scales in the atmosphere. Cyclone disturbances (zonal wavenumber  $\sim 15$ ) are rapidly growing waves that exhibit scales and vertical structure similar to the short wave end of the Charney spectrum. Longer waves (wavenumber  $\sim 6$ ) exhibit deeper structures generally reaching maximum amplitude in the upper troposphere as do the longer Charney modes. The growth rates at  $\gamma = 1$  are comparable for a fairly broad band of Charney modes and is not surprisingly to see short and long waves that have the characteristics of the Charney modes. Finally, Green modes (wavenumber  $\sim 2$ ) have been suggested for transient stratospheric disturbances.

It may be an ill-posed question to determine a single wavelength or structure for baroclinic waves in the atmosphere. Yet, examining the transport properties of the most unstable wave in the Charney mode spectrum will reveal the general behavior of waves of comparable growth rates. Because the Charney modes are the most rapidly growing and have heat fluxes in the lowest layers, they are expected to influence the mean tropospheric state. This premise directs the development of the parameterizations of Chapters III and IV.

## CHAPTER III

## PARAMETERIZATION OF HEAT FLUXES

## 1. Development of Parameterization

In this section a parameterization scheme for the horizontal and vertical heat fluxes for the Charney modes is developed. Some discussion is given concerning the response of these representations to changes in the mean flow parameters. In Section III-2 we test the scheme using observed mean flow data and in a symmetric climate model that includes other physical processes. In Section III-3 the parameterizations are used in an analytical energy balance model and applied to three planetary atmospheres. A brief summary is given in Section III-4.

We formulate the heat fluxes on the basis of the linear model of Chapter II. The perturbation streamfunction in dimensional terms is:

$$\psi' = A \phi \bar{\Psi}\left(\frac{z}{H}\right) e^{i(kx + ly - kct)}$$

where  $A$  is a dimensionless complex amplitude,  $\phi$  is a real dimensioned quantity,  $\bar{\Psi}$  is the form of the vertical structure from Section II-4, and  $K = (k^2 + \ell^2)^{\frac{1}{2}} (N_{SH}/f_0)$ . All co-ordinates are in dimensional form. The meridional entropy flux is:

$$\overline{v'\theta'} = \frac{\theta_s f_0}{g} \overline{\frac{\partial \psi'}{\partial x} \frac{\partial \psi'}{\partial z}} = \frac{\theta_s f_0}{2g} k |A|^2 \phi^2 \frac{K}{H} \left[ i \bar{\Psi} \frac{d\bar{\Psi}^*}{d\left(\frac{z}{H}\right)} \right]_r \quad (3.1.1)$$

where the overbar is a zonal average and  $\theta_s = \theta_s(z)$  is an average potential temperature profile. A secular term of  $e^{2kc_1 t}$  is absorbed into  $A$ . For the dimensionless quantity in brackets we will use the structure from eq. (2.4.23a) for the long Charney waves, namely

$$\left[ i \Psi \frac{d\Psi^*}{d\left(\frac{zK}{H}\right)} \right]_r = e^{-z/d} \quad \text{with} \quad d = \frac{H}{\sqrt{4K^2 + 1}} .$$

The vertical velocity is written as:

$$w' = W \omega\left(\frac{zK}{H}\right) e^{i(kx + ly - kct)}$$

where  $W$  is a dimensioned constant and  $\omega$  is a dimensionless structure.

From the thermodynamic equation

$$\left( \frac{\partial}{\partial t} + \bar{u} \frac{\partial}{\partial x} \right) \frac{\partial \psi'}{\partial z} - \frac{\partial \bar{u}}{\partial z} \frac{\partial \psi'}{\partial x} + \frac{N^2}{f_0} w' = 0$$

we find

$$W = k \frac{\partial \bar{u}}{\partial z} \frac{f_0}{N_s^2} \phi A \quad \text{and}$$

$$\omega\left(\frac{zK}{H}\right) = i \left[ \left( \frac{kC}{\frac{\partial \bar{u}}{\partial z} H} - \frac{zK}{H} \right) \frac{d\Psi}{d\left(\frac{zK}{H}\right)} + \Psi \right].$$

The vertical heat flux is:

$$\overline{w'\theta'} = \frac{\theta_s f_0}{g} \overline{w'\psi'_z} = \frac{\theta_s f_0^2 k \frac{\partial \bar{u}}{\partial z} |A|^2 \phi^2 k}{2g N_s^2 H} \left[ \omega\left(\frac{zK}{H}\right) \frac{d\Psi^*}{d\left(\frac{zK}{H}\right)} \right]_r \quad (3.1.2)$$

and the form of the bracketed quantity is

$$\left[ \omega\left(\frac{zK}{H}\right) \frac{d\Psi^*}{d\left(\frac{zK}{H}\right)} \right]_r = \left( \frac{z}{d} - \left( \frac{z}{2d} \right)^2 \right) e^{-z/d}$$

from eq. (2.4.23b).

The ratio of the fluxes, (3.1.1) and 3.1.2), is:

$$\frac{\overline{w'\theta'}}{\overline{v'\theta'}} = \left[ \frac{z}{d} - \left( \frac{z}{2d} \right)^2 \right] \frac{\partial \bar{u}}{\partial z} \frac{f_0}{N_s^2} \quad (3.1.3)$$

with

$$\frac{\partial \bar{u}}{\partial z} \frac{f_0}{N_s^2} = - \frac{\partial \bar{\theta}}{\partial y} / \frac{\partial \theta_s}{\partial z} .$$

The gradient,  $\frac{\partial \bar{\theta}}{\partial y}$ , is the zonal-time mean gradient superimposed on  $\theta_s(z)$ , i.e. the gradient associated with the thermal wind shear. Scaled by the isentropic slope,  $-\frac{\partial \bar{\theta}}{\partial y} / \frac{\partial \theta_s}{\partial z}$ , the flux ratio of eq. (3.1.3) is plotted against height in Fig. 3.1. Note that in the lower levels where the fluxes are largest the angle of the heat flux is restricted between the horizontal plane and the isentropes as expected from energy conversion considerations.

For the Charney modes ( $r < 1$ ) the lowest order approximation to the steering level,  $z_c$ , is found from eq. (2.4.21) and is:

$$z_c = d(1-r) \left( \frac{3}{2} - \frac{1}{2\sqrt{4K^2+1}} \right).$$

It is easily seen that for the shortest waves ( $r \ll 1, K \ll 1$ )  $z_c \approx 3/2 d$  and for the longest Charney modes ( $r \approx 1$ )  $z_c \sim d(1-r) \ll d$ . The fastest growing waves will have an intermediate value and, near their steering level, we see from Fig. 3.1 that the flux vector falls about halfway between the horizontal plane and isentropes. This agrees with Green's (1970) physical arguments for optimal energy conversion near the steering level where particle displacements will be largest.

While the vertical average of the scaled flux ratio is about 1/2 as expected, it can attain a value of 1 at mid-tropospheric levels for the most unstable wave ( $K \approx 1.5$ ,  $\gamma = 1$ ). Therefore, it may not be generally assumed that the scaled ratio is nearly 1/2 at all levels far from the surface where  $w' = 0$ .

To proceed in the modeling of the heat fluxes, we propose the following simplifications. First, the heat flux will be represented by a single wave, namely, the most unstable Charney mode. Second, the shape of the wave will be given by the linear stability analysis. Third, the amplitude of the wave and its corresponding heat fluxes will be represented by a

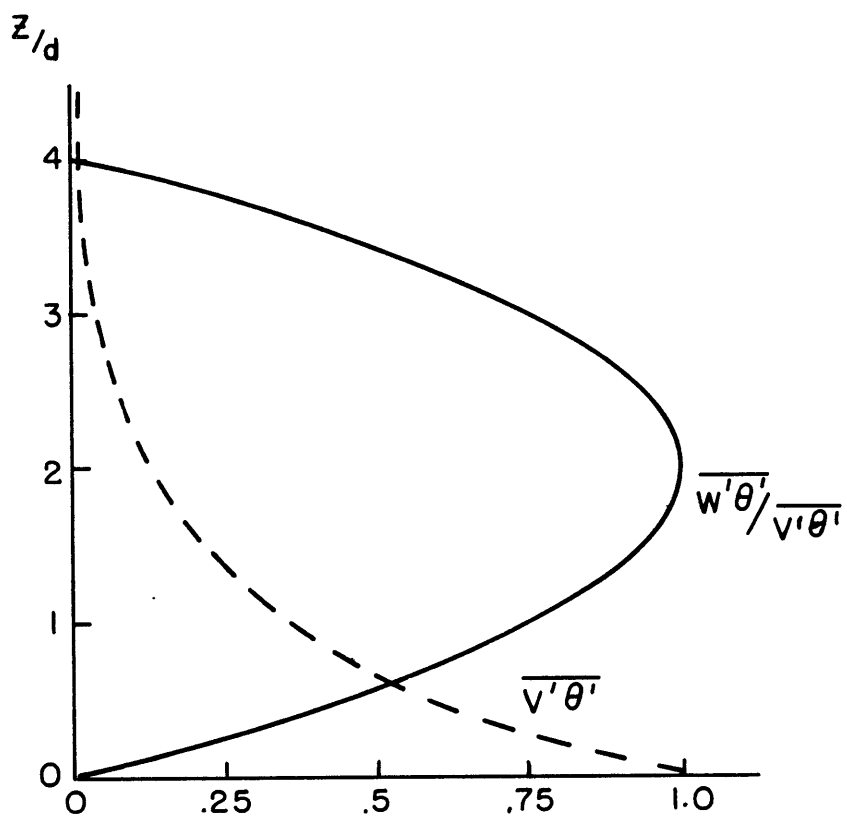


Fig. 3.1. Ratio of  $\overline{w'\theta'}/\overline{v'\theta'}$  scaled by isentropic slope and plotted against  $z/d$  where  $d$  is the eddy depth. Also shown is  $\overline{v'\theta'} \sim e^{-z/d}$

a time mean amplitude. Fourth, this mean amplitude will depend on the mean flow parameters. These basic assumptions have been used by Charney (1959) and Stone (1972) in analytic models of the general circulation. In the following discussion, we will present evidence from analytical, numerical, and experimental studies that supports these simplifications.

Though a spectrum of wavenumbers surrounding the most unstable mode will contribute to the heat flux, we can represent its general behavior by choosing a single, rapidly growing wave. Thus, the energy exchange between the mean flow and the eddies is dominated by the most linearly unstable mode. This mechanism is analogous to the behavior of baroclinic waves in annulus experiments (e.g. Pfeffer et al 1974, Hart, 1976). Hart (1974, 1976) has compared weakly nonlinear theory that includes interaction between the only unstable mode and the mean flow with laboratory experiments. He finds the single wave model is successful in predicting the experimental eddy amplitudes, even for fairly large values of the expansion or stability parameter. While baroclinic conversions occur on many scales in the atmosphere, we will simulate the heat flux spectrum by the mode that is most unstable with respect to the zonally averaged state.

The vertical structure of the wave will be determined by linear stability analysis. In the early growing stage of the waves we expect this shape assumption to be fairly accurate. In later applications we will find that the vertical structure of the horizontal and vertical fluxes is well simulated by the linear structure. The finite amplitude theory of Pedlosky (1979) examined weakly unstable Charney modes near the  $r=1$  neutral curve and, at lowest order, these waves have the same vertical structure as in the linear analysis. Simmons and Hoskins (1978)

show some enhancement of upper-level, horizontal transport in a numerical study of nonlinear baroclinic instability. However, approximation with the linear wave structure will be satisfactory for most applications.

The amplitude of the wave flux will be represented by a time mean. Theoretical and experimental results (Boville, 1980, Pfeffer et al, 1974) demonstrate that conversion from zonal to eddy available potential energy is dominated by the growing phase of the most unstable mode. Under substantially supercritical conditions little or no conversion in the opposite direction occurs during the decaying phase with most of the eddy energy lost to frictional dissipation. Since the decaying phase is not longer than the growing, energy-converting stage, the time mean heat flux is of the same order as the heat flux during the growing phase.

In Boville's multi-mode, numerical f-plane study potential energy generation is relatively constant during the amplitude vacillation cycle. The zonal available potential energy (Z.A.P.E.) is periodically depleted by baroclinic conversions to eddy energy. The Z.A.P.E. is replenished by differential heating after the baroclinic wave has consumed much of its energy source (Z.A.P.E.) and is dissipated by friction. As the Z.A.P.E. is restored, energy is again converted to the eddy field. Energetics studies indicate a similar process occurs in annulus experiments (Pfeffer, et al 1974) and in the atmosphere. Therefore, we will model the time mean flux of the baroclinic eddies that maintain the conversion process.

Now we must determine the parameter dependence of the unspecified amplitude,  $|A|^2 \phi^2$ . The weakly nonlinear theory of Pedlosky (1971) examines the interaction between a single unstable mode and the mean flow in a two-level, f-plane model. For weak viscosity the wave's equilibrium

amplitude is given by:

$$|\psi'|^2 \sim (U_1 - U_2)^2 L_y^2 \left[ (4\pi^2 R_d^2 (L_x^{-2} + L_y^{-2}))^{-1} - \frac{1}{2} \right]$$

where  $U_1 - U_2 =$  mean shear,  $R_d = N_s H / f_0$ , and  $L_x, L_y =$  zonal and meridional wavelengths. The term in brackets is the "small" expansion parameter that measures the instability of the flow. Similar amplitudes are found by Hart (1973) for cylindrical geometry and by Drazin (1972) for a continuous, f-plane model. Hart (1974) has shown that the weakly nonlinear theory agrees with experimental flow even for  $O(1)$  values of the expansion parameter, i.e. for more rapidly growing waves. For the most unstable mode ( $L_x \sim R_d$ ) and with  $L_y \gtrsim R_d$ , we find:

$$|\psi'|^2 \sim (U_1 - U_2)^2 L_y^2 .$$

This expression for the amplitude can also be derived from scaling arguments. For quasi-geostrophic flow we expect:

$$|v'| \sim |u'| L_y / L_x .$$

The only scale for  $|u'|$  is given by the thermal wind shear and the fluid depth so that  $|u'| \sim \frac{\partial \bar{u}}{\partial z} H$ . In this case, we find:

$$|\psi'|^2 \sim |v'|^2 L_x^2 \sim \left( \frac{\partial \bar{u}}{\partial z} H \right)^2 L_y^2$$

which is equivalent to Pedlosky's result.

This is also equivalent to an equi-partitioning between eddy kinetic energy and zonal available potential energy across the meridional eddy scale. For the baroclinic waves it can be shown that

$$|v'| \sim \frac{g|\theta'|}{N_s \theta_s}$$

which states equivalence of kinetic and available potential energies of the eddies. If the eddy potential energy is equal to the zonal available

potential energy across  $L_y$ , that is,

$$\left( \frac{g|\theta'|}{N_s \theta_s} \right)^2 \sim \left( \frac{g \left| \frac{\partial \bar{\theta}}{\partial y} \right| L_y}{N_s \theta_s} \right)^2,$$

then we obtain

$$|v'| \sim \frac{f_0 \frac{\partial \bar{u}}{\partial z}}{N_s} L_y \sim \frac{\partial \bar{u}}{\partial z} H \frac{L_y}{L_x}.$$

This closure assumption has been used by Stone (1972) to parameterize baroclinic eddy fluxes on an  $f$ -plane.

Pedlosky (1979) has also performed the weakly nonlinear analysis for the Charney model which includes the  $\beta$ -effect. An analogous amplitude in the presence of weak dissipation is found, specifically,

$$|\psi'|^2 \sim \left( \frac{\partial \bar{u}}{\partial z} \frac{f_0 L_x}{N_s} \right)^2 L_y^2.$$

For the most unstable Charney mode, we have found:

$$L_x \sim \frac{N_s d_e}{f_0} \quad \text{where} \quad d_e = \frac{H}{1+\gamma}$$

so that 
$$|\psi'|^2 \sim \left( \frac{\partial \bar{u}}{\partial z} d_e \right)^2 L_y^2.$$

The height scale of the wave has been corrected to account for the  $\beta$ -effect.

Now the meridional eddy scale,  $L_y$ , is chosen by considering the ratio,  $\lambda = \frac{L_{\bar{u}}}{\left( \frac{N_s d_e}{f_0} \right)}$  where  $L_{\bar{u}}$  is the meridional scale of the mean zonal flow. In the Charney model of Chapter II this ratio is assumed to be infinite and no meridional wavelength is selected. In the atmosphere  $\lambda$  is about 5. Killworth (1980) has examined the Boussinesq, vertically bounded form of eq. (2.1.5) with  $\bar{u} = \bar{u}(y, z)$  for large  $\lambda$ . For general structures of  $\bar{u}$  within the constraint of large  $\lambda$ , he

found the perturbation streamfunction oscillates meridionally on a scale of the deformation radius. It has also been shown that in the presence of basic state baroclinic waves, the instabilities will draw on eddy available potential energy and have a meridional scale of the deformation radius (Pedlosky, 1975a; Kim, 1978; Lin, 1979). Therefore, the appropriate scale for  $L_y$  is also  $N_s d_e / f_0$  and

$$|\psi'|^2 \sim \left( \frac{\partial \bar{u}}{\partial z} d_e \right)^2 \left( \frac{N_s d_e}{f_0} \right)^2 \text{ or } |v'| \sim \frac{\partial \bar{u}}{\partial z} d_e.$$

This choice of  $L_y$  is different from Green's (1970) parameterization method in which he chose  $L_y$  to be the planetary radius. This is equivalent to assuming the eddy draws zonal available potential energy across the planetary rather than eddy scale. As suggested by Pedlosky (1975b), only potential energy across the wave scale will be available to the growing wave.

Boundary conditions may alter the choice of  $L_y$  in other physical systems. As an example, the baroclinic waves in annulus experiments have meridional scales fixed at the annular radius. The introduction of topography may influence the selection of both  $L_x$  and  $L_y$ . In either case the dependence of the heat flux on the mean flow parameters may be different from the system considered here.

In summary, we will choose a closure assumption on the basis of

$$|\psi'|^2 \sim |A|^2 \phi^2 \sim \left( \frac{\partial \bar{u}}{\partial z} d_e \right)^2 \left( \frac{N_s d_e}{f_0} \right)^2$$

where  $d_e$ , the eddy depth, depends on the mean flow parameters according to the Charney model. In terms of the horizontal heat flux, we find from

eq. (3.1.1): 
$$\overline{v'\theta'} \sim \left( \frac{\partial \bar{u}}{\partial z} d_e \right)^2 \frac{\theta_s N_s}{g}.$$

This amplitude is the same as the scaling arguments developed by Held (1978) for the  $\beta$ -plane and the energy partitioning assumption of Stone (1972) if  $d_e$  is replaced by  $H$  (i.e.  $\beta=0$ ). We assume that  $\bar{u}$  varies on a meridional scale larger than  $N_S d_e / f_0$  and no topographic features change the scale selection.

In the context of the stability analysis, an equivalent closure assumption is used. We assume the vertically averaged amplitude of the perturbation's meridional momentum equals the mean zonal momentum weighted by the heat flux structure of the wave. That is, we take the scale for  $|v'|$  to be proportional to  $\frac{\partial \bar{u}}{\partial z} d$  where  $d$  is the scale height of the horizontal heat flux. Only layers in which the energy is effectively converted will contribute to the wave amplitude just as only potential energy across the meridional scale will be converted. Since  $d \sim d_e$ , this amplitude scaling is essentially the same one described above.

Specifically,

$$\int_0^\infty \rho_s \bar{u} e^{-z/d} dz = \int_0^\infty \rho_s |v'| dz \quad (3.1.4)$$

and substituting  $\bar{u} = \frac{\partial \bar{\Psi}}{\partial z} z$  and  $v' = \frac{\partial \Psi'}{\partial x}$  (using the lowest order representation of  $\bar{\Psi}$ ), we find:

$$|A| \phi = \frac{\partial \bar{u}}{\partial z} \frac{H}{k} \left( \frac{1 + H/2d}{1 + H/d} \right)^2.$$

The quantity in parentheses is  $O(1)$  for  $d \lesssim H$ , and is dropped, leaving

$$k |A| \phi = \frac{\partial \bar{u}}{\partial z} \frac{H}{k}. \quad (3.1.5)$$

For the rapidly growing Charney modes  $K \sim 1 + \gamma$  and since the left side of eq. (3.1.5) is  $|v'|$ , this simply states  $|v'| \sim \frac{\partial \bar{u}}{\partial z} d_e$ .

Substituting eq. (3.1.5) into (3.1.1) and (3.1.2), we obtain:

$$\overline{v'\theta'} = \frac{\theta_s f_0 \left(\frac{\partial \bar{u}}{\partial z}\right)^2 H}{2g k K} e^{-z/d} \quad (3.1.6)$$

$$\overline{w'\theta'} = \frac{\theta_s f_0^2 \left(\frac{\partial \bar{u}}{\partial z}\right)^3 H}{2g N_s^2 k K} \left(\frac{z}{d} - \left(\frac{z}{2d}\right)^2\right) e^{-z/d} \quad (3.1.7)$$

where  $d = H / (\sqrt{1+4K^2} - 1)$ .

In the discussions above, it was mentioned that the heat flux would be represented by the most rapidly growing wave. In particular, we choose  $k = \frac{f_0(1+\gamma)}{\sqrt{2} N_s H}$  and since we have assumed  $L_y \sim L_x$ , also set  $l = k$ . This is equivalent to choosing  $K = 1 + \gamma$  or a wavenumber to within an  $O(1)$  factor of the most unstable wave of the short-wave approximation of Chapter II. To simplify later applications, we approximate  $d$  at  $K = 1 + \gamma$  by  $H/(1+\gamma)$ . Then eqs. (3.1.6) and (3.1.7) become:

$$\overline{v'\theta'} = \frac{\theta_s N_s d^2}{\sqrt{2} g} \left(\frac{\partial \bar{u}}{\partial z}\right)^2 e^{-z/d} \quad (3.1.8)$$

$$\overline{w'\theta'} = \frac{\theta_s f_0 d^2}{\sqrt{2} g N_s} \left(\frac{\partial \bar{u}}{\partial z}\right)^3 \left(\frac{z}{d} - \left(\frac{z}{2d}\right)^2\right) e^{-z/d} \quad (3.1.9)$$

with  $d = H/(1+\gamma)$  and  $\gamma = \frac{\beta_0 N_s^2 H}{f_0^2 \frac{\partial \bar{u}}{\partial z}}$ .

The amplitude of  $\overline{v'\theta'}$  is the same as that given by the scaling argument above.

The expressions (3.1.8) and (3.1.9) are now compared with the previous representations of Stone (1972) and Held (1978). For  $\gamma \ll 1$ ,

$$\begin{aligned} \langle \overline{v'\theta'} \rangle &\sim \frac{g H^2}{\theta_s f_0^2} \left| \frac{\partial \bar{\theta}}{\partial y} \right|^2 \left( \frac{g}{\theta_s} \frac{\partial \theta_s}{\partial z} \right)^{1/2} \\ \langle \overline{w'\theta'} \rangle &\sim \frac{g^2 H^2}{\theta_s^2 f_0^2} \left| \frac{\partial \bar{\theta}}{\partial y} \right|^3 \left( \frac{g}{\theta_s} \frac{\partial \theta_s}{\partial z} \right)^{-1/2} \end{aligned}$$

where  $\langle F \rangle = \int_0^\infty F \rho_s(z) dz / \int_0^\infty \rho_s dz.$

This limit has the same parameter dependence as Stone's f-plane modeling.

For  $\gamma \gg 1$ , we find

$$\langle \overline{v'\theta'} \rangle \sim \frac{f_0 g^4}{\beta_0^3 \theta_s^4 H} \left| \frac{\partial \bar{\theta}}{\partial y} \right|^5 \left( \frac{g}{\theta_s} \frac{\partial \theta_s}{\partial z} \right)^{-5/2} \quad \text{and}$$

$$\langle \overline{w'\theta'} \rangle \sim \frac{f_0 g^5}{\beta_0^3 \theta_s^5 H} \left| \frac{\partial \bar{\theta}}{\partial y} \right|^6 \left( \frac{g}{\theta_s} \frac{\partial \theta_s}{\partial z} \right)^{-7/2}.$$

Held first pointed out the different dependence of  $\langle \overline{v'\theta'} \rangle$  on  $\frac{\partial \bar{\theta}}{\partial y}$  in these two limits. It is seen that as  $\gamma$  becomes large or equivalently,  $\left| \frac{\partial \bar{\theta}}{\partial y} \right|$  small, the horizontal flux will fall rapidly. In effect, the waves become very short and shallow as  $\left| \frac{\partial \bar{\theta}}{\partial y} \right|$  or  $\frac{\partial \bar{u}}{\partial z}$  decreases with other parameters fixed.

Shown in Fig. 3.2 is  $\langle \overline{v'\theta'} \rangle$  plotted against shear with other parameters held constant. The shear has been scaled by its value at  $\gamma = 1$ , the analogue of the critical shear of the two-layer model. For large  $\frac{\partial \bar{u}}{\partial z}$  the flux obeys a square law and for small shear, a fifth power law. Held (1978) has a similar graph but, in his scaling analysis, could not obtain the transition region near  $\gamma = 1$ .

Note the rapid increase in flux for  $\gamma \ll 1$ . The correspondence to baroclinic transports in two-layer models is obvious. Stone (1978a) has shown the observed atmospheric shears in baroclinically active latitudes do not stray from the two-layer critical shear. From the continuous model considered here it is clear the fluxes rise dramatically for stronger shears. Near  $\gamma = 1$  a 10% increase in  $\frac{\partial \bar{u}}{\partial z}$  causes a 40% increase in flux.

The dependence on static stability is shown in Fig. 3.3. Here  $N_s'^2$

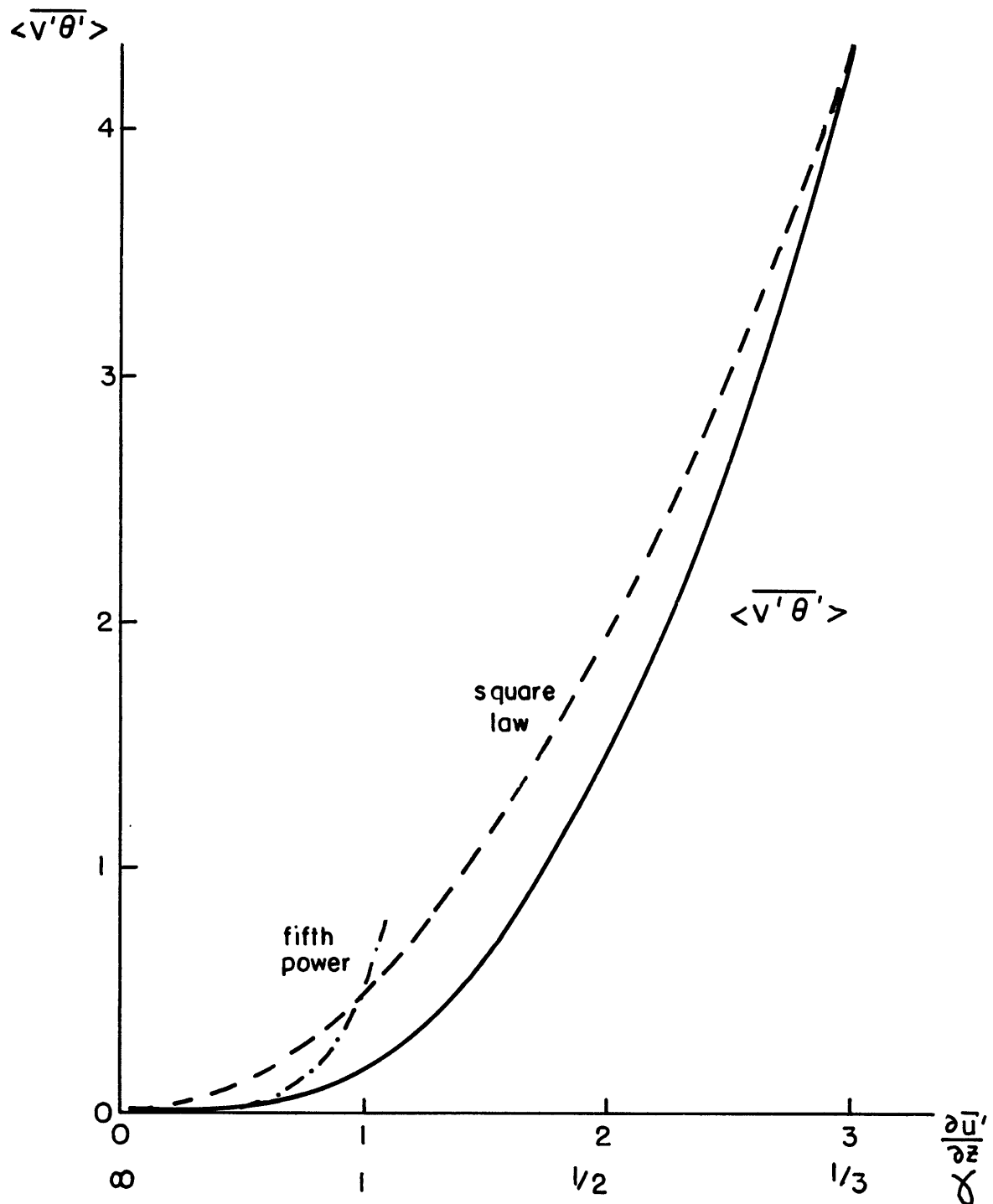


Fig. 3.2. Dimensionless vertical average of horizontal heat flux,  $\langle \overline{v'\theta'} \rangle$ , vs. scaled shear  $\frac{\partial \bar{u}'}{\partial z} = \frac{\partial \bar{u}}{\partial z} / \left( \frac{\beta_0 N_s^2 H}{f_0^2} \right)$  and  $\gamma$ .

Other parameters are fixed. Also plotted are square and fifth power laws for small and large  $\gamma$ .

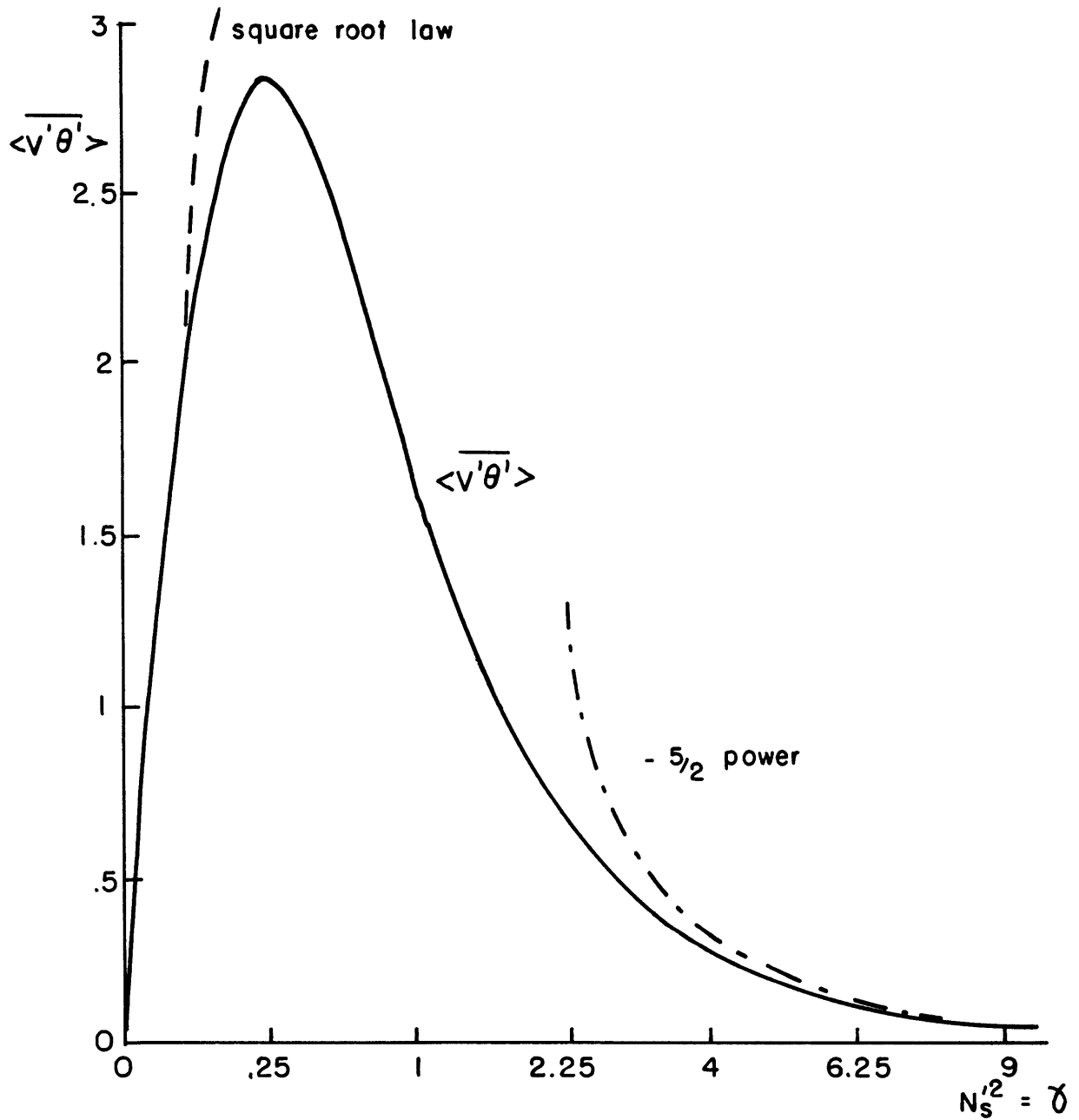


Fig. 3.3. Dimensionless  $\overline{\langle v'\theta' \rangle}$  vs. scaled static stability,

$$N_s'^2 = N_s^2 \left( -\frac{\beta_0 H}{f_0^2 \frac{\partial u}{\partial z}} \right). \text{ Other parameters are fixed. Also plotted}$$

are square root (dash) and  $-5/2$  power law (dash-dot).

is a dimensionless measure of static stability,  $N_s'^2$  scaled by its value at  $\gamma = 1$ . For  $N_s'^2 \ll 1$  ( $\gamma \ll 1$ ) the waves have the characteristics of Eady waves and have horizontal and vertical scales of  $N_s H / f_0$  and  $H$ . Consequently, the vertically integrated horizontal flux has a square root dependence on  $\frac{\partial \theta_s}{\partial z}$ . For  $N_s'^2 \gg 1$  ( $\gamma \gg 1$ ) the waves are shallow with  $d \sim f_0^2 \frac{\partial \bar{u}}{\partial z} / \beta_0 N_s'^2$  and short,  $L_x \sim f_0 \frac{\partial \bar{u}}{\partial z} / \beta N_s'$ . In this limit both height and length scales decrease as the static stability increases and the flux is rapidly reduced at a  $-5/2$  power law.

At intermediate values of  $N_s'^2$  the flux rapidly increases as  $N_s'^2$  decreases and passes through unity. Near  $N_s'^2 = \gamma = 1$  a 10% decrease in  $N_s'^2$  causes a 10% increase in  $\overline{v'\theta'}$ . A two-layer model would become unstable in this neighborhood and the flux would increase dramatically. With a continuing decrease in  $N_s'^2$  or  $\gamma$  the waves fill the fluid vertically. Finally, in the Eady limit, their horizontal scales begin to decrease with  $N_s$  and they become less effective heat transporters. A maximum flux is reached at  $N_s'^2 \approx 1/4$  in the transition region.

Fig. 3.4 shows the dependence of vertically averaged vertical flux on the shear or, equivalently, horizontal temperature gradient. Again the flux increases rapidly as the shear approaches its value at  $\gamma = 1$ . Near  $\gamma = 1$  the flux increases by 50% for a 10% increase in shear. The flux obeys a sixth power for small shear and a third power dependence for large shear.

Increasing static stability will decrease the vertical flux in either limit as vertical motions will be suppressed. Again the response is stronger in the short, shallow wave limit of  $\gamma \gg 1$  as the scale dependences change. This dependence on  $\frac{\partial \theta_s}{\partial z}$  is shown in Fig. 3.5. The flux increases rapidly as  $N_s'^2$  decreases and passes through unity, indicating

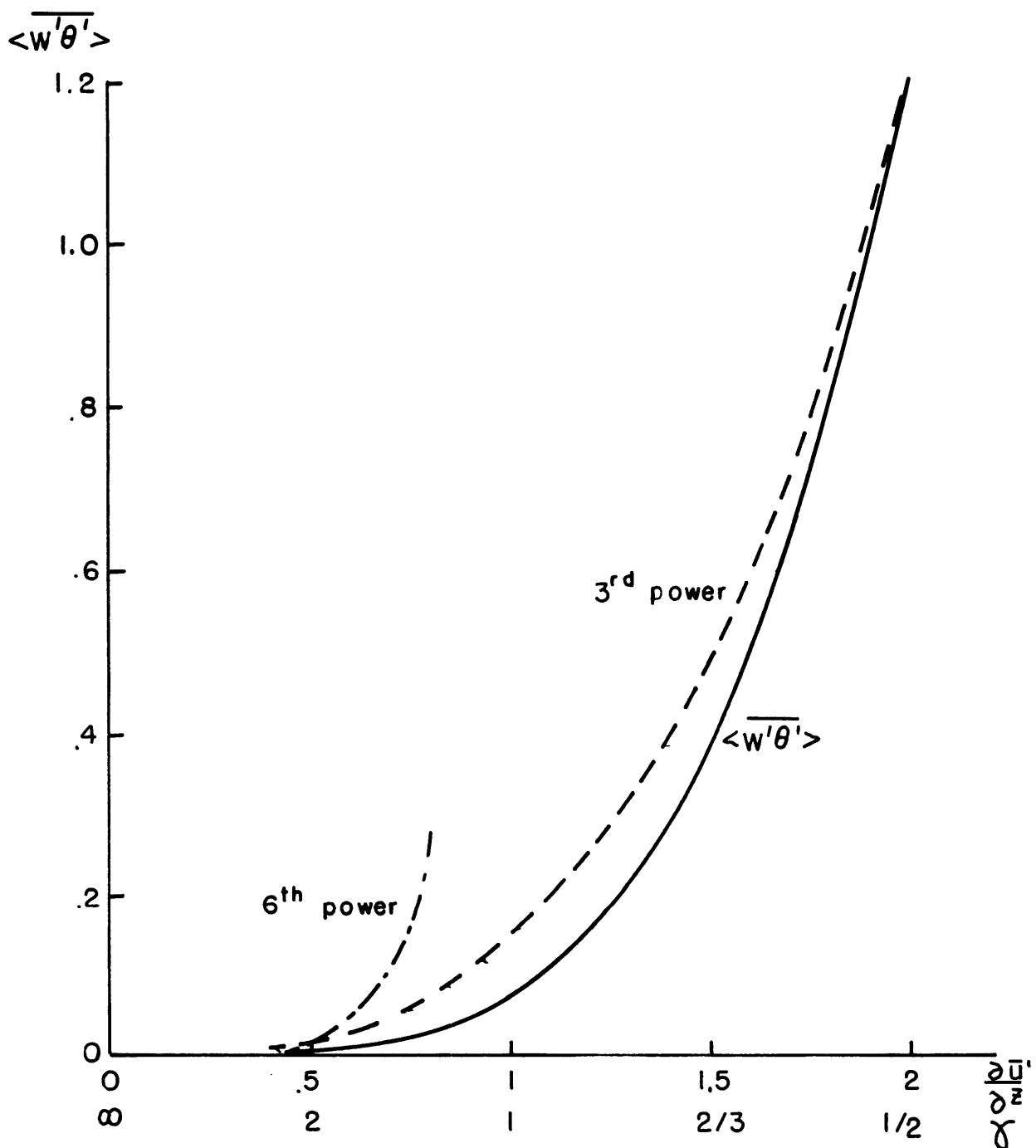


Fig. 3.4. Dimensionless vertical average of vertical heat flux,  $\overline{\langle w'\theta' \rangle}$ , vs. scaled shear,  $\frac{\partial \bar{u}'}{\partial z} \frac{\bar{u}'}{\gamma}$ . Also shown are third and sixth power laws.

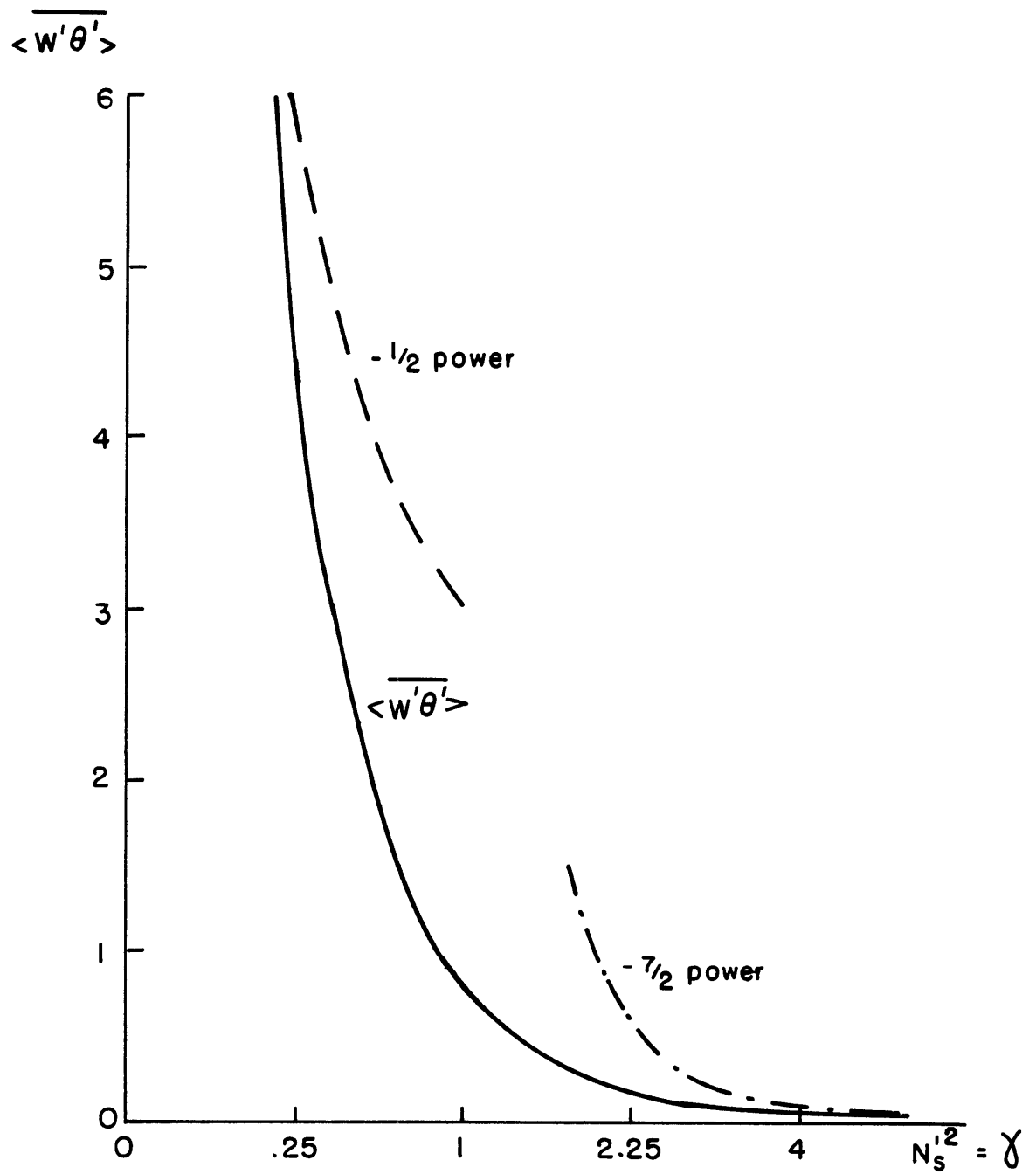


Fig. 3.5. Same as Fig. 3.4 vs.  $N_s'^2$ . Also shown are -1/2 and -7/2 power laws.

a strong negative feedback as the eddies attempt to stabilize the atmosphere. Near  $\gamma = 1$  the flux increases by 20% when the static stability decreases by 10%.

To summarize the flux-temperature gradient feedbacks, we have seen that the fluxes rapidly increase as  $\gamma$  decreases to 0(1) by either decreasing static stability or increasing the vertical shear by some unspecified external forcing. Corresponding behavior is seen in two-layer models when the instability criterion is satisfied. For all values of  $\gamma$  the vertical flux increases as static stability decreases acting as a negative feedback. Similarly, horizontal transport increases as the shear increases for all  $\gamma$ , again a negative feedback.

For  $\gamma > 1/4$  an increase in shear leads to an increase in vertical flux which stabilizes the atmosphere. This decreases the horizontal heat flux and, therefore, the combination of responses causes a positive feedback. Similarly, a forced increase in static stability causes less horizontal flux and greater meridional temperature gradients. This causes a strengthening of vertical flux and further vertical stabilization. For  $\gamma < 1/4$ , these feedback loops are negative as in Stone's (1972) f-plane parameterization because the horizontal flux will increase for greater static stability.

Whether positive or negative feedbacks dominate cannot be determined without specifying the external forcing that initiates the responses. These responses are further examined in Section III-3 in an analytical model which balances the radiative processes and eddy transports.

The application of eqs. (3.1.8) and (3.1.9) to atmospheric profiles in which  $\bar{u}$  is not linear in  $z$  nor independent of  $y$  and similarly,  $N_s$  is

not uniform, requires a procedure to evaluate the mean flow parameters. Since the stability calculations are performed locally with  $\bar{u} = \bar{u}(z)$ , no meridional structure for the perturbation is found. Furthermore, we have assumed the mean flow parameters vary on scales at least as large as the meridional wave scale. Consequently, the mean flow parameters should be evaluated locally in order to stay within the constraints of the stability analysis and the closure assumption.

The quantities  $\theta_s$ ,  $N_s$ ,  $H$ ,  $\frac{\partial \bar{u}}{\partial z}$  should be considered slowly varying functions of  $y$  and  $z$ . To determine the local value of the heat flux, we employ a method similar to the amplitude calculation. Vertical means of these parameters are found for a given latitude, weighted by the horizontal heat flux structure (i.e. the eddy depth). Thus, the important contributions are from the layers in which potential energy is readily converted. Furthermore, stability calculations have shown the Charney modes are largely insensitive to changes in shear and static stability well above layers of significant wave amplitude (Staley and Gall, 1977; Fullmer, 1979). An example of the averaging scheme is:

$$\left(\frac{\partial \bar{u}}{\partial z}\right)_w = \int_0^{\infty} \frac{\partial \bar{u}}{\partial z}(\gamma_0, z) e^{-z/d} dz / \int_0^{\infty} e^{-z/d} dz$$

with  $d$  as function of  $z$  in this integral. Once  $\left(\frac{\partial \bar{u}}{\partial z}\right)_w$ ,  $(N_s)_w$ ,  $(H)_w$  are determined, an average  $d$  is calculated. After these averages are found, the eddy fluxes will have meridional structures based on the variation of these averages and of  $\beta_0$  and  $f_0$ . This method approximates the heat transport characteristics of the most unstable baroclinic eddies at different latitudes.

### 3. Applications to Observations and Symmetric Model

In testing the parameterization scheme the observational data permits a comparison of predicted horizontal heat flux with the observed transport. Vertical flux is not well measured, but some comments will also apply to its variation.

While  $N_S$ ,  $\theta_S$ , and  $g$  are not strongly latitude dependent,  $\frac{\partial \bar{u}}{\partial z}$ ,  $f_0$ , and  $\beta_0$  are and will dominate variations in the heat flux. Equatorward of the subtropical jet  $\gamma$  increases rapidly as  $f_0^2 \frac{\partial \bar{u}}{\partial z}$  decreases. The implied decrease of  $d$  and observed drop-off in  $\frac{\partial \bar{u}}{\partial z}$  will cause a rapid reduction in the flux magnitude. In mid and high latitudes  $\gamma$  is  $O(1)$  as the observed shear is not far from the two-layer instability criterion (Stone, 1978a). However,  $\frac{\partial \bar{u}}{\partial z}$  decreases approximately as  $\sin^2 \phi / \cos \phi$  and so the transports will vanish. Consequently, the horizontal and vertical fluxes will vary on the planetary scale with a maximum at mid-latitudes.

The observed transient flux reaches a maximum at 850-900 mb at all latitudes (see Fig. 3.6). A weaker, secondary peak occurs near the tropopause. The flux is weaker in summer than winter with the greatest reduction at lower latitudes. In Northern Hemisphere winter the latitude of maximum flux at 1000 mb is about  $35^\circ\text{N}$ . Through the lower and mid-troposphere this latitude of peak flux shifts poleward with increasing altitude and occurs at  $60^\circ\text{N}$  at 500 mb (see Fig. 3.10 for January structure). This indicates increasing depth of the eddy flux at higher latitudes and it occurs in all seasons, though the shift is most pronounced in winter.

The parameterized flux has a maximum at the surface and decays exponentially aloft. A planetary boundary layer has not been included in this model and it is quite likely that frictional drag near the surface causes the observed flux to peak near the top of the boundary layer instead

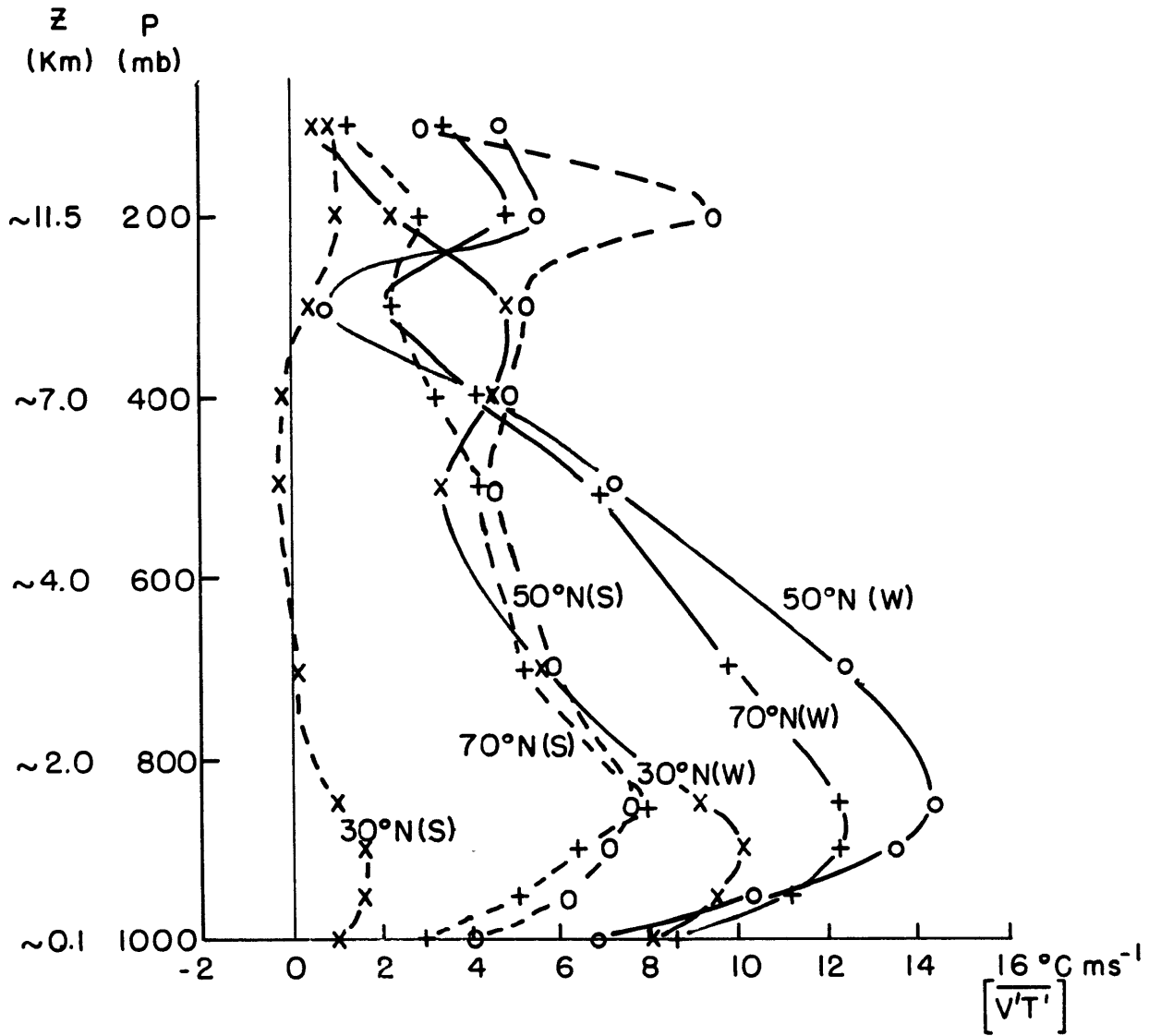


Fig. 3.6. Transient eddy sensible heat flux,  $[\overline{v'T'}]$ , at three latitudes,  $30^\circ\text{N}$  (x),  $50^\circ\text{N}$  (o),  $70^\circ\text{N}$  (+) for winter (w) and summer (s). From Oort and Rasmusson (1971).

at the surface. The effect of a stratosphere is also not included which may be responsible for the secondary heat flux peak (Fullmer, 1979). Therefore, comparisons of theory and data are limited to the tropospheric layers above the friction layer.

Using observed data for the mean flow parameters to obtain estimates of the flux can lead to large discrepancies with observed transports. Recalling that the atmosphere at middle and high latitudes is near  $\gamma = 1$  for which a 10% error in shear causes a 40% error in flux, very accurate observational data is required for flux estimates. However, it is also true that a wide range of flux values will correspond to realistic mean flow statistics.

Table 1 shows the winter and summer values of the mean flow parameters as found by the averaging procedure described in the preceding section. The data is taken from Oort and Rasmusson (1971) at three latitudes, 30°, 50°, and 70°N. To demonstrate the effect of the uncertainty in shear, the averages were also computed with zonal wind data of Newell et al (1972) and are given in parentheses when significantly different from the other means.

The fluxes are calculated from (3.1.8) for the 850 mb level and compared to the observed transient eddy flux at 850 mb from Oort and Rasmusson. The mass-weighted vertical mean of the flux is also computed and compared with observations. The observed tropospheric scale height of the transient flux and the flux depth predicted by the model can be compared in Table 1.

The total (transient and standing) eddy flux at 850 mb and for a vertical mean is also listed in Table 1. As discussed earlier, it is difficult to extract the correct sensible heat flux from the data for

TABLE 1

	30°N		50°N		70°N	
<u>Mean Flow Parameters</u>	Winter	Summer	Winter	Summer	Winter	Summer
$(\frac{\partial \bar{u}}{\partial z})_w$ (m sec <sup>-1</sup> km <sup>-1</sup> )	3.1(3.0)	0.7(0.6)	1.4(2.2)	1.4(1.5)	0.8(0.6)	0.7(1.2)
$(N_s)^2$ (10 <sup>-4</sup> sec <sup>-2</sup> )	1.48	1.71	1.63	1.80	2.68	1.71
$(d)_w$ (Km)	3.3(3.2)	1.0(0.9)	3.5(4.4)	3.8(3.9)	3.6(3.2)	4.3(5.2)
$(\gamma)_w$	1.44	7.3(8.7)	1.07(.72)	1.13(1.00)	.99(1.2)	.78(.48)
<u>Parameterized Flux(°K m sec<sup>-1</sup>)</u>						
1. at 850 mb	17.5(15.1)	.03(.02)	4.3(18.1)	5.4(6.5)	1.8(0.8)	1.8(8.5)
2. $\langle \overline{v'\theta'} \rangle$ - vert. avg.	8.1(7.0)	.02(.01)	2.1(9.1)	2.6(3.2)	0.9(0.4)	0.9(4.5)
<u>Transient Observed Flux</u>						
1. at 850 mb	9.1	1.0	14.4	7.6	12.3	8.0
2. $\langle \overline{v'\theta'} \rangle$ - vert. avg.	5.1	.5	8.1	5.8	7.3	4.3
3. scale height (Km)	4.2	1.0	4.9	6.5?	4.5	6.0
<u>Total Observed Flux</u>						
1. at 850 mb	10.7	0.7	28.6	5.9	11.2	8.6
2. $\langle \overline{v'\theta'} \rangle$ - vert. avg.	6.3	0.5	18.4	4.8	7.1	4.4

comparison with the parameterized flux. Furthermore, Stone and Miller (1980) have found strong negative feedbacks between transient and stationary fluxes in the observed transports. Stationary baroclinic waves would be expected to have some characteristics in scales and amplitudes that are similar to transient eddies. Therefore, it is wise to include total sensible heat flux for comparison with parameterized values.

The sensitivity to the shear when  $\gamma \approx 1$  is demonstrated in Table 1. A 3% change in the vertical shear causes 13% change in winter flux at 30°N. Similar degrees of sensitivity are seen at other latitudes. Relative errors in static stability are much less important because of the comparatively weak dependence on this parameter.

While close comparisons between theory and observations are difficult because of the aforementioned uncertainties, a few general comments can be made. The subtropics have larger values of  $\gamma$  than higher latitudes especially during the summer. This is also evident in Stone's (1978a) calculations of the two-layer instability criterion in the atmosphere. These higher values of  $\gamma$  suggest greater flux sensitivity to the meridional temperature gradient near 30°N as was found in the observed flux by Stone and Miller (1980). At 50° and 70°  $\gamma$  remains near unity through all seasons.

In response to the large fluctuations in shear at 30°N, the parameterization mimics the substantial seasonal fluctuation in flux magnitude and depth. The vertical averaged parameterized flux for the summer is much smaller than values that could be accurately measured with atmospheric data. The modeling scheme essentially predicts that baroclinic instability will be very ineffective in transporting heat. Of course, this is expected

for this particular latitude and season and other modes of heat transport may be occurring. Weak counter-gradient transient flux is observed in the mid-troposphere, extending from a tropical region of principally equatorward transport.

At 50°N the zonal wind data for winter of Oort and Rasmusson evidently has some error. No seasonal change is found in  $(\frac{\partial \bar{u}}{\partial z})_w$ , while their temperature data suggests a 30% increase from summer to winter. This variation would give a much more accurate parameterized flux as is found using Newell's data. Allowing for this error, the parameterization scheme again provides a reasonable seasonal variation of the flux magnitude. Comparison of the flux depth for summer is obscured by the presence of exceptionally strong upper tropospheric flux (see Fig. 3.6).

Using Newell's winter data at 50°N, the vertical mean model flux exceeds the observed transient flux by about 12%, but accounts for only 50% of the total flux. This particular latitude and season has the largest contribution from stationary eddy flux. Apparently, the parameterization scheme underestimates the total heat transport when significant stationary flux is present. However, when applying the scheme to a climate model with no asymmetric forcing, it is likely the parameterized transport will be closer to the total transport to compensate for the loss of the stationary eddy flux. As mentioned in Chapter I, this is frequently the case in three-dimensional simulations which explicitly calculate eddy transports.

For 70°N the lack of adequate data makes verification of the flux modeling difficult. The zonal wind data of both Oort and Rasmusson and Newell give considerable smaller than observed fluxes in the winter.

However, temperature data from Oort and Rasmusson would give a mean shear of  $1.2 \text{ m sec}^{-1} \text{ km}^{-1}$  corresponding to a 850 mb flux of  $7 \text{ }^\circ\text{K m sec}^{-1}$ . Considerable uncertainty is also evident in the summer calculation, although Newell's data gives an accurate flux.

Figures 3.7a and 3.7b compare the parameterized flux using Newell's zonal wind data with Newell's total flux observations (3.7a) and Oort and Rasmusson's transient flux (3.7b). Plotted as functions of pressure for the three different latitudes, it is seen that the model flux is a first approximation to the actual energy transport. The two major deficiencies in the vertical structure are caused by the lack of a frictional boundary layer and a tropopause.. The mid-tropospheric magnitudes predicted by the model are fairly accurate, esp. compared to the transient flux. One exception is the  $70^\circ\text{N}$  winter which has unreliable data for the mean flow parameters.

The parameterization reproduces the observed tendency of deeper heat fluxes in higher latitudes. This is principally due to the smaller values of  $\gamma$  at the higher latitudes. Also, seasonal changes in the depth are greatest at subtropical latitudes because of the larger variability in shear and thus,  $\gamma$ .

As in the observed transient heat flux, this scheme shifts the horizontal flux to higher latitudes in summer. While the parameterized transport is not easily compared to the magnitude of the observed flux, it does show many of the features of the seasonal changes and meridional structure.

An application of the parameterization scheme has been made in a symmetric version of the GISS general circulation climate model. Developed by Yao and Stone, this version includes explicit calculations of mean

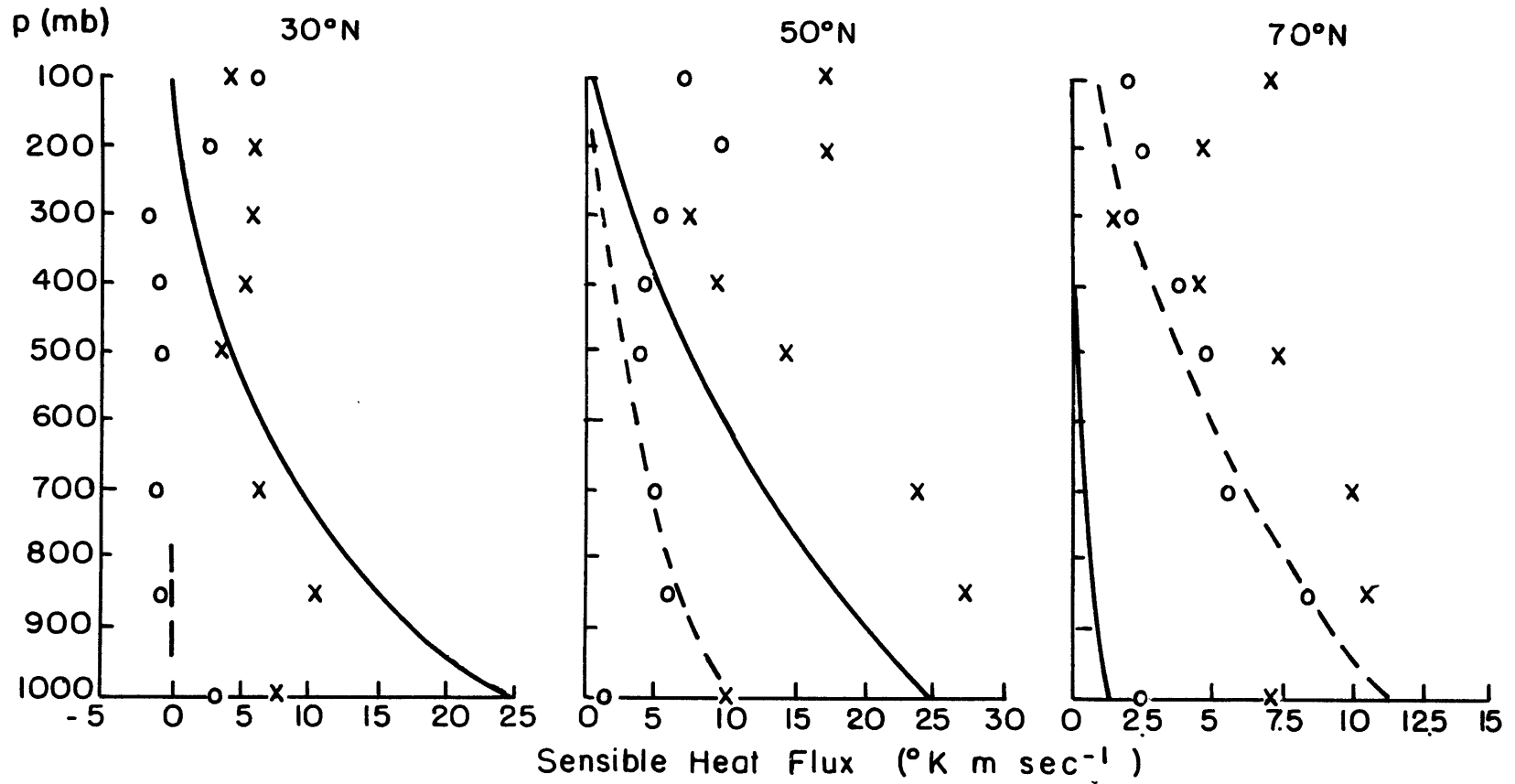


Fig. 3.7a. Parameterized flux using Newell's zonal wind data (dash-summer, solid-winter) vs. observed total flux from Newell et al (1974) (x-winter, o-summer).

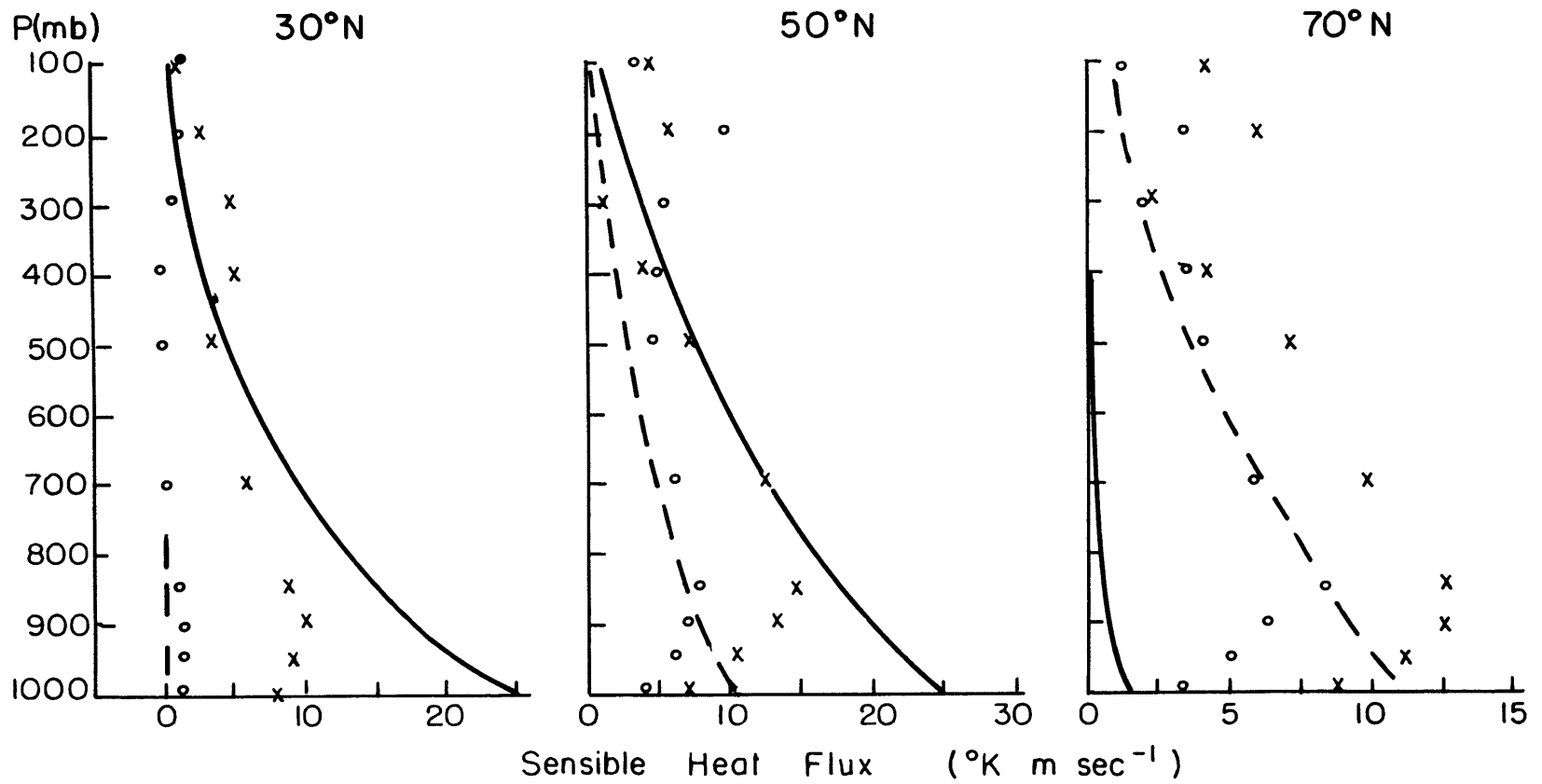


Fig. 3.7b. Same as Fig. 3.7a except observations are transient fluxes from Oort and Rasmusson (1971).

meridional circulations and physical processes such as radiation and moist convection. The effects of eddies, baroclinic or otherwise, must be evaluated on the basis of the model's mean flow statistics. For the horizontal and vertical heat flux by eddies the parameterization scheme of the previous section is used. The model has five tropospheric levels, the lowest at 933 mb, and a horizontal grid resolution of  $8^\circ$  latitude. After initialization with observations of December 1, 1976, the model is integrated in time with perpetual January insolation. The mean flow time averages are found over January 1, 1977 to February 1, 1977, a period in which the model has reached a quasi-equilibrium state. Since the model results are preliminary, discussion will be limited here to the effectiveness of the heat flux modeling.

Fig. 3.8 shows the time mean zonal wind of the model and the observed flow given by Newell et al (1972). The model's subtropical jets are nearer the equator and stronger than the observed jets. This is due to the lack of large scale eddy momentum transport in the model with poleward branches of Hadley circulation generating strong zonal flow through angular momentum conservation. The introduction of proper eddy momentum mixing will weaken the jets and shift them polewards. Simultaneously, the Hadley circulation will be enhanced to balance the momentum fluxes and transport more energy, reducing the vertical shear in the subtropics.

Because the model's vertical shear is unusually large in the subtropics, the eddy heat flux peaks nearer the equator than is found in observations. If we use the three-dimensional model's zonal mean state as the input data for the parameterization, the transport would peak at  $47^\circ\text{N}$  or much nearer the observed latitude. Fig. 3.9 shows the eddy sensible heat transport as found in the symmetric model. For comparison the transient

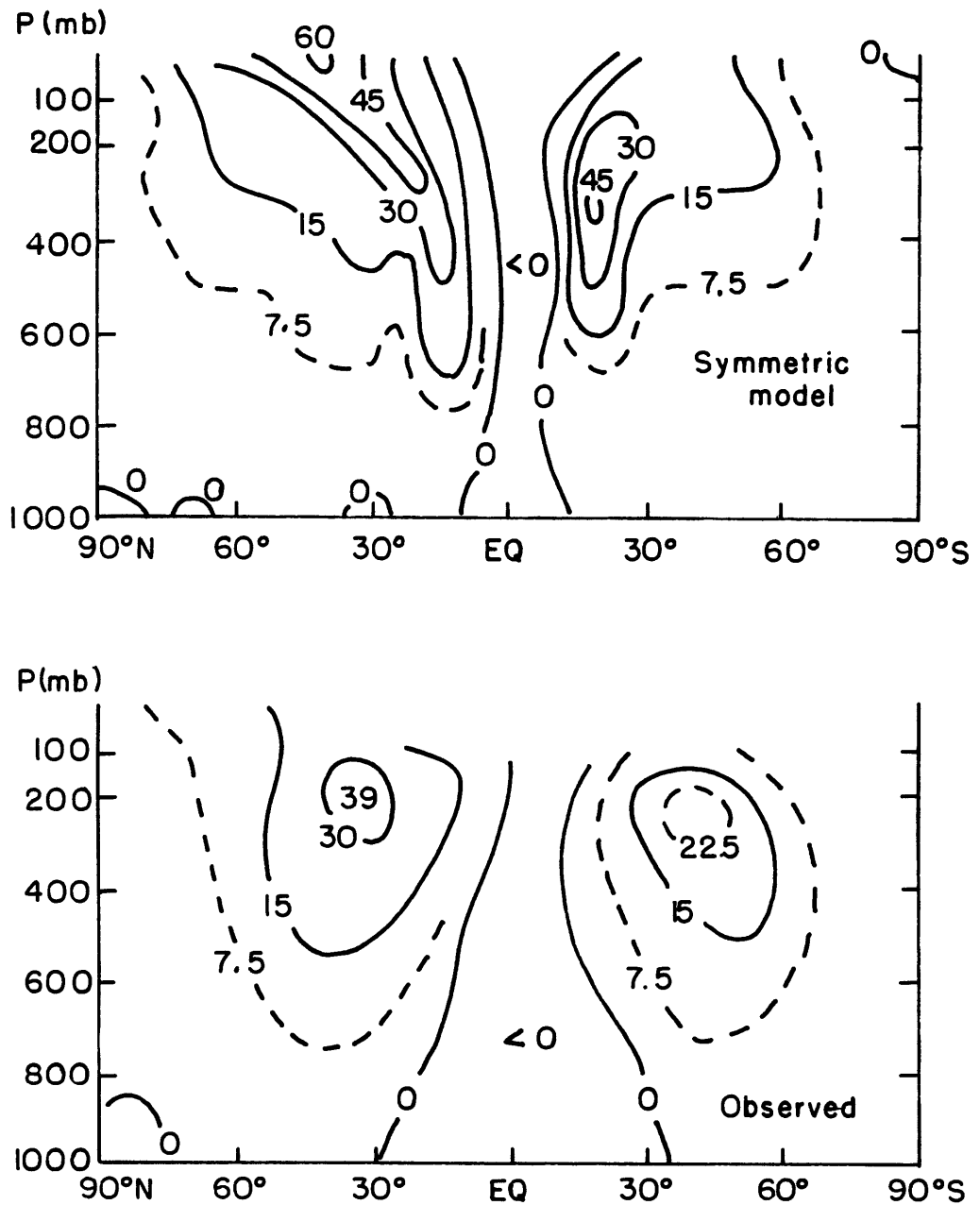


Fig. 3.8. Zonal wind ( $\text{msec}^{-1}$ ) from symmetric model and winter observations from Newell et al. (1972).

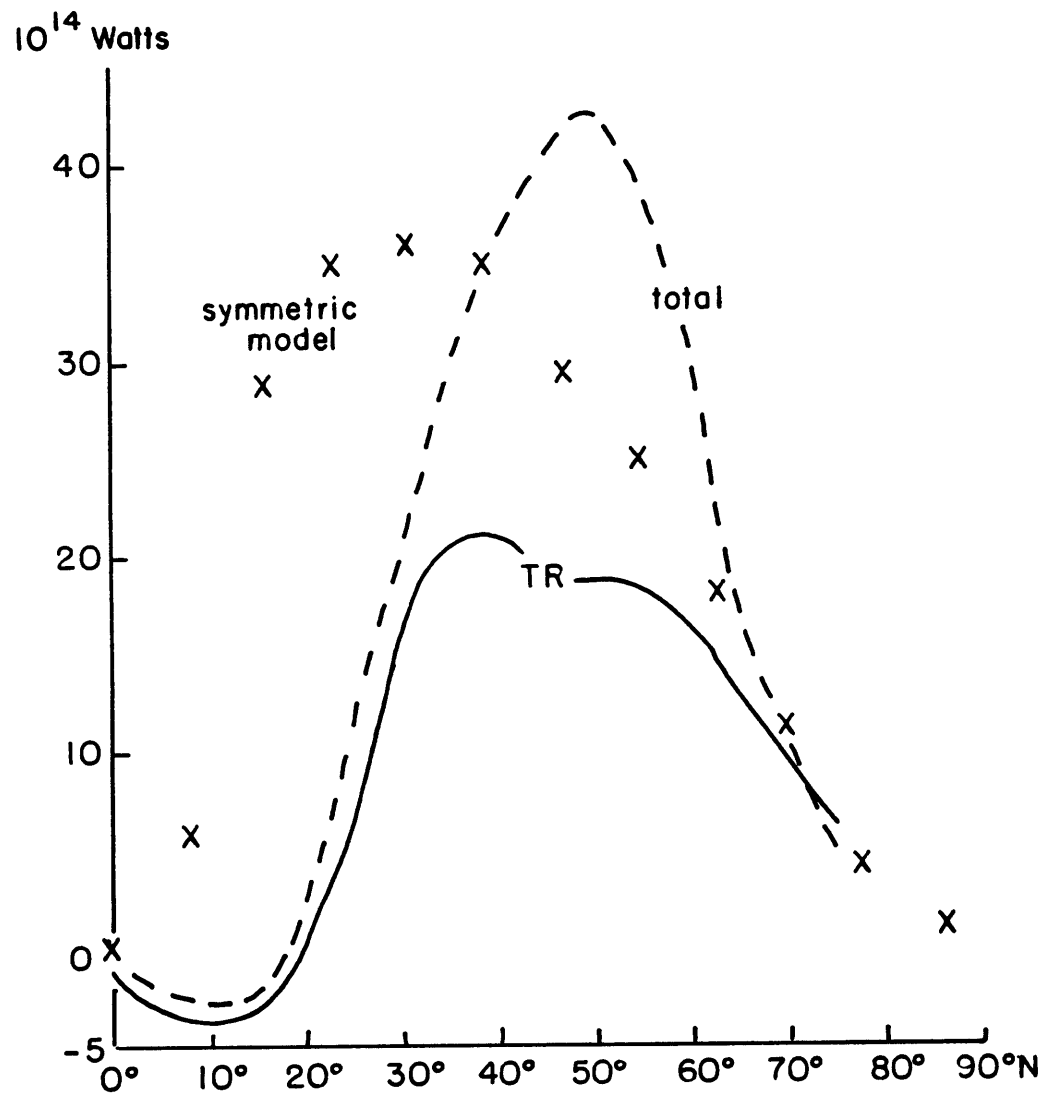


Fig. 3.9. Vertically integrated sensible heat transport in symmetric model (x) and observed January values of transient (TR) and total eddy transport from Oort Rasmusson (1971).

eddy transport from Oort and Rasmusson's January observations is included.

While the parameterization should be most representative of the transient fluxes, the transport due purely to the instability of the zonally averaged flow is not completely defined by observational techniques. Stationary eddies also draw energy from the zonal mean shear and may respond to mean flow changes as do the transient eddies. Similarly, the transient flux may be in part due to the presence of asymmetric forcing. Hence, the total flux is included for comparison in Fig. 3.9. The magnitude of the parameterized transport in the symmetric model falls between the transient and total observed transport, partially compensating for the lack of stationary eddy flux.

The magnitude and depth of the model heat flux is similar to the observed tropospheric fluxes (Fig. 3.10). The model flux also exhibits the poleward tilt with height of the latitude of maximum flux. As expected from the zonal wind field, the flux peaks too far south. It is unable to account for weak equatorward fluxes in the tropics and for additional poleward transport near the tropopause. Not shown in Fig. 3.10, the model heat flux in the Southern Hemisphere is of similar structure but approximately one-half as strong as in the Northern Hemisphere.

In Fig. 3.11 the vertical eddy heat flux ( $-\rho g \overline{w'\theta'}$ ) of the symmetric model is compared with the computed flux of a January simulation of the three-dimensional version of the model. Again the parameterized flux is of correct magnitude and structure through shifted towards the subtropics. The peak in the three-dimensional model may be at an anomalously high latitude since the original GISS G.C.M. January simulation (Somerville et al 1974) located a peak of  $-20 \times 10^{-4}$  mb °K sec<sup>-1</sup> near 45°N. If the three-dimensional model's zonal mean state were used to determine the

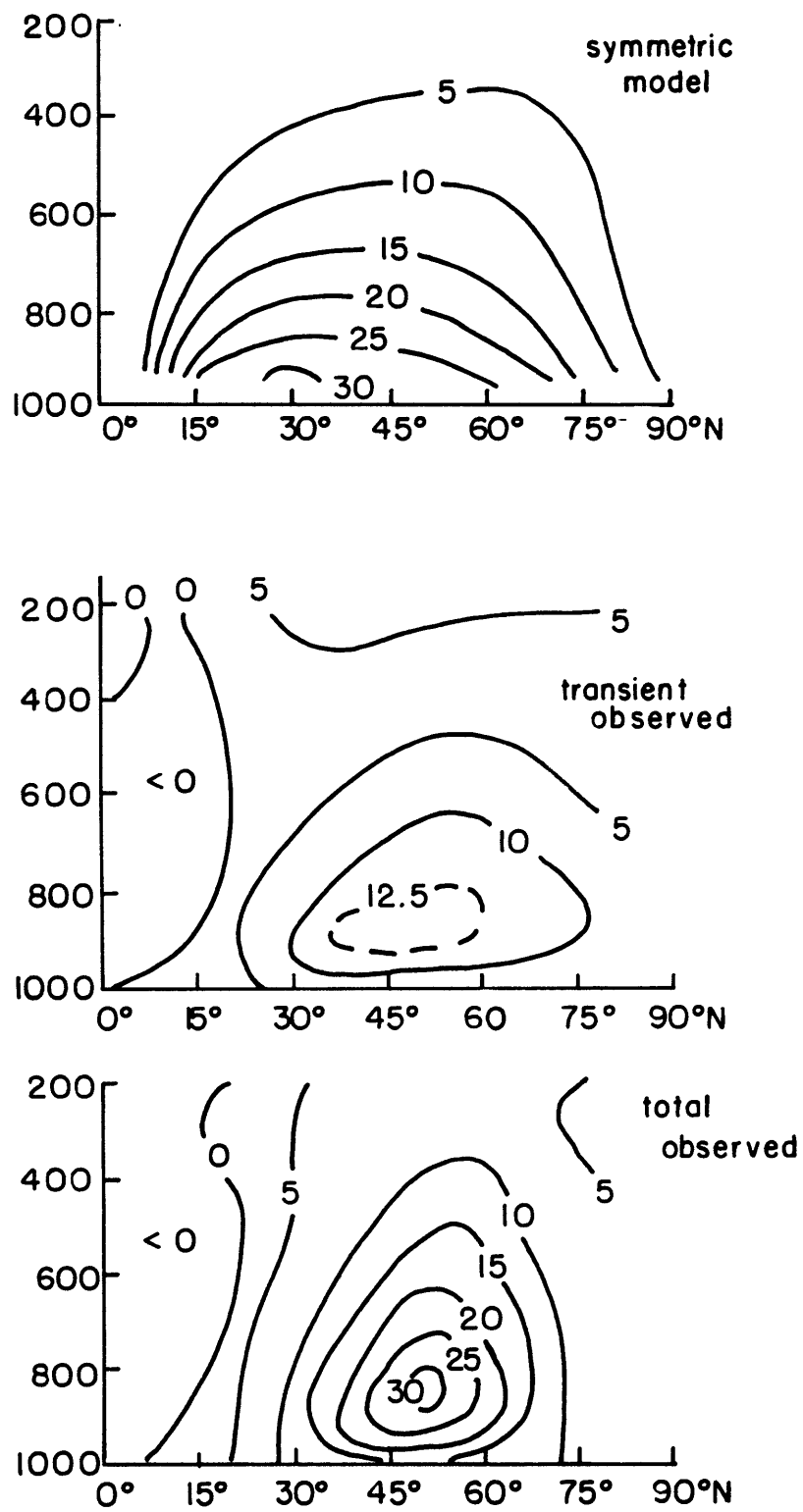


Fig. 3.10. Northward sensible heat flux ( $^{\circ}\text{K m sec}^{-1}$ ) from symmetric model and observed transient and total eddy flux for January (Oort and Rasmusson, 1971).

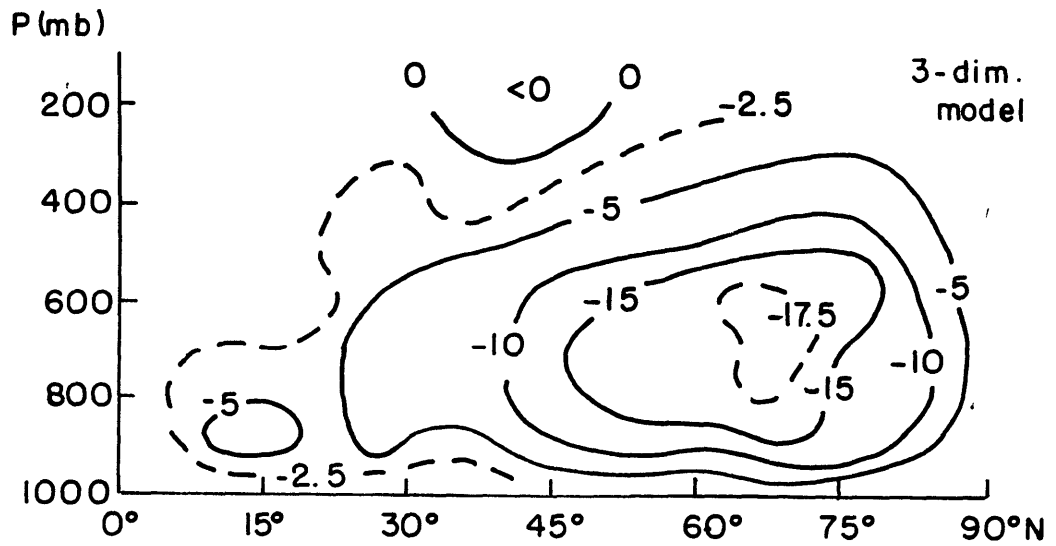
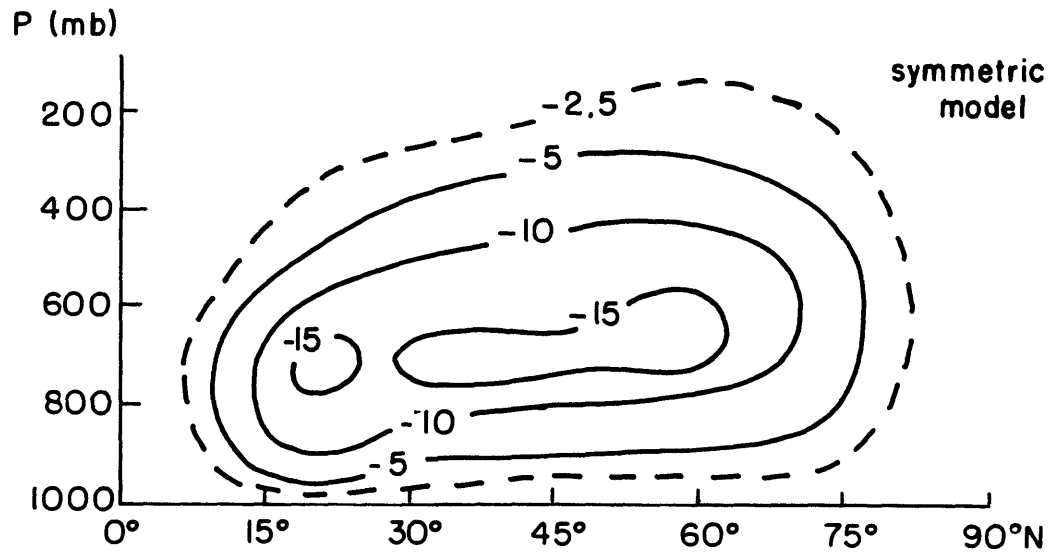


Fig. 3.11. Vertical transport of sensible heat by eddies ( $10^{-4}$  mb  $^{\circ}\text{K sec}^{-1}$ ) for symmetric and 3-dimensional GISS climate models.

the parameterized flux, we would find a maximum vertical flux of  $-15 \times 10^{-4}$  mb °K sec<sup>-1</sup> at 47°N and 700 mb. In the symmetric model's Southern Hemisphere the flux decays more rapidly towards higher latitudes than in the other hemisphere. The magnitudes of the maximum transport in both hemispheres are similar.

It is also interesting to examine the values of  $\gamma$  for the symmetric model as an indication of the stability of the zonal flow and as a measure of the baroclinic transports. Fig. 3.12a shows the meridional structure of  $\gamma_w$ , the vertical average weighted by the eddy depth and used to determine the transport characteristics in the symmetric model. Also shown is  $\gamma$  for 733 mb in the three-dimensional model and for the 700-850 mb layer as found from the data of Oort and Rasmusson (1971). Using the temperature data rather than the less certain zonal wind data, the vertical shear was calculated by the thermal wind relation. Values of  $\gamma$  near 750 mb will be nearly identical to  $\gamma_w$  which is weighted towards the lower troposphere and will also be at a level of substantial vertical and horizontal transport. Towards the tropics  $\gamma$  increases quite rapidly and eventually becomes negative and large in regions of weak easterly shear. In the subtropics and polewards it is  $O(1)$  until reaching polar latitudes where it may fluctuate greatly depending on the behavior of the ratio,  $\beta_0 / \frac{\partial \bar{u}}{\partial z}$ .

Except at the highest latitudes  $\gamma_w$  in the symmetric model is smaller than the  $\gamma$  values of the three-dimensional model or observations. In the subtropics this must be primarily attributed to the anomalously large vertical shears. However, Fig. 3.12b shows that the static stability in the lower troposphere is too small in the symmetric model's mid and high latitudes and is responsible for the smaller  $\gamma$  values there. Since the

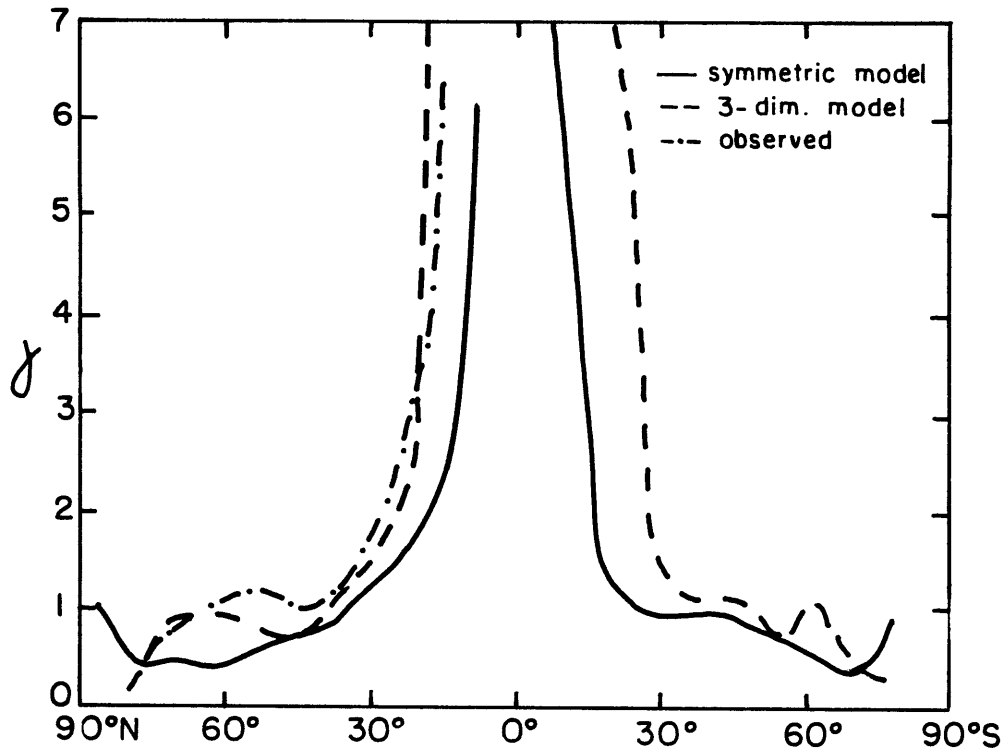


Fig. 3.12a. Values of  $\gamma_w$  from symmetric model (solid),  $\gamma$  at 733 mb in 3-dimensional model (dashed), and  $\gamma$  in 700-850 mb layer of January observations of Oort & Rasmusson (1971) (dashed-dot).

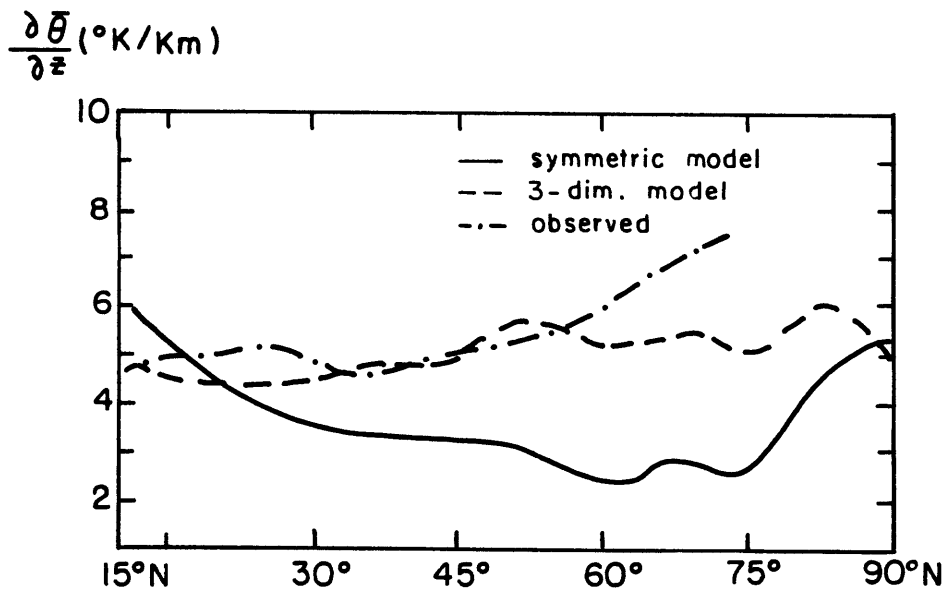


Fig. 3.12b. Static stability in 500-1000 mb layer of symmetric and 3-dimensional models and observations (Oort and Rasmusson).

vertical heat flux is reproduced reasonably well by the parameterization, another mechanism important in controlling the static stability must be inadequately represented in the model.

Evaporative and sensible heat fluxes from the surface of the symmetric model are an order of magnitude smaller than the fluxes in the three-dimensional model. This is caused by an artificially small transfer coefficient, determined by the strength of the near surface wind. In the symmetric model the only contribution is from the mean circulation, whereas in the three-dimensional model the contribution from eddies is much larger. Correction of this deficiency should lead to enhanced heating by moist convection which is about 50% weaker in the symmetric model than in the three-dimensional model.<sup>1</sup> The moist convection is also much shallower in the symmetric model.

It is interesting to note that static stabilities predicted by the symmetric model at mid-latitudes are nearly the same as those found by Stone (1972) in his radiative-dynamical heat balance model. Stone balanced radiative heating and baroclinic fluxes to explain part of the vertical stabilization that occurs in the atmosphere. The symmetric model is dominated by this balance and provides an independent check on Stone's analytical model with a more complicated model. In the following section a similar analytic model is developed that includes the effect of the  $\beta$ -plane on baroclinic transports. As seen earlier, some of the feedbacks in the parameterization developed here have potentially different behavior than Stone's original model.

---

<sup>1</sup>A parameterization for the eddy-generated surface wind variance is developed in Chapter IV. Its use in the symmetric model enhanced surface heat transfer and reduced the subtropical meridional temperature gradient. The westerly jet weakened and shifted to more realistic latitudes. The maximum eddy heat flux shifted polewards to  $40^{\circ}$  N. No substantial improvement was found in extratropical lapse rates.

### 3. Energy Balance Model

In this section we examine an analytical energy balance model that includes the transport properties of the baroclinic eddies and radiative heating. The emphasis will be on understanding the response of the baroclinic transports to changes in the radiative forcing. As this does not include other heat transfer mechanisms such as moist convection, large-scale water vapor transport, and the mean meridional circulation, the model cannot be considered a complete climate model. However, sensible heat transport by transient eddies is the largest single component of the meridional flux in the atmosphere and ocean, accounting for 40% of the annual total (Vonder Haar and Oort, 1973). Thus, the model can be considered a first approximation to a complete climate model since it retains the two most important heat transfer mechanisms, i.e. radiative heating and sensible heat flux by baroclinic eddies.

The model can indicate what feedbacks are likely to be important in eddy sensible heat transfer and must be retained in a more elaborate model. It will also determine the average characteristics of the most unstable baroclinic wave, while allowing that wave to adjust the mean flow parameters, in particular, the static stability and vertical shear.

The development here is quite similar to Stone's (1972) study of a radiative-dynamical model. It has been modified by including the  $\beta$ -effect in a quasi-Boussinesq atmosphere, whereas Stone investigated a Boussinesq,  $f$ -plane model. As noted earlier, the feedbacks may be of opposite sign of Stone's heat flux parameterization depending on the value of  $\gamma$ .

Balancing eddy flux divergences and radiative heating, the zonal and time mean thermodynamic equation for quasi-Boussinesq, quasi-geostrophic

flow is:

$$-\frac{1}{\rho_s} \frac{\partial}{\partial y} \left( \rho_s \overline{\frac{\partial \psi'}{\partial x} \frac{\partial \psi'}{\partial z}} \right) - \frac{1}{\rho_s} \frac{\partial}{\partial z} \left( \rho_s \overline{w' \frac{\partial \psi'}{\partial z}} \right) + \frac{g \bar{Q}}{f_0 c_p \bar{T}} = 0 \quad (3.3.1)$$

where  $\bar{Q}$  is the heating rate per unit mass. We use a linear radiative relaxation law for the diabatic heating term, i.e.

$$\frac{\bar{Q}}{c_p} = \frac{\bar{T}_r - \bar{T}}{\tau_r} \quad \text{where} \quad \bar{T}_r = \bar{T}_r(y, z) \quad \text{is}$$

the zonal mean radiative equilibrium temperature and  $\tau_r$  is the radiative relaxation time. For the eddy fluxes we use eqs. (3.1.8) and (3.1.9) in which  $\frac{\partial \psi'}{\partial z} = \frac{g \theta'}{f_0 \theta_s}$  so that eq. (3.3.1) becomes:

$$-\frac{\partial}{\partial y} \left[ A(y, z) e^{-z/d} \right] - \frac{1}{\rho_s} \frac{\partial}{\partial z} \left[ \rho_s B(y, z) e^{-z/d} \left( \frac{z}{d} - \left( \frac{z}{2d} \right)^2 \right) \right] + \frac{g}{f_0 \bar{T}} \frac{\bar{T}_r - \bar{T}}{\tau_r} = 0 \quad (3.3.2)$$

where  $A(y, z) = \frac{N_s \left( \frac{\partial \bar{u}}{\partial z} d \right)^2}{\sqrt{2} f_0}$  and  $B(y, z) = \frac{f_0}{N_s^2} \frac{\partial \bar{u}}{\partial z} A(y, z)$ .

The solution of eq. (3.3.2) with appropriate boundary conditions cannot be found analytically if the mean flow parameters are considered functions of latitude and height. Therefore, further simplifying assumptions must be made. First we assume the mean flow parameters  $N_s$ ,  $\frac{\partial \bar{u}}{\partial z}$ , and  $d$  are vertical averages weighted by the eddy heat flux structure as previously discussed. The magnitudes  $A(y, z)$  and  $B(y, z)$  lose their  $z$ -dependence as formulated in the previous section and used in the symmetric model. However, these functions still have complicated  $y$ -structure and we further assume:

$$A = \frac{[N_s] \left( \left[ \frac{\partial \bar{u}}{\partial z} \right] [d] \right)^2}{\sqrt{2} f_0} F(y)$$

where the mean flow variables,  $[N_s]$ ,  $\left[ \frac{\partial \bar{u}}{\partial z} \right]$ , and  $[d]$  are now meridional averages as well as vertical. Specifically we define

$$[G(y, z)] \equiv \frac{1}{2L[d]} \int_{-L}^L \int_0^\infty G(y, z) e^{-z/[d]} dz dy.$$

The Coriolis parameter,  $f_0$ , will be evaluated at a mid-latitude halfway between  $y=L$  and  $-L$ , the polar and tropical boundaries of the model.

The function  $F(y)$  will be chosen to simulate the planetary variation of the flux as seen in Fig. 3.9 with a maximum at mid-latitudes and vanishing at the two boundaries in the tropics and near the pole. If the structure of the atmosphere and ocean is dominated by the planetary scale and inter-hemispheric exchange is small, Stone (1978b) has demonstrated the meridional energy flux distribution is independent of the structure of the atmospheric-oceanic system. The flux distribution can be approximated within 10% by the function  $(\sin \phi - \sin^3 \phi)$  with a maximum flux per unit area at  $45^\circ$ . Similar distributions for the flux have been used in other climate models (Stone, 1972, North, 1975) and  $F(y)$  will be selected to approximate this form. For consistency the vertical flux also varies like  $F(y)$ . We can now write eq. (3.3.2) as:

$$-\frac{[N_s] \left( \left[ \frac{\partial \bar{u}}{\partial z} \right] [d] \right)^2}{\sqrt{2} f_0} e^{-z/[d]} \frac{dF}{dy} - \frac{e^{z/[d]} \left( \left[ \frac{\partial \bar{u}}{\partial z} \right] [d] \right)^2 \left[ \frac{\partial \bar{u}}{\partial z} \right]}{\sqrt{2} [N_s]} F(y) \frac{d}{dz} \left( e^{-z/[d]} W(z) \right) + \frac{g}{f_0 \bar{T}} (\bar{T}_r - \bar{T}) = 0 \quad (3.3.3)$$

where 
$$W(z) = e^{-z/[d]} \left( \frac{z}{[d]} - \left( \frac{z}{2[d]} \right)^2 \right).$$

For  $z \gg [d]$  it is clear from eq. (3.3.3) that the atmosphere will

be approximately in radiative equilibrium as the eddy divergences will be small. The depth of the lower atmosphere which can be substantially different from radiative equilibrium is  $O([d])$ . Thus, we are interested in solutions for the temperature structure through this layer.

First using the thermal wind relation, define a vertical shear of the radiative state as

$$\frac{\partial \bar{u}_r}{\partial z} = -\frac{g}{\bar{T}_r f_0} \frac{\partial \bar{T}_r}{\partial y} .$$

Then, taking the  $y$ -derivative of eq. (3.3.3), we obtain, recalling  $[N_s]$ ,  $[\frac{\partial \bar{u}}{\partial z}]$ ,  $[d]$ , and  $[H]$  are mean values in the flux terms,

$$\begin{aligned} & -\frac{[N_s]}{\sqrt{2} f_0} \left( \left[ \frac{\partial \bar{u}}{\partial z} \right] [d] \right)^2 e^{-z/[d]} \frac{d^2 F}{dy^2} - e^{z/[H]} \frac{\left( \left[ \frac{\partial \bar{u}}{\partial z} \right] [d] \right)^2 \left[ \frac{\partial \bar{u}}{\partial z} \right]}{\sqrt{2} [N_s]} . \\ & \frac{dF}{dy} \frac{d}{dz} \left( e^{-z/[H]} W(z) \right) + \frac{1}{\tau_r} \left( \left[ \frac{\partial \bar{u}}{\partial z} \right] - \left[ \frac{\partial \bar{u}_r}{\partial z} \right] \right) \frac{\bar{T}_r}{\bar{T}} = 0 . \end{aligned} \quad (3.3.4)$$

As yet the radiative heating term is not averaged. Multiplying eq. (3.3.4) by  $e^{-z/[d]}$ , integrating over  $z$ , and meridionally averaging, we obtain:

$$\begin{aligned} & -\frac{[N_s]}{2\sqrt{2} f_0} \left( \left[ \frac{\partial \bar{u}}{\partial z} \right] [d] \right)^2 \left[ \frac{d^2 F}{dy^2} \right] - \frac{3}{16\sqrt{2}} \left[ \frac{\partial \bar{u}}{\partial z} \right]^3 \frac{[d]}{[N_s]} \left[ \frac{dF}{dy} \right] \left( 1 - \frac{[d]}{[H]} \right) \\ & + \frac{1}{\tau_r} \left( \left[ \frac{\partial \bar{u}}{\partial z} \right] - \left[ \frac{\partial \bar{u}_r}{\partial z} \right] \right) = 0 . \end{aligned} \quad (3.3.5)$$

Here the  $O(1)$  term  $\bar{T}_r/\bar{T}$  is absorbed into a fixed mean of  $\tau_r$ . In further development of similar models, the radiative time scale should be considered a function of  $[d]$  as one would expect somewhat shorter relaxation times for shallower baroclinic waves. But for the current study, using a

constant value is sufficient.

Returning to eq. (3.3.3), now differentiate by  $z$  to get:

$$\frac{[N_s]}{\sqrt{2} f_0} \left[ \frac{\partial \bar{u}}{\partial z} \right]^2 [d] \frac{dF}{dy} e^{-z/[d]} - \frac{\left[ \frac{\partial \bar{u}}{\partial z} \right]^3 [d]^2 F}{\sqrt{2} [N_s]} .$$

$$\frac{d}{dz} e^{z/[H]} \frac{d}{dz} \left( e^{-z/[H]} W(z) \right) + \frac{g}{f_0 \tau_r} \left( \frac{1}{\bar{T}_r} \frac{\partial \bar{T}_r}{\partial z} - \frac{1}{\bar{T}} \frac{\partial \bar{T}}{\partial z} \right) = 0. \quad (3.3.6)$$

For a hydrostatic atmosphere, we find

$$\frac{g}{T} \frac{\partial T}{\partial z} = N^2 - \frac{g^2}{c_p T} .$$

Defining a radiative equilibrium Brunt-Vaisala frequency,  $N_r$ , we approximate

the last term of eq. (3.3.6) as  $\frac{N_r^2 - N_s^2}{\tau_r f_0}$ . Averaging over  $y$  and,

after multiplying by  $e^{-z/[d]}$ , integrating over  $z$ , eq. (3.3.6) becomes:

$$\frac{[N_s]}{\sqrt{2} 2} \left[ \frac{\partial \bar{u}}{\partial z} \right]^2 [d] \left[ \frac{dF}{dy} \right] + \frac{\left[ \frac{\partial \bar{u}}{\partial z} \right]^3 f_0 [F]}{16\sqrt{2} [N_s]} \left( 13 + 3 \frac{[d]}{[H]} \right)$$

$$+ \frac{1}{\tau_r} \left( [N_r^2] - [N_s^2] \right) = 0. \quad (3.3.7)$$

If we define  $[d]$  as  $\frac{[H]}{\left( 1 + \frac{\beta_0 [N_s^2] [H]}{f_0 \left[ \frac{\partial \bar{u}}{\partial z} \right]^2} \right)}$ , let  $[N_s^2] = [N_s]^2$ ,

and consider  $[H]$  a known constant dependent on a global mean temperature,

eqs. (3.3.5) and (3.3.7) can be solved for  $\left[ \frac{\partial \bar{u}}{\partial z} \right]$  and  $[N_s]$  as functions of the radiative forcing gradients  $[N_r^2]$  and  $\left[ \frac{\partial \bar{u}}{\partial z} \right]$ . To mimic the planetary

scale convergence, the meridional variation of the flux is taken as:

$$F(y) = \frac{3}{2} (1 - (y/L)^2) \quad \text{so that}$$

$$[F] = 1, \quad \left[ \frac{dF}{dy} \right] = 0, \quad \text{and} \quad \left[ \frac{d^2 F}{dy^2} \right] = -\frac{3}{L^2} .$$

Substituting into eqs. (3.3.5) and (3.3.7), respectively, we find (dropping brackets):

$$\frac{3 N_s \left( \frac{\partial \bar{u}}{\partial z} \right)^2 H^2}{2 \sqrt{2} L^2 f_0 \left( 1 + \frac{\beta_0 N_s^2 H}{f_0^2 \frac{\partial \bar{u}}{\partial z}} \right)^2} = \frac{1}{\tau_r} \left( \frac{\partial \bar{u}_r}{\partial z} - \frac{\partial \bar{u}}{\partial z} \right) \quad (3.3.8)$$

$$\frac{f_0 \left( \frac{\partial \bar{u}}{\partial z} \right)^3}{16 \sqrt{2} N_s} \left[ 13 + \frac{3}{1 + \frac{\beta_0 N_s^2 H}{f_0^2 \frac{\partial \bar{u}}{\partial z}}} \right] = \frac{1}{\tau_r} (N_s^2 - N_r^2) \quad (3.3.9)$$

Eqs. (3.3.8) and (3.3.9) balance relaxation to mean radiative gradients with mean baroclinic transports that attempt to reduce the gradient, horizontally (3.3.8) or vertically (3.3.9).

The equations differ from Stone's formulation (see eqs. (2.33) and (2.34) of Stone (1972)) in two respects. First, the radiative-dynamical balance occurs over a depth of  $O(H/(1+\gamma))$  in the model and therefore, is dependent on the values of  $N_s$  and  $\frac{\partial \bar{u}}{\partial z}$ . For depths much greater than  $H/(1+\gamma)$ , the model atmosphere is near radiative equilibrium. In Stone's Boussinesq, f-plane model, this depth is fixed at  $H$ .

Secondly, the wave depth of  $H/(1+\gamma)$  appears in the horizontal transport of eq. (3.3.8) as opposed to  $H$  in Stone's model of Eady wave transport. Eq. (3.3.9) is essentially unchanged from Stone's vertical balance (except for the small correction of  $3/(1+\gamma)$  in the bracketed term) as the depth of the waves will not explicitly appear in this balance. The vertical flux is proportional to  $d^2$  (eq. 3.1.9), but  $\left[ \frac{\partial^2}{\partial z^2} \overline{w'\theta'} \right]$ , which determines the stabilization, is not dependent on  $d$ . The balances in eqs. (3.3.8) and (3.3.9) could be deduced on the basis of scaling arguments to  $O(1)$  multiplicative factors using these modifications of the wave scales.

To determine the radiative equilibrium state, either the incoming

solar flux or the surface temperature must be specified. Using observed surface temperatures, Manabe and Möller (1961) found the tropospheric lapse rate in radiative equilibrium was nearly dry adiabatic. The use of observed surface temperatures implicitly assumes some dynamical transport is occurring. With the specification of the incoming flux the radiative lapse rate is very unstable because of high surface temperatures. In context of the model presented here, it is appropriate to assume turbulent heat flux is occurring in a near surface layer to reduce the ground temperature and transfer energy into the free atmosphere. Further transport would then be provided by baroclinic eddies.

Before finding numerical solutions to eqs. (3.3.8) and (3.3.9), it is enlightening to examine certain parameter limits. First, the example of  $N_r^2=0$ , corresponding to a neutral radiative state, is studied.

Eqs. (3.3.8) and 3.3.9) can easily be reduced to a single equation for  $\frac{\partial \bar{u}'}{\partial z} = \frac{\partial \bar{u}}{\partial z} / \frac{\partial \bar{u}_r}{\partial z}$  if we drop the  $3/(1+\gamma)$  term in eq. (3.3.9). Its deletion will cause at most a 23% error in the bracketed quantity in eq. (3.3.9) and not alter the feedbacks. In this case, we find:

$$\left(\frac{\partial \bar{u}'}{\partial z}\right)^3 (A+B^2) + \left(\frac{\partial \bar{u}'}{\partial z}\right)^2 (2B-B^2) + \left(\frac{\partial \bar{u}'}{\partial z}\right) (1-2B) - 1 = 0 \quad (3.3.10)$$

where  $A = .88 \left(\frac{\partial \bar{u}_r}{\partial z} H / L f_0\right)^2 (f_0 \tau_r)^{4/3}$

and  $B = .69 \frac{\beta_0 H \frac{\partial \bar{u}_r}{\partial z}}{f_0^2} (f_0 \tau_r)^{2/3} .$

The Richardson number, giving the relation between  $\frac{\partial \bar{u}}{\partial z}$  and  $N_s$ , is

$$Ri_c = N_s^2 / \left(\frac{\partial \bar{u}}{\partial z}\right)^2 = (.57 f_0 \tau_r)^{2/3} \quad (3.3.11)$$

and will be large for most planetary atmospheres. This result is essentially identical to Stone's (1972) solution for the case of  $N_r^2 = 0$  and is independent of  $\beta_0$ . From eq. (3.3.11) we find  $\gamma = B \frac{\partial \bar{u}'}{\partial z}$ .

For further comparison, if  $B = 0$  (an f-plane model), the parameter dependence of  $\frac{\partial \bar{u}}{\partial z}$  is the same as Stone's model. In the case of strong radiative forcing ( $\frac{\partial \bar{u}_r}{\partial z}$  large and  $A \gg 1$ ),  $\frac{\partial \bar{u}'}{\partial z} \approx A^{-1/3} \ll 1$  ( $\frac{\partial \bar{u}}{\partial z} \sim (\frac{\partial \bar{u}_r}{\partial z})^{1/3}$ ) and dynamical fluxes are very efficient as the shear or meridional temperature gradient is much less than the radiative gradient. For comparatively weak radiative gradients ( $A \ll 1$ ),  $\frac{\partial \bar{u}}{\partial z} \approx 1$  corresponding to very ineffective baroclinic transports. For the limit of  $B \gg A$  and  $B \gg 1$  (a strong  $\beta$ -effect) it can be shown from eq. (3.3.10) that  $\frac{\partial \bar{u}'}{\partial z} \approx 1$  and  $\gamma \approx B$ , so that the baroclinic waves are very short and shallow and will be inefficient heat transporters.

For mid-latitudes for which this model was developed we expect  $A \sim B^2$ . Specifically, we find  $\frac{A}{B^2} = 1.85 \left(\frac{f_0}{\beta_0 L}\right)^2$ . For  $45^\circ$  lat. and  $L = \frac{\pi}{4} a$  with  $a =$  planetary radius,  $\frac{A}{B^2} = 3$ . In the case of weak radiative forcing ( $A \sim B^2 \ll 1$ ), we find an approximate solution to eq. (3.3.10) of  $\frac{\partial \bar{u}'}{\partial z} \approx 1$  and as before, the waves are inefficient heat transporters. From eq. (3.3.11) we find  $N_s^2 \sim \left(\frac{\partial \bar{u}_r}{\partial z}\right)^2 (f_0 \tau)^{2/3}$ . Here  $\gamma \approx B \ll 1$  so that the waves are deep Eady waves. In this small  $\gamma$  limit, the appropriate eddy scale is  $\frac{N_s H}{f_0}$  and, comparing this scale to the planetary radius,  $\frac{N_s H}{f_0 a} = B / (f_0 \tau_r)^{1/3} \rightarrow 0$ . Therefore, the waves are deep but short. The weak forcing leads to weak shear and, referring to Fig. 3.4, very little vertical transport. The reduced static stability decreases the horizontal scale and flux of the Eady waves as seen in the small  $N_s$  limit of Fig. 3.3.

For strong radiative forcing ( $A \sim B^2 \gg 1$ ), we find  $\frac{\partial \bar{u}'}{\partial z} \approx \frac{B^2}{A+B^2} < 1$  or,

for the previous choice of  $L$ ,  $\frac{\partial \bar{u}}{\partial z} \approx \frac{1}{4}$  and  $N_s^2 \sim \left(\frac{\partial \bar{u}_r}{\partial z}\right)^2 (f_0 \tau)^{2/3}$ . This result differs from the  $f$ -plane model in which the eddies became very efficient in this limit. The  $\beta$ -effect has placed an upper bound on this efficiency. Here  $\gamma \sim B \gg 1$  and the eddies are very short and shallow. The forced increase in vertical flux has strongly stabilized the atmosphere and reduced the eddy scales by increasing  $\gamma$ . This effect mitigates increases in the horizontal flux caused by forced increases in shear. The horizontal flux for large  $\gamma$  is inversely dependent on  $N_s$  rather than directly proportional to  $N_s$  as for small  $\gamma$ .

Specific solution of eqs. (3.3.10) and (3.3.11) as functions of  $\frac{\partial \bar{u}_r}{\partial z}$  are shown in Fig. 3.13. Parameters representative of a terrestrial  $\beta$ -plane centered at  $45^\circ$  lat. with boundaries at  $18^\circ$  and  $72^\circ$  are chosen (i.e.  $L = 3000$  km), namely,  $f_0 = 1 \times 10^{-4}$ ,  $H = 7300$  m,  $\beta_0 = 1.6 \times 10^{-11} \text{ sec}^{-1} \text{ m}^{-1}$ ,  $\tau_r = 3 \times 10^6$  sec (35 days).

An approximate winter value for  $\frac{\partial \bar{u}_r}{\partial z}$  of  $5 \text{ m sec}^{-1} \text{ km}^{-1}$  (equivalent to a  $70^\circ \text{ K}$  temperature difference across the model) corresponds to  $\gamma = .7$ ,  $\frac{\partial \bar{u}}{\partial z} = 2 \text{ m sec}^{-1} \text{ km}^{-1}$ ,  $\frac{\partial \bar{\theta}}{\partial z} = 4 \text{ }^\circ\text{K/Km}$ , and  $Ri = 30$  or within 25% of the observed values. These parameter values correspond to a heat transporting mode of zonal wavenumber 6 at  $45^\circ$ . From Fig. 3.13 note that static stability is more sensitive to the radiative forcing than the shear, indicative of the strong dependence of the vertical flux on the shear. A 50% decrease in  $\frac{\partial \bar{u}_r}{\partial z}$  causes a 33% decrease in  $\frac{\partial \bar{u}}{\partial z}$  and a 56% decrease in static stability. This suggests the importance of baroclinic eddies in determining the static stability may vary greatly through the seasonal cycle. Other processes, particularly moist convection, may dominate in summer as suggested by Stone and Carlson (1979).

The solutions shown in Fig. 3.13 exhibit the same behavior in limits of

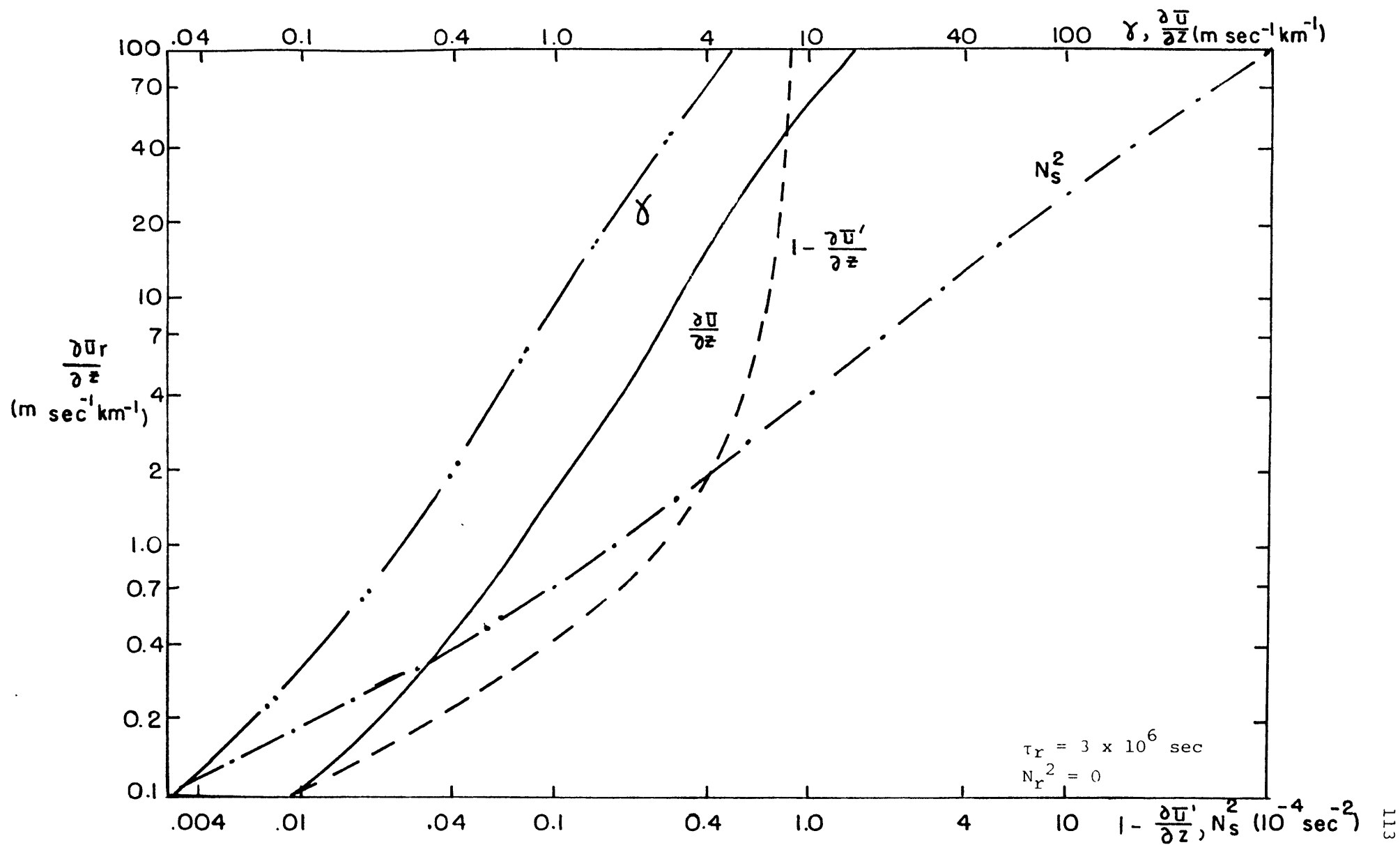


Fig. 3.13. Terrestrial radiative-dynamical model with variable  $\frac{\partial \bar{u}_r}{\partial z}$ .

large and small  $\frac{\partial \bar{u}_r}{\partial z}$  as described above. One modification is in  $1 - \frac{\partial \bar{u}'}{\partial z}$  which approaches .89 instead of .75 because the choice of channel width is somewhat less than the equator to pole distance. The quantity,  $1 - \frac{\partial \bar{u}'}{\partial z}$ , measures the efficiency of the horizontal flux to smooth out the radiative temperature gradient. For observed  $\frac{\partial \bar{u}_r}{\partial z}$  values, this efficiency is greater than 50% and not far from its asymptotic limit.

Because  $N_s^2$  increases rapidly for increased forcing,  $\gamma$  also increases, though more slowly. The strong negative feedback that apparently keeps  $\gamma$  very near unity (Stone, 1978) in the atmosphere is not evident in the model. However, radiative forcing that is four times weaker or stronger than the observed restricts  $\gamma$  to a 0.3 - 1.6 range in this analytical model.

Fig.3.14 shows the dependence of the solutions on the radiative relaxation time,  $\tau_r$ . For large  $\tau_r$  the solutions will have the same behavior as under strong radiative forcing (i.e.  $A \sim B^2 \gg 1$ ). Longer radiative times allow baroclinic fluxes to more effectively transport heat vertically and horizontally.

If the static stability is predetermined in eq. (3.3.8) as if by moist convection rather than baroclinic fluxes, the  $\gamma$  parameter will decrease for increased forcing or opposite the behavior seen in Fig. 3.13. If we specify  $N_s$  in eq. (3.3.8), the horizontal temperature gradient may be directly found as (3.3.8) takes the form:

$$A \left( \frac{\partial \bar{u}'}{\partial z} \right)^4 + \left( \frac{\partial \bar{u}'}{\partial z} \right)^3 + (2\gamma_r - 1) \left( \frac{\partial \bar{u}'}{\partial z} \right)^2 + (\gamma_r^2 - 2\gamma_r) \frac{\partial \bar{u}'}{\partial z} - \gamma_r^2 = 0 \quad (3.3.12)$$

$$\text{where } A = 1.06 \frac{\partial \bar{u}_r}{\partial z} \frac{N_s H^2 \tau_r}{f_0 L^2} \quad \text{and} \quad \gamma_r = \frac{\beta_0 N_s^2 H}{f_0^2 \frac{\partial \bar{u}_r}{\partial z}} .$$

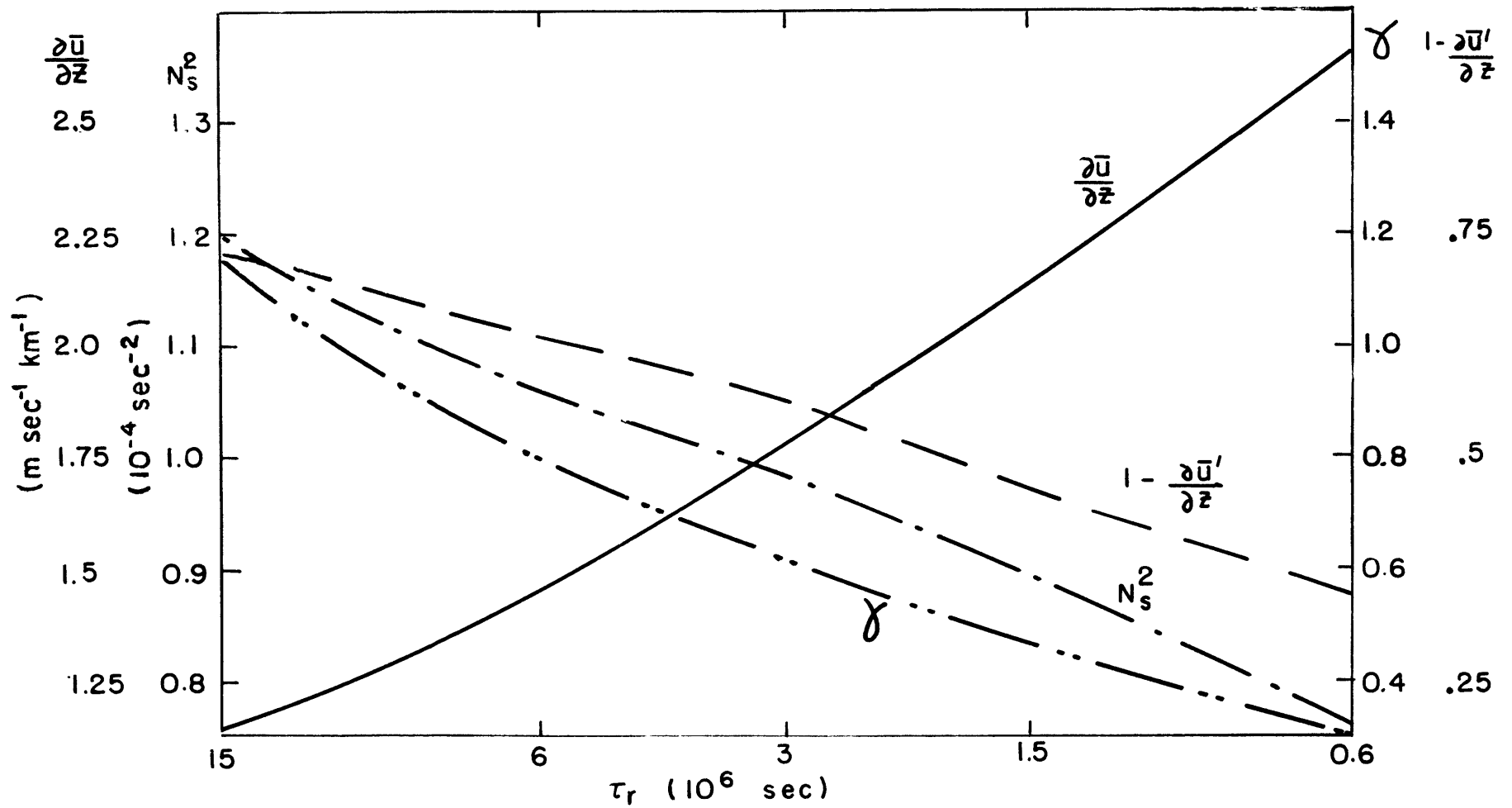


Fig. 3.14. Terrestrial radiative-dynamical model with variable radiative time scale,  $\tau_r$ , and  $\frac{\partial \bar{u}}{\partial z} = 4 \text{ m sec}^{-1} \text{km}^{-1}$  and  $N_r^2 = 0$ . Other parameters same as Fig. 3.13.

In case of strong forcing ( $A \gg 1$ ,  $\gamma_r \ll 1$ ),

$$\frac{\partial \bar{u}'}{\partial z} \approx A^{-1/2} \ll 1 \quad \text{or} \quad \frac{\partial \bar{u}}{\partial z} \approx \left( \frac{\partial \bar{u}_r}{\partial z} \frac{f_0}{N_s \tau_r} \right)^{1/2} \frac{L}{H} \quad \text{and } 1 \gg \gamma \approx A^{-1/2} \gg \gamma_r.$$

This is efficient baroclinic transport by Eady waves as is found in the f-plane model. For  $A \ll 1$  (weaking forcing),  $\frac{\partial \bar{u}'}{\partial z} \approx 1$  and  $\gamma \approx \gamma_r \gg 1$  or inefficient transport by shallow, short waves. With the strong feedback on vertical fluxes removed,  $\gamma$  decreases for increased forcing. Fig. 3.15 shows the dependence of  $\gamma$  and  $\gamma_r$  on  $\frac{\partial \bar{u}_r}{\partial z}$  for  $\frac{\partial \theta_s}{\partial z} = 4^\circ \text{ K/Km}$ . Though of opposite sign, the sensitivity of  $\gamma$  to  $\frac{\partial \bar{u}_r}{\partial z}$  is as large as in the full model with variable static stability. However, it does indicate that an additional vertical transport mechanism such as moist convection could reduce the sensitivity of  $\gamma$  to radiative forcing by moderating the response of the vertical fluxes.

Because some planetary atmospheres (e.g. Mars) may have radiative equilibrium states which are stably stratified, it is also worth examining the energy balance with  $N_r^2 > 0$ . Discussion is also given for equilibrium states with  $N_r^2 \leq 0$ . Eqs. (3.3.8) and (3.3.9) can be reduced to a single equation in

$$N'^2 = \frac{N_s^2}{\text{Ric} \left( \frac{\partial \bar{u}_r}{\partial z} \right)^2} = \frac{1.45 N_s^2}{(f_0 \tau)^{2/3}} ;$$

$$\begin{aligned} N'^3 \{ A(1 + R/N'^2)^{2/3} + B^2(1 + R/N'^2)^{-1/3} \} + N'^2 \{ 2B - B^2(1 + R/N'^2)^{-2/3} \} \\ + N' \{ (1 + R/N'^2)^{1/3} - 2B(1 + R/N'^2)^{-1/3} \} - 1 = 0 \end{aligned} \quad (3.3.13)$$

with A, B defined above and  $R = \frac{-N_r^2}{\text{Ric} \left( \frac{\partial \bar{u}_r}{\partial z} \right)^2} \equiv \frac{-R_{ir}}{\text{Ric}}$ .

We also find:

$$\frac{\partial \bar{u}}{\partial z} = \frac{\partial \bar{u}_r}{\partial z} [N'^3 + N'R]^{1/3} \quad \gamma = BN'(1 + R/N'^2)^{-1/3}$$

$$R_i = \frac{\text{Ric} N'^2}{\left( \frac{\partial \bar{u}'}{\partial z} \right)^2} .$$

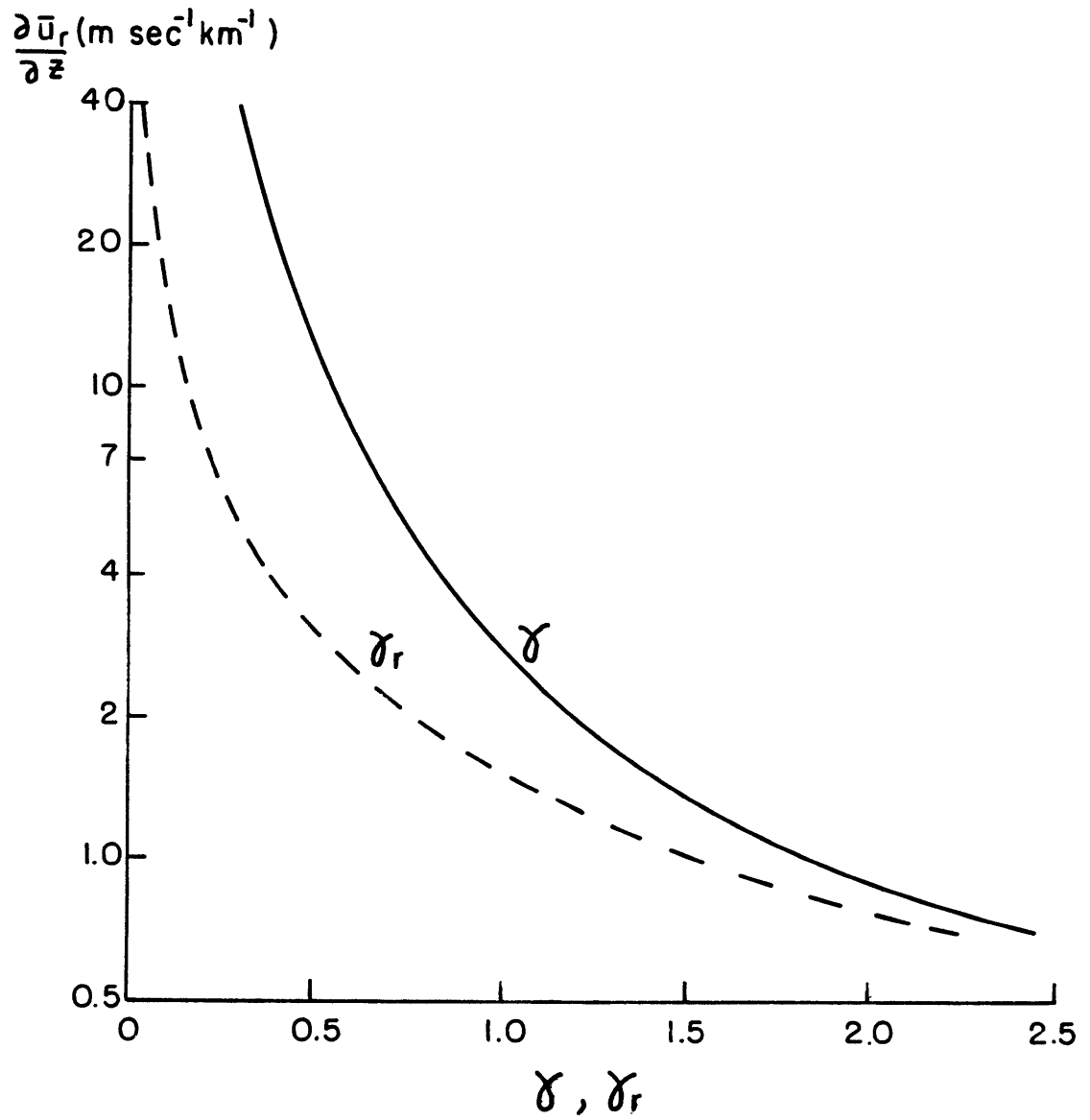


Fig. 3.15. Terrestrial radiative-dynamical model for fixed static stability. Values of  $\gamma$  and  $\gamma_r = \gamma \frac{\partial \bar{u}}{\partial z} / \frac{\partial \bar{u}_r}{\partial z}$  vs. radiative shear,  $\frac{\partial \bar{u}_r}{\partial z}$ .

The case of  $R = 0$  has been discussed.

For fixed  $N_r^2$  (positive or negative) and large  $\frac{\partial \bar{u}_r}{\partial z}$  ( $A \sim B^2 \gg 1, |R| \ll 1$ ) the solution to eq. (3.3.13) is:

$$N' \approx \frac{B^2}{A+B^2} \approx \frac{1}{4} \quad \text{or} \quad N_s^2 \sim Ric \left( \frac{\partial \bar{u}_r}{\partial z} \right)^2 \sim (f_0 \tau)^{2/3} \left( \frac{\partial \bar{u}_r}{\partial z} \right)^2,$$

$$\frac{\partial \bar{u}}{\partial z} \approx \frac{\partial \bar{u}_r}{\partial z} \frac{B^2}{A+B^2}, \quad \gamma \sim B, \quad \text{and} \quad Ric \approx Ric_c.$$

This limit is identical to the previously discussed case of strong horizontal forcing with  $N_r^2 = 0$ .

For fixed  $N_r^2$  and small  $\frac{\partial \bar{u}_r}{\partial z}$  ( $A \sim B^2 \ll 1, |R| \gg 1$ ) we must consider two cases,  $N_r^2 < 0$  and  $N_r^2 > 0$ . First, if  $N_r^2 < 0$  ( $R > 0$ ), we find:

$$N' \approx R^{-1} \quad \text{or} \quad N_s^2 \approx -N_r^2 / R^3 \ll -N_r^2$$

$$\frac{\partial \bar{u}}{\partial z} \approx \frac{\partial \bar{u}_r}{\partial z}, \quad \gamma \approx B/R^2 \ll 1, \quad \text{and} \quad Ric \approx Ric_c R^{-2} = \frac{Ric_c^3}{Ric_r^2} \ll 1.$$

These solutions are also valid for fixed  $\frac{\partial \bar{u}_r}{\partial z}$  ( $A, B$  fixed) and large and negative  $N_r^2$  ( $R \gg 1$ ). Thus, for either weak horizontal radiative gradients or strongly statically unstable radiative state the dynamically adjusted state is weakly statically stable as  $N_s^2 \sim (\frac{\partial \bar{u}_r}{\partial z})^6$  (for fixed  $N_r^2$ ) or  $N_s^2 \sim 1/(-N_r)^4$  (for fixed  $\frac{\partial \bar{u}_r}{\partial z}$ ). The waves are deep (Eady) but ineffective in heat transport. In this limit  $Ri$  becomes small and geostrophic baroclinic instability may no longer dominate the transports.

If  $N_r^2 > 0$  ( $R < 0$ ) a balance of terms in eq. (3.3.13) requires  $N'^3 + N' R \approx 1$  which implies  $N' \approx (-R)^{1/2} \gg 1$ . Then we find

$$N_s^2 \approx N_r^2, \quad \frac{\partial \bar{u}}{\partial z} \approx \frac{\partial \bar{u}_r}{\partial z}$$

$\gamma \approx -RB \approx \frac{N_r^2 \beta_0 H}{\frac{\partial \bar{u}_r}{\partial z} f_0^2} \gg 1$ , and  $Ri \approx Ri_r$ . For fixed  $N_r^2$  and small  $\frac{\partial \bar{u}_r}{\partial z}$

the eddies are shallow ( $\gamma \gg 1$ ) and ineffective in adjusting the temperature gradients from radiative equilibrium. This is somewhat different from the radiatively neutral and weak forcing case where  $\gamma \ll 1$  because weak vertical fluxes could not maintain a statically stable atmosphere. Here the static stability has a lower bound of the radiative value and  $\gamma$  increases as the horizontal forcing decreases. These results are also valid for fixed  $\frac{\partial \bar{u}_r}{\partial z}$  and large and positive  $N_r^2$ . In this case the eddy motions are suppressed by strong static stability.

The dependence on  $N_r^2$  with fixed horizontal forcing is further detailed in Fig. 3.16. In this example,  $\frac{\partial \bar{u}_r}{\partial z} = 4 \text{ m sec}^{-1} \text{ km}^{-1}$  and other parameters are unchanged from Fig. 3.13. Since strongly statically stable or unstable radiative states lead to weak heat transport, a minimum in the adjusted shear occurs near  $N_r^2 = 0$ , though the shear is only weakly dependent on  $N_r^2$ . For  $|N_r^2| \gg 1$  the shear approaches the radiative equilibrium value. As previously discussed,  $\gamma$  and  $N_s^2$  rapidly approach zero for increasingly unstable radiative states. The adjusted static stability slowly approaches  $N_r^2$  in the limit of large, positive  $N_r^2$ ; specifically,

$$N_s^2 - N_r^2 \approx \frac{\left( R_{ic}^{1/2} \frac{\partial \bar{u}_r}{\partial z} \right)^3}{N_r} \quad (N_r \gg 1).$$

Again it is seen that the behavior of the vertical dynamical fluxes plays a dominant role in determining the behavior of the static stability and  $\gamma$ .

The model is also applied to the Martian and Jovian atmosphere. Its application to Mars is probably more reliable as baroclinic waves have been observed on the planet. Jupiter has no known surface and therefore, use of a rigid lower boundary may not be reasonable unless it

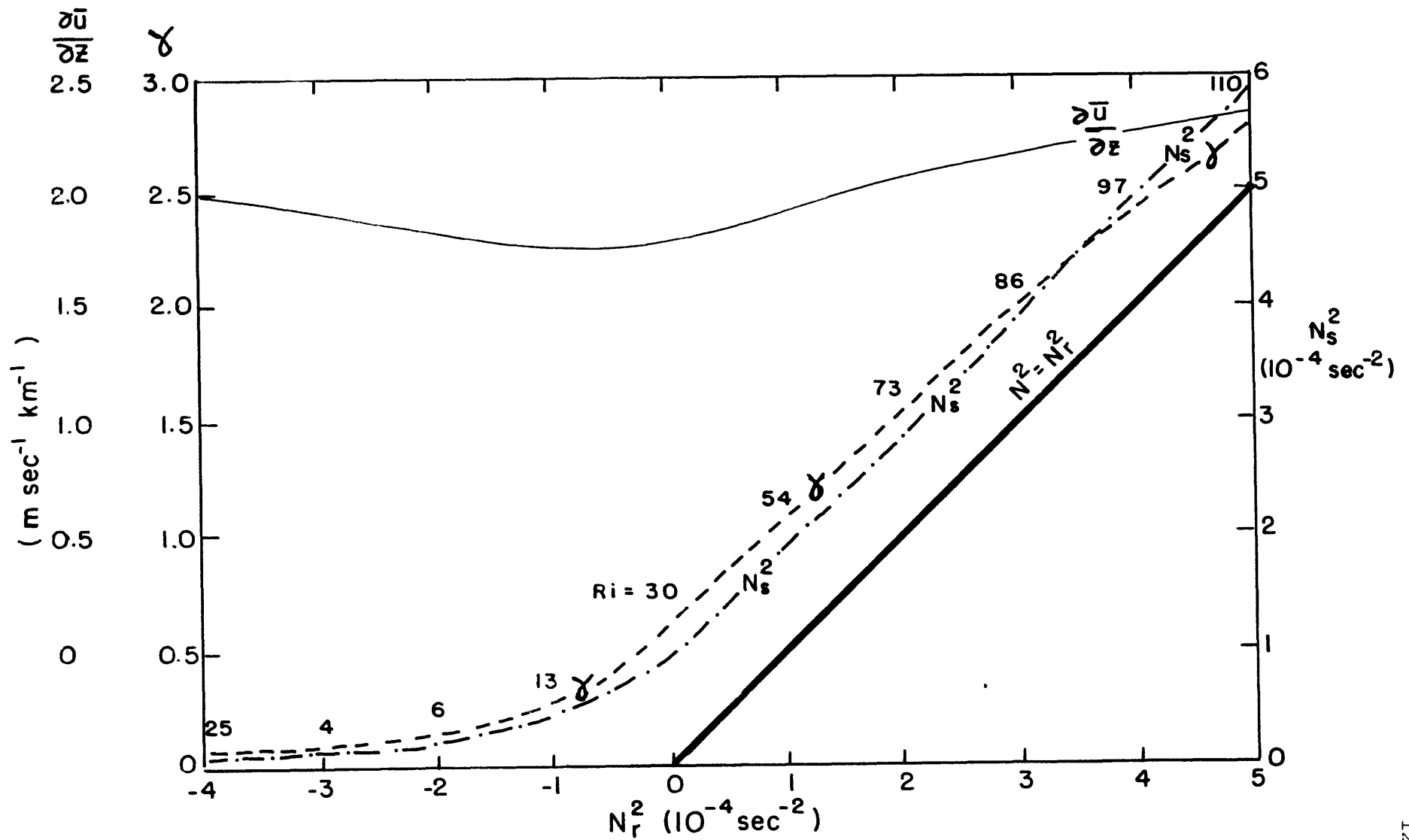


Fig. 3.16. Terrestrial radiative-dynamical model with  $\tau_r = 3 \times 10^6 \text{ sec}$ ,  $\frac{\partial \bar{u}_r}{\partial z} = 4 \frac{\text{m sec}^{-1}}{\text{Km}}$ , and variable  $N_r^2$ . Other parameters same as in Fig. 3.13.  $Ri$  given at intervals of  $1 \times 10^{-4} \text{ sec}^{-4}$  in  $N_r^2$ .

corresponds to a deep layer of strong static stability. This may be provided by water vapor condensation below visible cloud layers. The circulation of Jupiter is discussed in more detail in Chapter V. Table 2 shows the results for the two atmospheres and a range of specified parameters is used with a standard model listed first.

The major difference between the Earth and Mars is the shorter radiative time for Mars. Referring to the expression for the non-dimensional parameter  $A$ , we see this effect is partially mitigated by a smaller planetary radius and the results are not greatly different from the terrestrial model. It is worth noting the predicted static stability is smaller ( $\sim 2$  °K/Km) as observed and the efficiency of the dynamical flux as measured by  $1 - \frac{\partial \bar{u}'}{\partial z}$  is lower ( $\sim .4$ ) because of the short radiative time scale and somewhat weaker horizontal forcing. The Martian atmosphere's radiative equilibrium state is probably statically stable because of the presence of dust particles and this weakens the baroclinic transports. For the standard model the wavelength of maximum growth is about 3000 Km or a planetary wavenumber 5 at 45° lat. Baroclinic waves of this scale have been observed at mid-latitudes on Mars (Barnes, 1979).

The solutions for Jupiter are very sensitive to the externally specified parameters, esp. the radiative static stability, as also found by Stone (1972). In general the horizontal transports are less efficient than for the Earth and Mars, particularly for radiatively unstable states. With  $N_r^2 = 0$  the baroclinic eddies sufficiently stabilize the atmosphere vertically to create very large Richardson numbers. The standard model uses an estimate of  $\frac{\partial \bar{u}_r}{\partial z}$  based on Stone's (1972) eq. (3.11) which accounts for a uniformly distributed internal heat source with a magnitude equal to solar absorption. Other tests include no internal heating

TABLE 2

<div style="display: flex; justify-content: space-between; align-items: center;"> <div style="text-align: center;"><u>Mars</u></div> <div style="border: 1px solid black; padding: 5px;"> <math>f_0 = 1.0 \times 10^{-4} \text{ sec}^{-1}</math>      <math>L = 1600 \text{ Km}</math>  <math>\beta_0 = 3 \times 10^{-11} \text{ sec}^{-1} \text{ m}^{-1}</math>      <math>H = 11 \text{ Km}</math>      <math>g = 3.8 \text{ m sec}^{-2}</math> </div> </div>							
$\frac{\partial \bar{u}_r}{\partial z} \left( \frac{\text{m sec}^{-1}}{\text{Km}} \right)$	$\frac{\partial \theta_r}{\partial z} \left( \frac{^\circ\text{K}}{\text{Km}} \right)$	$\tau (10^5 \text{ sec})$	$\frac{\partial \bar{u}}{\partial z} \left( \frac{\text{m sec}^{-1}}{\text{Km}} \right)$	$\frac{\partial \theta}{\partial z} \left( \frac{^\circ\text{K}}{\text{Km}} \right)$	$\gamma$	$1 - \frac{\partial \bar{u}'}{\partial z}$	Ri
2.7	+1	4	1.60	1.9	.69	.41	13
2.7	+2	4	1.65	2.8	.99	.39	18
2.7	0	4	1.55	1.1	.41	.59	8
2.7	-2	4	1.62	0.3	.11	.40	2
4.0	+1	4	2.03	2.7	.74	.49	11
1.3	+1	4	.98	1.3	.74	.25	23
2.7	+1	1.2	1.84	1.77	.54	.32	9
2.7	+1	8	1.23	2.2	1.02	.40	25

<div style="display: flex; justify-content: space-between; align-items: center;"> <div style="text-align: center;"><u>Jupiter</u></div> <div style="border: 1px solid black; padding: 5px;"> <math>f_0 = 2.5 \times 10^{-4} \text{ sec}</math>      <math>L = 35000 \text{ Km}</math>  <math>\beta_0 = 3.5 \times 10^{-12} \text{ sec}^{-1} \text{ m}^{-1}</math>      <math>H = 20 \text{ Km}</math>      <math>g = 24 \text{ m sec}^{-2}</math> </div> </div>							
$\frac{\partial \bar{u}_r}{\partial z} \left( \frac{\text{m sec}^{-1}}{\text{Km}} \right)$	$\frac{\partial \theta_r}{\partial z} \left( \frac{^\circ\text{K}}{\text{Km}} \right)$	$\tau (10^8 \text{ sec})$	$\frac{\partial \bar{u}}{\partial z} \left( \frac{\text{m sec}^{-1}}{\text{Km}} \right)$	$\frac{\partial \theta}{\partial z} \left( \frac{^\circ\text{K}}{\text{Km}} \right)$	$\gamma$	$1 - \frac{\partial \bar{u}'}{\partial z}$	Ri
.16	0	3	.134	.16	.18	.16	$10^3$
.16	0	6	.120	.21	.26	.25	$10^3$
.16	0	1	.150	.10	.10	.06	600
.10	0	3	.091	.08	.12	.09	$10^3$
.33	0	3	.228	.48	.31	.31	$10^3$
.16	1	3	.139	1.12	1.18	.13	800
.16	-3	3	.156	$10^{-3}$	.001	.025	6

$(\frac{\partial \bar{u}_r}{\partial z} = .33 \frac{\text{m sec}^{-1}}{\text{Km}})$  and twice as much  $(\frac{\partial \bar{u}_r}{\partial z} = .10 \frac{\text{m sec}^{-1}}{\text{Km}})$ . Provided  $N_r^2$  is zero, the nature of the solution is not altered. Except for  $N_r^2 > 0$ ,  $\gamma$  remains much less than unity indicating a weak  $\beta$ -effect on baroclinic waves. The standard model gives a instability wavelength of 300 Km. Eddies of this and much greater scales have been observed by spacecraft, but the nature of their dynamical processes remains speculative. The presence of a cloud layer in which the atmosphere is stabilized by condensation may increase the wave scale as addressed in Chapter V.

#### 4. Summary

A method for modeling transient baroclinic heat fluxes was developed based on the nature of Charney modes as studied in Chapter II and studies of nonlinear baroclinic waves. The response of the parameterized fluxes to changes in shear and static stability suggests that strong feedbacks occur, particularly between the vertical shear or meridional temperature gradient and both horizontal and vertical fluxes. Though two-layer climate models will roughly imitate the behavior of the fluxes, it is also clear that more complete investigations will require better vertical resolution, esp. in studies of radiative forcing considerably removed from current conditions. In the case of  $\gamma > 1$  when the two-layer instability criterion is not satisfied, baroclinic fluxes may yet play an active role in determining the mean flow.

Application of the parameterization to an axisymmetric climate model under development proved to be successful in reproducing several features of mid-latitude heat transports. Further investigation of this model should provide insight into the maintenance of the general circulation. It is also likely to give more satisfactory answers to climate problems than one-dimensional models. The considerable importance of vertical heat fluxes and variable static stability in determining transport properties and mean flow characteristics is clearly demonstrated in the analytical model studied in Section III-3. In addition, other vertical fluxes, esp. moist convection, may alter the response of static stability and baroclinic fluxes to imposed forcing.

Finally, the importance of baroclinic instability in other planetary atmospheres was re-examined with inclusion of the  $\beta$ -effect on eddy scales. The results are not significantly different from Stone's (1972). On Mars

baroclinic transports are slightly less important in determining the temperature structure than on the Earth and the  $\beta$ -effect is of comparable importance to the baroclinic waves. Conclusions for Jupiter are much more speculative, but the modeling suggests the least effective baroclinic transports and weakest  $\beta$ -effect.

## CHAPTER IV

## MOMENTUM BALANCE MODEL

## 1. Modeling Eddy Momentum Flux

In this section we will use results from previous chapters to model eddy momentum flux in mid-latitudes. In the Charney model of baroclinic instability of Chapter II the zonal flow has no meridional structure and consequently, meridional eddy transport of zonal momentum cannot be directly determined from the stability analysis. An indirect means of estimating this transport must be found. The development follows Green's (1970) method of mixing length theory for quasi-conservative quantities,  $q$  and  $\theta$ . For example, to find  $\overline{\vec{v}'\theta'}$ , the eddy heat flux vector, we correlate  $\vec{v}'$  and  $\theta' = \Delta\bar{\theta} = \bar{\theta}(\vec{x}_0) - \bar{\theta}(\vec{x}_0 + \Delta\vec{x}')$  where  $\vec{x}_0$  = position vector and  $\Delta\vec{x}'$  is the displacement vector in the direction of the eddy velocity. The magnitude of  $\Delta\vec{x}'$  is the eddy mixing length. If  $|\Delta\vec{x}'| \ll \bar{\theta}/|\nabla\bar{\theta}|$  where  $\nabla$  is the three-dimensional gradient, then we expand  $\Delta\bar{\theta}$  to obtain:

$$\Delta\bar{\theta} \approx -\Delta\vec{x}' \cdot \nabla\bar{\theta}.$$

Thus we find  $\overline{\vec{v}'\theta'} \approx -\overline{\vec{v}'(\Delta\vec{x}' \cdot \nabla\bar{\theta})} = -\left(\overline{v'_y \Delta y'} \frac{\partial\bar{\theta}}{\partial y} + \overline{v'_z \Delta z'} \frac{\partial\bar{\theta}}{\partial z}\right)$

where  $\Delta y$  and  $\Delta z$  are the meridional and vertical eddy displacements.

We define mixing coefficients

$$K_{vy} = \overline{v'_y \Delta y'} \quad \text{and} \quad K_{vz} = \overline{v'_z \Delta z'}$$

and note that the formulation above will also apply to the eddy transport of quasi-geostrophic potential vorticity,  $q$ . Therefore, the meridional transports are:

$$\overline{v'\theta'} = -K_{vy} \frac{\partial\bar{\theta}}{\partial y} - K_{vz} \frac{\partial\bar{\theta}}{\partial z} \quad (4.1.1)$$

$$\overline{v'q'} = -K_{vy} \frac{\partial\bar{q}}{\partial y} - K_{vz} \frac{\partial\bar{q}}{\partial z} \quad (4.1.2)$$

It can be shown from the stability analysis of Section II-4 that  $\overline{v'\Delta y'} \propto e^{-z/d}$  with  $d = H/\sqrt{1+4K^2}$  and  $\overline{v'\Delta z'} = 0$  to the order retained in the heat flux structure found in Chapter II. The choice of the wavenumber,  $K$ , for the mixing scale will again be predicated on the stability analysis. The magnitude of the mixing coefficient will be determined by this choice and the scaling analysis of Section III-1.

From the expression for  $q'$  of eq. (2.1.7) we find:

$$\overline{v'q'} = -\overline{v'\nabla^2\psi'} + \frac{f_0^2}{\rho_s} \overline{v' \frac{\partial}{\partial z} \frac{\rho_s}{N_s^2} \frac{\partial \psi'}{\partial z}}$$

and after using  $\vec{v}' = \hat{k} \times \nabla \psi'$  and  $\frac{\partial \psi'}{\partial z} = g/f_0 \theta'_s$ ,

this reduces to:

$$\overline{v'q'} = -\frac{\partial \overline{u'v'}}{\partial y} + \frac{f_0}{\rho_s} \frac{\partial}{\partial z} \left( \frac{\rho_s \overline{v'\theta'_s}}{\partial \theta_s} \right). \quad (4.1.3)$$

Introducing the relations for  $\overline{v'q'}$  and  $\overline{v'\theta'_s}$  from eqs. (4.1.1) and (4.1.2) with  $K_{vz} = 0$ , eq. (4.1.3) becomes:

$$\frac{\partial \overline{u'v'}}{\partial y} = -\frac{f_0}{\rho_s} \frac{\partial}{\partial z} \left( \frac{\rho_s K_{vy}}{\partial \theta_s} \frac{\partial \overline{\theta}}{\partial y} \right) + K_{vy} \frac{\partial \overline{q}}{\partial y} \quad (4.1.4)$$

where  $\frac{\partial \overline{q}}{\partial y} = \beta_0 - \frac{f_0^2}{\rho_s} \frac{\partial}{\partial z} \left( \frac{\rho_s}{N_s^2} \frac{\partial \overline{u}}{\partial z} \right) - \frac{\partial^2 \overline{u}}{\partial y^2}$ .

To examine the behavior of the momentum flux divergence of eq.

(4.1.4), we substitute for  $\frac{\partial \overline{q}}{\partial y}$  and simplify the divergence expression.

We find:

$$\frac{\partial \overline{u'v'}}{\partial y} \approx -\frac{f_0}{\rho_s} \left( \frac{\partial \overline{\theta}/\partial y}{\partial \theta_s} \right) \frac{\partial}{\partial z} \rho_s K_{vy} + K_{vy} \left( \beta_0 + \frac{f_0^2}{N_s^2 H} \frac{\partial \overline{u}}{\partial z} - \frac{\partial^2 \overline{u}}{\partial y^2} \right)$$

and if  $\frac{\partial}{\partial z} K_{vy} = -K_{vy}/d$ , this further reduces to:

$$\frac{\partial \overline{u'v'}}{\partial y} \approx K_{vy} \left[ \beta_0 - \frac{f_0^2}{N_s^2 d} \frac{\partial \overline{u}}{\partial z} - \frac{\partial^2 \overline{u}}{\partial y^2} \right]. \quad (4.1.5)$$

The sum of the first two terms in brackets is  $\beta_0(1 - \frac{H}{\gamma d})$ . From stability analysis of the Charney model it can be shown  $d < H/\gamma$  for all growing Charney modes. For momentum mixing by these modes, the sum of the first two terms will be negative. Only where  $\frac{\partial^2 \bar{u}}{\partial y^2}$  is negative, as in a westerly jet, can the flux divergence of eq. (4.1.5) be positive or zero.

If we choose to model the heat flux for the most unstable wave as in Section III-1, then we can equate the expressions for flux, (4.1.1)

and (3.1.8), to find 
$$K_{vy} = \frac{N_s d^2}{\sqrt{2} f_0} \frac{\partial \bar{u}}{\partial z} e^{-z/d}.$$

At high latitudes  $d \sim H$  and  $\frac{\partial \bar{u}}{\partial z}$  decreases polewards so that the mixing is less effective. In the low latitudes where  $\gamma \gg 1$  and

$d \sim H/\gamma$ , 
$$K_{vy} \approx \frac{\left(\frac{-g}{\theta_s} \frac{\partial \bar{\theta}}{\partial y}\right)^3}{N_s^3 \beta_0^2} e^{-z/H}$$
 so that the mixing is

weak and shallow because of weak meridional temperature gradients.

Momentum convergence by baroclinic eddies will be small as expected.

In the tropics it is not potential vorticity,  $q$ , that is

approximately conserved, but instead the vorticity,  $\bar{S} + f = \frac{\partial v}{\partial x} - \frac{\partial u}{\partial y} + f$  as noted by Charney (1963). In this case, the vorticity flux by

tropical eddies is  $\overline{v' \bar{S}'} = -\frac{\partial}{\partial y} \overline{u' v'}$  and a mixing length argument

for the momentum flux convergence would give:

$$\begin{aligned} \frac{\partial \overline{u' v'}}{\partial y} &= K_{vy}^T \frac{\partial (\bar{S} + f)}{\partial y} + K_{vz}^T \frac{\partial \bar{S}}{\partial z} \\ &= K_{vy}^T \left( \beta - \frac{\partial^2 \bar{u}}{\partial y^2} \right) - K_{vz}^T \frac{\partial^2 \bar{u}}{\partial y \partial z} \end{aligned} \quad (4.1.6)$$

with  $K_{vy}^T, K_{vz}^T$  as mixing coefficients appropriate to the tropics.

Since vertical velocities are weaker in the tropics (Charney, loc. cit.),

we expect the vertical mixing coefficient to be small and eq. (4.1.6) to

be approximately:

$$\frac{\partial \overline{u'v'}}{\partial y} \approx K_{v1} \left( \beta - \frac{\partial^2 \overline{u}}{\partial y^2} \right). \quad (4.1.7)$$

For the tropical troposphere  $\beta > \frac{\partial^2 \overline{u}}{\partial y^2}$  so that  $\frac{\partial \overline{u'v'}}{\partial y} > 0$  implying the eddies transport westerly momentum out of the tropics as observed. Also if  $\frac{\partial^2 \overline{u}}{\partial y^2} > \beta$  as for strong easterlies, the mixing law of eq. (4.1.7) would give convergence into equatorial regions.

The determination of the mixing coefficient is more difficult in the tropics than at mid-latitudes where horizontal scales can be estimated from baroclinic theory. Free and forced tropical motions can have widely varying length scales. Furthermore, the scaling analysis of Charney (1963) which implies vorticity conservation will not be valid if strong forcing such as deep convection causes strong vertical motion or efficient vertical mixing of momentum. Here we will limit our study to quasi-geostrophic motion in extratropical latitudes, though a further analysis of tropical momentum flux would be useful in the formulation of globally valid parameterizations.

Returning to eq. (4.1.5), we note the mixing coefficient is proportional to  $e^{-z/d}$  and since  $d \approx 4$  km for mid-latitudes (see Table 1), the momentum flux divergence will be small in the upper troposphere. However, the observed transient flux reaches a maximum at 200 mb. The nature of these fluxes is unknown, though they may be caused by finite amplitude development of baroclinic waves (Simmons and Hoskins, 1978) or intermittent standing eddies.

Coriolis torques of the induced mean meridional circulation largely cancel eddy flux divergences in the deep baroclinic waves in the upper troposphere of Simmons and Hoskins' model. For non-dissipative, standing waves, this cancellation would be exact. While the observation

of the mean meridional flow is prone to large error, the primary components of the upper tropospheric momentum balance are horizontal eddy flux divergence and Coriolis torques of the mean circulation (Newell et al, 1972). The net contribution of the waves causing the upper level momentum flux is uncertain.

In any case, the parameterization scheme developed here is restricted to momentum mixing by the most unstable modes as required by the constraints of potential vorticity and entropy conservation. The precise vertical structure of the transport proves to be of lesser importance to the surface momentum balance, provided the magnitude of the vertically integrated momentum flux is correct.

## 2. Momentum Balance Model

Following Green (1970) a momentum balance model is developed to study the maintenance of surface winds at mid and high latitudes. It departs from Green's study in that he assumed the baroclinic eddies draw available potential energy across the planetary scale rather than eddy scale in his formulation of the mixing coefficient. Green's model was Boussinesq and vertically bounded as opposed to the unbounded, quasi-Boussinesq model considered here.

In his determination of the vertical dependence of  $K_{vy}$ , Green considered the case of a Boussinesq model with no horizontal shear and approximately linear vertical shear. In this situation,  $\frac{\partial \overline{u'v'}}{\partial y} = 0$  and eq. (4.1.4) reduces to  $\frac{\partial K_{vy}}{\partial z} = -K_{vy}/(D/\gamma)$  where the density scale height in  $\gamma$  is now replaced by the fluid depth,  $D$ . This gives a different behavior than

$$\frac{\partial K_{vy}}{\partial z} = -\frac{K_{vy}}{H/(1+\gamma)}$$

derived from the stability problem. In the case of small  $\gamma$ , the depth of mixing in Green's model is infinite rather than limited by the density scale height. For  $\gamma = 1$ , as in the atmosphere, the vertical scales of the two models are similar. A different surface drag formulation, dependent on the eddy velocity scale, will be used here.

The time-zonal mean momentum equation is

$$\overline{\rho_s v \frac{\partial u}{\partial y}} + \overline{\rho_s w \frac{\partial u}{\partial z}} = \frac{\partial \bar{\tau}}{\partial z} + \rho_s f \bar{v} \quad (4.2.1)$$

where  $\tau$  is a frictional stress. Integrating vertically and applying the zonally averaged continuity equation, eq. (4.2.1) becomes:

$$\int_0^{\infty} \rho_s \frac{\partial \bar{u} \bar{v}}{\partial y} dz = -\bar{\tau}_{sfc} \quad (4.2.2)$$

where  $\tau_{sfc}$  is frictional surface stress.

We approximate the momentum flux divergence by the baroclinic eddy transport as parameterized in the previous section. The vertical integral of the mean meridional transport is neglected. The observations of Newell et al (1972) show that transient eddies account for at least two-thirds of the vertically averaged transport at mid-latitudes through all seasons. The transport by mean meridional motions is negligible (< 10% of total) outside of the tropics. Thus, the model developed here will represent the two major components of the vertically integrated momentum balance, horizontal transport by transient eddies and surface stress. To find the net flux divergence in a column outside the tropics, eq. (4.1.4) is used:

$$\int_0^{\infty} \rho_s \frac{\partial}{\partial y} \overline{u'v'} dz = \int_0^{\infty} \rho_s \left\{ K_{vy} \left( \beta_0 - \frac{\partial^2 \bar{u}}{\partial y^2} \right) + \frac{f_0^2}{N_s^2} \frac{\partial \bar{u}}{\partial z} \frac{\partial K_{vy}}{\partial z} \right\} dz.$$

If we assume the mean flow parameters appearing in  $K_{vy}$  are vertical averages weighted by the eddy depth so that  $\frac{\partial K_{vy}}{\partial z} = -\frac{K_{vy}}{d}$ , this expression becomes:

$$\int_0^{\infty} \rho_s \frac{\partial \overline{u'v'}}{\partial y} dz = \int_0^{\infty} \rho_s K_{vy} \left\{ \beta_0 - \frac{\partial^2 \bar{u}}{\partial y^2} - \frac{f_0^2}{N_s^2 d} \frac{\partial \bar{u}}{\partial z} \right\} dz \quad (4.2.3)$$

where  $d$  is the eddy depth using the eddy-weighted vertical means of the mean flow parameters.

The mean zonal flow is defined as the sum of barotropic and baroclinic components,  $\bar{u}(y,z) = \bar{u}_s(y) + \bar{u}_B(y,z)$ , where  $\bar{u}_B(y,0) = 0$  and  $\bar{u}_s(y)$  is the surface wind. Using a drag law for the surface stress,  $\tau_{sfc} = D' \bar{u}_s(y)$ , with  $D' = \text{constant}$ , eq. (4.2.2) can be written:

$$\left( \beta_0 - \frac{d^2 \bar{u}_s}{dy^2} \right) \int_0^{\infty} \rho_s K_{vy} dz - \int_0^{\infty} \frac{\partial^2 \bar{u}_B}{\partial y^2} \rho_s K_{vy} dz - \frac{f_0^2}{d} \int_0^{\infty} \frac{\partial \bar{u}_B}{\partial z} \frac{\rho_s K_{vy}}{N_s^2} dz = -D' \bar{u}_s. \quad (4.2.4)$$

We take  $v' = 0$  at rigid boundaries at  $y = \pm L$  spanning a mid-latitude channel. This condition requires  $\frac{\partial \overline{u'v'}}{\partial y} = 0$  for quasi-geostrophic transport and, from (4.2.2),  $\bar{u}_s = 0$  at the sidewalls. If the thermal field is specified and therefore, the baroclinic component is known,  $K_{vy}$  can be determined and eq. (4.2.4) can be solved for  $\bar{u}_s$ .

Normally,  $K_{vy}$  is a function of  $y$ . However, to facilitate analytic solutions to (4.2.4) we will represent it by a meridional mean. Eq. (4.2.4) becomes constant coefficient with inhomogeneous forcing terms which cause a redistribution of momentum through eddy mixing. Some error is expected near the boundaries where  $K_{vy}$  would normally be small. The emphasis will center on the response of the

barotropic component to changes in the mean gradients in the thermal field. Also assume  $\beta_0$ ,  $f_0$ ,  $N_s^2$  and  $d$  are constant, consistent with assuming  $K_{vy}$  independent of  $y$ .

If eq. (4.2.2) is integrated meridionally between  $y = \pm L$  where  $\overline{u'v'} = 0$  then  $\int_{-L}^{+L} \tau_{sfc} dy = 0$  or a condition of no net surface stress.

This implies the following constraint on the L.H.S. of (4.2.4):

$$\beta_0 - \left\langle \frac{d^2 \bar{u}_s}{dy^2} \right\rangle - \left\langle \frac{\partial^2 \bar{u}_B}{\partial y^2} \right\rangle - \frac{f_0^2}{N_s^2 d} \left\langle \frac{\partial \bar{u}_B}{\partial z} \right\rangle = 0$$

where

$$\langle F \rangle = \frac{\int_{-L}^{+L} \int_0^{\infty} F \rho_s K_{vy} dz dy}{\int_{-L}^{+L} \int_0^{\infty} \rho_s K_{vy} dz dy}$$

Using this constraint in (4.2.4), we find:

$$\begin{aligned} \frac{d^2 \bar{u}_s}{dy^2} - \mu^2 \bar{u}_s &= \left\langle \frac{d^2 \bar{u}_s}{dy^2} \right\rangle + \left\langle \frac{\partial^2 \bar{u}_B}{\partial y^2} \right\rangle + \frac{f_0^2}{N_s^2 d} \left\langle \frac{\partial \bar{u}_B}{\partial z} \right\rangle \\ &- \overline{\frac{\partial^2 \bar{u}_B}{\partial y^2}} - \frac{f_0^2}{N_s^2 d} \overline{\frac{\partial \bar{u}_B}{\partial z}} \end{aligned} \quad (4.2.5)$$

where

$$\overline{F}^z = \frac{\int_0^{\infty} F \rho_s K_{vy} dz}{\int_0^{\infty} \rho_s K_{vy} dz} \quad \text{and} \quad \mu^2 = \frac{D'}{\int_0^{\infty} \rho_s K_{vy} dz}$$

We now define the baroclinic component as  $\bar{u}_B(z) = S A(y) z$

where  $S$  is a dimensional shear and  $A(y)$  is an  $O(1)$  meridional structure.

Then

$$\begin{aligned} \overline{\frac{\partial^2 \bar{u}_B}{\partial y^2}}^z &= S \frac{d^2 A}{dy^2} \int_0^{\infty} z \rho_s K_{vy} dz / \int_0^{\infty} \rho_s K_{vy} dz, \\ \overline{\frac{\partial \bar{u}_B}{\partial z}}^z &= SA, \quad \left\langle \frac{\partial^2 \bar{u}_B}{\partial y^2} \right\rangle = \frac{S \int_{-L}^{+L} \frac{d^2 A}{dy^2} \int_0^{\infty} \rho_s K_{vy} dz dy}{\int_{-L}^{+L} \int_0^{\infty} \rho_s K_{vy} dz dy} \end{aligned}$$

and  $\left\langle \frac{\partial \bar{u}_B}{\partial z} \right\rangle = \frac{S \int_{-L}^{+L} \int_0^{\infty} \rho_s K_{vy} dz dy}{\int_{-L}^{+L} \int_0^{\infty} \rho_s K_{vy} dz dy}$ .

Now we take  $K_{vy} = \frac{N_s d^2}{\sqrt{2} f_0} \left( \frac{\partial \bar{u}_B}{\partial z} \right)_m e^{-z/d}$

where  $\left( \frac{\partial \bar{u}_B}{\partial z} \right)_m$  is a horizontal mean of the vertical shear in the channel and  $d = \frac{H}{\left( 1 + \frac{\beta_0 N_s^2 H}{f_0^2 \left( \frac{\partial \bar{u}_B}{\partial z} \right)_m} \right)}$ .

In this example,

$$\frac{\partial^2 \bar{u}_B}{\partial y^2} = S \frac{d^2 A}{dy^2} \left( \frac{1}{d} + \frac{1}{H} \right), \quad \left\langle \frac{\partial^2 \bar{u}_B}{\partial y^2} \right\rangle = \frac{S \left( \frac{dA}{dy}(L) - \frac{dA}{dy}(-L) \right)}{2L \left( \frac{1}{d} + \frac{1}{H} \right)},$$

$$\left\langle \frac{\partial \bar{u}_B}{\partial z} \right\rangle = \frac{S \int_{-L}^{+L} A dy}{2L}, \quad \left\langle \frac{d^2 \bar{u}_s}{dy^2} \right\rangle = \frac{d\bar{u}_s(L) - d\bar{u}_s(-L)}{2L}$$

and  $\mu^2 = \frac{\sqrt{2} f_0 D' \left( \frac{1}{d} + \frac{1}{H} \right)}{\rho_s(0) N_s d^2 \left( \frac{\partial \bar{u}_B}{\partial z} \right)_m}$ .

Next use  $A = 1 - (y/L)^2$  so that the vertical shear is maximized at the channel's center, a mid-latitude where the radiative differential heating is greatest. Then the solution of eq. (4.2.5) is:

$$\bar{u}_s(y) = U \left\{ \frac{2}{3} \left( \frac{\cosh \mu y - \frac{1}{\mu L} \sinh \mu L}{\cosh \mu L - \frac{1}{\mu L} \sinh \mu L} + \frac{1}{3} - \left( \frac{y}{L} \right)^2 \right) \right\} \quad (4.2.6)$$

where  $U = \frac{f_0^2 S}{\mu^2 N_s^2 d}$ , the magnitude of the barotropic or surface flow. This magnitude is proportional to  $\left( \frac{\partial \bar{u}_B}{\partial z} \right)_m^2 d^2 f_0 / u_f N_s$  where  $u_f \equiv$  friction velocity =  $D' / \rho_s(0)$ .

The friction velocity can be related by a drag law to the surface wind variance,  $u_f = c_D \left( \left( \bar{u}^2 + \bar{v}^2 \right)_{z=0} + \bar{u}_s^2 \right)^{1/2}$

where  $C_D$  = drag coefficient.

Usually the eddy variance exceeds  $\bar{u}_s$  by at least an order of magnitude.<sup>1</sup>

Using the amplitude and vertical structure expressions for the baroclinic wave responsible for the momentum mixing, we can show that

$$\left( \overline{u'^2} + \overline{v'^2} \right)_{z=0}^{1/2} = F(\gamma) \frac{\partial \bar{u}}{\partial z} d.$$

The function  $F(\gamma)$  is only weakly dependent on  $\gamma$ ,

$$F(\gamma) = \left[ \frac{2(1+\gamma)^2}{4(1+\gamma)^2+1} \cdot \frac{\sqrt{4(1+\gamma)^2+1} - 1 - \gamma}{\sqrt{4(1+\gamma)^2+1} - 1} \right]^{1/2}$$

varying from .5 for  $\gamma \gg 1$  to .63 for  $\gamma = 0$ . Using Newell's mean flow data from Table 1 - Chapter III, this expression is compared with observed 1000mb values of Oort and Rasmusson.

	<u>WINTER</u>		<u>SUMMER</u>	
	<u>obs.</u>	<u>model</u>	<u>obs.</u>	<u>model</u>
30°N	7.7 m sec <sup>-1</sup>	5.3	4.8	0.4
50°N	8.9	5.6	6.6	3.2
70°N	8.2	1.1	6.3	3.6

The predicted standard deviation is generally smaller than observed values, especially in winter at 70°N where the mean flow data is most uncertain. Considerable error is also seen at 30°N in summer when we expect non-baroclinic eddies to greatly contribute to the variance. Overlooking these uncertainties, modeling  $u_f$  by the eddy variance should be more realistic than Green's assumption that  $u_f$  is constant and independent of the vertical shear. A similar formulation for an f-plane was used successfully by Mullan (1979) in a symmetric climate model.

<sup>1</sup> Furthermore, neglecting  $\bar{u}_s$  is required for a linear form of eq. (4.2.5) and then eq.(4.2.6) is a valid solution of (4.2.5).

We approximate the friction velocity by

$$u_f = C_D \left( \frac{\partial \bar{u}_B}{\partial z} \right)_M d \quad (4.2.7)$$

approximating the function  $F(\gamma)$  as a constant and absorbing it into  $C_D$ .

In this case, the amplitude  $\mathcal{V}$  is proportional to

$$\left( \frac{\partial \bar{u}_B}{\partial z} \right)_M \frac{d f_0}{C_D N_s}$$

and we see that the magnitude of the barotropic flow will increase for strong shear or weak stress as measured by  $C_D$ . For  $\gamma \ll 1$  (strong shear) we find

$$\mathcal{V} \sim \left( \frac{\partial \bar{u}_B}{\partial z} \right)_M \frac{H f_0}{C_D N_s}$$

and for  $\gamma \gg 1$  (weak shear),

$$\mathcal{V} \sim \left( \frac{\partial \bar{u}_B}{\partial z} \right)_M^2 \left( \frac{f_0}{N_s} \right)^3 / (\beta_0 C_D).$$

Two meridional scales appear in the meridional structure of  $\bar{u}_s$ ,

$$\mu^{-1} \sim d \sqrt{\frac{N_s}{f_0 C_D}} \quad \text{and } L.$$

When  $\mu L \gg 1$ , we find:

$$\bar{u}_s \approx \mathcal{V} \left[ \frac{2}{3} \frac{\cosh \mu y}{\cosh \mu L} + \frac{1}{3} - \left( \frac{y}{L} \right)^2 \right] \quad \text{and for}$$

$L - |y| \gg \mu^{-1}$  (i.e. well away from the boundaries), this becomes

$$\bar{u}_s \approx \mathcal{V} \left( \frac{1}{3} - \left( \frac{y}{L} \right)^2 \right). \quad \text{The scale } \mu^{-1} \text{ is the width of the}$$

boundary layers near  $y = \pm L$  and the barotropic wind varies on the planetary scale,  $L$ . It is seen that a westerly current exists between  $y \approx \pm L/\sqrt{3}$ , bounded by easterlies on either side.

When  $\mu L \ll 1$ , the barotropic flow is

$$\bar{u}_s \approx \frac{U(\mu L)^2}{12} \left[ \left( \frac{y}{L} \right)^4 - \frac{1}{5} \right]$$

so that an additional factor of  $(\mu L)^2$  appears in the amplitude. The amplitude is independent of the frictional coefficient since

$$U(\mu L)^2 \sim \left( \frac{\partial \bar{u}_B}{\partial z} \right)_M d \left( \frac{L f_0}{N_s d} \right)^2.$$

In this case, the variation of the flow is still on the planetary scale, but now easterlies occur at the center, bounded by westerlies at  $y = \pm 0.67L$ . The ratio  $\mu L$  is small if the frictional stress is weak or the eddy scale is large. The latter case would be unrealistic if the scale of the waves exceeds the planetary scale.

To obtain Green's model we must replace  $\mu^2$  in (4.2.6) by

$$\mu_G^2 = \frac{125 u_f N_s}{\left( \frac{\partial \bar{u}_B}{\partial z} \right)_M f_0 L^2 D}$$

and

$$U \text{ by } U_G = \frac{f_0^2 S \gamma}{\mu_G^2 N_s^2 D}$$

where  $D = \text{fluid depth}$

and

$$\gamma = \frac{\beta_0 N_s^2 D}{f_0^2 \left( \frac{\partial \bar{u}_B}{\partial z} \right)_M}.$$

The magnitude of the flow,  $U_G$ , is proportional to:

$$\left( \frac{\partial \bar{u}_B}{\partial z} \right)^2 \frac{L^2 \gamma}{u_f} \left( \frac{f_0}{N_s} \right)^3 \sim \frac{\beta_0 L^2 \left( \frac{\partial \bar{u}_B}{\partial z} \right)_M D}{u_f} \frac{f_0}{N_s}$$

so that the parameter dependence is unchanged for large or small  $\gamma$ .

The mixing coefficient in Green's model is independent of  $\gamma$  since he assumed the waves draw potential energy across the planetary scale rather than the eddy scale. For a strong  $\beta$ -effect the potential vorticity gradient of the mean field will be large and substantial vorticity

transport will be balanced by strong frictional stress. In the model presented here the barotropic flow becomes weak for a strong  $\beta$ -effect as the waves are shortened and are ineffective in mixing vorticity.

For a weak  $\beta$ -effect our model approaches an f-plane limit. The horizontal heat flux has a vertical scale of  $H$  and non-zero momentum flux divergence is possible (see eq. 4.1.3). As  $\beta_0 \rightarrow 0$  Green's model has vanishing barotropic flow. By assuming the vertical variation of the mixing coefficient or, equivalently, the heat flux vanishes in this limit, no momentum flux divergence is possible.

To calculate specific profiles typical parameters on a channel centered at  $45^\circ$  with boundaries at  $18^\circ$  and  $72^\circ$  are chosen:

$$\begin{aligned} \gamma &= 1 & H &= 8 \text{ Km} & \left(\frac{\partial \bar{u}_B}{\partial z}\right)_m &= 2 \text{ m sec}^{-1} \text{ Km}^{-1} \\ d &= 4 \text{ Km} & C_D &= .003 & N_S^2 &= 1.7 \times 10^{-4} \text{ sec}^{-2} & L &= 3000 \text{ Km} \end{aligned}$$

Equating  $\langle \frac{\partial \bar{u}_B}{\partial z} \rangle$  and  $\left(\frac{\partial \bar{u}_B}{\partial z}\right)_m$  so that  $S = \frac{3}{2} \left(\frac{\partial \bar{u}_B}{\partial z}\right)_m$ , we find:

$$\mu L = 5.2 \quad \text{and} \quad \mathcal{U} = 14.4 \text{ m sec}^{-1}.$$

The profile of  $\bar{u}_S(y)$  is shown in Fig. 4.1 along with annual mean 1000 mb winds from Oort and Rasmusson (1971). Given the simplifying approximations made for ease of calculation, the agreement is fairly good in magnitude and structure. The eddies transport heat in the specified thermal field and redistribute potential vorticity and momentum to create a westerly current at mid-latitudes. The profile is similar to Green's calculation because, in the current climatic state, the two measurements of eddy mixing are quantitatively similar.

Errors appear near the boundaries because of approximations made in the model. In the atmosphere the meridional flux convergence is non-zero in the tropics unlike the model assumption of vanishing convergence

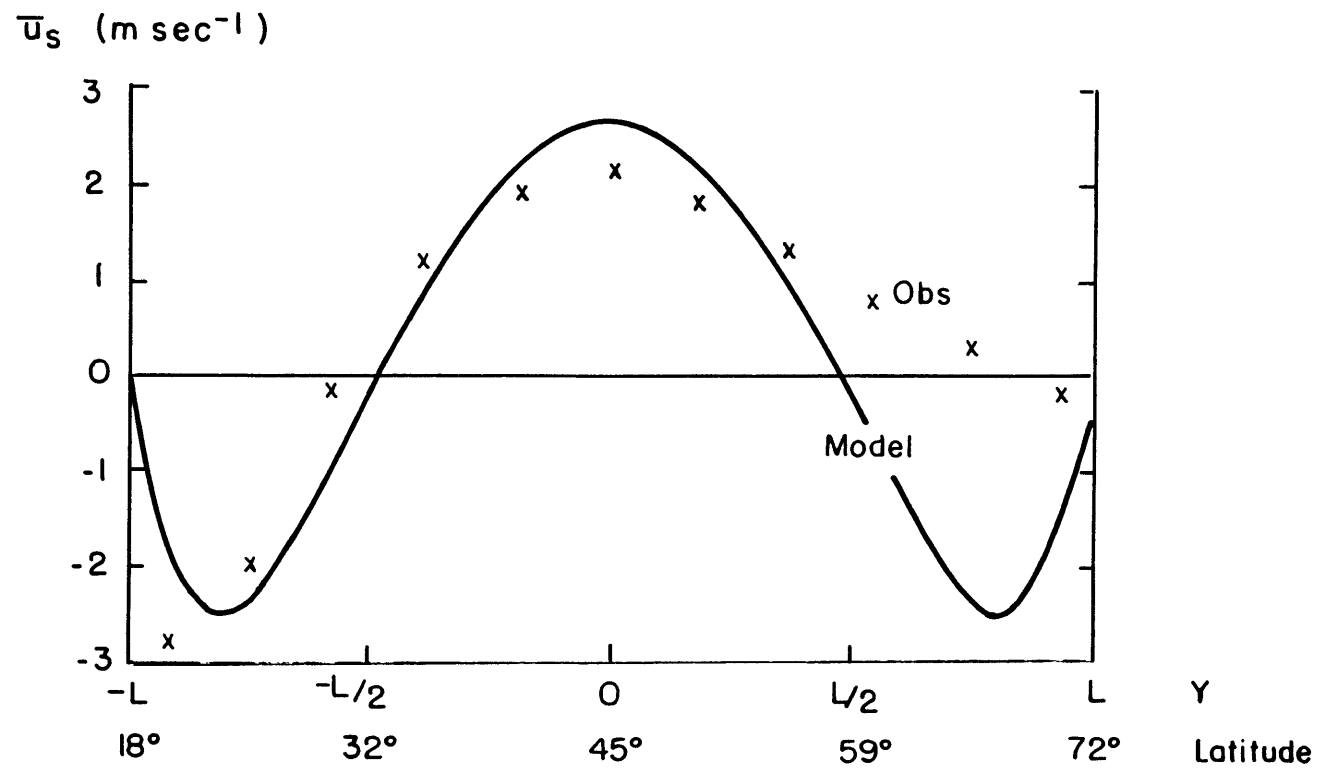


Fig. 4.1. Surface  $\bar{u}$  as calculated by momentum balance model and observed 1000 mb annual mean  $\bar{u}$  (x) from Oort and Rasmusson (1971).

at the tropical boundary. The parameterization of the eddy flux is not expected to apply at the equatorial latitudes. Some error is also seen in the overemphasis of polar easterlies which may be due to the assumption of constant  $K_{vy}$  or to lack of spherical effects as noted by White (1977) in his study of Green's model on a sphere.

In the profile of Fig. 4.1, the vertical mean eddy flux divergence can be directly calculated from eq. (4.2.2) given the relation  $\tau_{sfc} = D' \bar{u}_s(y) = \rho_s(0) u_f \bar{u}_s(y)$ . At the center of channel, the mean divergence is:

$$\int_0^{\infty} \rho_s \frac{\partial \overline{u'v'}}{\partial y} dz / \int_0^{\infty} \rho_s dz = \frac{-u_f \bar{u}_s(0)}{H} = \frac{-8 \text{ m}^2 \text{ sec}^{-2}}{10^3 \text{ Km}} .$$

This compares favorably with the 45°N annual mean transient flux divergence from Oort and Rasmusson of  $-7.9 \text{ m}^2 \text{ s}^{-2}/10^3 \text{ Km}$ .

The latitudinal distribution of the eddy momentum flux can be deduced from the boundary conditions and the structure of  $\bar{u}_s(y)$ . The flux must be antisymmetric about the westerly current maximum with westerly momentum transported poleward ( $\overline{u'v'} > 0$ ) on the equatorward side of the current. The observed flux has a similar structure though the equatorward flux at high latitudes is much weaker than in the model. Consequently, the strength of the polar easterlies is overestimated.

Finally, the energy balance model of Section III - 3 can be combined with the momentum balance model to study the effect of baroclinic eddies on both baroclinic and barotropic components of the mid-latitude zonal wind. From the standard terrestrial model [ $\frac{\partial \bar{u}_r}{\partial z} = 5 \frac{\text{m sec}^{-1}}{\text{Km}}$ ,  $N_r^2 = 0$ ], we found:

$$d = 4.7 \text{ Km} \quad \left(\frac{\partial \bar{u}_B}{\partial z}\right)_m = 2 \frac{\text{m sec}^{-1}}{\text{Km}} \quad N_s^2 = 1.3 \times 10^{-4} \text{ sec}^{-2} .$$

Using these parameters, we determine:

$$\mu L = 4.9 \quad \mathcal{U} = 18.4 \text{ m sec}^{-1}$$

which has essentially the same structure as the profile in Fig. 4.1.

The maximum westerly flow at  $y = 0$  is  $\bar{u}_S(0) = 3.2 \text{ m sec}^{-1}$ . Therefore, the combined model somewhat overestimates the strength of the observed barotropic flow.

For weaker radiative forcing [  $\frac{\partial \bar{u}_r}{\partial z} = 1 \frac{\text{m sec}^{-1}}{\text{Km}}$ ,  $N_r^2 = 0$  ], the energy balance model gives:

$$d = 6.4 \text{ Km} \quad \left( \frac{\partial \bar{u}_B}{\partial z} \right)_m = .73 \frac{\text{m sec}^{-1}}{\text{Km}} \quad N_S^2 = 1.8 \times 10^{-5} \text{ sec}^{-2}$$

For the momentum balance model this corresponds to:

$$\mu L = 6.3 \quad \text{and} \quad \mathcal{U} = 21.6 \text{ m sec}^{-1}$$

for which  $\bar{u}_S(0) = 4.5 \text{ m sec}^{-1}$ . The structure is relatively unchanged and the magnitude of the current increases by 40% which is opposite to the forced reduction of 65% in the baroclinic shear.

For stronger radiative forcing [  $\frac{\partial \bar{u}_r}{\partial z} = 25 \frac{\text{m sec}^{-1}}{\text{Km}}$ ,  $N_r^2 = 0$  ], the energy balance model gives:

$$d = 2.8 \text{ Km} \quad \left( \frac{\partial \bar{u}_B}{\partial z} \right)_m = 5.4 \frac{\text{m sec}^{-1}}{\text{Km}} \quad N_S^2 = 9 \times 10^{-4} \text{ sec}^{-2}$$

In this case, we find:

$$L = 4.7 \quad \mathcal{U} = 13.2 \text{ m sec}^{-1}$$

for which  $\bar{u}_S(0) = 2.2 \text{ m sec}^{-1}$  which is smaller than the weak radiative gradient case.

The strength of the westerly maximum at  $y = 0$  decreases for increased radiative forcing. This behavior does not agree with the observed seasonal variation of zonal average surface westerlies. The maximum westerly flow at 1000 mb in summer is  $1.6 \text{ m sec}^{-1}$  and occurs at  $45^\circ\text{N}$  (Oort and Rasmusson,

1971). The strongest 1000 mb westerly flow is  $2.8 \text{ m sec}^{-1}$  in winter and occurs at  $40^\circ\text{N}$ .

Much of the discrepancy between the observed seasonal variation and the combined model can be explained by the great sensitivity of static stability to changes in the model's radiative forcing. If we use observed values for the mean flow parameters at  $50^\circ\text{N}$  from Table 1, the momentum balance model predicts  $\bar{u}_s(0) = 1.9 \text{ m sec}^{-1}$  in summer and  $\bar{u}_s(0) = 3.0 \text{ m sec}^{-1}$  in winter. The largest seasonal variation among the mean flow parameters occurs in the vertical shear with a 47% increase from summer to winter in Newell's data as compared to a 10% decrease in static stability.

The energy balance model predicts the static stability is twice as sensitive to changes in the radiative forcing as the vertical shear (see Fig. 3.13). With stronger radiative forcing the increased static stability will reduce  $\mu L$  and  $\bar{U}$  which acts to decrease the strength of the westerly current. Referring to eq. (4.2.3), the vertical shear term in brackets dominates near the center of the channel and causes  $\frac{\partial \bar{u}'v'}{\partial y}$  to be negative. The enhanced static stability will act to decrease this term and weaken the convergence and the westerly current. Again the importance of understanding the controlling mechanisms of the static stability is demonstrated.

The structure of the barotropic flow as measured by  $\mu L$  remains relatively unchanged in these calculations. The ratio of horizontal scales

$$\mu L \sim \left( \frac{L f_0}{N_s d} \right) \left( \frac{N_s C_D}{f_0} \right)^{1/2}$$

remains large provided the mixing length of the eddies,  $N_s d / f_0$ , is less than planetary scale and friction is sufficiently strong. If the eddy scale was larger than  $L$ , then basic assumptions in the model's development

would not be valid.

In summary, a model was developed that includes the two largest components in the vertically integrated momentum balance, surface stress and horizontal transport by transient eddies. After finding the thermal field from either observations or an energy balance model, we can determine the mixing properties of the baroclinic eddies. The approximate conservation of potential vorticity and entropy places constraints on the momentum flux divergence which must be balanced by surface stress. The barotropic flow or surface wind distribution consistent with these constraints is then determined.

When using observed thermal field data, the model crudely simulates the strength and distribution of the barotropic flow. Its use in climate studies should be more accurate than Green's original formulation because it accounts for the effect of horizontal and vertical eddy scales on the mixing properties. Sophisticated versions would allow latitude-dependent mixing coefficients and less idealized structures in the baroclinic flow.

CHAPTER V  
JOVIAN DYNAMICS

1. Observations and Theories

In this section we will examine the importance of asymmetric motions in maintaining the Jovian zonal circulation. The latitudinal structure of the mean zonal winds as observed by the Voyager I spacecraft is shown in Fig. 5.1. Prior to spacecraft exploration, the major currents had been measured by earth-based tracking of large-scale cloud disturbances. These jets have remained essentially steady over decades of observations.

Improved resolution of the zonal flow has been provided by the Voyager photographs by following cloud features as small as 100-200 km (Beebe, et al, 1980). The zonal flow is axisymmetric to within 10-20  $\text{m sec}^{-1}$ . The curvature,  $\frac{\partial^2 \bar{u}}{\partial y^2}$ , and the planetary vorticity gradient,  $\beta$ , are also shown in Fig. 5.1. near extremes in the wind profile. As noted by Ingersoll et al (1979), most of the jets easily satisfy the necessary criterion for barotropic instability.

The zonal flow is correlated with alternating light and dark zonal cloud bands. Westerlies usually occur on the equatorward edges of dark "belts" and adjoining poleward edges of light "zones", while easterlies are found on the poleward edges of the belts (see Fig. 5.2). Because the Rossby number of the zonal flow indicates the jets are geostrophic to within a few degrees of the equator, we find from geostrophic balance:

$$\frac{\partial \bar{u}}{\partial y} = -\frac{1}{f_0 \rho_s} \frac{\partial^2 \bar{p}}{\partial y^2} .$$

Therefore, the cyclonic (anticyclonic) horizontal shear in the belts (zones) must be associated with relatively low (high) pressure. This correlation has been interpreted as convergence and sinking motion in

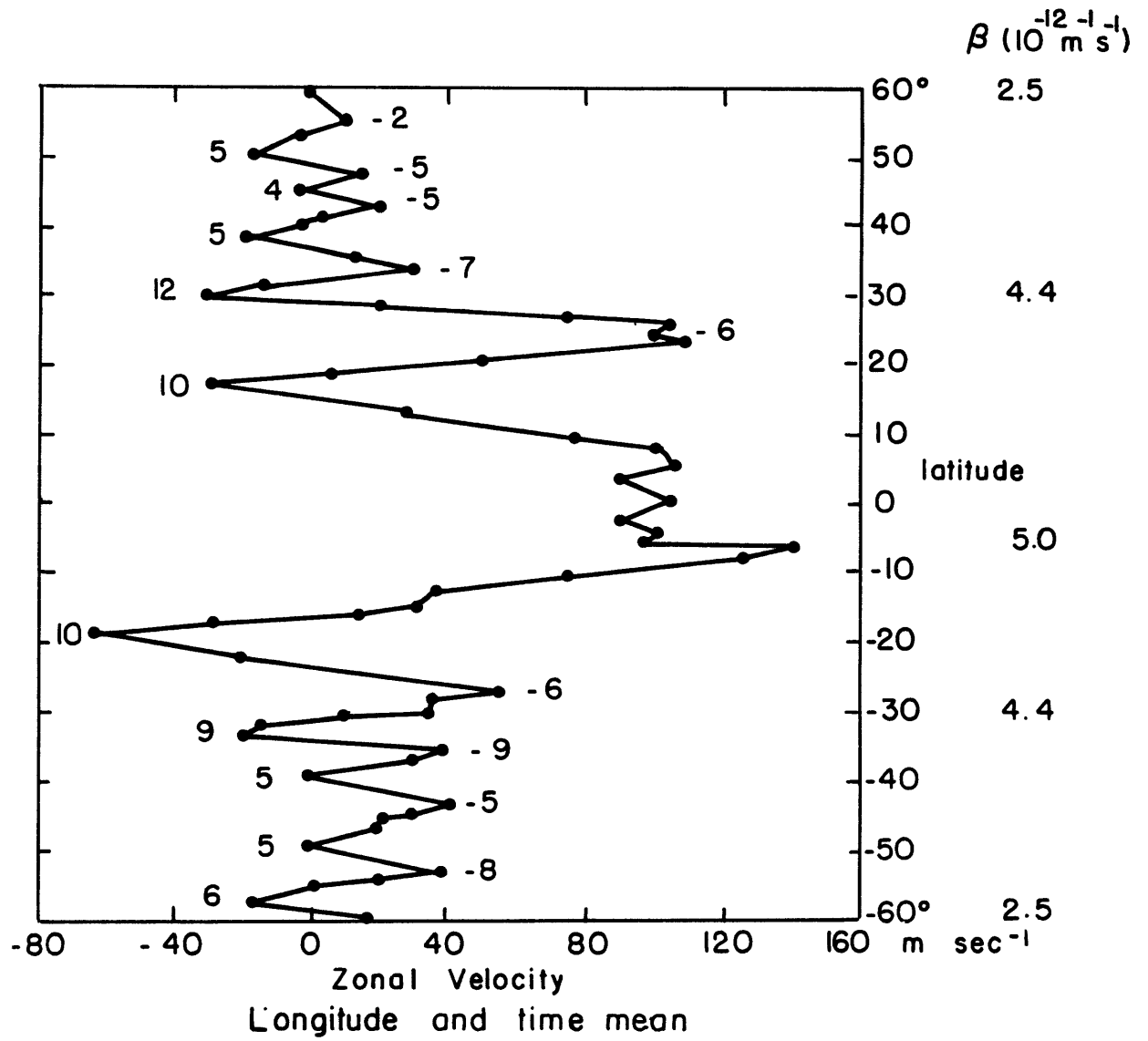


Fig. 5.1. Zonal velocity as observed by Voyager I (from Beebe et al, 1980). Values of  $\beta$  shown at right. Vorticity gradients ( $10^{-12} \text{m}^{-1} \text{s}^{-1}$ ), shown for selected jets, are measured by finite differencing across  $5^\circ$  spans centered on jets.

relatively cloudless belts and divergence and rising motion in cloudy zones (Hess and Panofsky, 1951). Poleward and equatorward meridional flow away from the zones would drive westerlies and easterlies through Coriolis torques. This traditional explanation of the observed flow and cloud bands is represented in Fig. 5.2.

Ingersoll and Cuzzi (1969) used the thermal wind relation to find the meridional structure of vertical mean temperature below the visible clouds. By assuming a level of no motion at some unspecified deep level, they found the zones were relatively warm and further concluded the zone-belt temperature differences dominate any planetary scale variation. They also suggested barotropic instability acts as a controlling mechanism on zonal jets driven by thermally direct meridional cells.

Energy sources for thermally direct circulations have been suggested by a number of authors:

Barcilon and Gierasch (1970) - condensational heating.

Gierasch (1973) - differential infrared cooling caused by thermal blanketing in cloudy zones.

Williams and Robinson (1973) - large-scale, free convection driven by internal heat source.

Flasar and Gierasch (1978), Hathaway et al (1979) - forced convection driven by internal and solar heating.

Symmetric baroclinic instability of meridional temperature gradients was suggested by Stone (1967, 1971) as another means of generating the zone-belt structure.

On the basis of angular momentum conservation it is evident the zonal jets are not the result of frictionless, axisymmetric circulation. Fig. 5.3

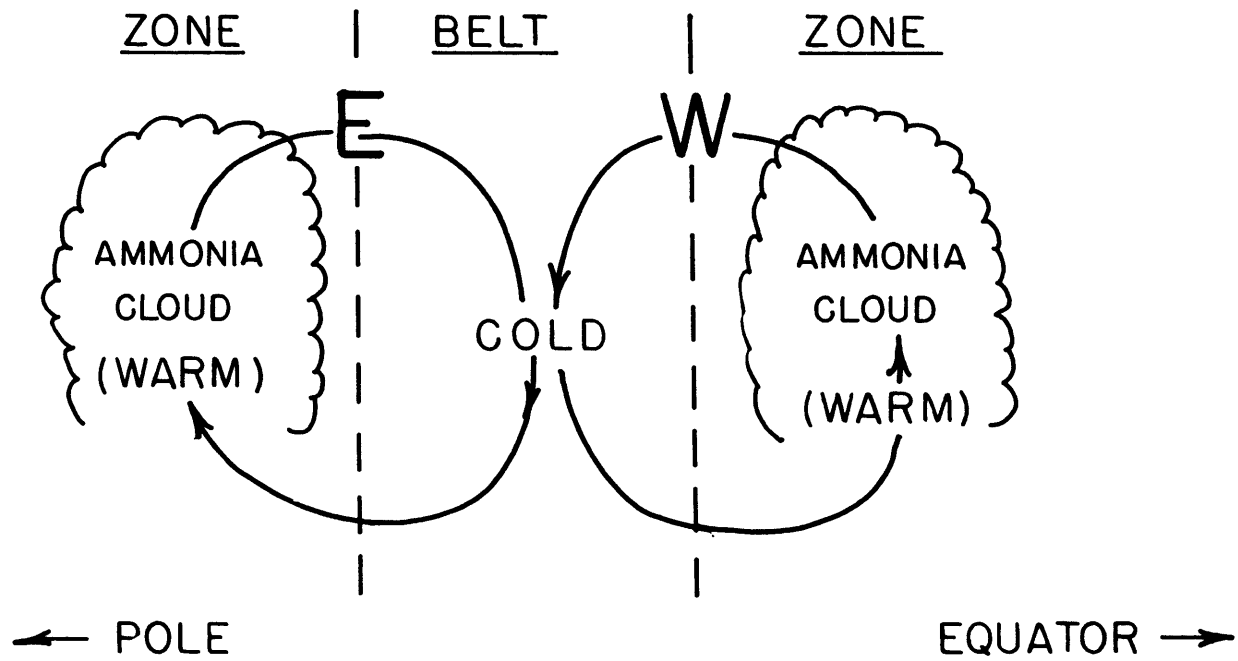


Fig. 5.2. Traditional view of zone-belt structure as thermally direct cells. Regions of generally easterly and westerly flow are indicated by E and W.

shows the zonal velocities that would develop if an initially motionless parcel is displaced poleward from either the equator or  $10^\circ$  lat., conserving angular momentum. The zonal velocity of the parcel becomes much larger than the observed currents after displacing it by a few degrees of latitude. Other mechanisms such as friction or asymmetric eddy fluxes must be important in the momentum balance.

The 200 mb zonal winds within  $10^\circ$  lat. of the terrestrial equator are near values expected from angular momentum conservation in the poleward branch of the Hadley cell. Horizontal eddy flux divergence becomes important in the momentum balance poleward of  $10^\circ$ . On Jupiter the influence of eddy fluxes must be at least as great. Frictional stress is expected to be small on Jupiter as the surface, if any exists, is thousands of kilometers beneath the visible cloud deck.

Following cloud features to determine  $\bar{u}$  also permits an estimate of  $\overline{u'v'}$ , the eddy momentum flux (Beebe et al, loc. cit.). A statistically significant, positive correlation between  $\overline{u'v'}$  and  $\frac{\partial \bar{u}}{\partial y}$  was found from the Voyager I observations. While the observations of flux were made over only 3 Jovian rotations, they were taken across most latitudes ( $60^\circ\text{N}$ - $60^\circ\text{S}$ ). During the observational period it is clear that barotropic instability is not controlling the jet strength. In fact, the conversion from eddy to zonal mean kinetic energy is sufficient to double the zonal mean energy in 50 terrestrial days. Without considering energy destroying mechanisms, only a rapid, global reversal of the eddy fluxes would prevent the zonal currents from reaching unobserved strength.

It is worthwhile to compare three time scales relevant to the maintenance of the Jovian general circulation. Terrestrial values are given in parentheses for comparison.

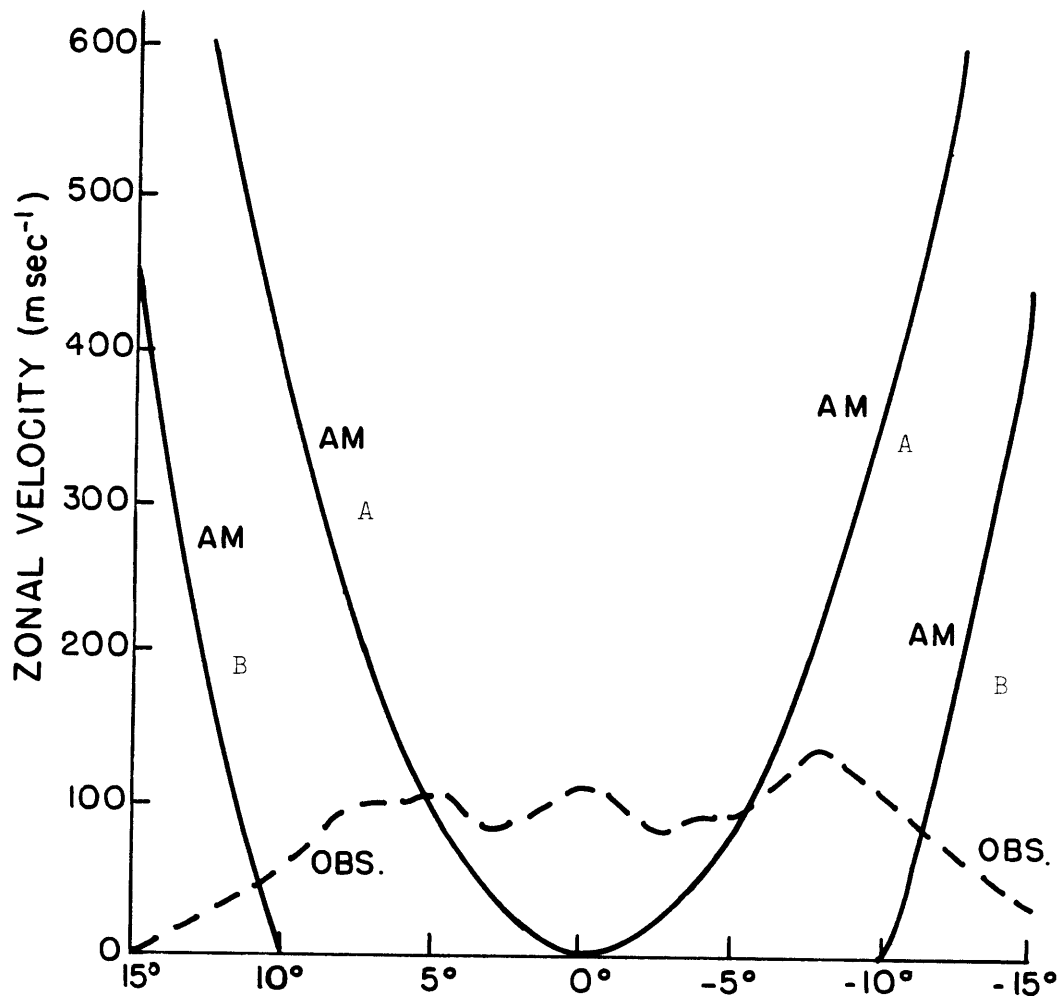


Fig. 5.3. Zonal velocity (AM) of a parcel displaced poleward from Jovian equator (A) or  $10^\circ$  (B), conserving angular momentum. Observed zonal flow near equator (dashed) from Fig. 5.1 is also shown.

$$\text{Dynamical (Eddy): } \tau_D \sim \bar{K} / C(K', \bar{K}) \sim 4 \times 10^6 \text{ sec } (2 \times 10^6 \text{ sec})$$

$$\text{Radiative: } \tau_r \sim 3 \times 10^8 \text{ sec } (2 \times 10^6 \text{ sec})$$

$$\text{Frictional: } \tau_f \sim \frac{H^2}{\nu} \sim \frac{(20 \times 10^5 \text{ cm})^2}{10^4 \text{ cm}^2 \text{ sec}^{-1}} \sim 4 \times 10^8 \text{ sec } \left( \frac{\bar{K}}{D(\bar{K})} \sim 4 \times 10^6 \text{ sec} \right)$$

The dynamical time scale is measured by the ratio of zonal mean kinetic energy,  $\bar{K}$ , to the eddy conversion rate,  $C(K', \bar{K})$ . The radiative time, as calculated by Gierasch and Goody (1969), is for near cloud top level on Jupiter. Because the Jovian atmosphere at this level is opaque in the infrared,  $\tau_r$  will depend on the square of the vertical wavelength of a perturbation. A wide range in the relaxation time is expected from  $10^6$  sec for vertical scales of 1 km to  $10^{10}$  sec for 100 km. To calculate Jovian and terrestrial time scales above we have assumed a vertical scale on the order of the density scale height.

The frictional time scale represents the action of scales smaller than those motions used in measuring  $C(K', \bar{K})$ . This time scale has an uncertainty of a few orders of magnitude. Here it is calculated using a viscosity appropriate for the terrestrial upper atmosphere. The frictional scale for Jupiter should represent vertical transfer between active upper layers and deeper, denser lower layers. Unless the motions are driven from below, the deep atmosphere should create a frictional drag on the upper layers similar to an oceanic surface but without the abrupt density change. The terrestrial friction is based on the dissipation of zonal mean kinetic energy.

Wide separation between dynamical and dissipative time scales is found for Jupiter unlike the Earth. For the terrestrial general circulation dissipation plays an immediate role in balancing net eddy

generation of zonal kinetic energy. On Jupiter a near-balance between generation by eddies and destruction by mean meridional circulation is probably occurring. Wave-mean flow interaction theorems may have direct application to Jovian dynamics. This dynamical quasi-equilibrium has terrestrial counterparts in the mid-latitude upper troposphere where dissipation (radiative or frictional) is small. As mentioned in Chapter IV, momentum transports by large-scale eddies are largely balanced by the Coriolis torque of mean circulations in stability analyses and observations.

An estimate of the mean cell strengths required to balance the eddy flux divergence can be made from the momentum balance equation,

$$\bar{v} \frac{\partial \bar{u}}{\partial y} + \bar{w} \frac{\partial \bar{u}}{\partial z} - f\bar{v} + \frac{\partial}{\partial y} \overline{u'v'} + \frac{\partial}{\partial z} \overline{u'w'} + F = 0$$

where  $F$  = frictional deceleration. For geostrophic flow the mean cell transport of relative momentum (first two terms) will be small relative to the Coriolis torque. From quasi-geostrophic theory we expect the vertical eddy transport to be  $O(Ro)$  smaller than the horizontal flux. The lowest order balance is:

$$-f\bar{v} + \frac{\partial \overline{u'v'}}{\partial y} + F = 0$$

From the observations of Beebe et al. we know that

$$\frac{\partial \overline{u'v'}}{\partial y} \sim \frac{75 \text{ m}^2 \text{ sec}^{-2}}{L_y}$$

where  $L_y$  is the meridional scale of the flux divergence and the zonal currents and is about 6000 km. In instances of weak friction, this implies a mean meridional wind,  $\bar{v}$ , of the order of  $10 \text{ cm sec}^{-1}$  at  $30^\circ$  lat. From the mass conservation the vertical velocity of the mean cells will be of the scale  $|\bar{v}| \frac{H_m}{L_y}$  where  $H_m$  is the depth of the mean cells. For a depth of the density scale height ( $H_m \sim 30 \text{ km}$ ) the vertical velocities are a few tenths of  $\text{mm sec}^{-1}$ . These velocities are an order of magnitude smaller than terrestrial Ferrel cell motions. These potentially quite weak mean circulations would be easily overwhelmed in cloud formation by eddies such as the spiral form clouds seen at the edges of the mid-latitude jets or the equatorial convective plumes.

By equating the sedimentation velocity of liquid droplets and a given upward velocity in the atmosphere, we can estimate the size of the largest cloud particle that can be supported by the mean upward

motion. We assume the ammonia cloud tops where the motions are observed are above levels of condensation (i.e., particle formation). In this case, steady-state cloud mass implies<sup>1</sup>:  $W = w_s / (H/H_c - 1)$  where  $W$  = large-scale upward velocity,  $w_s$  = mass-weighted mean sedimentation velocity,  $H_c$  = cloud mass scale height, and  $H$  = atmospheric mass scale height. The velocity,  $w_s$ , is related to a mean radius,  $\bar{r}$ , by  $w_s = \frac{2g\rho_L}{9\mu} \bar{r}^2$  where  $\bar{r} = \left[ \int_0^\infty r^5 f(r) dr / \int_0^\infty r^3 f(r) dr \right]^{1/2}$ ,  $f(r)$  = distribution of particle radii,  $\mu$  = gas viscosity, and  $\rho_L$  = mass density of droplet. This is the Stokes drag formula which will be accurate for pressures greater than 1 mb and will be applied to ammonia cloud tops at several hundred mb. The cloud mass scale height is unknown, though cloud models (Lewis, 1969) indicate  $H_c$  is 2-3 km.

Then the expression for  $W$  is approximately

$$W \approx \frac{H_c}{H} w_s = \frac{2H_c g \rho_L}{9H\mu} \bar{r}^2$$

which can be rewritten as  $\bar{r} \approx \left[ \frac{9H W \mu}{2H_c g \rho_L} \right]^{1/2}$ .

The velocity,  $W$ , is estimated from the scaling analysis of the momentum balance, namely  $W \sim 5 \times 10^{-2} \text{ cm sec}^{-1}$ . The estimate for  $\bar{r}$  will have less than an order of magnitude error if  $WH/H_c$  is known to a factor of 100. For parameters appropriate to the ammonia clouds and hydrogen (the main atmospheric constituent) at 170° K.,  $\rho_L = .7 \text{ gm cm}^{-3}$ ,  $\mu = 6 \times 10^{-5} \text{ gm cm}^{-1} \text{ sec}^{-1}$ ,  $H/H_c = 10$ , we find  $\bar{r} = 28 \text{ } \mu\text{m}$ .

The actual particle size in the ammonia clouds is not known. However, Sato and Hansen (1979) state the particles in the cirrus haze must be at least

<sup>1</sup> Prinn, R. G., 1974: Venus: Vertical transport rates in the visible atmosphere. J. Atmos. Sci., 31, 1691-1697.

1  $\mu\text{m}$  in diameter to fit reflection data. On the basis of cloud particle physics, Rossow(1978) estimates the cloud particles in the main ammonia cloud must be at least 10  $\mu\text{m}$  in radius. Therefore, the mean vertical motion is adequate to support particles above the lower limit of size estimates. Of course, upward motion in turbulent eddies would be expected to support larger particles.

The direction of the meridional flow required to balance the eddy flux divergence observed in the cloud features is in the opposite direction of the traditional view of Fig. 5.2. Convergence must be occurring at visible levels in the zones. The weakness of the mean meridional flow makes it impossible to observe in the presence of the rapidly moving currents and turbulent eddies. Only indirect methods of inferring the mean cell structure and circulation will be possible.

Destruction of  $\bar{K}$  by the mean circulation requires rising (sinking)

in relatively cold (warm) air. Infrared measurements from Pioneer and Voyager indicate the upper troposphere above zones is relatively cold compared to the surroundings. Thus, if convergence and upward motion were occurring in and above the visible layers of the zones, the destruction of  $\bar{K}$  would be accomplished in the vertical column.

This circulation is consistent with the cloud structure determined by Sato and Hansen (1979) who analyzed the solar reflection spectrum of Jupiter. They concluded an ammonia cirrus haze exists in the upper troposphere over zones with much thicker ammonia clouds at deeper levels in belts and zones. The presence of the cirrus would be partly responsible for the lighter appearance of the zones. They suggested on the basis of the cloud structure that the mean circulation might have the two cell structure shown in Fig. 5.4. Tops of the main cloud layer in the zones are somewhat below the tops in the belts and Sato and Hansen suggest a reverse cell at those levels.

It is uncertain which cloud layers are tracked during wind measurements. Since visible disturbances are probably the result of eddy vertical motion and condensation, this level may be somewhat higher than the average cloud top. It is also likely most of the easily observed disturbances are viewed at the top of the main ammonia cloud deck, not in the thin haze layer. Thus the zonal wind and eddy momentum flux is probably measured near the level of meridional flow from belt to zone shown in Fig. 5.4. Mean sinking motion in the lower cell of the zone would be consistent with the destruction of  $\bar{K}$  if layers below the observed motions were relatively warm in the zones as suggested by Ingersoll and Cuzzi (1969).

In summary it is possible to construct thermally indirect mean

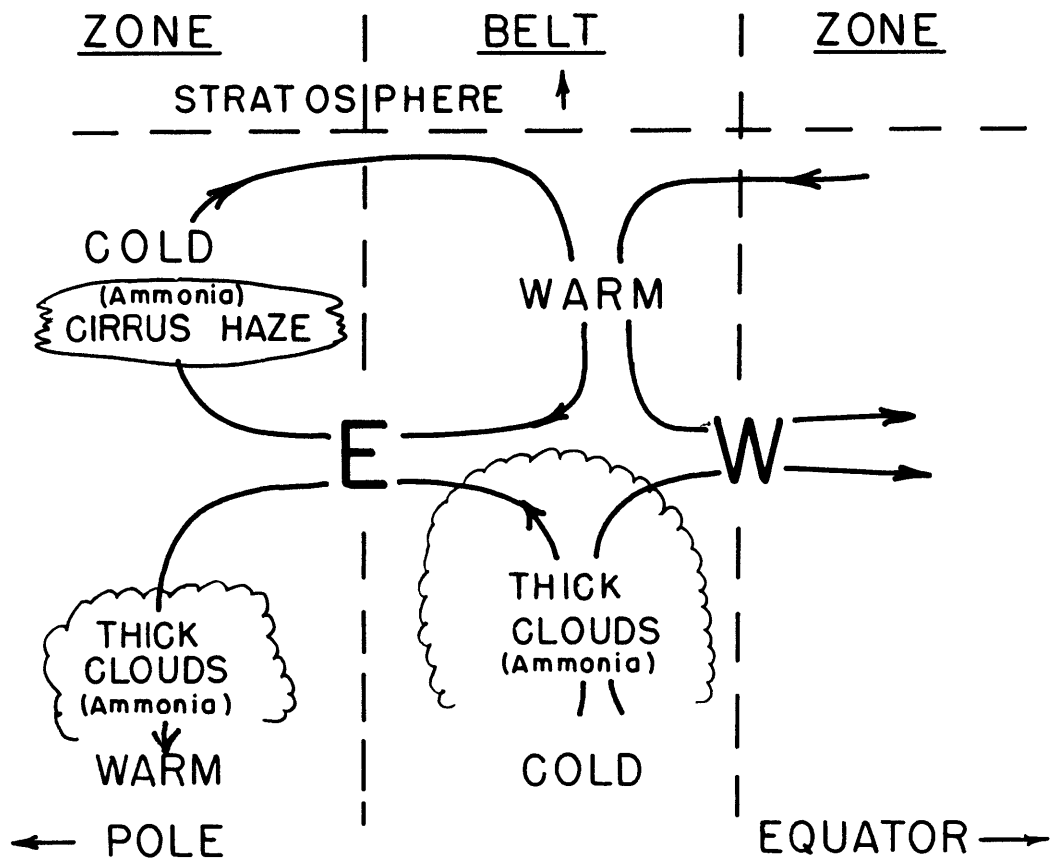


Fig. 5.4. Indirect circulation as an alternative to the traditional view of Fig. 5.2. Cloud structure shown here was suggested by Sato and Hansen (1979) who analyzed solar reflection spectrum. Regions of easterly and westerly flow are indicated by E and W. Relatively cold air over zones is indicated by infrared emission. Thermal wind balance indicates zones are relatively warm below the visible cloud deck.

meridional circulations which are consistent with inferred cloud structure, zonal flow and eddy transport, and infrared observations. The energy source which maintains the circulation against weak dissipation remains undetermined. The planet has a deep internal heat source which provides  $.67 \pm .13$  times as much energy as absorbed solar radiation (Hanel et al, 1980). The deep interior must be convective but the latitudinal distribution of the vertical transport is unknown. Since the thermal emission indicates only 5 degrees difference in effective temperature between low and high latitudes, it has been suggested that the deep convection transports heat more effectively at high latitudes (Ingersoll, 1976).

Since solar radiation is primarily absorbed in the vicinity of the cloud system, a considerable portion of the emitted thermal radiation has its energy source in a comparatively thin layer. As with the terrestrial and Martian atmospheres, the differential solar heating can provide a source of kinetic energy through baroclinic conversion. One objection to the importance of baroclinic instability has been the apparently weak planetary scale temperature gradient and the dominance of the zone-belt structure.

If we repeat the calculation of Ingersoll and Cuzzi (1969) for the meridional temperature structure using the Voyager wind profile of Fig. 5.1, we find the meridional temperature profile of Fig. 5.5. A level of no motion is assumed at an unspecified number of scale heights below the level of the observed winds. Fig. 5.5 shows the vertical mean temperature difference between a particular latitude and the equator based on the meridional integration of the thermal wind relation. The magnitude of the difference is inversely proportional to the depth of

the layer of non-zero shear. Profiles for layers that are one and three scale heights deep are shown in Fig. 5.5. One scale height is about 30 km at these levels.

It is immediately evident from Fig. 5.5 that the planetary scale variation is larger than the zone-belt differences. The zones (belts) appear as warm (cold) perturbations on a planetary-scale structure with the largest zone-belt amplitude occurring at low latitudes. This disagrees with the widely-accepted conclusion of Ingersoll and Cuzzi (1969) that the zone and belts dominate the thermal wind profile.

The meridional variation of infrared brightness temperatures at 20  $\mu\text{m}$  and 45  $\mu\text{m}$  is also shown in Fig. 5.5 as they were measured by Pioneer 10 and 11 (Ingersoll, 1976). These two bands account for most of the infrared emissions. At 45  $\mu\text{m}$  the thermal emissions are dominated by the zone-belt structure at low latitudes. The planetary-scale gradient is weak and the zones, which appear as warm perturbations in the thermal wind profile, are relatively cold as measured by infrared emission. It is important to note that the thermal emission comes from above the cloud decks, while the thermal wind profile would represent the vertical mean temperature below the cloud tops.

Unless the layer over which the vertical shear occurs is at least 10 scale heights or 300 km deep, the planetary-wide temperature difference as deduced from the wind profile will be larger than the difference indicated by thermal emissions. A layer of this thickness is about 5 times deeper than the cloud system of the solar composition model of Lewis (1969). Lewis' model predicts a thick water cloud deck at levels below the observable ammonia clouds. Its presence is confirmed by Sato and Hansen (1979) who find an optically thick cloud with a top about 1-2 scale heights below the ammonia clouds. Therefore, we expect

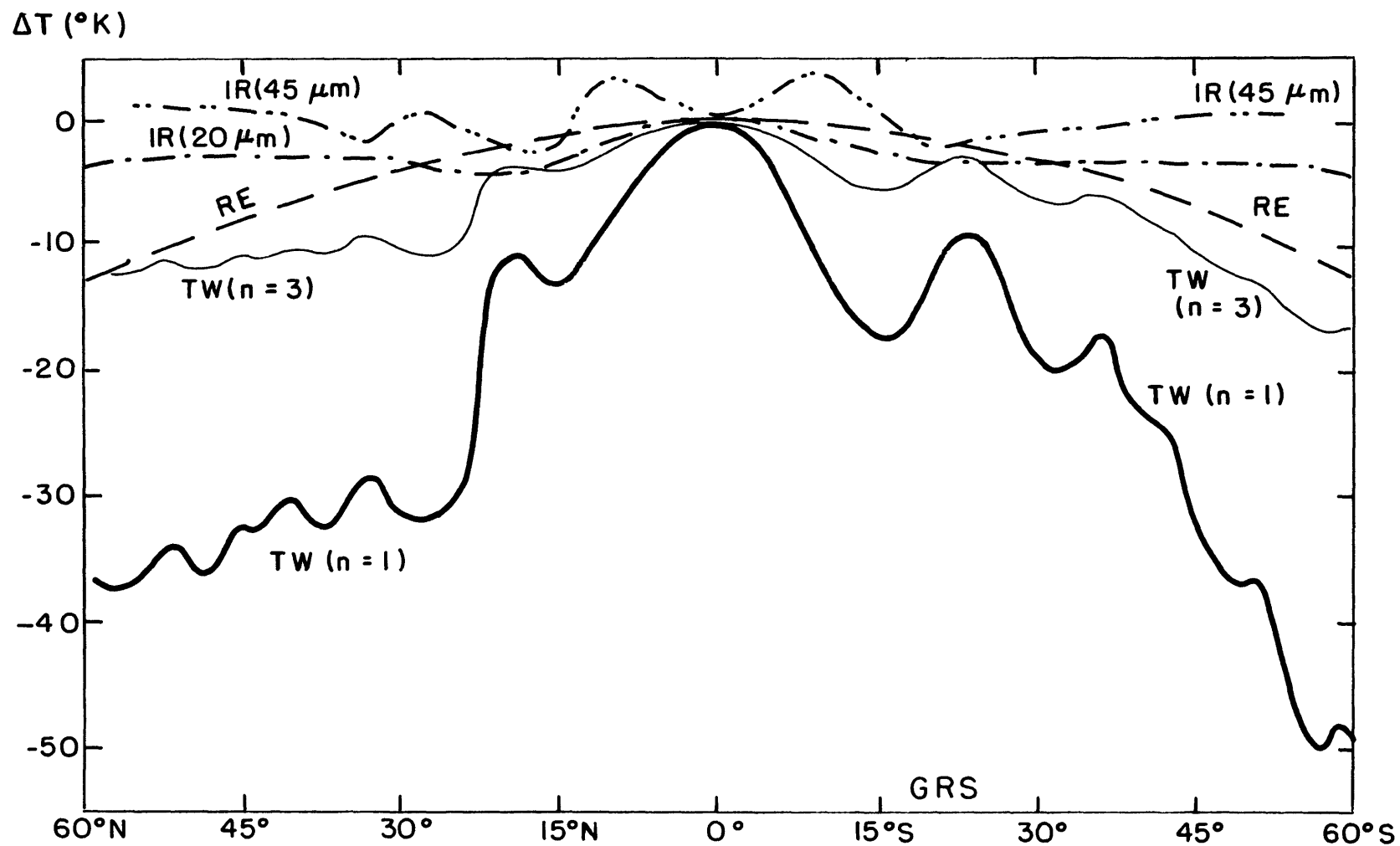


Fig. 5.5. Meridional temperature profiles derived from thermal wind balance (TW) for layers of 1( $n=1$ ) and 3( $n=3$ ) scale heights deep, infrared emissions (IR) at 20 and 45  $\mu\text{m}$ , and radiative equilibrium (RE).

most of the solar absorption and vertical shear to occur within the ammonia and water cloud system.

Two explanations of the discrepancy between thermal emission and wind profiles are offered. First, it is possible that the easterly currents are not easily observed. Only if they are underestimated by a factor of 3-5 would the planetary-wide gradient as seen in Fig. 5.5 be eliminated and the zone-belt structure become dominant. No current observational evidence lends support to this hypothesis, but it should not be discarded as we have no direct data on zonal flows.

Another interpretation is that significant meridional temperature gradients occur across constant pressure surfaces below the cloud tops, even though thermal emissions from higher levels are fairly constant over the planet. For example, the terrestrial subtropics annually emits more infrared radiation than the tropics (Vonder Haar and Suomi, 1971) even though those latitudes are colder than the tropics through most of the troposphere. Because the subtropical atmosphere contains less water vapor, the outgoing radiation comes from higher pressures and temperatures. For similar reasons the earth's annual mean effective temperature differs by 20°K between pole and equator whereas the lower tropospheric temperature difference is 40°K. Dynamical transports act to reduce the infrared gradient.

A similar situation may be occurring on Jupiter as suggested by Gehrels (1976) who concludes from polarimetry data that cloud tops in polar regions are deeper in the gaseous atmosphere. Infrared cooling from cloud tops will be important on Jupiter, compensating for the lack of solid surface blackbody emission. Therefore, infrared radiation at high latitudes would be originating from deeper, warmer levels. At an

adiabatic lapse rate of  $2^{\circ}\text{K}/\text{Km}$ , the effective emission level need only be a half scale height deeper at high latitudes to compensate for a  $30^{\circ}\text{C}$  temperature decrease from the equator along a constant pressure surface. Furthermore, the thermodynamic properties of the condensate will maintain relatively small temperature differences between cloud tops at various latitudes and thermal emission will be fairly constant over the planet.

It is also interesting to compare the thermal wind and infrared profiles in Fig. 5.5 with a radiative equilibrium structure. Fig. 5.5 shows the profile of the effective temperature expected from radiative equilibrium with a latitudinally uniform internal heating of .67 times the solar absorption. The difference between a particular latitude and the equator is found from Stone's (1972) eq. (3.10) for radiative equilibrium on Jupiter. The difference between the equator and pole is  $30^{\circ}\text{K}$  with 60% of the difference occurring between  $60^{\circ}$  lat. and the pole. With the assumption that the internal heating is uniform, the strongest temperature gradients are expected at the highest latitudes where the infrared data is least certain.

The thermal wind profile for a layer of three scale heights thickness, or about the depth of Lewis' cloud system, has a meridional structure similar to the assumed radiative equilibrium structure. This agreement suggests the internal heating does not greatly differ from a uniform meridional distribution. The implied deficit in radiative heating at high latitudes must be balanced by poleward dynamical transports as in the terrestrial atmosphere.

Substantial temperature gradients along pressure levels below the visible cloud tops need not be inconsistent with weak variations in thermal emissions which originate at higher levels. Therefore, the

importance of baroclinic instability to Jovian dynamics cannot be ruled out on the basis of the thermal emission profiles. In fact, because the observable eddies are feeding energy into the jets, the likelihood of baroclinic instability is enhanced. The influence of baroclinic eddies on the Jovian circulation has been considered by Stone (1967, 1972) and Williams (1979). Stone (1972) examined a radiative-dynamical model of baroclinic transports as discussed in Chapter III.

Williams used a two-level, quasi-geostrophic,  $\beta$ -plane model driven by fixed, weak differential heating. Periodically the model flow became baroclinically unstable and the baroclinic modes transferred energy into barotropic jets. As the meridional temperature gradient fell below the critical value, the flow entered a stable phase in which the jets were essentially steady until the differential heating re-established the vertical shear. The model presents another manner in which series of east-west currents can be generated by baroclinic stability. In the momentum balance model of Chapter IV, the baroclinic eddies formed barotropic currents because the entropy and potential vorticity transports by a single wave forced constraints on momentum fluxes in balance with surface stress. In William's model the baroclinic eddies transferred energy into barotropic modes of larger scales through nonlinear interactions.

One of the difficulties of studying baroclinic instability on Jupiter is understanding the influence of deep layers. Williams, for example, specified the static stability and, therefore, the instability scale. As indicated in Chapter III the static stability and shear are likely to be determined by a combination of dynamic and radiative transports. Furthermore, the vertical variation of these quantities will be very

important in the behavior of baroclinic eddies and the cloud model of Lewis (1969) suggests considerable structure in the static stability through condensation.

To examine the influence of the vertical variation of shear and static stability on baroclinic instability, an Eady-type model is examined in the following section. Applications will be made to the Jovian atmosphere, but the theoretical results will be important for general geophysical fluid systems with vertical structure.

Neglecting the  $\beta$ -effect will be reasonable for baroclinic waves on Jupiter. Its importance is measured by

$$\frac{\beta L_x^2}{U} \sim \frac{\beta N^2 H^2}{U f_0^2} \sim \gamma$$

and in the Jovian troposphere, the most stably stratified region should be in the water clouds where  $N^2 \lesssim 6 \times 10^{-5} \text{ sec}^{-2}$  (Lewis, 1969). For mid-latitudes with  $U \sim 30 \text{ m sec}^{-1}$ ,  $\frac{\beta L_x^2}{U} \lesssim .2$  for this upper bound on  $N^2$ . The energy balance model of Section III-3 also suggests a weak  $\beta$  influence.

## 2. Eady Model with Vertically Varying Shear and Static Stability

In this section we investigate a Boussinesq, f-plane model of baroclinic instability, allowing the vertical shear and static stability to be functions of height. The linearized equations are:

$$\left. \begin{aligned} \frac{\partial u'}{\partial t} + \bar{u} \frac{\partial u'}{\partial x} + w' \frac{\partial \bar{u}}{\partial z} &= f_0 v' - \frac{1}{\rho_0} \frac{\partial p'}{\partial x} \\ \frac{\partial v'}{\partial t} + \bar{u} \frac{\partial v'}{\partial x} &= -f_0 u' - \frac{1}{\rho_0} \frac{\partial p'}{\partial y} \\ \frac{\partial u'}{\partial x} + \frac{\partial v'}{\partial y} + \frac{\partial w'}{\partial z} &= 0 & \frac{\partial p'}{\partial z} &= \alpha \rho_0 g \theta' \\ \frac{\partial \theta'}{\partial t} + \bar{u} \frac{\partial \theta'}{\partial x} + v' \frac{\partial \bar{\theta}}{\partial y} + w' \frac{\partial \bar{\theta}}{\partial z} &= 0 \end{aligned} \right\} \quad (5.2.1)$$

The mean shear and static stability are functions of  $z$  only and  $\alpha$  is a thermal expansion coefficient. Rigid boundaries at which  $W' = 0$  are applied at  $z = 0, H$ . While these boundaries are unrealistic for the deep Jovian atmosphere, they are required for the Boussinesq approximation. The emphasis here is to study the effects of vertically varying static stability and vertical shear.

Use the following scales to non-dimensionalize eqs. (5.2.1):

$$\begin{aligned} (x, y) &= L(x', y') & z &= H z' & \alpha g \frac{\partial \bar{\theta}}{\partial z} &= N^2 B(z) \\ P' &= (\rho_0 N^2 H) P & \theta' &= \left(\frac{N^2 H}{\alpha g}\right) \theta & \bar{u} &= U S(z) \\ (u', v') &= U(u, v) & w' &= \left(\frac{UH}{L}\right) w & t &= \frac{L}{U} t' \end{aligned}$$

and from geostrophic balance,

$$\frac{\partial \bar{\theta}}{\partial y} = -\frac{f_0 U}{\alpha g H} \frac{dS}{dz}$$

Eqs. (5.2.1) become (dropping primes):

$$\left. \begin{aligned} R_0 \left( \frac{\partial u}{\partial t} + S(z) \frac{\partial u}{\partial x} + w \frac{dS}{dz} \right) &= v - R_0 Ri \frac{\partial p}{\partial x} \\ R_0 \left( \frac{\partial v}{\partial t} + S(z) \frac{\partial v}{\partial x} \right) &= -u - R_0 Ri \frac{\partial p}{\partial y} \\ \frac{\partial u}{\partial x} + \frac{\partial v}{\partial y} + \frac{\partial w}{\partial z} &= 0 & \frac{\partial p}{\partial z} &= \theta \\ \frac{\partial \theta}{\partial t} + S(z) \frac{\partial \theta}{\partial x} - \frac{v}{R_0 Ri} \frac{dS}{dz} + w B(z) &= 0 \\ R_0 &= \frac{U}{f_0 L} & Ri &= \frac{N^2 H^2}{U^2} \end{aligned} \right\} (5.2.2)$$

Taking the form of the perturbation as

$$\phi = \Phi(z) e^{i(kx + ly + kct)}$$

we can reduce eqs. (5.2.2) to a single equation in the vertical structure of  $W$  :

$$\begin{aligned}
& [1 - R_0^2 k^2 (c+s)^2] \frac{d^2 W}{dz^2} - 2 \frac{ds}{dz} \left[ \frac{1}{c+s} - i l R_0 \right] \frac{dW}{dz} + \\
& \left[ -B(z) Ri R_0^2 (k^2 + l^2) + \frac{d^2 s}{dz^2} (R_0^2 k^2 (c+s) + i R_0 l) \right. \\
& \quad \left. - \frac{2 i R_0 l}{c+s} \left( \frac{ds}{dz} \right)^2 \right] W = 0
\end{aligned} \tag{5.2.3}$$

with  $W = 0$  at  $z = 0, 1$ . This equation is similar to Stone's (1966) eq. (1.2) which he applied to the non-geostrophic baroclinic instability problem with constant shear and static stability, i.e.  $S(z) = z$ ,  $B(z) = 1$ .

Here we will examine quasi-geostrophic instabilities by neglecting terms with coefficients of  $R_0 k = \frac{2\pi U}{f_0 L_x}$  and  $R_0 l = \frac{2\pi U}{f_0 L_y}$

where  $L_x$ ,  $L_y$  are the zonal and meridional wavelengths. We assume that  $S(z)$  and its derivatives are  $O(1)$  functions and the eigenvalue,  $c$ , is also  $O(1)$ . The bulk Richardson number,  $Ri$ , is presumed large and the term multiplied by  $Ri$  is retained. Then, eq. (5.2.3) becomes:

$$\frac{d^2 W}{dz^2} - \frac{2 \frac{ds}{dz}}{c+s} \frac{dW}{dz} - B(z) \epsilon^2 W = 0 \tag{5.2.4}$$

where  $\epsilon^2 = Ri R_0^2 (k^2 + l^2) = \left( \frac{2\pi NH}{f_0} \right)^2 (L_x^{-2} + L_y^{-2})$ .

We examine waves that are long compared to the bulk radius of deformation,  $\frac{NH}{f_0}$ , so that  $\epsilon^2 \ll 1$ . By assuming  $B(z)$  is an  $O(1)$  function, the waves are also long compared to the local radius of deformation,  $\frac{NH\sqrt{B(z)}}{f_0}$ . Expanding  $W$  and  $c$  in powers of  $\epsilon^2$ ,

$$\begin{aligned}
W &= W_0 + \epsilon^2 W_1 + \dots \\
c &= c_0 + \epsilon^2 c_1 + \dots
\end{aligned}$$

the lowest order equation is:

$$\frac{d^2 W_0}{dz^2} - \frac{2 \frac{ds}{dz}}{c_0+s} \frac{dW_0}{dz} = 0 \tag{5.2.4}$$

$W_0 = 0$  at  $z = 0, 1$ .

The solution of (5.2.4) is:

$$W_0 = \int_0^z [c_0 + s(\eta)]^2 d\eta \quad (5.2.5a)$$

and the expression for the zero order eigenvalue is:

$$\int_0^1 [c_0 + s(z)]^2 dz = 0. \quad (5.2.5b)$$

Solving for  $c_0$ ,

$$c_0 = -u_m \pm \sqrt{u_m^2 - K_m}$$

where  $u_m = \int_0^1 s dz$  and  $K_m = \int_0^1 s^2 dz$ .

For non-zero  $s$ ,  $u_m^2 < K_m$  and the lowest order solution has growing and decaying modes. The phase speed is the vertical mean of the basic state zonal flow. The growth rate is proportional to a vertical mean standard deviation of the mean flow or a difference between the vertical average of twice the kinetic energy and the square of the vertical mean momentum. This standard deviation provides a measure of the instability of the fluid.

The  $O(\epsilon^2)$  equation is:

$$\frac{d^2 W_1}{dz^2} - \frac{2 \frac{ds}{dz}}{c_0 + s} \frac{dW_1}{dz} = - \frac{2c_1 \frac{ds}{dz}}{(c_0 + s)^2} \frac{dW_0}{dz} + B(z) W_0 \quad (5.2.6)$$

$W_1 = 0$  at  $z = 0, 1$ .

If eq. (5.2.6) is multiplied by  $W_0$  and integrated over  $z$ , we can find the next order eigenvalue contribution:

$$c_1 = \frac{\int_0^1 \frac{B(z)}{(c_0 + s)^2} W_0^2 dz}{\int_0^1 \frac{2 \frac{ds}{dz}}{(c_0 + s)^4} W_0 \frac{dW_0}{dz} dz} \quad (5.2.7)$$

The growth rate to two orders is:

$$\sigma_i = k c_{oi} + k \epsilon^2 c_{ii}$$

so that a maximum with  $l = k$  occurs at

$$k_{\max} = \sqrt{\frac{-c_{oi}}{6 R_i R_o^2 c_{ii}}} \quad (5.2.8)$$

It can be shown that the denominator of eq.(5.2.7) is  $2i c_{oi}$

so that

$$k_{\max} = \sqrt{\frac{I}{3}} |c_{oi}| \left[ \int_0^1 R_i R_o^2 B(z) \left( \frac{w_o^2}{(c_o + s)^2} \right)_r dz \right]^{-1/2}$$

or in dimensional terms, this result becomes:

$$L_{x \max} = 2\pi \sqrt{3} \left[ \int_0^1 \frac{N^2 B(z) H^2}{f_o^2} F(z) dz \right]^{1/2} / [K_m - u_m^2]^{1/2} \quad (5.2.9)$$

where  $F(z) = \left( \frac{w_o^2}{(c_o + s)^2} \right)_r$ .

For  $S(z) = z$  and  $B(z) = 1$  which corresponds to Eady's original model, it can be shown that for  $l = k$ ,  $k_{\max} = \left( \frac{5/4}{R_i R_o^2} \right)^{1/2}$  where  $R_i$  is the constant Richardson number of the fluid. The wavelength of this mode is  $L_x = 5.62 \frac{NH}{f_o}$  or within 2% of the exact results of the Eady model (cf. Charney (1973), Ch. 7). For this wavelength the expansion parameter is  $\epsilon^2 = 5/2$ . In a long-wave expansion of the non-geostrophic problem, Stone (1966, 1970) first demonstrated the approximate analytic results for growth rate and most unstable wavelength are quite accurate as compared to exact numerical solutions,

For the general result of eq. (5.2.8), the growth rate at

$k = k_{\max}$  is:

$$\sigma_{i \max} = c_{oi} k_{\max} \left[ 1 - \frac{1}{3} + \dots \right]$$

where the series in brackets indicates the contribution from each order. At least to the first two orders, the terms in the series are the same as in Stone's less complicated profile. The series in his study was an alternating, convergent series which was accurate at the first two orders as mentioned above. As in his example the series here appears to be convergent for any vertical profile of the Richardson number.

To examine the behavior of  $k_{\max}$  or equivalently,  $L_{x_{\max}}$ , as a function of the vertical shear and static stability, we will examine the function  $F$  for some simple profiles of  $\bar{u}$ . The function  $F$  serves as a weighting function, measuring the contribution from each level to a vertical mean radius of deformation. It is clear from the form of  $F$  that no contribution comes from the boundaries where  $w_0 = 0$ . The maximum contributions must come from the interior.

Fig. 5.6 shows  $F$  for three different shear profiles. It is clear from the profiles that the maximum of the weighting function  $F$  occurs in the interior and near levels of maximum shears. Contributions to the weighted mean of static stability will be small in regions of comparatively weak shear. The function  $F$  for  $S(z) = z^3$  is actually very small and negative for  $z < .3$ . This probably does not indicate actual negative contributions in an exact solution, but rather the expansion technique is beginning to lose validity when the derivatives of  $S(z)$  become large. For  $S(z) = z^4$ , the contributions are again very small and negative below  $z = .5$ .

For the profiles presented in Fig. 5.6, the dimensionless mean flow is  $S(z) = z^\alpha$ . For constant static stability throughout the fluid, the growth rate of the most unstable wave increases for increasing  $\alpha$  and

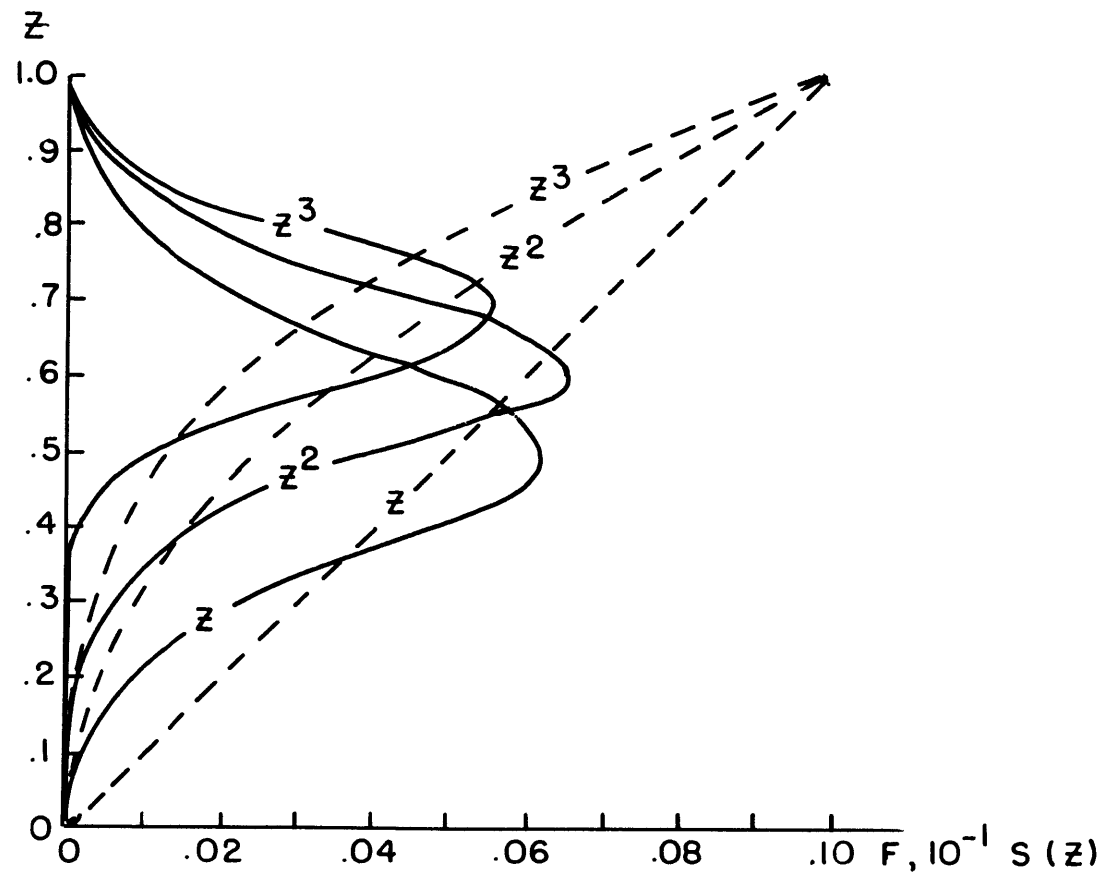


Fig. 5.6. Basic state zonal flow profiles (dashed) and weighting function,  $F$ , (solid) for Eady model of Section V - 2.

the wavelength decreases. This is shown in the table below with  $\sigma_{i_{\max}}$  and  $L_{x_{\max}}$  have been scaled by their values for  $\alpha = 1$ .

$\alpha$	$\sigma_{i_{\max}}$	$L_{x_{\max}}$
1	1.0	1.0
2	1.18	.87
3	1.21	.79

Referring to Fig. 5.6, the integral of the weighting function,  $F$ , decreases as  $\alpha$  increases and contributions are greatest at levels of significant shear. From eq. (5.2.9) with constant  $B(z)$ , we find

$$L_{x_{\max}} \sim \left[ \int_0^1 F(z) \right]^{1/2} / \left[ K_m - u_m^2 \right]^{1/2}.$$

Changes in the denominator as  $\alpha$  varies from 1 to 3 are less than 5%, while the numerator decreases by 22% when  $\alpha$  increases from 1 to 3. This result suggests that the effective depth of the wave is limited to the layer where the shear is significant. For  $\alpha = 1$  the appropriate depth in determining the radius of deformation and, thus, the scale of the wave is the entire depth,  $H$ . For  $\alpha > 1$ , this depth is less than  $H$ .

This interpretation is further clarified by the examination of the lowest order horizontal and vertical heat fluxes:

$$\overline{v' \frac{\partial p'}{\partial z}} \sim \frac{\partial s}{\partial z} \quad \overline{w' \frac{\partial p'}{\partial z}} \sim \frac{\partial s}{\partial z} w_{0i} \sim \frac{\partial s}{\partial z} \int_0^z (u_m - s) dz.$$

The fluxes are proportional to the shear and, therefore, most of the energy conversion will occur in layers of strong shear. The amplitude  $|w_0|$  is given in Fig. 5.7 for the profiles in Fig. 5.6 along with the vertical heat flux structure

$$\overline{w' \frac{\partial p'}{\partial z}} \sim z^\alpha - z^{2\alpha}.$$

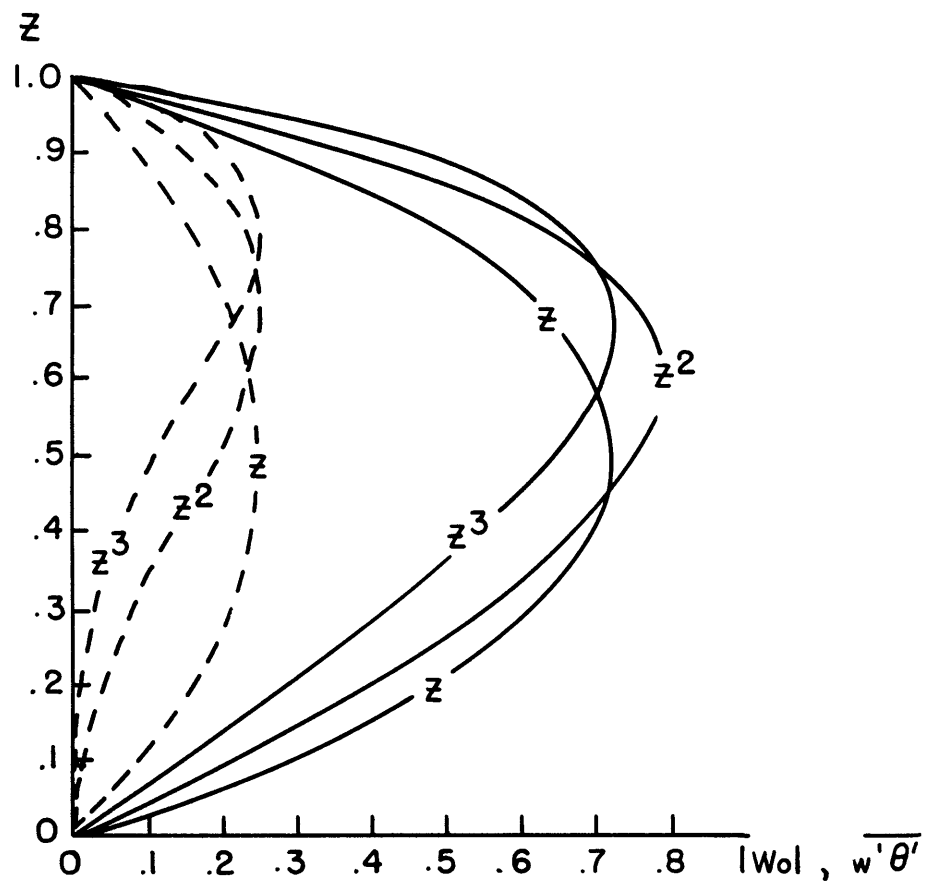


Fig. 5.7. Amplitude  $|w_0|$  (solid) for shear profiles of Fig. 5.6. Vertical heat flux (dashed) for same profiles.

The horizontal heat flux structure is proportional to  $z^{\alpha-1}$ . The maximum wave amplitude shifts upward for increasing  $\alpha$  but the wave still has significant amplitude at low levels. The heat fluxes are greatly reduced in regions of weak shear.

Blumen (1979) found exact solutions to the Eady model for constant linear shear throughout the fluid and static stability that was constant but differing in two layers of unequal depth. Two types of instability were found: long waves which filled the entire fluid with wavelengths determined by the vertical mean radius of deformation and short waves which were confined to the least statically stable layer with length scales of the radius of deformation of that layer. The length scales are similar when the layers are of nearly equal depth and stability. When the static stabilities differ by a factor of two or less, the long wave instability has the larger growth rate regardless of the interface height. The wavenumber and growth rate increase as the depth of the less stable layer decreases and the phase speeds of these modes remains fixed at the basic state of flow at the mid-point of the fluid. This behavior of the long wave instability is also found in the model examined here.

For Blumen's basic state, the most unstable wave from eq. (5.2.9) is proportional to:

$$L_{x \max} \sim \frac{H}{f_0} \left[ N_1^2 \int_0^d F dz + N_2^2 \int_d^1 F dz \right]^{1/2}$$

where  $N_1^2$ ,  $N_2^2$  are the buoyancies of the lower and upper layers with the interface at  $z = d$ . Examining the profile of  $F$  for  $S(z) = z$  in Fig. 5.6, we notice the change in the wavelength for a change in  $d$  will be greatest when  $d$  is near  $z = .5$  rather than near the boundaries. This also seen in Blumen's calculations of the most unstable wavenumber

as a function of  $d$ .

The interface acts a flexible lid for the short wave instability. This unstable mode is not contained in the analysis presented here. In this case the waves are much shorter than the local radius of deformation for regions where the static stability is strong. This requires retention of the term  $\epsilon^2 B(z)$  of eq. (5.2.4) in the lowest order problem, considerably complicating its solution.

The frequent assumption that a stable layer acts as a rigid lid must be treated with caution. The accuracy of such an approximation will depend on both shear and stratification differences between layers and the wavelengths to be examined. For long waves this assumption is expected to be poor. Whether long or short waves will dominate the growth rate spectrum must be determined by the details of the basic state. It is evident from the analysis presented here that the vertical variation of shear will also act as a means of forming an effective lid for baroclinic waves when the static stability variation is small. Blumen (1979) noted the mathematical equivalence of discontinuous static stability and shear for the short-wave instability. This conclusion also applies to the long waves.

The results of the long-wave expansion are now applied to a crude model of the Jovian atmosphere. Suppose the atmosphere consists of an ammonia cloud layer overlying a water cloud of equal depth,  $D \approx 35$  km. Since little information on vertical structure below the cloud tops is known, we assume the shear is constant in the model. Most of the incoming radiation is absorbed at these levels so the shear is likely to be strongest there. Contributions to the wave scale from layers of weaker shear will be less important. The long-wave expression for the most unstable wavelength is:

$$L_{x \max} (l=k) = \frac{75D}{f_0} \left[ \frac{(N_A^2 + N_W^2)}{2} \int_0^1 F(s(z)=z) dz \right]^{1/2}$$

$$= \frac{11D}{f_0} \left[ \frac{N_A^2 + N_W^2}{2} \right]^{1/2}$$

where  $N_A$ ,  $N_W$  are the Brunt-Vaisala frequencies of the ammonia and water cloud layers. The total depth of the model is  $2D$ . The Lewis' cloud model, the mean static stability in each layer is

$$\frac{\partial \theta_A}{\partial z} \approx .05 \text{ } ^\circ\text{K/km} \quad \text{and} \quad \frac{\partial \theta_W}{\partial z} = .25 \text{ } ^\circ\text{K/km}$$

Using expansion coefficients,  $\alpha_A = (170^\circ \text{K})^{-1}$  and  $\alpha_W = (250^\circ \text{K})^{-1}$ , we find  $L_{x \max} \approx \frac{8 N_W D}{f_0} = 8,000 \text{ km}$  at  $30^\circ$  lat.

Since the difference in the static stability is large, Blumen's calculations suggest the short-wave instability will have significant growth rates. In this limit the ammonia cloud layer is considered a single layer bounded by two "rigid lids" formed by the water clouds and stratosphere. The appropriate wavelength is  $L_{x \max} = \frac{5.6 N_A D}{f_0} = 3000 \text{ km}$ .

Wave-like disturbances of these scales are common over the face of the planet. Whether a separation of length scales occurs, as suggested above, is difficult to determine without further data. These estimates are at best tentative, pending further information on the vertical structure. In order to determine if the layers surrounding the visible layers act as rigid lids or contribute to the wavelength calculation, knowledge of the static stability and vertical shear to better than 50% error is required.

The stability analysis lends some justification to Williams (1979) choice of fixing the radius of deformation (i.e., static stability) at terrestrial values in his two-layer Jovian model. However, it is evident that consideration must be given to the vertical structure in

determining the eddy scales. Furthermore, if the presence of condensates is important choosing the unstable wavelength, then the transport of the condensible material must be included in future models.

Following the energy balance model of Chapter III, we can estimate the effect of the long-wave instability on the planetary heat balance. In this example, we will assume that the static stability is determined by condensational rather than dynamical stabilization. The horizontal scale of the baroclinic waves will be chosen on the basis of the cloud model results. Since mean meridional circulations may significantly reduce eddy heat transports, this must be considered an upper bound on the influence of the total dynamical flux.

As in Chapter III, the magnitude of the eddy heat flux is taken as:

$$\overline{v'\theta'} \sim \frac{\partial \bar{u}}{\partial z} D L \frac{\partial \bar{\theta}}{\partial y}$$

where  $L, D$  are the appropriate horizontal and vertical scales of the baroclinic waves. Suppose the flux varies on the planetary scale with a maximum at mid-latitudes, then

$$\frac{\partial^2 \overline{v'\theta'}}{\partial y^2} \sim \frac{-gH}{T_0 f_0} \left( \frac{\partial \bar{\theta}}{\partial y} \right)^2 \frac{L}{r^2} < 0$$

where  $r$  = planetary radius,  $T_0$  = mean temperature,  $D \sim H$  = density scale height ( $\beta$ -effects are neglected). The thermodynamic equation balancing dynamical and radiative fluxes is:

$$\frac{\partial \overline{v'\theta'}}{\partial y} + \frac{\partial \overline{w'\theta'}}{\partial z} \approx \frac{\partial_r \bar{\theta} - \partial \bar{\theta}}{\tau_r} \quad \text{and}$$

finding the  $y$ -derivative and integrating over the depth of the wave's influence,

$$\int_{-D}^0 \frac{\partial^2 \overline{v'\theta'}}{\partial y^2} = \int_{-D}^0 \left( \frac{\partial \bar{\theta}_r}{\partial y} - \frac{\partial \bar{\theta}}{\partial y} \right) \frac{1}{\tau_r} dz.$$

Assuming the expression for  $\frac{\partial^2 \overline{v'\theta'}}{\partial y^2}$  is in terms of vertical averages of the basic state parameters, we find from this scaling analysis:

$$\tau_r \frac{\partial^2 \overline{v'\theta'}}{\partial y^2} \sim -a \left( \frac{\partial \bar{\theta}}{\partial y} \right)^2 \sim \left( \frac{\partial \bar{\theta}_r}{\partial y} - \frac{\partial \bar{\theta}}{\partial y} \right) \quad (5.2.10)$$

with  $a = \tau_r g H L / (T_0 f_0 r^2)$ .

Turning the scale statement (5.2.10) into an equality, we have a simple model for the average meridional temperature gradient, similar to eq. (3.3.8) but with  $\beta = 0$ .

Solving for  $\frac{\partial \bar{\theta}}{\partial y}$ , we find

$$\frac{\partial \bar{\theta}}{\partial y} = \frac{1 - \sqrt{1 - 4a \frac{\partial \bar{\theta}_r}{\partial y}}}{2a} \quad (5.2.11)$$

where the parameter,  $a$ , is proportional to  $L$ .

For  $|a \frac{\partial \bar{\theta}_r}{\partial y}| \gg 1$  or large  $L$ ,

$$\frac{\partial \bar{\theta}}{\partial y} \approx \frac{\partial \bar{\theta}_r}{\partial y} \left( a \frac{\partial \bar{\theta}_r}{\partial y} \right)^{-1/2} \ll \frac{\partial \bar{\theta}_r}{\partial y}$$

and long waves are efficient transporters.

For  $|a \frac{\partial \bar{\theta}_r}{\partial y}| \ll 1$  or small  $L$ ,  $\frac{\partial \bar{\theta}}{\partial y} \approx \frac{\partial \bar{\theta}_r}{\partial y}$  and short waves are ineffective.

With  $H = \frac{RT_0}{g}$ ,  $a = \frac{\tau_r R L}{f_0 r^2}$  and using  $\tau_r = 3 \times 10^8$  sec,  $\frac{\partial \bar{\theta}_r}{\partial y} =$

$-3 \times 10^{-4} \text{ }^\circ\text{K}/\text{Km}$  (from radiative equilibrium in Fig. 5.4),

$R = 4000 \text{ m}^2 \text{ sec}^{-2} \text{ }^\circ\text{K}^{-1}$ ,  $r = 70,000 \text{ km}$ ,  $f_0 = 2.5 \times 10^{-4} \text{ sec}^{-1}$  (45° lat.),

we find  $a \frac{\partial \bar{\theta}_r}{\partial y} = -1.6$ .

With  $L = \frac{8N_w H}{f_0} = 5500 \text{ km}$  (long-wave instability at 45° lat.),

eq. (5.2.11) yields

$$\frac{\partial \bar{\theta}}{\partial y} = .53 \frac{\partial \bar{\theta}_r}{\partial y} = -1.6 \times 10^{-4} \text{ } ^\circ\text{K/km} .$$

This corresponds to an equator-pole temperature difference of  $16^\circ\text{K}$ . This is 4 - 5 times larger than the thermal emission gradient. To obtain an equator-pole difference of less than  $4^\circ\text{K}$  as suggested by infrared measurements, we require  $L \geq r$  or much longer than the observed disturbances.

This upper bound calculation suggests that baroclinic waves are unable to reduce the meridional temperature gradient to an order of magnitude less than the radiative equilibrium gradient. This need not conflict with infrared observations if the baroclinic transport is sufficient to smooth out the thermal emissions. The uniformity of the long-wave radiation does not require the temperature gradient along constant pressure surfaces to be negligible. This is especially true if the energy originates at deeper levels than the thermal emission level as in the terrestrial atmosphere. Weak gradients in the outgoing radiation only require that effective heat transport is occurring with the energy redistributed in the deep interior or in the layers of solar heating.

It is clear that the Jovian circulation cannot be represented by symmetric, thermally direct cells and a complete description requires transports by asymmetric motions. The scales of eddies will be determined by the details of the vertical structure of which we know very little. Whether or not changes in the profiles of shear and static stability are adequate to form effective lids will also influence the nonlinear transfer from energy-converting modes to longer barotropic modes.

This process is important in the driving of jets in Williams' model.

The long dissipation times suggest the eddy fluxes are largely balanced by mean circulations. In this case, weakly dissipative, quasi-equilibrium states may exist, explaining the steadiness of the zonal circulation. Terrestrial equilibrium states in the presence of strong dissipation and radiative and topographic forcing have been found by Charney and Straus (1980). One of two equilibria in their model was characterized by strong zonal flow. Similar studies of the Jovian circulation should clarify the balance between eddies and the mean circulation and their impact of the planetary energy budget and zonal motions.

CHAPTER VI  
CONCLUSIONS AND FUTURE WORK

The perturbation analysis of Chapter II provided relatively simple descriptions of the unstable modes of the classic Charney problem of baroclinic instability. These representations enabled us to examine the vertical structures of these waves and to determine their vertical and horizontal scales without resorting to numerical solutions or complicated exact solutions which require numerical analysis. This method was limited to the short and long Charney modes and the shortest Green modes. However, it could be repeated at neutral curves separating deeper, longer Green modes.

The appropriate measure of the  $\beta$ -effect is given by the dimensionless parameter,

$$\gamma = \frac{\beta N^2 H}{f^2 \frac{\partial U}{\partial z}}$$

The most unstable modes will have horizontal scales of  $\frac{NH}{f(1+\gamma)}$  and vertical scales of  $H/(1+\gamma)$ . The expression for the horizontal scale is a modification of the conventional scale of baroclinic instability which is the radius of deformation,  $NH/f$ .

The  $\gamma$  parameter provides a simple means of determining the adequacy of an  $f$ -plane for the study of baroclinic waves. The success of the Eady model for baroclinic instability is dependent on  $\gamma$  being not larger than  $O(1)$  as found in the mid-latitude atmosphere. Mean flows in which  $\gamma \gg 1$  are also of interest (e.g. Gill et al, 1974) and, in these cases, the scales of baroclinic waves will be greatly influenced by the  $\beta$ -effect. The magnitude of  $\gamma$  will also determine the horizontal and vertical resolution in finite difference models. Clearly, if  $\gamma \gg 1$ , two-level models are unlikely to properly simulate the unstable modes. They should be satisfactory for  $\gamma \lesssim 1$ .

The linear analysis of Chapter II provides the vertical structure of the horizontal and vertical heat fluxes of growing baroclinic waves. These relatively simple functions provide a first approximation to the observed structure of the fluxes. Some disagreement in the horizontal flux is seen in the frictional boundary layer and near the tropopause. It would be a challenging, but informative analytical problem to add near-surface friction and an idealized stratosphere in the Charney model. This would be important in the refinement of parameterizations schemes for use in models of the climate and the upper atmosphere.

Observations of the meridional temperature gradient show that the largest seasonal variation occurs near the surface. The difference in the seasonal variation near the surface and in the mid-troposphere is most pronounced at high latitudes. At these latitudes the baroclinic eddy heat flux remains an important transport through all seasons. Apparently, frictional effects prevent the horizontal transport from adjusting the boundary layer temperature gradient as efficiently as the mid-tropospheric gradient. Therefore, it is likely friction must be included in future modeling to obtain detailed vertical structure of the eddy heat flux and meridional temperature gradient.

Scaling arguments and nonlinear theory suggest a relationship between the length scales and the wave amplitude. A method for parameterizing heat fluxes by growing waves is offered in Chapter III and is based on this relationship. This hypothesis extends the suggestions of Stone (1972) and Held (1978) to a complete range of  $\gamma$ . The parameterization scheme accounts for the vertical and horizontal structure of the fluxes as well as the magnitude. We have seen that the flux magnitude and structure is greatly influenced by a non-zero potential vorticity gradient.

The behavior of the parameterized flux as a function of  $\gamma$  demonstrates that two-level models crudely simulate baroclinic heat fluxes. For  $\gamma > 1$  the parameterized fluxes are weak since the wave motions are restricted to smaller scales by the  $\beta$ -effect. Similarly, the two-level model is stable for  $\gamma > 1$  and no fluxes occur.

The parameterization scheme was used in a symmetric model of the terrestrial atmosphere. It was able to reproduce many features of the observed sensible heat transport by mid-latitude eddies. Its success is not dependent on the adjustment of unknown parameters but rests on the soundness of the basic modeling hypotheses. In the same or modified form the scheme is useful in simple climate models as examined in this thesis.

The modeling scheme also suggests that horizontal and vertical fluxes are very sensitive to the vertical shear or meridional temperature gradient. The process model of Section III-3 which balances radiative heating and baroclinic fluxes demonstrates that the feedbacks determining the vertical stabilization dominate the behavior of the wave scales and transports. For example, changes in the radiative meridional forcing greatly influence the vertical flux and, therefore, the static stability and wave scales.

Dynamical mechanisms controlling the extra-tropical static stability are not well understood. We expect the vertical large-scale eddy flux to be reduced in summer and the stabilization to be dominated by moist convection. In winter with stronger radiative forcing the baroclinic eddies should be important in determining the lapse rates.

This combined response of moist convection and baroclinic eddies was suggested by Stone and Carlson (1979) in their study of observed lapse rates. The details of the feedbacks between these two mechanisms are not

known and likely to be important in determining the total atmospheric response to forced changes. These feedbacks and balances may be studied at various levels of complexity ranging from the symmetric GISS model which includes most dynamical mechanisms to the process model of Section III-3 which includes only radiative forcing and baroclinic fluxes. It is clear that the behavior of the vertical temperature structure will be as important as the horizontal structure in determining the eddy transport properties and their influence on the climatic state.

With further modeling hypotheses we were able to construct a momentum flux parameterization on the basis of the same concepts of eddy mixing. Its limited success in the momentum balance model holds further promise for these modeling techniques. Its application to more complicated climate models such as the symmetric GISS model is anticipated.

The importance of baroclinic eddy transports is not limited to the terrestrial atmosphere. With the lack of significant amounts of water vapor the Martian atmosphere must be dominated by radiative heating and baroclinic fluxes. Its response to forced changes may be determined by the feedbacks discussed in the energy balance model. Without the moderating influence of moist convection we would expect large seasonal variation in static stability.

For Jupiter the eddy momentum transports are evidently important in the maintenance of the zonal circulation. The driving mechanism of the zonal currents is unlikely to be the result of purely axisymmetric motions. Long dissipative time scales suggest the Jovian atmosphere may be in near-equilibrium between the mean circulation and the eddies. Theories that account for such balances in a zonally symmetric, differentially heated fluid should be important in understanding the Jovian circulation.

The traditional view of thermal direct axisymmetric cells need not be the only explanation for the banded structure. Thermally indirect circulations can also agree with several independent observations of the Jovian atmosphere. Because the vertical velocities of the mean meridional circulations may be very weak compared to turbulent eddies or convective plumes, we expect cloud formation to be as much determined by eddy motions as by axisymmetric circulations. Of course, the observations of wave-like disturbances on the planet is only possible through cloud features. The mean circulations may provide a moisture source to eddy motions through large-scale convergence and may be responsible for the formation of haze layers of small particles.

The generation mechanism of Jovian eddy disturbances remains speculative. We have suggested that the weak gradients in infrared emissions do not necessarily require weak meridional gradients of temperature. Baroclinic instability may be occurring in the visible cloud layers and in Chapter V we examined a simple model to determine the wave scales.

Concentrating on the influence of the cloud system, the effects of a very deep, nearly neutral lower layer were neglected. Gierasch et al (1979) have studied the instability of a thin, statically stable layer of linear shear bounded below by a deep, nearly neutral layer of no motion. They found the horizontal wave scales were much longer than the radius of deformation of the upper layer. With a neutral lower layer the most unstable scale is proportional to  $R_u (\delta)^{1/4}$  where  $R_u$  = upper layer radius of deformation and  $\delta$  = ratio of lower to upper layer depths. The same result can be found from the model presented in Chapter V.

Future studies of baroclinic instability must account for the presence of the deep, convective layer, complicated cloud structure, and the

stratosphere. It is possible that statically stable water cloud and stratospheric layers acts as rigid boundaries, trapping baroclinic waves in a middle layer where absorbed solar radiation provides an energy source. The water cloud and deep convective layers may have some influence on the instability scales, depending on the shear and static stability of those layers.

It is clear that the success of theories of the Jovian circulation will depend on obtaining much more data on the mean vertical structure and examining its influence on wave structures. We must determine if treating the observable cloud layer layer as a vertically bounded fluid is valid. Perhaps more subtle methods of accounting for vertical structures must be used in modeling the Jovian circulation.

## Appendix A1 - Higher Orders of the Short-Wave Approximation

Here we will find the eigenfunction and eigenvalue contributions,

$\Psi_1$  and  $c_2$ , for the short-wave expansion of Section II-3. From eq.(2.3.9)

for  $n=1$ , we find:

$$\Psi_1(z) = -G(0; z) \Psi_0 + \int_0^\infty G(s; z) F_1(s) ds. \quad (\text{A1.1})$$

Using (2.3.7), eq.(A1.1) can be rearranged to:

$$\Psi_1(z) = \int_0^\infty F_1(s) [-G(0; z) \Psi_0(s) + G(s; z)] ds$$

and, substituting for  $F_1$ ,  $G$ , and  $\Psi_0$ , this becomes:

$$\Psi_1(z) = -e^{-z} \left[ \int_z^\infty e^{-2s} \left( \frac{1}{B} + \frac{1}{s-1} \right) \left( \frac{1-e^{2z}}{2} + s \right) ds + \int_0^z \left( \frac{1}{B} + \frac{1}{s-1} \right) \left( e^{-2s} \left( \frac{1}{2} + s \right) - \frac{1}{2} \right) ds \right].$$

Evaluation of the integrals yields:

$$\Psi_1(z) = \frac{ze^{-z}}{2B} + \frac{e^{-z}}{2} \ln|z-1| + f(z) + A_1 e^{-z} + \begin{cases} \frac{i\pi}{2} e^{-z} & (\infty > z > 1) \\ \frac{i\pi}{2} e^{z-2} & (1 > z > 0) \end{cases}$$

where  $A_1 = \frac{3}{2} E_i(2) e^{-2} - \frac{1}{2} - \frac{1}{4B} - \frac{i3\pi e^{-2}}{2}$

and  $f(z) = \begin{cases} \frac{e^{z-2}}{2} E_1(2(z-1)) & (\infty > z > 1) \\ -\frac{e^{z-2}}{2} E_i(2(1-z)) & (1 > z > 0) \end{cases}$

with  $E_1(x) = \int_x^\infty \frac{e^{-s}}{s} ds$  and  $E_i(x) = -\text{P.V.} \int_{-x}^\infty \frac{e^{-s}}{s} ds$ .

The integrals with singularities have been evaluated by following a contour that avoids the pole at  $z=1$ .

The eigenvalue contribution,  $c_2$ , is found from (2.3.8):

$$c_2 = c_1 \frac{d}{dz} \Psi_1(0) - \int_0^\infty \Psi_0(z) F_2(z) dz$$

where  $F_2 = -\mathcal{L}_1 \Psi_1 - \mathcal{L}_2 \Psi_0$

$$= \left( \frac{1}{B} \frac{d}{dz} - \frac{1}{z-1} \right) \Psi_1 - \frac{c_1}{(z-1)^2} \Psi_0.$$

We are primarily interested in the imaginary part of  $c_2$  to determine the

fastest growing mode. The imaginary part is:

$$c_{2i} = c_{1i} \frac{d}{dz} \Psi_{1r}(0) + c_{1r} \frac{d}{dz} \Psi_{1i}(0) - \left\{ \int_0^\infty \Psi_0 \left[ \left( \frac{1}{B} \frac{d}{dz} - \frac{1}{z-1} \right) \Psi_1 - \frac{c_1}{(z-1)^2} \Psi_0 \right] dz \right\}_i \quad (\text{A1.2})$$

where  $c_1 = \frac{1}{2B} - e^{-2} \text{Ei}(2) + i\pi e^{-2}$

and  $\frac{d\Psi_1}{dz}(0) = \frac{3}{4B} - 2e^{-2} \text{Ei}(2) + \frac{1}{2} + i\pi 2e^{-2}$ .

The integrals in (A1.2) are evaluated below:

$$c_1 \int_0^\infty \frac{\Psi_0^2}{(z-1)^2} dz = c_1 \int_0^\infty \frac{e^{-2z}}{(z-1)^2} dz = c_1 (-i2\pi e^{-2} + 2e^{-2} \text{Ei}(2) - 1)$$

$$-\int_0^\infty \frac{\Psi_0}{B} \frac{d\Psi_1}{dz} dz = \frac{\Psi_0(0)\Psi_1(0)}{B} = \frac{A_1 + \frac{e^{-2}}{2} (i\pi - \text{Ei}(2))}{B}$$

The evaluation of the imaginary part of the integral

$$I = \int_0^\infty \frac{\Psi_0 \Psi_1}{z-1} dz$$

is more detailed. First, we treat the contribution from the homogeneous

part of  $\Psi_1$ :  $\Psi_{1h} = (A_1 + \frac{i\pi}{2})e^{-z} + \begin{cases} 0 & (\infty > z > 1) \\ -\frac{i\pi}{2}(e^{-z} - e^{z-2}) & (1 > z \geq 0) \end{cases}$

This part of I is:

$$\int_0^\infty (A_1 + \frac{i\pi}{2}) \frac{e^{-2z}}{z-1} dz + \frac{i\pi}{2} \int_0^1 \frac{e^{-z} - e^{-2z}}{z-1} dz =$$

$$(A_1 + \frac{i\pi}{2})(i\pi e^{-2} - e^{-2} \text{Ei}(2)) + \frac{i\pi}{2} e^{-2} (\text{Ei}(2) - E_0 - \ln 2)$$

and the imaginary part is:

$$i \frac{\pi e^{-2}}{2} (6 \text{Ei}(2) e^{-2} - 1 - \frac{1}{2B} - E_0 - \ln 2)$$

with  $E_0 = \text{Euler's constant} = .577\dots$

The contribution from the

particular solution of  $\Psi_1$  is:  $\Psi_{1p} = \frac{ze^{-z}}{2B} + \frac{e^{-z}}{2} \ln|z-1| + f(z)$

which is continuous at  $z=1$  since  $\lim_{z \rightarrow 1^+} [\frac{e^{-z}}{2} \ln|z-1| + f(z)] = \lim_{z \rightarrow 1^-} [\frac{e^{-z}}{2} \ln|z-1|$

$+ f(z)] = (-E_0 - \ln 2) \frac{e^{-1}}{2}$ . The imaginary contribution to I from  $\Psi_{1p}$  is  $\frac{i\pi}{2} e^{-2}$ .

$(\frac{1}{2} - E_0 - \ln 2)$  as found from a half-residue. The entire imaginary part of

$c_2$  is then:

$$c_2 i = \pi e^{-2} [3e^{-2} \text{Ei}(2) - 1 - E_0 - \ln 2] = -.26\pi e^{-2}$$

$$= -.26 c_1 i.$$

## Appendix A2 - Uniform Approximation for Short-Wave Expansion

A direct method for demonstrating short-wave instability is presented here by including the critical layer near  $z = c_0$  (see Section II - 3). The method is similar to that applied to the critical layer instability of Section II - 4 and does not require a contour integration into the complex  $z$  - plane.

We can write eq. (2.3.2) as:

$$\left. \begin{aligned} (z - c_0 - \epsilon c_1 - \dots) \left( \frac{d^2 \Psi}{dz^2} - \frac{\epsilon}{B} \frac{d\Psi}{dz} - \Psi \right) + \epsilon \Psi &= 0 \\ (c_0 + \epsilon c_1 + \dots) \frac{d\Psi}{dz}(0) + \Psi(0) &= 0 \\ \Psi(\infty) &\rightarrow 0 \end{aligned} \right\} \quad (\text{A2.1})$$

where  $\Psi = \Psi_0 + \epsilon \Psi_1 + \dots$

Away from the critical layer near  $z = c_0$  (i.e.  $|z - c_0| \gg \epsilon$ ), we approximate (A2.1) at the lowest order as:

$$\left. \begin{aligned} (z - c_0) \left( \frac{d^2}{dz^2} - 1 \right) \Psi_0 &= \mathcal{L}_0 \Psi_0 = 0 \\ c_0 \frac{d\Psi_0}{dz}(0) + \Psi_0(0) &= 0 \\ \Psi_0(\infty) &\rightarrow 0 \end{aligned} \right\} \quad (\text{A2.2})$$

Around the critical level we define an "inner" variable,

$$\xi = (z - c_0) / \epsilon$$

so that the interior equation is:

$$\left( \xi - c_1 - \epsilon c_2 - \dots \right) \left( \frac{d^2 \tilde{\Psi}}{d\xi^2} - \frac{\epsilon^2}{B} \frac{d\tilde{\Psi}}{d\xi} - \epsilon^2 \tilde{\Psi} \right) + \epsilon^2 \tilde{\Psi} = 0. \quad (\text{A2.3})$$

At lowest order, this becomes:

$$(\mathcal{G}-c_1) \frac{d^2 \tilde{\Psi}_0}{ds^2} = \tilde{\mathcal{L}}_0 \tilde{\Psi}_0 = 0. \quad (\text{A2.4})$$

The upper exterior solution of (A2.2) is:

$$\Psi_0 = e^{-z} \quad (z > c_0)$$

and the lower exterior solution is:

$$\Psi_0 = A_0 e^{-z} + B_0 e^{+z} \quad (z < c_0).$$

These solutions must be matched to the inner solution,

$$\tilde{\Psi}_0 = \tilde{A}_0 \mathcal{G} + \tilde{B}_0$$

in a transition region of  $1 \gg |z - c_0| \gg \epsilon$ . Using the matching and lower boundary conditions, we find:

$$\tilde{A}_0 = 0 \quad \tilde{B}_0 = e^{-c_0}$$

$$A_0 = \frac{c_0 + 1}{e^{2c_0}(c_0 - 1) + c_0 + 1} \quad B_0 = \frac{c_0 - 1}{e^{2c_0}(c_0 - 1) + c_0 + 1}$$

To obtain  $c_0$ , we must continue to higher order.

At  $O(\epsilon)$  the exterior equation is:

$$\mathcal{L}_0 \Psi_1 = \frac{(z - c_0)}{B} \frac{d\Psi_0}{dz} - \Psi_0$$

and for  $z > c_0$

$$\Psi_1 = \frac{e^{z-2c_0}}{2} E_1(2(z-c_0)) + \frac{e^{-z}}{2} \ln(z-c_0) + \frac{ze^{-z}}{2B} \quad (\text{A2.5})$$

where  $E_1(x) = \int_x^\infty \frac{e^{-s}}{s} ds$ .

The homogeneous solution ( $\Psi_0$ )

is deleted from  $\Psi_1$  ( $z > c_0$ ) for convenience. For  $z < c_0$  the solution is:

$$\begin{aligned} \bar{\Psi}_1 = & \frac{-e^{\bar{z}-2c_0}}{2} \text{Ei}(2(c_0-\bar{z})) + \frac{e^{-\bar{z}}}{2} \ln(c_0-\bar{z}) \\ & + \frac{\bar{z}e^{-\bar{z}}}{2B} + A_1 e^{-\bar{z}} + B_1 e^{\bar{z}} \end{aligned} \quad (\text{A2.6})$$

where  $-\text{Ei}(x) = \text{P.V.} \int_{-x}^{\infty} e^{-t}/t \, dt$ .

The inner equation to  $O(\epsilon)$  is:

$$\mathcal{L}_0 \tilde{\Psi}_1 = 0$$

and the solution is:

$$\tilde{\Psi}_1 = \tilde{A}_1 \mathcal{S} + \tilde{B}_1. \quad (\text{A2.7})$$

At this order the lower boundary condition is:

$$c_0 \frac{d\bar{\Psi}_1(0)}{d\bar{z}} + \bar{\Psi}_1(0) = -c_1 \frac{d\bar{\Psi}_0(0)}{d\bar{z}}. \quad (\text{A2.8})$$

For small arguments,  $E_1(x) \approx -E_0 - \ln x$  (Abramowitz and

Stegun, 1971) and matching the upper exterior and inner solutions to

$O(\epsilon)$  requires:

$$\tilde{A}_1 = -e^{-c_0}, \quad \tilde{B}_1 = \frac{e^{-c_0}}{2} (-E_0 - \ln 2 + c_0/B).$$

Matching the lower exterior solution to the inner solution, we find  $c_0=1$

in agreement with the expansion of Section II-3. Using the boundary

condition (A2.8),  $A_1$  and  $B_1$  can be found in terms of  $c_1$ ,

$$A_1 = -B_1 e^2 \quad B_1 = \frac{1}{2} \left( c_1 + \frac{e^{-2}}{2} \text{Ei}(2) - \frac{1}{2B} \right).$$

The interior equation at  $O(\epsilon^2)$  is:

$$\mathcal{L}_0 \tilde{\Psi}_2 = (s - c_1 - 1) \tilde{\Psi}_0$$

and its solution is:

$$\tilde{\Psi}_2 = \frac{e^{-1}}{2} s^2 - e^{-1} (s - c_1) \ln(s - c_1) + \tilde{A}_2 \mathcal{S} + \tilde{B}_2. \quad (\text{A2.9})$$

To match the upper exterior solution to the function  $\tilde{A}_2 \mathcal{S}$  in the inner solution, the only contribution comes from  $\tilde{\Psi}_1$  (not  $\tilde{\Psi}_2$ ) and it can be shown that

$$\tilde{A}_2 = \frac{e^{-1}}{2} (-E_0 - \ln 2 + 2).$$

The eigenvalue contribution,  $c_1$ , is obtained by matching the interior solution to the lower solution to  $O(\epsilon^2)$ .

Now assume  $c_{1i} > 0$  and in the limit  $\mathcal{S} \rightarrow -\infty$ , eq. (A2.9) becomes:

$$\tilde{\Psi}_2 \sim \frac{e^{-1}}{2} \mathcal{S}^2 + e^{-1} (c_1 - \mathcal{S}) [\ln(-\mathcal{S}) - i\pi] - \tilde{A}_2(-\mathcal{S}) + \tilde{B}_2. \quad (\text{A2.10})$$

In the transition region,  $(c_0 - z) \gg \epsilon$ , the  $(-\mathcal{S})$  terms in (A2.10) must be matched to similar terms in the lower solution at  $O(\epsilon^2)$ . It can be shown that the only contribution comes from  $\epsilon \tilde{\Psi}_1$  and the match requires:

$$-\tilde{A}_2 - i\pi e^{-1} = e^{-1} \left( \frac{E_0 + \ln 2}{2} - 1 - 2B_1 e^2 \right).$$

Substituting for  $B_1$  and  $\tilde{A}_2$ , we find:

$$c_1 = i\pi e^{-2} + \frac{1}{2B} - e^{-2} \text{Ei}(z)$$

in agreement with Section II-3. In the transition and exterior regions the eigenfunction is unchanged from the solution found in that section.

For  $|z - c_0| \lesssim \epsilon$  the inner expansion must be used.

Appendix B1 - Matching  $\ln|\delta|$  Terms in the Near-Neutral Curve Expansion

Here we will show the matching of the  $O(|\delta|^{3/2} \ln|\delta|)$  terms in the near-neutral curve expansion. The exterior contribution  $|\delta| \Psi_2$  of eq.(2.4.11) will have terms of  $O(|\delta|)$  and  $O(|\delta|^{3/2} \ln|\delta|)$  in the transition region. This and higher order terms requires expansion of the interior solution in powers of  $|\delta|^{3/2} \ln|\delta|$ ,  $|\delta|^2 \ln|\delta|$ , etc. The  $O(|\delta|^{3/2} \ln|\delta|)$  contribution to the interior solution is designated  $\tilde{\Psi}_3$  and satisfies:  $\frac{\partial^2}{\partial s^2} \tilde{\Psi}_3 = 0$  so that  $\tilde{\Psi}_3 = a_3 s + b_3$ .

An additional contribution in the transition region at  $|\delta|^{3/2} \ln|\delta|$  comes from the exterior contribution,  $|\delta|^{3/2} \Psi_3$ , (see eq. (B2.2)). The total contribution from the exterior solution at  $|\delta|^{3/2} \ln|\delta|$  in the matching region is:

so that  $a_3 = \frac{\partial K}{2|\delta| B_1} (S - c_1)$  and  $b_3 = -c_1 a_3$ . Terms of  $|\delta|^2 \ln|\delta|$  appear in the  $|\delta|^2 \Psi_4$  contribution to the outer solution and matching to inner solutions of this order follow a similar analysis.

## Appendix B2 - Higher Orders of the Near-Neutral Curve Expansion

The higher order solutions of the near-neutral curve expansion are found here to determine  $c_2$  and  $c_3$  of eqs. (2.4.21,22). The  $|\delta|^{3/2}$  exterior solution,  $\Psi_3$ , is found from eq. (2.4.16) with

$$H_3(z) = -[\mathcal{L}_3 \Psi_0 + \mathcal{L}_2 \Psi_1 + \mathcal{L}_1 \Psi_2] e^{\alpha z}$$

and 
$$\mathcal{L}_3 = -\frac{B_1}{K} \left( \frac{c_3}{z^2} + \frac{2c_1 c_2}{z^3} + \frac{c_1^3}{z^4} \right).$$

Lower order solutions and operators are found in Section II-4. We

can show that 
$$H_3(z) = -\frac{B_1 c_3}{K z} - \frac{\delta}{|\delta|} c_1 \frac{\ln z}{z} + \frac{\delta}{|\delta|} \frac{c_1 K}{B_1 z^2}$$

and from eq. (2.4.16) that

$$\Psi_3 = -c_3 e^{-\alpha z} - \frac{\delta}{|\delta|} \frac{c_1 K}{B_1} (\ln z + 1) e^{-\alpha z}. \quad (B2.1)$$

The interior solution,  $|\delta|^{3/2} \tilde{\Psi}_3$ , is calculated from eq. (2.4.19)

with  $G_3(s) = -\tilde{\mathcal{L}}_2 \tilde{\Psi}_1 - \tilde{\mathcal{L}}_1 \tilde{\Psi}_2$  and  $\tilde{\mathcal{L}}_2 = 1 - \frac{c_2 B_1}{K(s-c_1)^2}$ .

We then find 
$$G_3(s) = s \left( \frac{B_1 \alpha}{K} + 1 - \frac{2\alpha}{K} \right) + c_1 \left( \frac{\alpha}{K} - 1 \right) + \frac{B_1 \alpha c_1^2}{K(s-c_1)}$$

and from eq. (2.4.19)

$$\begin{aligned} \tilde{\Psi}_3 = & \frac{\alpha^2}{2} s^3 - \frac{\alpha^2 c_1}{2} s^2 + \frac{\delta}{|\delta|} \frac{K}{B_1} (s-c_1) \ln(s-c_1) + \\ & \left[ -\frac{\delta}{|\delta|} \frac{K}{B_1} (1 + \ln(-c_1)) + a_3 \right] s + b_3 + \frac{\delta}{|\delta|} \frac{K c_1}{B_1} \ln(-c_1). \end{aligned} \quad (B2.2)$$

Including contributions from  $\Psi_0, \Psi_1, \Psi_2$ , and  $\Psi_3$  the outer

solution in the matching region is at  $O(|\delta|^{3/2})$ :

$$\frac{\alpha^2}{2} s^3 - \frac{\alpha^2 c_1}{2} s^2 + \frac{\delta}{|\delta|} \frac{K}{B_1} (s-c_1) \ln s + (c_2 \alpha + \alpha^2 c_1^2) s - c_3 - \frac{\delta}{|\delta|} \frac{c_1 K}{B_1}.$$

For  $s \gg 1$  the asymptotic behavior of  $\tilde{\Psi}_3$  of (B2.2) is:

$$\frac{\alpha^2}{2} s^3 - \frac{\alpha^2 c_1}{2} s^2 + \frac{\delta}{|\delta|} \frac{K}{B_1} (s-c_1) \ln s + \left[ \frac{\delta}{|\delta|} \frac{K}{B_1} (1 + \ln(-c_1)) + a_3 \right] s + b_3 + \frac{\delta}{|\delta|} \frac{K c_1}{B_1} (\ln(-c_1) - 1).$$

The matching of these relations requires:

$$a_3 = c_2 \alpha + \alpha^2 c_1^2 + \frac{\delta}{|\delta|} \frac{K}{B_1} (1 + \ln(-c_1))$$

and 
$$b_3 = -\frac{\delta}{|\delta|} \frac{K c_1}{B_1} \ln(-c_1) - c_3$$

and, after substituting into eq. (2.4.20), we find:

$$c_2 = -\frac{\alpha c_1^2}{2} - \frac{\delta K}{2|\delta| \alpha B_1} = -\frac{\delta}{|\delta|} \frac{K}{2B_1} \left[ \frac{K}{B_1} + \frac{1}{\alpha} \right].$$

To find the  $O(|\delta|^2)$  contribution,  $\tilde{\Psi}_4$ , to the outer solution, we first determine:  $H_4(z) = -[\mathcal{L}_4 \tilde{\Psi}_0 + \mathcal{L}_3 \tilde{\Psi}_1 + \mathcal{L}_2 \tilde{\Psi}_2 + \mathcal{L}_1 \tilde{\Psi}_3] e^{\alpha z}$  where  $\mathcal{L}_4 = -\frac{B_1}{K} \left( \frac{C_4}{z^2} + \frac{C_2^2}{z^3} + \frac{2C_1 C_3}{z^3} + \frac{3C_1^2 C_2}{z^4} + \frac{C_1^4}{z^5} \right) - \frac{\delta}{181} \left( \frac{C_2}{z^2} + \frac{C_1^2}{z^3} \right)$ .

Substituting for the other operators and eigenfunctions, we find:

$$H_4(z) = -\frac{B_1 C_4}{K z} - \frac{K}{B_1} \ln z - \frac{\delta}{181} \frac{C_2}{z} \ln z + \left( \frac{K}{B_1} \right)^2 \frac{1}{z} + \frac{\delta}{181} \frac{K}{B_1} \left( \frac{C_2}{z^2} + \frac{C_1^2}{z^3} \right) + \frac{\delta}{181} \frac{C_1^2}{z^2}.$$

from which we determine:

$$\tilde{\Psi}_4(z) = e^{-\alpha z} \left[ -C_4 + \left( \frac{K}{B_1} \right)^3 - \frac{\delta}{181} \frac{C_2 K}{B_1} (\ln z + 1) + \frac{\delta}{181} \frac{C_1^2 K}{2 B_1 z} - \left( \frac{K}{B_1} \right)^2 \left( -\frac{z (\ln z)^2}{2} + \frac{K}{B_1} \ln z + \frac{2K}{B_1} - z I \left( \frac{B_1}{K} z \right) \right) \right]$$

where  $I(x) = \int^x E_1(s) e^s s^{-2} ds$ .

The interior solution,  $|\delta|^4 \tilde{\Phi}_4$ , is found using:

$$G_4(s) = -\tilde{\mathcal{L}}_3 \tilde{\Psi}_1 - \tilde{\mathcal{L}}_2 \tilde{\Psi}_2 - \tilde{\mathcal{L}}_1 \tilde{\Psi}_3$$

with  $\tilde{\Psi}_3 = \frac{\delta}{181} \frac{1}{(s-c_1)} + \frac{B_1}{K} \left( \frac{C_3}{(s-c_1)^2} + \frac{C_2^2}{(s-c_1)^3} \right)$ .

After some substitution and algebra, we find from eq. (2.4.20):

$$\tilde{\Psi}_4 = -\frac{\alpha^3}{6} s^4 + \frac{\alpha^3 C_1}{6} s^3 - \left( \frac{C_2 \alpha^2}{2} + \frac{\delta}{2181} \left( \frac{K \alpha}{B_1} \right)^2 \right) s^2 + \left[ \frac{-\delta}{181} \frac{\alpha K}{B_1} (s-c_1)^2 - \frac{\delta}{181} \frac{\alpha C_1 K}{B_1} (s-c_1) - \alpha \frac{B_1 C_2 C_1^2}{K} \right] \ln(s-c_1) + \left( a_4 - \frac{\delta}{181} \frac{\alpha K C_1}{B_1} \ln(-c_1) - \alpha \frac{B_1 C_2 C_1}{K} \right) s + b_4 + \frac{\alpha B_1}{K} C_2 C_1^2 \ln(-c_1).$$

Following procedures similar to the  $O(|\delta|^{3/2})$  solution, it can

demonstrated that matching to  $O(|\delta|^2)$  requires:

$$a_4 = \alpha C_3 + \frac{\delta}{181} \frac{\alpha K C_1}{B_1} \ln(-c_1) + \frac{\alpha B_1 C_2 C_1}{K}$$

and  $b_4 = -C_4 + \left( \frac{K}{B_1} \right)^3 (E_0 + \ln B_1/K) - \frac{\alpha B_1}{K} C_2 C_1^2 \ln(-c_1) - \frac{\delta}{181} \frac{C_2 K}{B_1}$ .

From eq. (2.4.20) we then determine:

$$C_3 = \frac{\delta}{181} \frac{C_1}{2} \left[ \frac{-K}{B_1} (\ln(-c_1) + E_0 + \ln B_1/K) + \frac{1}{4\alpha} \left( \frac{\alpha K}{B_1} + 1 \right)^2 \right].$$

These eigenvalue contributions are used in Section II-4 to demonstrate the instability of the Green modes and determine the phase speeds of the Charney modes. Uniform approximations for  $\tilde{\Psi}$  can be calculated from the inner and outer expansions. The lowest order

imaginary part of  $\Psi$  for the Green modes is found from (B2.1) and (B2.2) since  $c_3$  has the first imaginary contribution to  $c$  for these modes. The lowest order expressions for the real and imaginary parts of  $\Psi$  for the Charney and Green modes are discussed in Section II-4.

## References

- Abramowitz, M. and I. Stegun, 1964: Handbook of Mathematic Functions. National Bureau of Standards. 1046 pp.
- Barcilon, A. and P. Gierasch, 1970: A moist, Hadley cell for Jupiter's cloud bands. J. Atmos. Sci., 27, 550-560.
- Barnes, J., 1979: Some aspects of baroclinic waves seen in the Viking Meteorology data. NASA Conference on Comparative Fluid Dynamics. Annapolis, Md.
- Beebe, R., A. Ingersoll, G. Hunt, J. Mitchell, and J. Miller, 1980: Measurements of wind vectors, eddy momentum transports, and energy conversions in Jupiter's atmosphere from Voyager 1 images. Geophys. Res. Lett., 7, 1-4.
- Blumen, W, 1979: On short-wave baroclinic instability. J. Atmos. Sci., 36, 1925-1933.
- Boville, B., 1980: Amplitude vacillation on an f-plane. J. Atmos. Sci., 37, 1413-1423.
- Burger, A.P., 1962: On the non-existence of critical wavelengths in a continuous baroclinic stability problem. J. Atmos. Sci., 19, 31-38.
- Charney, J.G., 1947: The dynamics of long waves in a baroclinic westerly current. J. Meteor., 4, 135-163.
- \_\_\_\_\_, 1959: On the general circulation of the atmosphere, The Atmosphere and The Sea in Motion. B. Bolin, ed., Oxford Univ. Press, 178-193.
- \_\_\_\_\_, 1963: A note on large-scale motions in the tropics. J. Atmos. Sci., 20, 607-609.
- \_\_\_\_\_, 1973: Planetary fluid dynamics. Dynamic Meteorology, P. Morel, ed., D. Reidel, 97-349.

- \_\_\_\_\_, and D. Straus, 1980: Form-drag instability, multiple equilibria, and propagating planetary waves in baroclinic, orographically forced, planetary wave systems. J. Atmos. Sci., 37, 1157-1176.
- Drazin, P.G., 1972: Nonlinear baroclinic instability of a continuous zonal flow of a viscous fluid. J. Fluid Mech., 55, 577-588.
- Eady, E.J., 1949: Long waves and cyclone waves. Tellus, 1, 33-52.
- Flasar, F.M. and P. Gierasch, 1978: Turbulent convection within rapidly rotating super adiabatic fluids with horizontal temperature gradients. Geophys. Astr. Fluid Dyn., 10, 175-212.
- Fullmer, J., 1979: The baroclinic instability of simple and highly structured one-dimensional basic states. Ph.D. Thesis, Dept. of Meteor., M.I.T., 235 pp.
- Gall, R., 1976: A comparison of linear baroclinic instability theory with eddy statistics of a general circulation model. J. Atmos. Sci., 33, 349-373.
- \_\_\_\_\_, R. Blakeslee, and R. C. Somerville, 1979: Baroclinic instability and selection of the zonal scale of the transient eddies of middle latitudes. J. Atmos. Sci., 36, 767-784.
- Gehrels, T., 1976: Results of the imaging photopolarimeter on Pioneer 10 and 11. Jupiter, Gehrels, ed., Univ. Ariz. Press, 531-563.
- Geisler, J. and R. Dickinson, 1975: External Rossby modes on a  $\beta$ -plane with realistic vertical wind shear. J. Atmos. Sci., 32, 2082-2093.
- \_\_\_\_\_, and R. Garcia, 1977: Baroclinic instability at long wavelengths on a  $\beta$ -plane. J. Atmos. Sci., 34, 311-321.
- Gierasch, P., 1973: Jupiter's cloud bands. Icarus, 19, 482-494.
- \_\_\_\_\_ and R. Goody, 1969: Radiative time constants in the atmosphere of Jupiter. J. Atmos. Sci., 26, 979-980.

- Gierasch P., A. Ingersoll, and D. Pollard. Baroclinic instabilities in Jupiter's zonal flow. Icarus, 40, 205-212.
- Gill, A.E., J. Green, and A.J. Simmons, 1974: Energy partition in the large-scale ocean circulation and the production of mid-ocean eddies. Deep-Sea Resch., 21, 499-528.
- Green, J., 1960: A problem in baroclinic instability. Quart. J.R. Met. Soc., 86, 237-251.
- \_\_\_\_\_, 1970: Transfer properties of the large-scale eddies and the general circulation of the atmosphere. Quart. J.R. Met. Soc., 96, 157-185.
- Grotjahn, R., 1979: Cyclone development along weak thermal fronts, J. Atmos. Sci., 36, 2049-2074.
- Hanel, R., B. Conrath, L. Herath, V. Kunde, and J. Pirraglia, 1980: Albedo, internal heat, and energy balance of Jupiter, preliminary results of Voyager infrared investigation. Submitted to Geophys. Res. Lett.
- Hart, J.E., 1973: On the behavior of large amplitude baroclinic waves. J. Atmos. Sci., 30, 1017-1034.
- \_\_\_\_\_, 1974: On the saturation amplitude for unstable baroclinic waves. Tellus, 26, 417-424.
- \_\_\_\_\_, 1976: The modulation of an unstable baroclinic wave field. J. Atmos. Sci., 33, 1874-1889.
- Hathaway, D., P. Gilman and J. Toomre, 1979: Convective instability when the temperature gradient and rotation vector are oblique to gravity. 1. Fluids without diffusion. Geophys. Astr. Fluid Dyn., 13, 289-316.
- Hess, S. and A. Panofsky, 1951: The atmospheres of the other planets. Compendium of Meteorology, A.M.S., 391-400.
- Held, I., 1978: The vertical scale of an unstable baroclinic wave and its importance for eddy heat flux parameterization. J. Atmos. Sci., 35, 572-576.

- Holopainen, E.O., 1970: An observational study of the energy balance of the stationary disturbances in the atmosphere. Quart. J.R. Met. Soc., 96, 626-644.
- Ingersoll, A.P., 1976: Pioneer 10 and 11 observations and the dynamics of Jupiter's atmosphere. Icarus, 29, 245-253.
- \_\_\_\_\_ and J. Cuzzi, 1969: Dynamics of Jupiter's cloud bands. J. Atmos. Sci., 26, 981-985.
- \_\_\_\_\_, R. Beebe, S. Collins, G. Hunt, J. Mitchell, P. Muller, B. Smith and R. Terrile, 1979: Zonal velocity and texture in the Jovian atmosphere inferred from Voyager images. Nature, 30, 773-775.
- Killworth, P., 1980: Barotropic and baroclinic instability in rotating stratified fluids. Dyn. Atm. Ocn., 4, 143-184.
- Kim, K., 1978: Instability of baroclinic Rossby waves; energetics in a two-layer ocean. Deep-Sea Rsch., 25, 795-814.
- Kuo, H.-L., 1952: Three-dimensional disturbances in a baroclinic zonal current. J. Meteor., 9, 260-278.
- \_\_\_\_\_, 1973: Dynamics of quasigeostrophic flows and instability theory. Adv. Appl. Mech., 13, 247-330.
- Lewis, J., 1969: The clouds of Jupiter and the NH<sub>3</sub>-H<sub>2</sub>O and NH<sub>3</sub>-H<sub>2</sub>S systems. Icarus, 10, 365-378.
- Lin, C., 1979: Eddy heat fluxes and stability of planetary waves. Ph.D. thesis, Dept. of Meteor., M.I.T., 147 pp.
- Lindzen, R., B. Farrell, and K.-K. Tung, 1980: The concept of wave over-reflection and its application to baroclinic instability. J. Atmos. Sci., 37, 44-63.

- Lorenz, E.N., 1967: The nature and theory of the general circulation of the atmosphere. W.M.O, 159 pp.
- Manabe, S. and F. Möller, 1961: On the radiative equilibrium and heat balance of the atmosphere. Mon. Wea. Rev., 89, 503-532.
- \_\_\_\_\_ and T. Terpstra, 1974: The effects of mountains on the general circulation of the atmosphere as identified by numerical experiments. J. Atmos. Sci., 31, 3-42.
- McIntyre, M., 1970: On the non-separable baroclinic parallel flow instability problem. J. Fluid Mech., 40, 273-306.
- \_\_\_\_\_, 1972: Baroclinic instability of an idealized model of the polar night jet. Quart. J.R. Met. Soc., 98, 165-174.
- Miles, J., 1964a: A note on Charney's model of zonal wind instability. J. Atmos. Sci., 21, 451-452.
- \_\_\_\_\_, 1964b: Baroclinic instability of the zonal wind. Rev. Geophys., 2, 155-176.
- \_\_\_\_\_, 1964c: Baroclinic instability of the zonal wind: Part II. J. Atmos. Sci., 21, 500-506
- Mullan, B., 1979: A mechanistic model for mid-latitude mean temperature structure. Ph.D. thesis, Dept. of Meteor., M.I.T. 248 pp.
- Newell, R., J. Kidson, D. Vincent, and G. Boer, 1972: The General Circulation of the Tropical Atmosphere and Interactions with Extratropical Latitudes. M.I.T. Press. Vol. I. 258 pp.
- North, G., 1975: Analytical solution to a simple climate model with diffusive heat transport. J. Atmos. Sci., 32, 1301-1307.
- Oort, A. and E. Rasmusson, 1971: Atmospheric Circulation Statistics. NOAA Prof. Paper 5, 323 pp.

- Oort, A. and J. Peixoto, 1974: The annual cycle of the energetics of the atmosphere on a planetary scale. J. Geophys. Res., 79, 2705-2719.
- Pedlosky, J., 1971: Finite amplitude baroclinic waves with small dissipation. J. Atmos. Sci., 28, 587-597.
- \_\_\_\_\_, 1975a: On secondary baroclinic instability and the meridional scale of motion in the ocean. J. Phys. Ocean., 5, 603-607.
- \_\_\_\_\_, 1975b: A note on the amplitude of baroclinic waves in the mid-ocean. Deep-Sea Res., 22, 575-576.
- \_\_\_\_\_, 1979a: Geophysical Fluid Dynamics. Springer-Verlag. 624 pp.
- \_\_\_\_\_, 1979b: Finite amplitude baroclinic waves in a continuous model of the atmosphere. J. Atmos. Sci., 1908-1924.
- Pfeffer, R., G. Buzyna, and W.W. Fowles, 1974: Synoptic features and energetics of wave-amplitude vacillation in a rotating, differentially-heated fluid. J. Atmos. Sci., 31, 622-645.
- Rossow, W., 1978: Cloud microphysics: Analysis of the clouds of earth, Venus, Mars, and Jupiter. Icarus, 36, 1-50.
- Sato, M. and J. Hansen, 1979: Jupiter's atmospheric composition and cloud structure deduced from absorption bands in reflected sunlight. J. Atmos. Sci., 36, 1133-1167.
- Simmons, A.J. and B. Hoskins, 1977: Baroclinic instability on the sphere: Solutions with a more realistic tropopause. J. Atmos. Sci., 34, 581-588.
- \_\_\_\_\_ and \_\_\_\_\_, 1978: The life cycles of some nonlinear baroclinic waves. J. Atmos. Sci., 414-432.
- Somerville, R., P. Stone, M. Halem, J. Hansen, J. Hogan, L. Druryan, G. Russell, A. Lacis, W. Quirk and J. Tenenbaum, 1974: The GISS model of the global atmosphere. Mon. Wea. Rev., 31, 84-117.

- Staley, D.O. and R. Gall, 1977: On the wavelength of maximum baroclinic instability. J. Atmos. Sci., 34, 1679-1688.
- Stone, P.H., 1966: On non-geostrophic baroclinic instability. J. Atmos. Sci., 23, 390-400.
- \_\_\_\_\_, 1967: An application of baroclinic stability theory to the dynamics of the Jovian atmosphere. J. Atmos. Sci., 24, 642-652.
- \_\_\_\_\_, 1970: On non-geostrophic baroclinic instability: Part II. J. Atmos. Sci., 27, 721-726.
- \_\_\_\_\_, 1971: The symmetric baroclinic instability of an equatorial current. Geophys. Fluid Dyn., 2, 147-164.
- \_\_\_\_\_, 1972: A simplified radiative-dynamical model for the static stability of rotating atmospheres. J. Atmos. Sci., 29, 405-418.
- \_\_\_\_\_, 1978a: Baroclinic adjustment. J. Atmos. Sci., 35, 561-571.
- \_\_\_\_\_, 1978b: Constraints on dynamical transports of energy on a spherical planet. Dyn. Atmos. Oceans, 2, 123-140.
- \_\_\_\_\_ and J. Carlson, 1979: Atmospheric lapse rates regimes and their parameterization. J. Atmos. Sci., 36, 415-423.
- \_\_\_\_\_ and D. Miller, 1980: Empirical relations between seasonal changes in meridional temperature gradients and meridional fluxes of heat. J. Atmos. Sci., 37, 1708-1721.
- Tenenbaum, J., 1976: Spectral and spatial energetics of the GISS model atmosphere. Mon. Wea. Rev., 104, 15-30.
- Vonder Haar, T. and V. Suomi, 1971: Measurements of the earth's radiation budget from satellites during a five-year period: Part I. Extended time and space means. J. Atmos. Sci., 28, 305-314.
- \_\_\_\_\_ and A. Oort, 1973: New estimate of annual poleward energy transport by Northern Hemisphere oceans. J. Phys. Ocean., 3, 169-172.

- White, A.A., 1977: The surface flow in a statistical climate model - a test of parameterization of large-scale momentum fluxes. Quart. J.R. Met. Soc., 103, 93-119.
- Williams, G.P., 1979: Planetary circulations: 2. The Jovian quasi-geostrophic regime. J. Atmos. Sci., 36, 932-968.
- \_\_\_\_\_ and J. Robinson, 1973: Dynamics of a convectively unstable atmosphere: Jupiter? J. Atmos. Sci., 30, 684-717.
- Yao, J.-S., 1980: Maintenance of quasi-stationary waves in a two-level quasi-geostrophic spectral model with topography. J. Atmos. Sci., 37, 29-43.

## BIOGRAPHICAL NOTE

The author was born in Miami, Florida on December 31, 1953. He attended public schools in Miami and Fort Lauderdale, Florida and received a B.S. degree in meteorology (Summa Cum Laude) from Florida State University, June 1975. He was awarded a UCAR Graduate Fellowship (1975-1977) and entered graduate school at M.I.T. in September, 1975.